Low-Energy Electron Interactions with Radiosensitisers and Hydrated Biomolecular Clusters

PhD-Thesis

submitted in partial fulfilment of the requirements for the degree of
Philosophiae Doctor (PhD)

to the
Faculty of Mathematics, Computer Science and Physics
of the Universität Innsbruck, Austria

and to the
Department of Physics
of the Universidade NOVA de Lisboa, Portugal

by
Rebecca Meißner, M. Sc. RWTH

First Supervisor:
Assoz. Prof. Dr. Stephan Denifl
Institute for Ion Physics and Applied Physics, Universität Innsbruck

Second Supervisor:
Prof. Dr. Paulo Limão-Vieira
CEFITEC, Department of Physics, Universidade NOVA de Lisboa

Innsbruck, November 2019

Abstract

Interactions of free electrons with kinetic energies between 0 eV and 100 eV with isolated biomolecules, (hydrated) radiosensitisers and doped neon clusters were studied, with focus on associative and dissociative electron attachment (AA and DEA, respectively) processes and electron ionisation. Radiosensitisers are applied in radiotherapy to enhance the ratio of damage to malignant compared to healthy cells. The principle of action on a physico-chemical stage is yet unknown and was studied within this thesis. Clusters are an intermediate state of matter between gaseous and solid state. In this thesis, cluster size dependencies and effects in doped clusters were studied. Two different mass spectrometry setups were used. Data from electron interactions with both gas-phase biomolecules and doped neon clusters was taken at the experimental apparatus in Innsbruck. A hemispherical electron monochromator enables high energy resolution measurements and is combined with a quadrupole mass filter. For the acquisition of hydrated radiosensitiser data, the setup in Prague was used. There, an electron gun is combined with a time-of-flight mass analyser. The clusters were in both cases produced via supersonic expansion. The radiosensitisers studied include 5-selenocyanato-2'-deoxyuridine (SeCNdU), nimorazole and misonidazole. All of them exhibit efficient electron capturing characteristics. SeCNdU is a potential radiosensitiser for highly proliferating cells and exhibits $(\text{SeU-yl})^{\bullet-}$ and CN^- as strongest fragment anions upon DEA, formed already at virtually 0 eV kinetic energy of the incoming electron. The formation of highly reactive species reinforce SeCNdU as a promising candidate. Nimorazole and misonidazole both exhibit an intense ion signal for the parent anion upon electron attachment. The absolute cross section at 0 eV electron energy was determined for nimorazole and is in the order of $3 \cdot 10^{-18}\,\text{m}^2$. For misonidazole, the absolute cross section is estimated to be of the same order of magnitude. The fragmentation channels upon DEA are at least one order of magnitude weaker, with NO_2^- being the most intense among them. They are further quenched upon hydration of the agent. It is suggested that the radiosensitising action is caused by the associative attachment channel and the DEA products only play a minor role, opposing previous assumptions. In case of the doped neon clusters, indications for the formation of a conduction band were found in the form of an energy barrier for incoming electrons: Comparing previous results of electron attachment to pure carbon dioxide clusters with neon clusters doped with CO_2 results in a blue-shift of the resonance positions by up to 0.8 eV. The effect depends on the size of the neon cluster. For molecular oxygen as the dopant, evidence was found that an incoming electron can first react with the neon cluster via an excitation event and subsequently attach to the dopant cluster. Both the study of radiosensitisers and of neon clusters should be continued. Further radiosensitisers should be studied in order to implement a model in which the effects on a physico-chemical stage are investigated and compared to radiosensitisers already in use. From such a study, potential new radiosensitisers can be derived. In the study of doped neon clustes, the solvation of different complexes with neon was investigated. Particularly, the formation of a conduction band, neon cluster - dopant interactions, and quenching of molecular processes in dopants by neon as a collision partner are analysed. The results require further investigations of additional dopants to unambiguously explain those effects.

Resumo

Nesta tese foram estudadas interacções entre electrões livres (com energias entre 0 e 100 eV) e biomoléculas isoladas, radio-sensibilizadores hidratados e agregados de néon dopados, para investigar os processos associativos e dissociativos por captura de electrões e ionização por impacto electrónico. Os radio-sensibilizadores são usados em radioterapia para amplificar o dano causado pela radiação no tecido maligno, reduzindo a dose sobre o tecido saudável. A etapa inicial do processo físico-químico é ainda pouco conhecida e foi estudada no âmbito da temática desta tese. Os agregados moleculares são vistos como estados intermediários da matéria entre a fase gasosa e a sólida pelo que estudámos a dependência dos processos causados em colisões com electrões com o tamanho dos mesmos. Para o estudo das interacções de electrões com moléculas biológicas em fase gasosa e em agregados moleculares de néon dopados com as mesmas, utilizou-se um dispositivo experimental instalado em Innsbruck, onde um monocromador hemisférico permite obter um feixe de electrões de elevada resolução na energia de colisão, e a detecção dos iões é efectuada por um espectrómetro de massa do tipo quadrupolo. Para os estudos dos radio-sensibilizadores foi utilizado um dispositivo experimental instalado em Praga, que consiste num canhão de electrões combinado com um espectrómetro de massa do tipo tempo-de-vôo. Os agregados moleculares em ambos os casos foram produzidos através da uma expansão supersónica. Os radio-sensibilizadores incluem o 5-selenocianato-2-deoxi uridina (SeCNdU), o nimorazol e o misonidazol. Todos estes exibem características de captura eletrónica eficiente. O SeCNdU é utilizado em células de proliferação rápida e após captura electrónica a $\sim$0 eV exibe como iões mais abundantes o $(\text{SeU-yl})^{\bullet-}$ e o CN^-. Acresce ainda que a formação de espécies reactivas deste composto confere-lhe uma característica muito relevante de utilização em processos de radiossensibilização. Nos processos de captura electrónica com nimorazol e misonidazol, estes exibem um sinal muito intenso na formação do anião progenitor. O valor da secção eficaz absoluta a 0eV de energia de colisão está na ordem de $3 \cdot 10^{-18}\,\text{m}^2$ e no caso do misonidazol o valor é da mesma ordem. Relativamente aos fragmentos aniónicos formados, as suas intensidades são pelo menos uma ordem de grandeza abaixo do anião progenitor, onde NO_2^- aparece como o mais intenso. No caso da hidratação destas moléculas, os canais de fragmentação aparecem suprimidos. Sugerimos, que o efeito radio-sensibilizador é causado pelo processo de captura electrónica e que os produtos dos canais dissociativos desempenham um papel menos relevante, o que contraria estudos anteriores. No caso de agregados de néon dopados, observou-se a presença de uma banda de condução resultante da barreira de potencial para os electrões incidentes. Comparando estudos anteriores de captura electrónica dissociativa em agregados moleculares de CO_2 com os agregados moleculares de néon dopados com CO_2, observamos que as energias das ressonâncias se deslocam cerca de 0,8 eV. O efeito depende do tamanho dos agregados de néon. No caso da dopagem com O_2, há evidência de que a interacção do electrão incidente com o agregado molecular de néon resulta primeiramente numa excitação deste e subsequentemente é capturado pelo dopante. Ambos os estudos sobre os radio-sensibilizadores e sobre os agregados de néon devem prosseguir. Outros radio-sensibilizadores deveriam ser estudados para construir um modelo em que os efeitos físico-químicos da acção da radiação sejam esclarecidos, com o objectivo futuro de desenvolver novos fármacos. Finalmente, os estudos em agregados de néon fornecem indicações para efeitos até agora não reportados, cuja explicação e compreensão dos mecanismos envolvidos necessitarão de estudos futuros.

Zusammenfassung

Die Wechselwirkungen von freien Elektronen mit einer kinetischen Energie zwischen 0 eV und 100 eV mit isolierten Biomolekülen, (hydratisierten) Radiosensitisern und dotierten Neonclustern wurde untersucht, mit dem Fokus auf assoziative und dissoziative Elektronenanlagerung (AA, DEA) und Elektronenionisation. Radiosensitiser werden in der Strahlentherapie eingesetzt um die Schädigungsverhältnis von bösartigen zu gesunden Zellen zu erhöhen. Das Wirkungsprinzip auf einer physikalisch-chemischen Ebene ist noch unbekannt und wurde im Rahmen der Dissertation untersucht. Cluster sind ein Aggregatzustand zwischen Gasphase und Festkörper, deren Eigenschaften erst noch klassifiziert werden müssen. In dieser Arbeit wurden Clustergrößeneffekte und Effekte in dotierten Clustern untersucht. Es wurden zwei verschiedene Massenspektrometrieversuchsaufbauten verwendet. Die Daten zu Wechselwirkungen zwischen Elektronen und isolierten Radiosensitisern und dotierten Neonclustern wurden mit dem experimentellen Aufbau in Innsbruck gemessen. Ein hemisphärischer Elektronenmonochromator ermöglicht Messungen mit hoher Elektronenenergieauflösung und ist mit einem Quadrupol Massenanalysator kombiniert. Die Daten der hydratisierten Radiosensitiser wurden an einem Aufbau in Prag gemessen. Dort wurden die Elektronen in einer Elektronenkanone erzeugt und die gebildeten Ionen wurden mit einem Flugzeitmassenspektrometer analysiert. In beiden Fällen wurden die Cluster mittels Überschallexpansion erzeugt. Die untersuchten Radiosensitiser sind 5-Selenocyanato-2'-deoxyuridin (SeCNdU), Nimorazol und Misonidazol. Für alle ist ein effizienter Elektroneneinfang charakteristisch. SeCNdU ist ein potentieller Radiosensitiser für schnell proliferierenden Zellen. $(\text{SeU-yl})^{\bullet-}$ und CN^- sind die stärksten Fragmentionen nach DEA und das bereits bei 0 eV kinetischer Energie des streuenden Elektrons. Die Bildung von hoch reaktiven Teilchen bestätigt SeCNdU als Radiosensitiserkandidat. Nimorazol und Misonidazol weisen beide ein intensives Ionensignal des Mutteranions auf nach AA. Der absolute Wirkungsquerschnitt wurde für Nimorazol bei 0 eV bestimmt und liegt in der Größenordnung $3 \cdot 10^{-18}\,\text{m}^2$. Der Wirkungsquerschnitt für Misonidazol wird in der gleichen Größenordnung geschätzt. Die Ionensignale der Fragmente nach DEA sind mindestens eine Größenordnung kleiner, wobei NO_2^- das stärkste Fragmentanion stellt. Unter Hydrierung werden die Fragmentierungskanäle noch weiter abgeschwächt. Im Gegensatz zu bisherigen Vermutungen weist dies darauf hin, dass die Wirkung der Radiosensitiser vom AA Kanal anstelle der DEA Kanälen ausgeht. Im Fall der dotierten Neoncluster wurden Hinweise auf die Bildung eines Leitungsbandes gefunden, das sich durch eine Energiebarriere für die Streuelektronen darstellt: Im Gegensatz zu vorherigen Studien reiner Kohlenstoffdioxidcluster weisen die aktuellen Ergebnisse an CO_2 dotierten Neonclustern eine Verschiebung der Resonanzpositionen um bis zu 0,8 eV auf. Der Effekt ist abhängig von der Größe des Neonclusters. Im Falle von molekularem Sauerstoff als Dotant wurde beobachtet, dass das Streuelektron zuerst mit der Neonmatrix wechselwirken kann bevor es mit dem Sauerstoffcluster reagiert. Sowohl die wissenschaftlichen Studien zu Radiosensitisern als auch zu Neonclustern sollten fortgesetzt werden. Zusätzliche Ergebnisse über Radiosensitiser sind nötig um ein Modell zu entwerfen, in dem basierend auf Elektronenanlagerungscharakteristika und dem Vergleich zu bereits angewendeten Radiosensitisern neue potentielle Kandidaten vorgeschlagen werden können. Bei der Untersuchung dotierter Neonclustern wurde die Solvatisierung von Molekülen analysiert. Hier wurden die Bildung eines Leitungsbandes im Neoncluster und Cluster-Dotanteninteraktionen beobachtet. Messungen mit zusätzlichen Dotanten sind notwendig, um diese Effekte eindeutig zu erklären.

Contents

1 Introduction **1**

2 Electron Scattering Processes **5**
2.1 Quantum Mechanical Formalism 5
2.1.1 Schrödinger Equation 5
2.1.2 Born-Oppenheimer Approximation 6
2.1.3 Potential Surface and Energy Levels 7
2.1.4 Franck-Condon Principle 8
2.1.5 Cross Section 10
2.2 Electron Ionisation 11
2.2.1 Basic Processes and Reaction Products 11
2.2.2 Ionisation Threshold and Cross Section 13
2.3 Electron Attachment 16
2.3.1 Formation of Temporary Negative Ions 16
2.3.2 Dissociative Electron Attachment 20
2.4 Clusters as Collision Partner 23
2.4.1 Cluster Properties 23
2.4.2 Electron Interactions with Clusters 26
2.4.3 Formation of Clusters 28

3 Mass Spectrometry Setups **33**
3.1 Wippi 34
3.1.1 Inlet System 35
3.1.2 Hemispherical Electron Monochromator 37
3.1.3 Quadrupole Mass Filter 39
3.1.4 Channel Electron Multiplier 41
3.1.5 Data Processing and Acquisition 42
3.1.6 Vacuum System 43
3.2 Cluster Beam Apparatus 43
3.2.1 Molecular Beam Source 44
3.2.2 Electron Gun 45
3.2.3 Time-of-Flight Mass Analyser 46
3.2.4 Multi-Channel Plate Detector 48
3.2.5 Vacuum System 49
3.3 Analysis and Calibration Methods 51
3.3.1 Data Analysis Software 51
3.3.2 Energy Scale Calibration 53

4 Relevance of Electron Interactions for Radiotherapy **57**
4.1 Radio-Physical Aspects 57
4.1.1 Interactions of Radiation with Matter 58
4.1.2 Secondary Electrons in Water 59
4.1.3 Direct and Indirect Radiation Effects 60

4.2 Radio-Biological Aspects 60
4.2.1 DNA, RNA, and Proteins 61
4.2.2 Cancer 62
4.2.3 Radiosensitisers 65
4.2.4 Time Scale of Events 68
4.3 Current Scientific Status 68
4.3.1 DNA Damage by Low-Energy Electrons 68
4.3.2 Experimental Considerations 69
4.3.3 Electron Interactions with Biological Building Blocks 70

5 Results and Discussion **73**
5.1 Biomolecules and Radiosensitisers 73
5.1.1 Imidazole, 2-Nitroimidazole, Histidine 74
5.1.2 SeCNdU 90
5.1.3 Misonidazole 108
5.1.4 Hydrated Misonidazole 124
5.1.5 (Hydrated) Nimorazole 137
5.2 Doped Neon Cluster 153
5.2.1 Cationic Mass Spectra upon Electron Ionisation 155
5.2.2 Electron Attachment to Neon Clusters Doped with CO_2 163
5.2.3 Electron Attachment to Neon Clusters Doped with O_2 172
5.2.4 Conclusions 179

6 Conclusion and Outlook **181**

Bibliography **185**

Acknowledgements **207**

Chapter 1

Introduction

Electron interactions are a wide field of research. Even though the electron was already discovered in 1897 by Sir J. J. Thomson [1], research concerning their interactions still attract broad interest. This is due to several factors: 1) The kinetic energy range of naturally occurring electrons extends over several orders of magnitude. Starting from essentially 0 eV (a possible source is pair production arising from a 1.022 MeV photon), the scale continues to the highest energetic electrons currently observed at above 1 TeV with astrophysical origins [2]. The interaction pathways of electrons with matter and their products highly depend on the kinetic energy of the electron. Current efforts often focus on both the production of energetically more precise electron beams and the more efficient production of low and high energy beams [3–5]. 2) The origin or sources of the unbound, or free electrons are diverse. Electrons are emitted both naturally, like in supernova remnants, or in specifically controlled process, e.g. within the thermal emission of electrons in a filament. 3) With the continuous definition of new interaction partners, new ideas and possible applications are constantly being investigated. Just to list a few examples, these include electron interactions with particles important in atmospheric processes or in radiotherapy, the application of electrons in focused electron beam induced deposition, and questions regarding basic research [6].

In this thesis, interactions of 0 - 100 eV electrons, here also referred to as low-energy electrons (LEEs), with molecules and clusters are studied. The compounds of interest as interaction partners can be divided into two groups. The first group integrates into the research field of the interactions of ionising irradiation with biomolecules and radiosensitisers. Thus, the research presented in this thesis covers an example of a study with an immediate application. For the second group, rare gas clusters of neon are doped with carbon dioxide, molecular oxygen, and (deuterated) water in order to study fundamental research questions regarding electron-cluster interaction processes. These include the determination of particularly stable cluster sizes and the possible formation of a conduction band in the neon cluster. The studies of doped neon clusters were added to the research topic of this thesis after its initial announcement and are thus not reflected in the title.

Radiotherapy is applied to kill tumour cells by irradiation. Most commonly, the primary beam consists of γ-rays, but depending on the application, also electron beams or proton beams are used [7]. During their interaction with the tissue, secondary species are produced, such as electrons and radicals. These can further interact with the surrounding environment of the cell [7]. Unfortunately, the radiation is not selective regarding healthy or malignant cells. This means that also healthy tissue is exposed to radiation. To increase the ratio of induced damage to malignant versus healthy cells, specialised agents, referred to as radiosensitisers, are administered. These are designed such that they specifically accumulate in tumour cells and sensitise them via an increased interaction with the primary and seconday particles of radiation [8, 9]. Depending on the tumour type, different agents are used which also act differently in

the cells. Their accumulation processes are not unambigiously explained yet. In recent years, the interactions of secondary electrons with both biomolecules and radiosensitisers gained a lot of interest and their importance was discussed [10–13].

In this thesis, electron interactions with biomolecules and radiosensitisers are studied. For the biomolecules, a reduced interaction rate would be favourable in order to keep them intact during irradiation. Since the working mechanisms of radiosensitisers on a physico-chemical stage are not fully understood yet, two types of radiosensitisers are investigated in this thesis. Specifically, the first group are radiosensitisers administered for tumour cells characterised by a high proliferation rate and the second group are radiosensitising agents accumulating in tumour regions characterised by a deprival of oxygen. Determining their principle of action could help the future development of radiosensitisers, where first the physico-chemical properties of the potential candidates could be investigated and new proposals being made based on those, which would have financial and temporal advantages. Clinical tests would still be required, but the chances of a successful outcome would be enhanced since inefficiencies from a physico-chemical point of view would be reduced.

The second topic of electron interactions covered in this thesis deals with fundamental research regarding rare gas cluster properties. In general, clusters are an intermediate state of matter between gas-phase and bulk matter [14]. Neutral rare gas clusters in particular are of interest since they are only bound by the weak van-der-Waals force. In this thesis, the solvation of neutral and charged complexes in a neon environment are studied. In matrix isolation spectroscopy, solid neon is already a common material for the host lattice [15, 16]. In this technique, a host material is frozen in order to form a lattice in which guest molecules can be trapped. Then, the trapped guest compounds are activated and their neutral and charged reaction intermediated can be investigated upon e.g. vibrational and electronic spectroscopy [15, 16]. From this data, the production, stabilisation and the matrix shift can be surveyed. Examples include the electronic spectroscopy of ytterbium in a neon matrix [17], and neon matrix isolation spectroscopy of CO_2 isotopologues [18]. To the author‘s knowledge, no matrix shift after electron attachment in a neon host lattice was reported so far. In contrast, doped neon clusters represent a suitable environment which allow for a detailed investigation of the matrix shift and solvation effects. Here, doped neon clusters are investigated regarding their state of matter and whether they form a conduction band, which would be a typical property of bulk matter rather than of a gaseous compound. Additionally, the neon cluster can serve as a stabilising environment for the dopant, and electron interactions with dopants embedded inside or attached to it can change in comparison to the isolated molecule in the gas phase or pristine clusters of the dopant, which is a further topic addressed in this thesis.

The thesis starts with an introduction into the physical background of electron interactions in chapter 2. After giving a brief overview of the quantum mechanical formalism relevant for the topics addressed in this thesis, the focus lies on electron ionisation and electron attachment processes. Furthermore, selected known properties of clusters are discussed, and electron interaction pathways of clusters are presented. Supersonic expansion is explained as an exemplifying cluster production process that is also applied in the experiments. In chapter 3, the experimental setups employed for studying electron interactions are elucidated. Two different instruments were used, both mass spectrometers. Since a common set of calibration and analysis tools are applied on the acquired data, an overview of these is provided at the end of chapter 3. Subsequently, the relevance of electron interactions with molecules of interest for radiotherapy is discussed

in chapter 4. The radio-physical and radio-biological aspects are presented before an overview of the current scientific status is provided. In chapter 5, the results are presented and discussed. This chapter is split into two parts, first covering the results on electron interactions with biomolecules and radiosensitisers, and in the second part presenting the data and knowledge obtained by the experiments with doped neon clusters. The thesis is summarised with a conclusion and outlook in chapter 6.

Chapter 2

Electron Scattering Processes

In classical physics, interaction processes of free electrons with atoms, molecules, clusters, or condensed matter can be divided into two different processes: Elastic and inelastic scattering. Elastic scattering describes processes in which only kinetic energy can be transferred among the collision partners. Above all, this means that the total kinetic energy and the internal energy of the particles are conserved as such. In contrast, during inelastic scattering, the kinetic energy of the collision partners is decreased or increased due to excitation or de-excitation of the collision partners, thus changing the internal energy of the system [19].

While classical physics provides appropriate descriptions of, for instance, scattering mechanics or energy conversation, it is not able to explain other phenomena like e.g. the Heisenberg uncertainty principle, the stability of atoms or discrete energy levels of atoms. For those effects, a quantum mechanical description is required. A short introduction into the basic concepts of the quantum mechanical formalism, physically motivated approximations and the description of atoms and molecules as well as their interaction with electrons within this principle is provided in section 2.1. For a detailed description, the interested reader is referred to the relevant literature, for example references [20–24]. Section 2.2 is dedicated to the formation of cations via electron ionisation. In section 2.3, electron attachment is discussed as an inelastic electron scattering processes leading to the formation of anions. While sections 2.1-2.3 cover electron scattering processes with atoms or molecules as collision partner, section 2.4 introduces clusters, which are an intermediate stage between atoms or molecules and bulk matter.

2.1 Quantum Mechanical Formalism

In quantum mechanics, a system is described by a wave function $\Psi(t, \boldsymbol{x})$. In 1801, Thomas Young's early version of a double-slit experiment gave a first indication for the wave nature of light [21]. Some years later, Louis de Broglie was the first to ascribe matter a wave nature, opposing the particle description of light prevailing in classical physics [21]. This led to the wave-particle dualism where light and matter possess both characteristics from particles and waves. In 1926, Erwin Schrödinger formulated a basic wave equation. As a postulate, it was not derived by fundamental principles but rather proved its validity by accurate predictions which were validated by experiments. A successful example application are the energy levels of the hydrogen atom [21].

2.1.1 Schrödinger Equation

The time independent Schrödinger equation describes the propagation of particles in space. Generally, the particle moves within a force field. If it is conservative, it is given

by the potential energy V. The Schrödinger equation is given by

$$\hat{H}\Psi = \left(\hat{T} + \hat{V}\right)\Psi = E\Psi \tag{2.1}$$

where $\hat{H}$ is the Hamilton operator composed of $\hat{T}$ and $\hat{V}$ which are the kinetic energy operator and the potential energy operator of the system, respectively. The total energy of the system is given by E. For a molecule with N nuclei which have the masses m_N and the charges $Z_N \cdot e$, and n electrons, each with mass m and charge e, the Hamiltonian is given by

$$\begin{aligned} \hat{H} &= \hat{T}_n + \hat{T}_N + \hat{V} && (2.2)\\ &= -\frac{\hbar^2}{2m}\sum_{i=1}^{n}\nabla_i^2 - \frac{\hbar^2}{2}\sum_{k=1}^{N}\frac{1}{m_N}\nabla_k^2 + V\left(\vec{r},\vec{R}\right) && (2.3) \end{aligned}$$

with $\vec{r}$ and $\vec{R}$ the position vectors of electrons and nuclei, respectively [20]. The first term describes the kinetic energy of the electrons $\hat{T}_n$ and the second term the kinetic energy of the nuclei $\hat{T}_N$. Neglecting interactions of electron and nuclear spins, i.e. considering a non-rotating, stationary molecule, the potential energy is composed of the Coloumb repulsion of the nuclei $\hat{V}_{NN}$, the attraction of electrons and nuclei $\hat{V}_{Nn}$, and the repulsion of the electrons among each other $\hat{V}_{nn}$ [20] and can thus be expressed by

$$\begin{aligned} \hat{V} &= \hat{V}_{NN} + \hat{V}_{Nn} + \hat{V}_{nn} && (2.4)\\ &= \frac{e^2}{4\pi\varepsilon_0}\left[\sum_{k>k'}\sum_{k=1}^{N}\frac{Z_k Z_{k'}}{|\vec{R_k} - \vec{R_{k'}}|} - \sum_{k=1}^{N}\sum_{i=1}^{n}\frac{Z_k}{|\vec{r_i} - \vec{R_k}|} + \sum_{i>i'}\sum_{i=1}^{n}\frac{1}{|\vec{r_i} - \vec{r_{i'}}|}\right] && (2.5) \end{aligned}$$

The real eigenvalues of the Schrödinger equation are interpreted as the electronic energy levels of the molecule and the squared wave function $|\Psi|^2$ as the probability of finding the particle, e.g. the electron, at a certain position in space. So far, vibrational and rotational modes are excluded from the potential and will be discussed in section 2.1.3. The Schrödinger equation can only be solved analytically for the hydrogen atom and atomic ions with only one electron. The H_2^+ cation describes a case of special interest, as freezing the bond length decreases the number of free parameters and makes it thus analytically solvable. For all other atoms and molecules, the Schrödinger equation becomes an n-body problem. Thus, physically reasonable approximations are necessary to simplify most problems.

2.1.2 Born-Oppenheimer Approximation

As the mass of a nucleus is about three orders of magnitude higher than the mass of the electrons, a valid approximation is to separate the interdependency between the nuclei and electron cloud motion: The nuclei typically move much more slowly than the electrons due to their higher masses, allowing one to assume that the electrons instantaneously adapt to a new constellation of nuclei. Thus, each nuclear configuration $\vec{R}$ exhibits a well-defined electron distribution. This approximation is known as the adiabatic or Born-Oppenheimer approximation. While the coupling of the electronic states to the movement of the nuclei is considered in the adiabatic approximation, the Born-Oppenheimer approximation sets this coupling to zero. Equations 2.1-2.4 give the electronic energy E_{el}. Applying the Born-Oppenheimer approximation to these

equations implies setting the terms $\hat{T}_N$ and $\hat{V}_{NN}$ constant since the internuclear distance is regarded constant. It should be mentioned that, although $\hat{T}_N$ and $\hat{V}_{NN}$ are set constant, $\hat{V}_{Nn}$ still includes both the electronic and nuclear coordinates as parameters. With these simplifications, it is possible to solve the Schrödinger equation numerically [20].

The total energy E of a stationary molecule is given by the sum of its electronic, vibrational, and rotational energies, E_{el}, E_{vib}, and E_{rot}, respectively:

$$E = E_{\mathrm{el}} + E_{\mathrm{vib}} + E_{\mathrm{rot}} \tag{2.6}$$

The vibrational and rotational energies are discussed in the next section. The translational motion is usually assumed to be classical.

2.1.3 Potential Surface and Energy Levels

The electronic energy resulting of the Schrödinger equation is quantised. Thus, discrete energy levels are formed, as shown in figure 2.1 a) for the case of the hydrogen atom. In the simplified picture of atoms with only one electron, the energy level of a state uniquely depends on the principle quantum number n. In contrast to the energy level, the states are the solution of the Schrödinger equation and are described by an additional three parameters. Those are the orbital angular momentum quantum number, $l = 0, 1, ...n-1$, the magnetic quantum number, $m_l = -l, .., -1, 0, 1, .., l$, and the spin quantum number $m_s = \pm 1/2$. Thus, states with different l, m_l, and m_s but the same n result in the same energy level. This implies that the energy levels are k-fold degenerated with

$$k = 2 \cdot \sum_{l=0}^{n-1} (2l + 1) = 2\,n^2 \tag{2.7}$$

and cannot be assigned to an individual state [20]. In case of atoms with more than one electron or for molecules, the solution of the Schrödinger equation becomes more complex and also the energy levels depend on all quantum numbers and are thus no longer degenerated. Additional to their energy value, the states of the electronic wave function are defined by symmetry characteristics of the corresponding wave function and the angular momentum of all spins and their coupling. According to Pauli's exclusion principle, two fermions, in this case electrons, cannot occupy the same quantum state, i.e. each set of quantum numbers n, l, m_l, and m_s is unique for each electron. In other words, a state defined by n, l, and m_l can be occupied by two electrons with opposite alignment of the electron spin ($m_s = \pm 1/2$). Hund's rule states that in the ground state the electrons occupying orbital of the same energy are arranged such that the total spin is maximised, still fulfilling Pauli's principle [21].

The electronic energy is a function of the nuclear coordinates and can graphically be represented as a hypersurface of the energy as a function of the intermolecular distance. In case of a diatomic molecule, this reduces to a one-dimensional potential energy curve, as shown in figure 2.1 b) for a ground state and an electronically excited state. The potential defines the classical boundaries of nuclear motion. The equilibrium distance R_e is at the point of the potential energy minimum, see figure 2.1 b). To separate the molecule into its individual atoms, the dissociation energy is given by

$$E_D = E_{\mathrm{el}}(R = \infty) - E_{\mathrm{el}}(R_e) \tag{2.8}$$

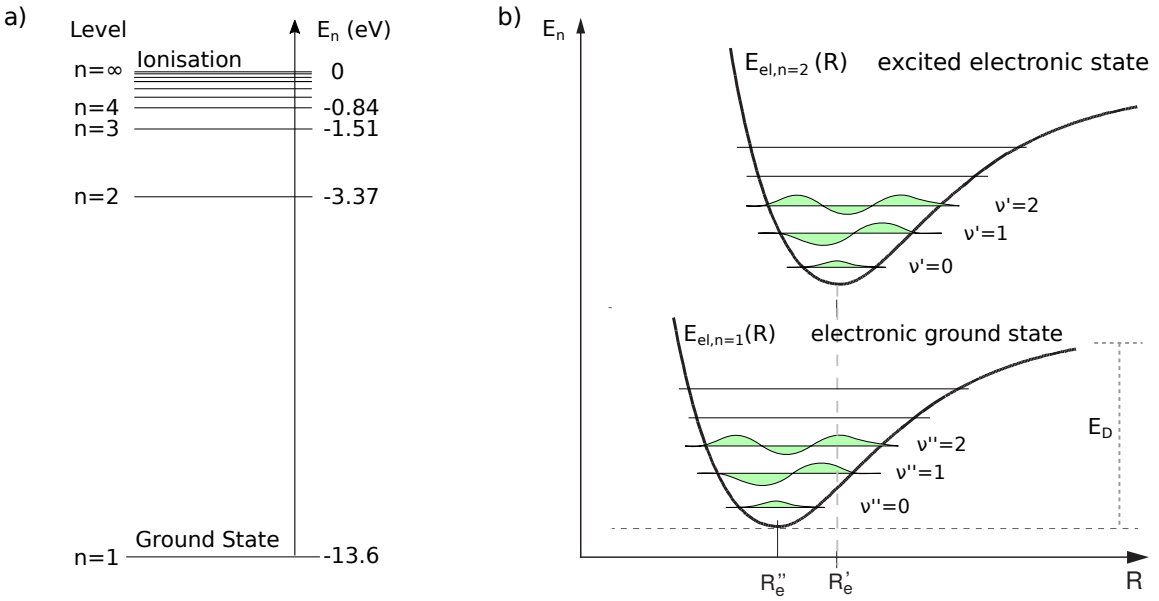

Figure 2.1: Electronic energy levels. a) Level scheme of the hydrogen atom as derived from the Schrödinger equation [20]. b) Schematics of the potential energy as a function of the intermolecular distance R for two separate electronic states. Each n contains a set of vibrational states, denoted with ν. The green areas mark the area below the vibrational wave functions Ψ_ν, adapted from [21].

In order to determine the vibrational energies and the vibrational wave functions Ψ_ν, or the probability density $|\Psi_\nu|^2$, the potential energy surface can be approximated by e.g. the harmonic oscillator or the Morse potential, in particular for the lower vibrational levels. The approximation is required as the exact analytical form of the according potential energy curve is usually unknown. Subsequently, the Schrödinger equation is solved for a free electron in that potential. As for the electronic states, this results in a set of discrete vibrational levels for each n. The resulting vibrational energy levels together with the schematic wave functions for the nuclei are shown in figure 2.1 b). Additionally, to each vibrational state belongs a set of quantised rotational levels. The energy ranges of electronic, vibrational, and rotational energy, E_{el}, E_{vib}, and E_{rot}, respectively, differ in orders of magnitude, following $E_{\mathrm{el}} > E_{\mathrm{vib}} > E_{\mathrm{rot}}$. The electronic energy is typically in the eV range, the vibrational energy amounts to $E_{\mathrm{vib}} = (0.01 - 0.5)\,\mathrm{eV}$, and the rotational energy lies in the range of $E_{\mathrm{rot}} < 0.01\,\mathrm{eV}$ [25]. It should be noted that these numbers are highly system-dependent.

The discrete energy levels in atoms and molecules entail that absorption or emission of energy is quantised, too. The more atoms a molecule is composed of, the more complex is the electronic configuration. To calculate the exact values of the energy levels, several additional corrections are required, including fine structure, lamb shift, and relativistic corrections. The interested reader is referred to the relevant literature [20–24].

2.1.4 Franck-Condon Principle

The Franck-Condon principle describes the transition of a molecule between different electronic states, including vibronic excitation, transition probabilities and intensities. The absorption or emission of energy in the form of electrons or photons and the related change of the electronic structure take place in a timespan much shorter than

the oscillation period of the nuclei. This implies that little to no change in the nuclear configuration occurs during the transition. Only afterwards will the positions and velocities of the nuclei adapt to the new electronic state [20]. In terms of the potential energy curve of the molecule, this implies that the transition is vertical. Hence, depending on the form and the relative position of the two electronic states involved, a vibronic excitation comes along with the transition, see figure 2.2 a) and b). The effective Franck-Condon region is restricted by the internuclear distance in the boundaries of the initial potential curve at the height of the given vibrational level, see green region in figure 2.2 a) [20, 26].

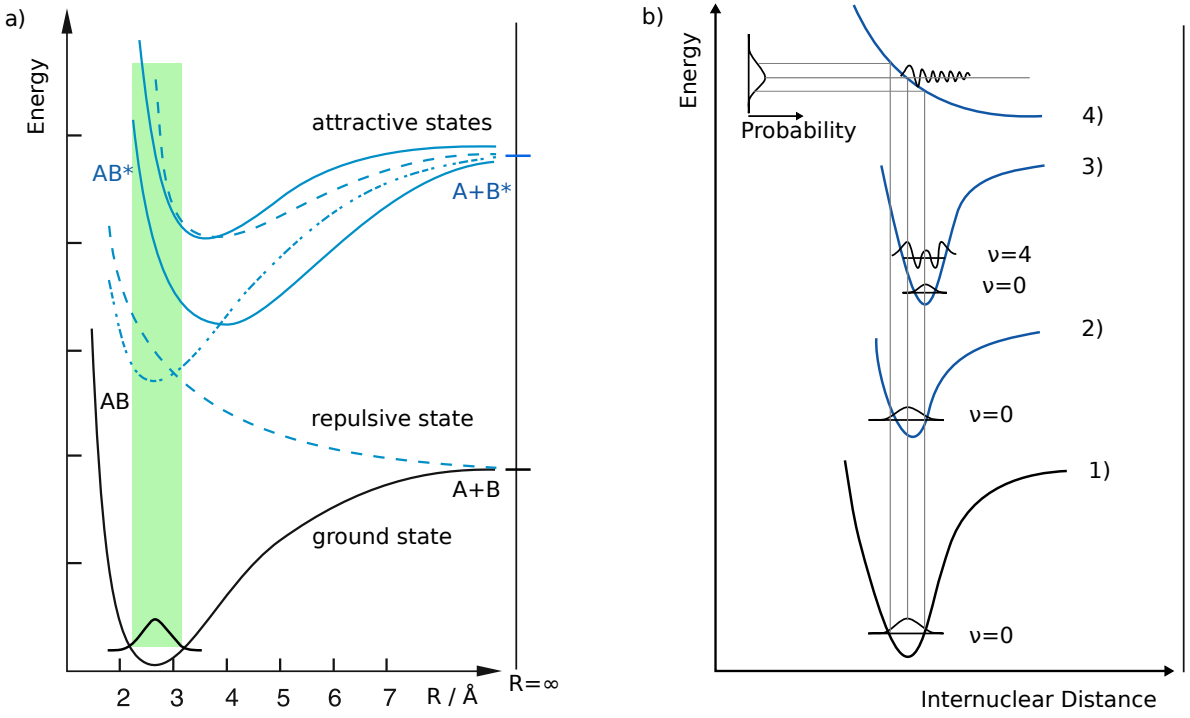

Figure 2.2: Schematic representation of the Franck-Condon principle. a) Some representative potential curves for a diatomic molecule AB. The green area represents the Franck-Condon region for a given initial internal energy. Attractive states are excited below and above their according dissociation limit. In the asymptotic limit (R$\rightarrow \infty$), the states leading to A+B, or A+B* collapse in each case, i.e. their enery is the same. Adapted from [20]. b) Example of overlap of wave functions: From 1) $\rightarrow$ 2) maximal overlap of wave functions with no vibronic excitation, in contrast to transition 1) $\rightarrow$ 3) where the overlap is smaller and hence the transition probability is reduced compared to the previous case. Both state 2) and 3) are bound states. State 4) is repulsive. The wave function has the form of an outgoing sine wave and the molecule dissociates. The case demonstrates the reflection principle as described in the text. Adapted from [26].

Within the quantum mechanical formalism, the transition probability $P_{a,b}$ from vibrational level a in the initial state to vibrational level b in the final state is given by

$$P_{a,b} \propto \left| \int \Psi_a \Psi_b^* \, \mathrm{d}R \right|^2 \tag{2.9}$$

where Ψ_a and Ψ_b are the respective vibrational wave functions and R the internuclear distance [26]. Commonly, this is referred to as overlap integral, as its value is max-

imised in the case of a maximal overlap of the wave functions in the initial and final states. Transitions can lead both into bound, or attractive, and unbound, or repulsive, states, see figure 2.2 b). If a transition occurs into an attractive state, discrete vibrational levels with finite wave functions are the solution of the Schrödinger equation. In contrast, in repulsive states or in attractive states above the dissociation asymptote, those conditions are replaced by a continuum of energy levels and continuously declining wave functions [26]. In case of a transition into one of the latter states, the main contribution originates from the overlap of the wave function of the initial state and the first few oscillations of the decaying sine in the final state. Taking advantage of this, and in order to achieve a reasonable level of complexity, the wave functions of those states are usually replaced by the Dirac δ function placed right at the position where the vibrational level intersects with the potential energy curve. Thus, the transition probability in equation 2.9 simplifies to $P_{a,b} \propto \Psi_a^2$ [26]. The method of replacing the wave functions by δ functions is also commonly applied for attractive states as it enables easy and fast predictions and analyses. Instead of overlapping wave functions of initial and final state, the wave function of the initial state is reflected on the potential energy curve of the final state, giving the probability distribution of the transition energies, see figure 2.2 b) [20, 26]. This is know as the reflection principle.

2.1.5 Cross Section

A measure for the probability of a scattering process between an electron and the target atoms or molecules is the cross section. Typically, it is given in units of cm^2, barn or $Å^2$. The cross section is a function of the impact energy E and describes the number of reactions N_r per projectile particle N_p within a given area A containing N_t target atoms or molecules [20]:

$$\sigma_{\text{tot}} = \frac{N_r}{N_p} \frac{A}{N_t} \tag{2.10}$$

All electron interaction processes, including excitation (σ_{exc}), ionisation (σ_{ion}), attachment (σ_{A}), can be theoretically assigned to a dedicated cross section σ_i. The total cross section is the sum of all these individual processes

$$\sigma_{\text{tot}} = \sum_{i \in \{\text{el,inel}\}} \sigma_i(E) = \sigma_{\text{el}}(E) + \sigma_{\text{inel}}(E) \tag{2.11}$$

$$\sigma_{\text{inel}} = \sum \sigma_{\text{exc}} + \sum \sigma_{\text{ion}} + \sum \sigma_{\text{A}} \tag{2.12}$$

where σ_{el} and σ_{inel} sum up all elastic and inelastic interactions, respectively [27].

The elastic cross section includes all processes where no quantum number defining the state of the system is changed [27]. In experiments, usually only the differential cross section can be measured, i.e. the cross section additionally depends on the polar and azimuthal angles of the scattered particle with respect to the incoming particle. However, pure elastic cross sections are not attained due to the limited angular resolution that does not allow to discriminate unscattered electrons to those elastically scattered in the forward direction, i.e. scattering angles close to zero. Additionally, the electron resolutions in such experiments do not permit to exclude a rotational excitation in the lower scattering angles, thus experimental cross sections are considered elastic. The total elastic cross section is given by the integration over the solid angle. During the inelastic processes, at least one quantum number changes [27]. Those comprise the

excitation events, including electronic, vibrational, and rotational excitation, ionisation processes, and electron attachment processes. The latter two will be described in detail in the two following sections.

2.2 Electron Ionisation

Electron ionisation (EI), or formerly electron impact ionisation, describes the process when an energetic electron collides with an atom, molecule, or cluster, transferring enough energy to cause the ejection of an electron from the target particle, thus ionising it. This interaction is a threshold process, i.e. it only occurs above a certain energy transferred from the scattering electron. The amount of energy transferred depends on the interaction time. Ideally, this time is long enough to transfer (nearly) all kinetic energy of the electron to the atom or molecule. In that case, precise measurements of the threshold region are accessible even without a laser. The lowest energy at which an ion is formed is the ionisation energy, IE. With increasing kinetic energy of the incoming electron, the probability for interaction, expressed by the cross section, also increases until it reaches a maximum and then decreases. While for atoms the only possible outcome of ionisation is forming a parent cation which is optionally electronically excited, molecules and clusters feature many more final products caused by e.g. fragmentation and recombination processes.

2.2.1 Basic Processes and Reaction Products

In the case of an arbitrary atom, X, the single interaction process can be written as

$$X + e_s\,(E_1) \longrightarrow X^+ + e_s\,(E_1 - IE(X) - E_2) + e_r\,(E_2) \tag{2.13}$$

where the incoming, or scattered electron e_s carries the initial energy E_1 and the released electron e_r carries the energy E_2. In order to produce the ion X^+, enough energy is required to first ionise the atom (i.e. the energy transferred to the atom must succeed the IE) and subsequently remove both electrons from the vicinity of the newly formed ion to avoid immediate recombination [20]. The ionisation energy is strongly dependent on the electron configuration of the atom. While alkalis with only one electron in the outermost, or valence, shell in general have the smallest IEs, nobel gases with a closed shell configuration feature the highest IEs [20]. Besides single ionisation, also multiple ionisation of the atom can occur, when at least two electrons are removed from the atom.

In contrast to atoms which cannot fragment further, in molecules additional ionisation processes can occur. Generally, they can be divided into two groups. Direct ionisation processes are those where the scattering and the released electron leave the ion either simultaneously or within a time span of up to 10^{-6} s [28]. These channels compete with indirect processes which involve a metastable intermediate state and are also summarised as autoionisation processes. Here, the incoming and the ejected electrons are released successively [28]. For both direct and indirect ionisation, either the stabilised molecular ion, also denoted as the parent ion, is formed, or dissociation leads to charged and neutral fragment products. Examples for such processes are listed below for a diatomic molecule AB.

Direct Processes

single ionisation	$e_s^- + \mathrm{AB} \rightarrow \mathrm{AB}^+ + e_s^- + e_r^-$	(2.14)
multiple ionisation	$e_s^- + \mathrm{AB} \rightarrow \mathrm{AB}^{n+} + e_s^- + n \cdot e_r^-$	(2.15)
inner shell ionisation	$e_s^- + \mathrm{AB} \rightarrow \mathrm{AB}_K^+ + e_s^- + e_r^-$	(2.16)
dissociative ionisation	$e_s^- + \mathrm{AB} \rightarrow \mathrm{A}^+ + \mathrm{B} + e_s^- + e_r^-$	(2.17)
ion-pair formation	$e_s^- + \mathrm{AB} \rightarrow \mathrm{A}^+ + \mathrm{B}^- + e_s^-$	(2.18)

Indirect Processes (with intermediate excited state)

autoionisation	$e_s^- + \mathrm{AB} \rightarrow \mathrm{AB}^{**} + e_s^- \rightarrow \mathrm{AB}^+ + e_s^- + e_r^-$	(2.19)
dissociative i. (metastable)	$e_s^- + \mathrm{AB} \rightarrow \mathrm{AB}^{+*} + e_s^- + e_r^- \rightarrow \mathrm{A}^+ + \mathrm{B} + e_s^- + e_r^-$	(2.20)
multiple i. (metastable)	$e_s^- + \mathrm{AB} \rightarrow \mathrm{AB}^{+*} + e_s^- + e_r^- \rightarrow \mathrm{AB}^{n+} + e_s^- + n \cdot e_r^-$	(2.21)

It should be noted that the incoming electron e_s^- transfers energy to the compound AB which results in a decreased kinetic energy of the electron e_s^- after the interaction. For most examples given above, only one electron is removed from the target compound during the ionisation event. Nevertheless, multiple ionisation processes can also occur, resulting in the ejection of n electrons and leaving the compound multiply charged, see equation 2.15. A typical timescale for an ionisation event amounts to the low femtosecond range [29]. Generally, it is most common to remove an outermost shell or valence electron as their binding energies are smaller than for inner-shell electrons. An exception is given in equation 2.16 where an inner-shell, e.g. the K-shell, or core electron is removed to form an ion. These reactions usually lead to an unstable product due to the extremely high excitation energy (e.g. to remove a core electron of the carbon atom, an energy of more than 300 eV is required). This generally leads to subsequent processes like the release of an Auger electron and the subsequent dissociation of the ion AB_K^+ [28]. Unlike the case for atoms, which cannot further dissociate, in molecules bonds can break and the atoms even rearrange. Thus, the final state can often contain a fragment cation and at least one neutral fragment, see equation 2.17.

A special case is the ion-pair formation as described in equation 2.18. Both positive and negative fragments are formed at the same time and no electron is released from the compound. During the electron interaction, the molecule is brought into a repulsive excited state via an electronic transition and subsequently fragments. The process is accessible in a large energy scale as any excess energy is carried away by the electron [28].

As can be seen in equations 2.19, autoionisation is a two-stage process via a superexcited bound state. This can either be neutral, AB^{**}, or ionised, AB^{+*}. The existence of such a state is bound to the presence of several degrees of freedom, which can take up the energy in form of e.g. electronic excitation, vibration, and rotation [28]. After a finite amount of time in the order of a few nuclear vibrations (fs), the energy is redistributed and the superexcited state couples to a continuum state, finally resulting in ionisation. Since only specific amounts of energy can be stored in AB^{**} or AB^{+*}, it is a resonant process [28].

While the initial state, i.e. the target molecule, and the ionisation method, i.e. electron ionisation, remains per definition the same for all processes within this group of interactions, the final state products can be summarised in different groups. The first classification is between neutral and charged products. While the definition for a neutral particle is unambiguous, the charged products comprise those with single and multiple

charges. Further, each atom or molecule or its according (fragment) ion either has an open- or closed-shell electron configuration. Those with an unpaired electron have a higher likelihood of further interaction with the surrounding and are called radicals. They are commonly denoted with a dot as for example in $A^{\bullet}$ for neutrals or $B^{+\bullet}$ for cations. As described earlier, the molecule either stabilises after the electron ionisation process or dissociates. The former gives rise to the parent cation with lifetimes $\geq 10^{-5}$ s [28, 29], which is regarded as stable in the context of mass spectrometry. The other option is that the molecule dissociates. Some molecules contain one or more functional groups which are defined moieties responsible for specific chemical properties, and thus are worth considering as a unit. For those molecules, three possible dissociation products, or fragments, can be classified: 1) The fragment contains the functional group of the molecule; 2) a bond cleavage of the functional group occurs and only part of it forms the fragment; 3) one or more rupture(s) occur and additionally may give rise to a newly structured fragment by rearrangement. The fragments observed and their relative abundances give an indication of the strength of the bond which has to be cleaved in order to give rise to the particular ion [28]. Besides the bond dissociation energies and rearrangements, several other factors influence the reaction pathways, including the electron configuration and the ionisation potentials [28]. Also the timescales of events vary for the different types of fragmentation. While direct bond cleavages require between some picoseconds and several tens of nanoseconds, rearrangements can take up to microseconds [29]. It is worth noting that a fragmentation pathway can consist of several steps of individual fragmentation, i.e. a product can further dissociate into competing channels. Also, one final state may be reached by several different pathways. There are no simple rules to predetermine the relative abundances of the fragment products.

2.2.2 Ionisation Threshold and Cross Section

Electron ionisation is a threshold process, requiring a minimum amount of energy to be transferred to an atom or molecule to access a specific channel. This can graphically be represented by the potential energy curves as described in section 2.1.3 and shown in figure 2.3 for a diatomic molecule. Assuming an electron impact energy of 70 eV, an electron requires only approximately 10^{-16} s to travel a distance of 1 nm, equivalent to about 5 bond lengths. Hence, even for large molecules the time range for an electron to pass the whole molecule does not exceed the low femtosecond range. In contrast, molecular motions occur at much longer timescales, such as translational thermal motion with velocities in an order of 100 m/s ($\widehat{=}10^{-11}$ s for travelling 1 nm) or vibrations with frequencies below 10^{14} Hz ($\widehat{=}10^{-14}$ s for a vibration) [29]. Thus, the Born-Oppenheimer approximation holds and together with the Franck-Condon principle, see section 2.1.2 and 2.1.4, this implies that the molecules can be assumed to be at rest, not changing their position during the transition from the molecular ground state to the ionic state. Thus, the transition is vertical.

As has already been described in section 2.1, the Franck-Condon region is small but finite, typically in the range between 0.1 Å - 0.2Å. The following specifications are made [26], see figure 2.3. The **vertical ionisation energy (VIE)** is defined as the energy difference between the lowest electronic state in its ground vibrational and rotational levels to the ionic state, possibly at excited vibrational and rotational levels, reached in a vertical transition. The **adiabatic ionisation energy (AIE)** describes the energy of the transition from the molecular ground state to the ionic ground state, thus

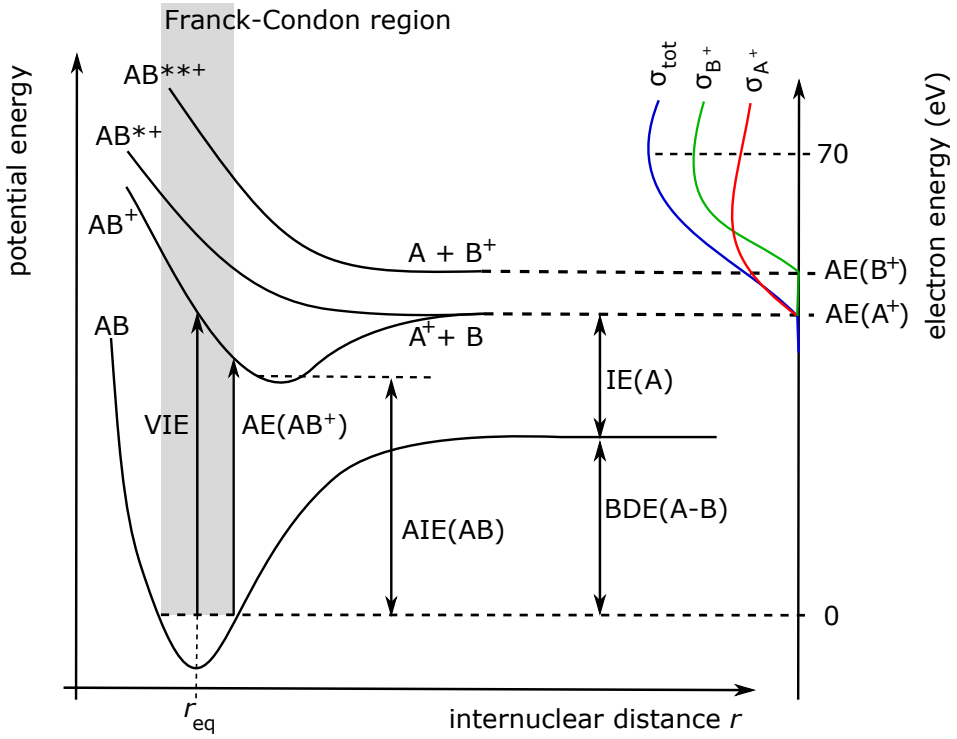

Figure 2.3: Schematic representation of the electron ionisation process. Potential curves of the electronic ground state AB and three exemplary ionic states are shown. The molecular cation is formed with an onset value of AE(AB^+) but dissociates for values above AE(A^+), which is also the threshold for the formation of A^++B. The energy dependence of the cross section are shown on the right side. Adapted from [30].

in most cases it goes along with a shift of nuclei positions. Depending on the shift, no overlap between the vibrational wave functions of the intial ground state and ionic ground state need to exist within the Franck-Condon region, making the AIE not accessible for experimental data taking, as illustrated in figure 2.4 a). Instead the so called **appearance energy (AE)** is measured. It is defined as the minimal energy value required for the formation of a given cation. In case of a molecular parent cation (AB^+ in figure 2.3), it is the minimal VIE, graphically located at the outer end of the effective Franck-Condon region. In excitation processes leading to dissociative states, fragmentation occurs leading to e.g. A^++B, and the dynamics of the process change. Thus, the appearance energy is given by the sum of the **bond dissociation energy (BDE)**, which is the energy required to dissociate the neutral molecule, and the ionisation energy of the neutral fragment A. Thus, electron ionisation experiments define upper limits for the AIE [26].

It is worth noting that another experimental challenge in determining the correct AIE is that most molecules are not encountered in their vibrational and rotational ground states, but are rather thermally excited to some higher level. This effect lowers the measured value compared to the theoretical value if the correct temperature is not taken into account.

Each reaction has a characteristic ionisation energy threshold. Even those channels resulting in identical final state products may have different onset values. At this value, the interaction probability, expressed by the cross section, is still close to zero. With increasing energy, the process becomes more and more probable, see figure 2.4 b). Since the final state contains three particles or more, excess energy can be transformed into

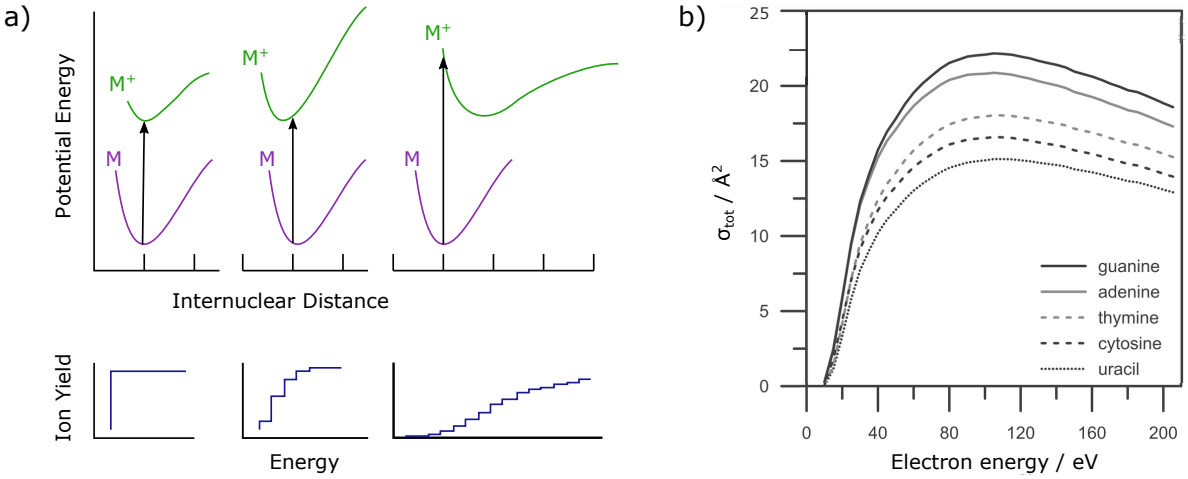

Figure 2.4: Ionisation cross sections. a) Schematic representation of the potential energy curves (top) and threshold region (bottom) for a diatomic molecule AB and corresponding ion AB^+ at different internuclear distances upon electron and photo-ionisation. Taken from [31]. b) Experimental data for the nucleic acids of DNA and RNA upon electron ionisation. Taken from [32].

kinetic energy. During the vertical transition from the ground state to the (excited) state of the ion, the required amount of energy to ionise the state is transferred and the remaining difference to the impact energy is transformed into kinetic energy. At some point, the cross section curve reaches a plateau at around 70-100 eV. Here, the de Broglie wavelength of the electron matches the typical bond length of most molecules which is approximately 0.14 nm. After that, the interaction probability starts decreasing as the de Broglie wavelength gets smaller and the electron becomes increasingly transparent for the molecule [33]. In a more graphical picture, the decrease is due to the reduced interaction time between electron and molecule.

The total cross section includes all electron ionisation processes and exhibits a similar progression as an individual process. At the threshold value, only one process is accessible. Usually, the non-dissociative channels feature the lower threshold values and are thus the first to be observed. With increasing energy, further pathways become accessible until reaching a cross section plateau region, see figure 2.3. With the decrease in cross section of the individual channels, also the total cross section declines.

The cross section description in the energy region near the ionisation energy is a complex many-body problem concerning both quantum and classical physics [34]. It was first described by Wigner [35] with a classical approach. The basic idea was to separate the escape process from the reaction zone which finally implicated that the threshold is a result of missing kinetic energy for a complete separation of the final state particles [34]. While Wigner described a two particle final state only, Wannier extended the theory to a collinear system with a three particle final state, including one ion and two electrons escaping in opposing directions [36]. Finally, this led to a simple power law to describe the threshold region,

$$\sigma(E) = c \cdot (E - \mathrm{AE})^n \tag{2.22}$$

$$n = \frac{1}{4}\left[\left(\frac{100\,Z - 9}{4\,Z - 1}\right)^{1/2} - 1\right] \tag{2.23}$$

where c is a constant and Z is the charge of the cation [34, 36]. The definition for n is

only valid for sequential ionisation of atoms or ions and is calculated for $Z = 1$, 2, and 3 to $n = 1.127$, 1.056, and 1.036, respectively. This finding has been confirmed by various quantum chemical theories applying different degrees of (semi-)classical approximations [37, 38]. Wannier generalised the threshold description later to multiple ionisation, motivated by a simple classical phase space argument [39]. The form of equation 2.22 remains the same, only the exponent changes to, in general, slightly higher values when Coulomb interaction between the electrons are considered [34]. At the same time, Geltman treated the problem with a quantum mechanical approach, coming to the same result as Wannier [37]. Hence, the dependency is also know as n^{th} power Wannier-Geltman threshold law.

Most organic molecules have an electron ionisation threshold which varies between around 6-12 eV. When conducting experiments, the plateau region around 70 to 100 eV is favourable for data taking since all atoms or molecules can be ionised. Additionally, measurements are stable towards slight deviations in electron energy, also making them more comparable with data from other experimental setups [29].

2.3 Electron Attachment

Electron attachment is an electron interaction process accessible at even lower energies than electron ionisation, basically from 0 eV electron energy and upwards. It is a resonant process, and as a consequence only a defined amount of energy can be absorbed by the target particle. This is given by the energy difference between neutral and anionic state within the Franck-Condon region. A quasi-bound negatively charged state is formed with a finite lifetime. This transition state, also referred to as resonance, can be formed via different mechanisms which can be divided according to the potential energy, trapping mechanism, and excitation state. For non-radiative stabilisation processes, the intermediate state can either decay back into the neutral parent under the emission of an electron (autodetachment), be stabilised (associated attachment), or fragment into negatively charged and neutral products (dissociative electron attachment).

2.3.1 Formation of Temporary Negative Ions

Electron interaction processes have already been classified at the beginning of chapter 2 into elastic and inelastic scattering events. They belong into the group of direct scattering, describing an interaction of an incoming electron with a target particle under single collision conditions, resulting in a deviation in the path of the electron. Electron attachment can be further specified as resonant scattering. Instead of only spending the transit time in the vicinity of the atom or molecule, the electron is temporarily trapped by the target particle. A quasi-bound negative state is formed. As this corresponds to a change of the electronic configuration, transition rules between states apply. Since the interaction is fast, the Born-Oppenheimer approximation, see section 2.1.2, can be applied and the Franck-Condon principle, section 2.1.4, describes a vertical transition from the continuum state to the discrete quasi-bound state [3, 40]. Thus, the capture of the electron is only allowed for specific electron energy values. The formed state is commonly referred to as a transient negative ion (TNI), or simply as a resonance. In contrast to electron ionisation, this is a one particle intermediate state which entails that excess energy from the electron cannot be transformed into kinetic energy of the products, thus the complete energy (kinetic energy and electron affinity) is stored in the TNI, resulting in resonances rather than a threshold process.

The lifetime of the resonances depends on the electronic structure and molecular size, the electron energy, the surrounding medium of the TNI, and its internal energy [3, 28]. It covers more than 13 orders of magnitude from as short as a few vibrational periods on the order of 10^{-14} s (e.g. N_2^- resonance at 2-3 eV [41]), over some µs for larger polyatomic molecules (e.g. SF_6^- resonance at 0 eV [42]) and can extend to some tens of ms (e.g. C_{60}^- at 10 eV [43]) [28]. Even the shortest lifetimes extend the transit time of an electron in direct scattering by approximately two orders of magnitude. According to Heisenberg's uncertainty principle

$$\Gamma \geq \frac{\hbar}{\tau} \tag{2.24}$$

with Γ the linewidth of the resonance, $\hbar$ the Planck constant, and τ the lifetime, the shortest lifetime results in the broadest linewidth [3]. The final width of the resonance is mainly defined by the Franck-Condon region [3] as will be seen in section 2.3.2.

The formation and stability of a TNI is additionally described by the following terms, also illustrated in figure 2.5 a): The **adiabatic electron affinity (EA)** is defined as the energy difference between the neutral molecule with an additional electron at rest in the continuum and the molecular anion, both in their electronic, vibrational and rotational ground states [3, 28]. Thus, the EA of a neutral atom is equivalent to the ionisation energy of the respective anion [3, 40]. Per definition, the EA is positive if the anionic state lies below the neutral state and negative otherwise. A positive EA implies that the according anion is thermodynamically stable [3, 40]. Another important parameter is the **vertical attachment energy (VAE)**, given by the energy difference of the vertical transition between the neutral molecular in its ground state plus electron at rest in the continuum and molecular anion state. Since only vertical transitions are accessible, this corresponds to the appearance energy of the anion. The **vertical detachment energy (VDE)** describes the reverse process, i.e. to eject an electron in a vertical transition from the anionic state [28, 40].

Classification of Resonances

Different mechanisms lead to the formation of a TNI. They can be classified into single particle (1p) and two particle - one hole (2p1h) resonances. During the interaction resulting in 1p resonances, the incoming electron is added into a (virtual) molecular orbital (MO) while the electron configuration of the already present electrons from the target particle remains unchanged. In case of 2p1h resonances, in addition to the attachment, an electronic excitation occurs. Thus, two electrons occupy a formerly virtual molecular orbital, see figure 2.6 [3]. Hence, they are also referred to as core excited resonances. A further differentiation of resonances addresses the capturing mechanism. In shape resonances, the potential energy surface is responsible for the formation of the TNI, capturing the electron by a potential well, or the shape of the interaction potential. The anionic state comprises a higher energy level than the according neutral, usually resulting in short lifetimes. For Feshbach resonances, the kinetic energy of the electron couples to the vibrational states. Those resonances lie energetically below the according neutral state, mostly leading to stable molecular anions [3, 28]. Due to their stability towards detachment processes, shape and Feshbach resonances are also referred to as open and closed channel resonances, respectively. Combining both classifications finally differentiates between four transient negative ions: Core excited shape resonance, core excited Feshbach resonance, shape resonance, and vibrational Feshbach resonance, see

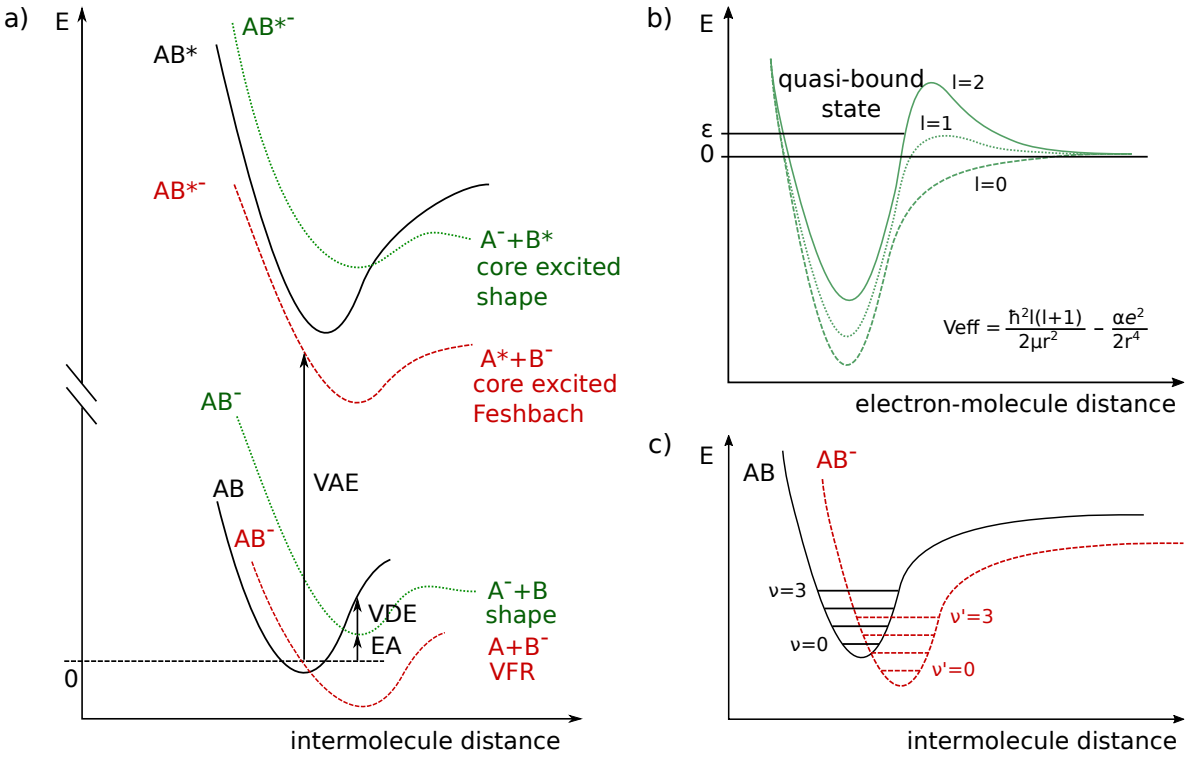

Figure 2.5: Schematic potential energy curves for electron attachment. a) The formation of core excited or 2p1h resonances require higher energy than in case of 1p resonances. Shape resonances (green) lie above the according neutral state while (vibrational) Feshbach resonances (red, VFR) lie below the neutral. The vertical attachment energy (VAE), the vertical detachment energy (VDE), and the adiabatic electron affinity (EA) are indicated exemplary. Adapted from [44]. b) The effective potential for a shape resonance for different angular quantum momentum l values. The electron with energy ϵ is trapped by the potential well in a quasi-bound state. Adapted from [44]. c) A vibrational Feshbach resonance exhibits a positive electron affinity, thus having the minimum of its anionic state below the neutral one. Adapted from [28].

figure 2.5 a)-c) and figure 2.6.

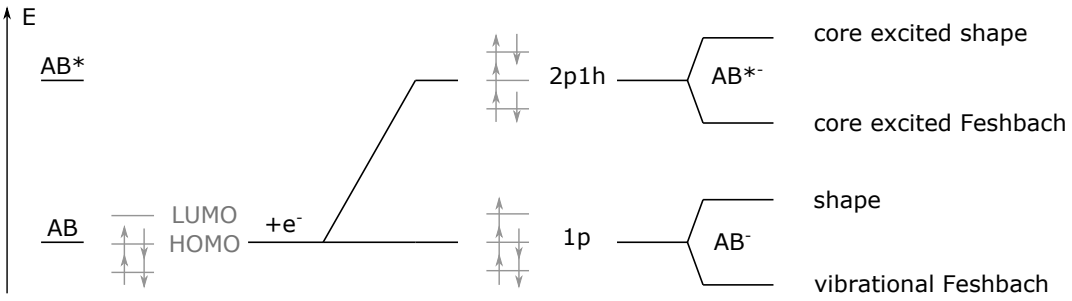

Figure 2.6: Classification of transient negative ion resonances including a schematic representation of the occupation of molecular orbitals. 2p1h represent the two particle one hole, or core resonances and 1p include single particle resonances.

Shape resonances belong to the single-particle resonances where the additional electron is trapped by a potential well originating from electron-molecule interactions [28]. It arises from the combination of two effects, the attractive long-range polarization potential $V_{\text{attractive}}$ caused by charge induced dipole interactions [44], and the repulsive

short-range centrifugal pseudo-potential $V_{\text{repulsive}}$, giving

$$V_{\text{eff}} = V_{\text{attractive}} + V_{\text{repulsive}} = -\frac{\alpha\, e^2}{2\, r^4} + \frac{\hbar^2\, l\,(l+1)}{2\,\mu\, r^2} \tag{2.25}$$

where α is the molecular polarizability, e the electron charge, r the distance between electron and molecule, l the angular momentum quantum number, and $\mu \approx m_e$ the reduced mass, i.e. approximately the mass of the electron. As can be seen in figure 2.5 b), no potential barrier forms for $l = 0$. Thus, no s-wave electrons can be bound to form a TNI via this mechanism. Electrons of higher angular momentum quantum number tunnel through the barrier and form a quasi-bound state [3]. According to equation 2.25, the minimum of the energy well is pushed up by increasing angular momentum, too. As mentioned above, a shape resonance lies energetically above the neutral ground state. Hence, the lifetime of such a TNI is rather small, depending mainly on the size of the potential well and the internal energy of the anion. Typically, the lifetime is within the range of $10^{-15} - 10^{-10}$ s [28]. Nevertheless, exceptions exist, as in the case of SF_6 where, due to intramolecular vibrational energy redistribution, lifetimes of above 10^{-5} s are observed [44].

Core-excited shape resonances follow the basic formation mechanism for shape resonances. The difference is that they belong to the 2p1h resonances, meaning that an excited state of the neutral target particle is involved instead of the ground state. While the effective potential, lifetime and energetic considerations follow the same principles [28], a major difference exists concerning the decay of the TNI. The additional electron in the negatively charged and excited molecule occupies a virtual state which couples stronger to neutral excited states than to the ground state. Thus, it is more likely that an excited anionic molecule remains instead of reverting back into the initial ground state [45].

Vibrational Feshbach resonances (VFR), see figure 2.5 c), belong to the single-particle resonances which energetically lie below the neutral ground state, thus having a positive electron affinity. The incoming electron causes a strong coupling between electronic and vibrational degrees of freedom, causing the break-down of the Born-Oppenheim approximation. This is accompanied with rearrangements in the electronic structure which finally hinders autodetachment to a certain level [3, 28]. Hence, the lifetimes are typically longer than for shape resonance, exceeding 10^{-6} s for polyatomic molecules [28]. If those states are accessible, they typically have high cross sections which can reach values above $10^{-14}\,\text{cm}^2$ [28]. Dipole-bound state, i.e. states of high polarisability and large dipole moment binding the electron by large range dipole interactions, can also give rise to Feshbach resonances [44].

Core-excited Feshbach resonances are comparable to VFR but with the difference that they are 2p1h resonances, thus including electronic excitation of the target molecule. If an electron from the neutral molecule is excited into a higher lying molecular orbital, the positive charge from the nuclei is less screened. The incident electron is bound by this field, creating the TNI. Autodetachment is not simply accessible anymore as soon as the TNI is in an vibrational state ν' which is energetically lower than the vibrational level ν from the excited state [28, 44]. Instead, either the TNI decays into the ground state, which is unfavourable due to the rearrangements in the electronic structure, or a relaxation into another excited state occurs via a two electron transition.

2.3.2 Dissociative Electron Attachment

In general, the decomposition pathways of a transient negative ion can be summarised by four processes:

$$\mathrm{AB}^{(*)-} \xrightarrow{\tau_{AD}} \mathrm{AB}^{(*)} + e^- \qquad \text{Autodetachment} \tag{2.26}$$

$$\mathrm{AB}^{(*)-} \xrightarrow{\tau_{RS}} \mathrm{AB}^- + h\nu \qquad \text{Radiative Stabilisation} \tag{2.27}$$

$$\mathrm{AB}^{(*)-} \xrightarrow{\tau_{DEA}} \mathrm{A} + \mathrm{B}^- \qquad \text{Dissociative Electron Attachment} \tag{2.28}$$

$$\mathrm{AB}^{(*)-} \xrightarrow{\tau_{AA}} \mathrm{AB}^{\#-} \qquad \text{Associative Attachment} \tag{2.29}$$

The denotation * is used for electronically excited molecules whereas # is applied for vibrationally excited molecules. After the initial interaction, where the electron attaches to the molecule forming a negatively charged state, the system relaxes according to its potential surface into a new minimum. This can either be a repulsive state or a state forming a potential minimum. Together with the energy of the incident electron, the potential energy of the state defines the energetically favourable final state of the reaction. Finally, the lifetimes of the processes are pivotal for whether autodetachment (AD), radiative stabilisation, or associative or dissociative electron attachment (AA, DEA) occurs.

Radiative stabilisation is typically a slow process compared to the other three. A photon with $h\nu$ is irradiated by the charged, possibly excited molecule, carrying away the excess energy in order to stabilise the molecular anion. The lifetime τ_{RS} is in the order of $10^{-9} - 10^{-8}\,\mathrm{s}$ [3], but they can be even longer for infrared photons from vibrationally excited systems and extend to the ms regime [46]. Additionally, it competes with internal conversion mechanisms, also stabilising the molecular anion. Hence, only low contributions arise from this process.

Autodetachment does not lead to a charged final state as the temporarily attached electron is re-emitted, thus the neutral molecule remains after the process. When the TNI state relaxes following the potential curve (or surface), energy from the electronic degrees of freedom is transferred to kinetic energy of the nuclei. In AD, this excess energy is released by the emission of an electron. As for the attachment process, the detachment is a vertical process following the Franck-Condon principle. Thus, it is only accessible until the potential surfaces of molecular ground state and TNI cross [3], see figure 2.7. While AD can extend to lifetimes τ_{AD} of up to µs in case of some polyatoms, the prevailing time domain lies in the range between $10^{-15}\,\mathrm{s}$ and $10^{-10}\,\mathrm{s}$ [3].

Associative attachment can occur under the condition that the potential energy surface of the anionic state contains a minimum and crosses the potential curve belonging to the ground state at energies close to 0 eV. This is typically the case for Feshbach resonances. In this case, a metastable anion is formed. The excess energy arising from the relaxation into the potential minimum is converted by intramolecular vibrational energy redistribution (IVR), see figure 2.7. This strong coupling of electronic and vibrational degrees of freedom stabilises the molecular anion, preventing autodetachment and dissociation [44].

Dissociative electron attachment (DEA) describes the process where the TNI fragments into one negatively charged ion and at least one neutral fragment, forming the according counterpart. In order for it to happen, the lifetime of the TNI must be long enough to allow the relaxation beyond the crossing point of the TNI and ground potential curve. After that point, DEA and AA are the only possible pathways. If the potential curve is either repulsive or the excess energy cannot be converted by IVR,

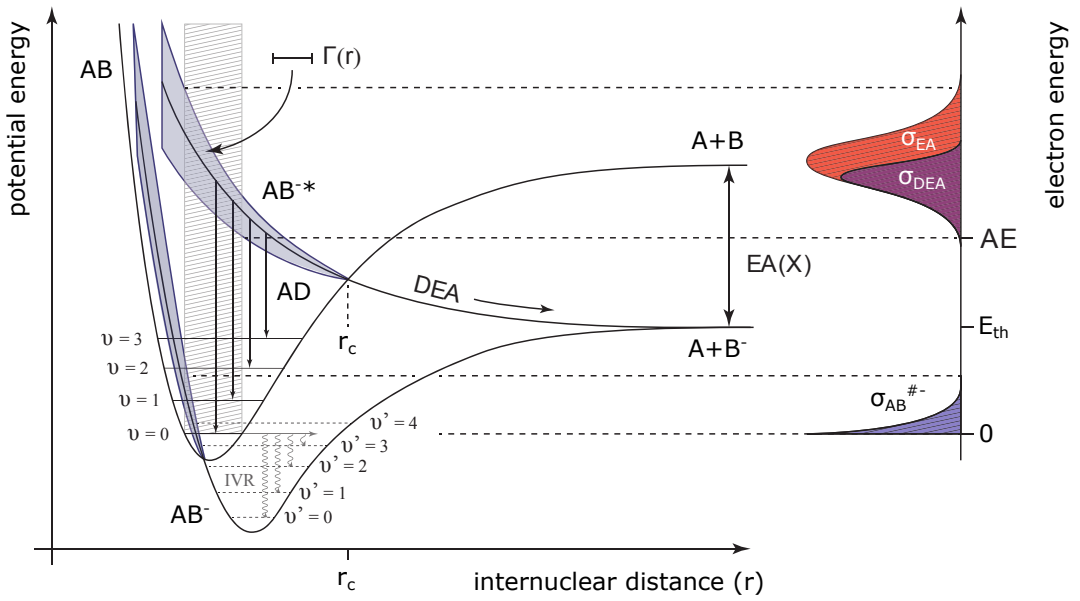

Figure 2.7: Schematic representation of the electron attachment process, including a ground state, a repulsive anion potential and a Feshbach resonance potential. Attachment can only occur in the Franck-Condon region, depicted by the shaded area, autodetachment is possible until the crossing distance r_c and afterwards only DEA. The ion yield curves derived from the reflection principle are also shown. Adapted from [47].

the charged molecule dissociates. In figure 2.7 this is shown schematically for a bond cleavage between A and B. Considering a complex molecule, simple bond breakage, as represented by equation 2.29 for a diatomic bond, is not the only possible outcome. Additionally, rearrangement reactions can give rise to neutral and charged fragments with bonds not present in the parent molecule. This is usually coupled to a considerable amount of vibrational degrees of freedom which extend the lifetime of the TNI, thus enabling complex reactions [44]. The prevailing time scale of DEA and AA reactions is in the order of $10^{-14} - 10^{-12}$ s and thus in the same range as AD [3]. Hence, autodetachment reactions compete with associative and dissociative attachment decomposition pathways. Only the concrete timescales of available channels for a given molecule define the process actually occurring [44].

The cross section of DEA processes is related to the attachment cross section σ_A, already defined in equation 2.12 by

$$\sigma_\mathrm{DEA} = \sigma_\mathrm{A} \cdot \exp\left(-\frac{\tau_\mathrm{DEA}}{\tau_\mathrm{AD}}\right) \tag{2.30}$$

where the exponential term expresses the survival probability of the TNI before reaching the crossing point r_c, see figure 2.7. τ_DEA is the characteristic time to dissociate the TNI and τ_AD is the autodetachment lifetime [3, 44]. The absolute cross section is often not accessible by experimental measurements. Instead, the ion yield curve is measured, which is (ideally) proportional to the cross section. The line shape is defined by the reflection principle as described in section 2.1.4 and shown in figure 2.8: The squared vibrational wavefunction of the ground state is reflected in the potential curve of the anionic state. Thus, the width of the resonance is given by

$$\Gamma_\mathrm{DEA} = \frac{\partial V_f}{\partial r} \cdot |r_2 - r_1| \tag{2.31}$$

where V_f is the anionic state potential curve, r the internuclear distance and r_1 and r_2 the borders of the effective Franck-Condon region, see figure 2.8 [3]. The exact position and shape is influenced by the autodetachment lifetime [44]. The DEA cross section can also be expressed by a Gaussian profile related to the width of the resonance by

$$\sigma_{\mathrm{DEA}} \sim \exp\left(-\frac{4(\epsilon-\epsilon_0)^2}{\Gamma^2_{\mathrm{DEA}}}\right) \tag{2.32}$$

where ϵ_0 is the energy where the ion yield curve has its maximum. The DEA cross section can exceed the geometrical cross section [3].

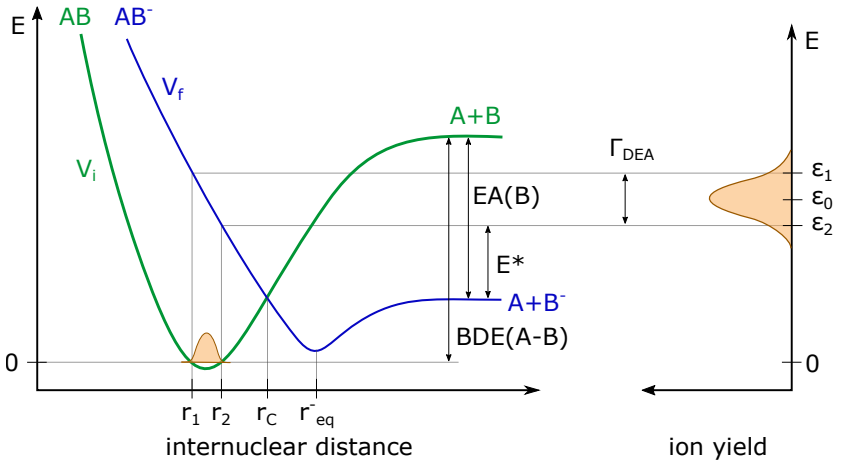

Figure 2.8: Schematic illustrating the reflection principle for a shape resonance and including major definitions: EA is the electron affinity, BDE is the bond dissociation energy, and E* the excess energy required for the observation of the fragment. Adapted from [3, 44].

The thermochemical threshold for the DEA reaction $\mathrm{AB} + e^- \rightarrow \mathrm{A} + \mathrm{B}^-$ can be calculated by

$$\Delta H_0 = \mathrm{BDE(A\text{-}B)} - \mathrm{EA(B)} \tag{2.33}$$

which is also know as the minimum heat of formation and where BDE(A-B) is the dissociation energy of the A-B bond and EA(B) the electron affinity of B [3]. In experiments, instead of measuring ΔH_0, a higher energy is measured given by

$$\epsilon = \mathrm{BDE(A\text{-}B)} - \mathrm{EA(B)} + E^* \tag{2.34}$$

where E* is the excess energy released in the form of translational and internal energy of the fragments [3]. The energy range is given by $\epsilon_2 < \epsilon < \epsilon_1$ defined by the reflection principle.

In the case of polyatomic molecules, the reaction pathways and according threshold energies are more complex as multiple bond cleavages and rearrangement processes can occur. Furthermore, some channels involve reaction barriers which are caused by transition states which are energetically higher than the threshold. For those, additional energy is required shifting the ion yield curves towards higher energies.

It should be noted that, besides DEA, ion pair formation also gives rise to negative ions. While DEA is a resonant process mainly occurring at low energies (up to 20 eV), ion pair formation is a threshold process at slightly higher energies, see section 2.2.1.

2.4 Clusters as Collision Partner

The previous sections have shown that interaction processes increase in complexity with size. In addition to the study of electron interactions with atoms and molecules, those processes can be investigated with clusters as collision partners. Clusters are aggregates of atoms or molecules with a defined, yet variable number of components. Thus, they act as link between isolated molecules or atoms and bulk matter, forming the transition between molecular physics and physics of condensed matters proving them interesting for the study of their intrinsic properties. This includes questions concerning size dependent properties, such as if a band structure and band gap can already be observed in clusters and if so, from which size onwards. Also, clusters can serve as micro-environments into which other atoms or molecules can be embedded. In those cases, clusters mimic the natural surrounding of the dopant molecule or simply serve as cooling environment for the dopant. For example, helium clusters represent cold environments in astrophysical studies and water clusters are employed for biologically interesting purposes. Subsequently, selected cluster properties are described before focusing on van-der-Waals and rare gas clusters, which were studied in the course of this thesis. Additionally, differences in the interaction mechanism with electrons compared to single atoms or molecules are reviewed.

2.4.1 Cluster Properties

Clusters often neither obtain the properties from isolated molecules nor from bulk matter, but form a category of their own. While a molecule has a defined composition, including a fixed number of atoms, a cluster can principally contain an arbitrary number of atoms or molecules above one and below several tens of thousands [14, 48]. A possible classification divides clusters among their size: Small clusters with in between 3 and around 12 constituents have only surface molecules and the concepts from molecular physics are applicable at low temperatures. Medium sized clusters contain between around 12 and 100 molecules and already feature a great amount of isomers; their properties strongly depend on size and molecular concepts become invalid. Large clusters with 100 to 1,000 components feature the transition to characteristics attributed to bulk matter. Clusters with more than 1,000 molecules or atoms already have several, although not all, properties from condensed matter [48].

Also the structure, uniquely defined for a molecule, can adopt different (locally) stable forms. Exact consideration identifies those as different chemical isomers, but usually they are encapsulated for further analysis [14, 48]. Some configurations at a specific number of constituents can prove especially stable. These are usually referred to as magic numbers [49]. Comparing clusters to bulk matter, it is apparent that for a cluster of a limited number of components, a large number of them are on the surface, while for bulk matter most of them are inside. For isolated molecules, the individual energy levels of the states are well separated. For clusters, the number of levels increases with size, resulting in a reduced spacing between the levels. Finally, for bulk matter those levels merge into energy bands. It is important to note that the energy gap between the valence and conduction band still prevails, which is one of the properties of bulk matter that separates isolators from conductors.

Clusters can be divided according to their binding properties into van der Waals, molecular, hydrogen-bonded, ionic, valence, and metal clusters. Table 2.1 shows a classification of clusters including the binding type and energy.

Cluster Type	Type of Binding	Binding Energy [eV]	Examples
van der Waals	dispersion forces	<0.3	$(Ar)_n$, $(CO_2)_n$
molecular	dispersion forces, weak electrostatic forces	0.3-1	(organic M)$_n$ $(I)_n$
hydrogen-bonded	intermolecular hydrogen bridges	0.3-0.5	$(H_2O)_n$, $(HF)_n$
ionic	heteropolar bonding	2-4	$(NaCl)_n$, $(CaF_2)_n$
valence	covalent bonding	1-4	C_n, S_8, As_4
metal	metallic bonding	0.5-3	Na_n, Al_n, Cu_n

Table 2.1: Cluster classification based on their binding properties. Adapted from [50].

Rare Gas Clusters

Rare gases are characterised by their closed electronic shell configuration and high ionisation energies. In a molecular orbital diagram, as shown for helium in figure 2.9, this translates to a cancellation of bonding and anti-bonding molecular orbitals which are occupied. Thus, the net covalent bonding is zero and only weak interatomic interactions prevail.

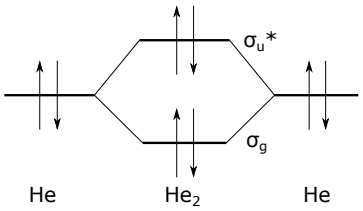

Figure 2.9: Molecular orbital (MO) diagram for the helium dimer. The arrows mark the spin orientation of the electron occupying the MO. $\sigma_u{}^*$ and σ_g identify the anti-bonding and bonding MO, respectively. Adapted from [51].

For rare gas, or van der Waals clusters, the attractive force is the dispersion force. The electron distribution exhibits random fluctuations which induce an electric dipole in the atom. As a consequence, the neighbouring atoms are influenced, reacting by inducing a dipole of their own. This effect gives rise to the long-range van der Waals force binding the atoms together in a cluster. The dispersion potential can be described by the London formula

$$V_{\text{disp}} = -\frac{3\,\alpha^2\,IE}{4\,(4\,\pi\,\epsilon_0)^2}\cdot\frac{1}{r^6} \tag{2.35}$$

where α is the atomic polarisability, IE the ionisation energy, and r the interatomic distance [51]. At short interatomic distances, the repulsion caused by electrostatic effects and the Pauli exclusion principle dominate and are usually modelled by an $\exp(-\alpha r)$ or a $1/r^{12}$ potential. In combination with the attractive dispersion force, the latter one gives rise to the Lennard-Jones potential

$$V_{\text{LJ}} = \epsilon\left[\left(\frac{r_0}{r}\right)^{12} - \left(\frac{r_0}{r}\right)^{6}\right] \tag{2.36}$$

where r_0 is the equilibrium distance and ϵ the potential well, or binding energy of the

dimer [48, 51]. It can directly be related to the temperature T below which dimers can form by

$$\epsilon = k \cdot T \tag{2.37}$$

where k is the Boltzmann constant [51]. If the temperature exceeds the calculated one, the thermal energy is high enough to overcome the potential well and decompose the dimer into its components. In table 2.2, the binding potentials of the rare gasses are listed together with the dimerisation temperature, the boiling and melting point. The gerenal trend reveals that heavier gases possess higher maximal formation temperatures. This is due to their higher polarisability and lower ionisation potentials which causes an increase in the dispersion forces according to equation 2.35 and thus a higher binding energy according to equation 2.36. But even for xenon the van der Waals binding force of 24 meV is still low compared to e.g. the covalent bond of the hydrogen molecule of 4.8 eV [51].

Element	ϵ / meV	T / K	T_b / K	T_m / K
He	0.9	11	4.2	0.95
Ne	4	42	27.1	24.6
Ar	12	142	87.3	83.8
Kr	17	200	120	116
Xe	24	281	165	161

Table 2.2: Well depth ϵ for rare gas dimers and the according dimerisation temperature T as calculated from equation 2.37, boiling point T_b, and melting point T_m. Values from [51].

The values stated in table 2.2 only refer to dimers. For higher order clusters, many body forces have to be considered, too. The interested reader is referred to the literature as they contribute only with minor effects [51].

Hydrogen-Bonded Clusters

Hydrogen-bonded clusters are constituted of molecules composed of one or more hydrogen atom(s) and at least one electronegative atom. A well-known example are H_2O-clusters. The molecule itself is internally bound by strong covalent forces. The hydrogen bond forms between the hydrogen of one molecule and the electronegative atom Y of a second molecule of the same type. This linkage can be represented in the form X-H$\cdots$Y, where X is the atom the hydrogen is bond to via a covalent bond within the molecule. The interaction itself is of electrostatic nature. While the electronegative atom Y supplies a lone electron pair and is thus carrying a fractional negative charge δ^-, the hydrogen carries a positive fractional charge δ^+. Those opposite sign charges attract each other, forming the hydrogen bond. The typical binding energy is at 250 meV about 10 times higher than van der Waals bonds, but also an order of magnitude weaker than covalent bonds [51]. It should be noted that besides covalent and hydrogen bonds, further intermolecular forces are present in most molecular clusters held together by hydrogen bonds. Those include dispersion interactions, dipole-dipole interactions, and induction forces, but those usually only have minor contributions [51].

2.4.2 Electron Interactions with Clusters

Clusters depict much more complex systems than atoms or molecules. Hence, more possible pathways arise for electron interaction processes. The differences are mainly governed by the electron affinity, which can change with cluster size, the immediate surrounding of collision partners in form of other cluster constituents, and additional available electronic states [49]. The subsequent discussion is mainly focusing on electron attachment processes, but while the initial formation process of a charged state differs for electron ionisation, the concepts of stabilisation can be transferred to the positive ion. Concerning the formation process, an additional pathway for EI is given at the end of the section.

Stability of Clusters

The constituent of a cluster are stabilised during the formation process as when compared to an isolated molecule. For the potential energy curves this results in a shift to lower energies, see figure 2.10 a) for neutral and anions and b) for cations.

Once the cluster is negatively or positively charged, the forces within it change due to the higher polarisation interaction. This results in an overall stabilisation of the charged cluster when compared to its neutral precursor [44]. This is shown for the rare gas dimer of argon in figure 2.10 b): The neutral argon dimer has no net covalent binding, as described in the previous section, but the removal of an electron of a molecular orbital results in an increase in the binding energy caused by a net covalent binding. As an additional effect, the equilibrium distance decreases [51]. While the example in figure 2.10 b) is showing cations, the effect is the same for anions as schematically shown in figure 2.10 a)

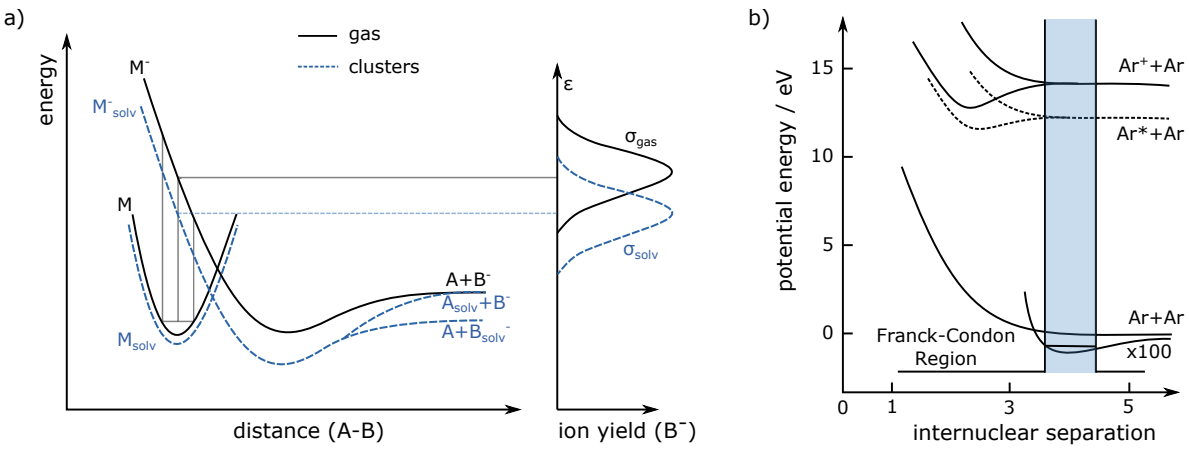

Figure 2.10: Potential energy curves showing effects of a cluster environment. a) Schematics comparing DEA in the gas phase and in a solvated environment like a cluster, also in terms of the ion yield curves. Adapted from [44]. b) Potentials comparing neutral, charged and excited Ar_2, showing representatively the increased stability of charged clusters. Adapted from [14].

Formation of the TNI

For low incident electron energies, the formation of the TNI is similar as for atoms or molecules via an individual shape resonance in the cluster [40]. For higher energetic electrons, the formation can either be direct or indirect. In the former, the TNI is

accessed by a core excited shape resonance. In the latter, the electron is slowed down by inelastic scattering events with other components within the cluster. Subsequently, the electron with now close to 0 eV is captured by another cluster molecule via the same process as an initially low energetic electron. The difference is visible within the ion yield curve which appears "blue-shifted" as it is recorded against the initial energy of the electron [44]. If the capturing molecule is of the same type as the scattering molecule, it is referred to as self-scavenging while if they are of different types it is called auto-scavenging, which is only possible for heterogeneous clusters [40].

The decisive factor for the localisation of the excess electron and finally for the further evolution of the TNI is the electron affinity. Basically, three pathways exist: 1) Dissociative attachment, either emitting a anionic fragment X^- or a solvated anion X^-M_n, assuming the molecule M contains the atom X and the cluster is composed of $n < N$ particles. 2) Evaporative attachment, leading to M_n^- via the stabilising emission of neutral cluster molecules. 3) Auto-scavenging, stabilising the ionised cluster via intracluster energy redistribution [40]. In clusters of molecules or atoms with a positive EA, the electron is bound to an individual component forming a localised anion within the surrounding which acts as a solvent [49, 52]. The excess energy is either located at this anion or distributes over the whole cluster. Intermolecular collisions and vibrations of the molecules are in the same order of magnitude which allows for an efficient coupling and thus stabilisation of the TNI. Nevertheless, the cluster anion is also likely to evaporate single components carrying away the excess energy. Alternatively, dissociation pathways are accessible. The reaction pathways can be summarised as

$$\mathrm{M}_n + e^- \longrightarrow \mathrm{M}^{*-}M_{n-1} \tag{2.38}$$

$$\longrightarrow (\mathrm{M}^-\mathrm{M}_{n-1})^* \longrightarrow \mathrm{M}^-\mathrm{M}_{n-2} + \mathrm{M} \tag{2.39}$$

$$\longrightarrow (\mathrm{A}^-\mathrm{M}_{n-1})^* + \mathrm{B} \longrightarrow \mathrm{A}^-\mathrm{M}_{n-2} + \mathrm{M} + \mathrm{B} \tag{2.40}$$

An example for clusters with positive EA is O_2. Molecular cluster anions containing molecules with negative EA are prone to dissociation after electron attachment. After the ejection of some neutral fragments, the remaining charged cluster stabilises further by isomerisation and evaporation. In the case of CO_2, this gives rise to the cluster series of $CO_3^-(CO_2)_n$ [49]. Atoms or molecules with close to 0 eV EA are characterised in general by a closed shell electronic configuration and are not prone binding an additional electron. In contrast, clusters composed of those molecules regularly bind the extra electron, indicating even a positive EA. Apparently, this is a cluster size dependent effect. If the cluster is large enough, the cluster is polarised which can result in extensive intermolecular electronic configuration changes. The additional electron becomes trapped in the arising potential. It is thus not associated with a single component but rather with the whole cluster and is hence referred to as solvated or hydrated electron. Rare gases and H_2O are typical examples for this [49].

Penning Ionisation

For electron ionisation processes, the formation of a cluster cation can occur via the processes described in chapter 2.2. Stabilisation is mostly achieved by evaporation of single components as described for the anionic case. For heterogeneous clusters, an additional formation channel exists, Penning ionisation. In a first step, one of the molecules of the component with the higher ionisation potential is electronically excited

by inelastic scattering of the impinging electron. The second step can be described via

$$\mathrm{W^*M} \longrightarrow \mathrm{WM^+} + e^- \tag{2.41}$$
$$\longrightarrow \mathrm{WM^*} \longrightarrow \mathrm{WM^+} + e^- \tag{2.42}$$

In the first channel, one of the electrons of the excited molecule W* is ejected from the outer shell into the ionisation continuum. Then, an electron from the molecule M of the cluster component with lower ionisation potential is transferred to a vacant position in the inner shell of W*. Overall, the cluster has emitted one electron, and thus now carries a positive charge. In the second channel, the excitation energy is transferred from W* to M and if it is above the ionisation potential, M emits one of its electrons, leaving the cluster positively charged [53]. For reasons of completeness it should be noted that also homogeneous clusters can undergo Penning ionisation. In this case, at least two components must be electronically excited. This energy is transferred to a third particle. If the excess energy is higher than the ionisation energy, an electron is emitted [54].

2.4.3 Formation of Clusters

Different mechanisms for the formation of clusters exist [14]. Here, only the supersonic jet expansion is discussed as this is the working principle of the cluster sources used for this thesis. Basically, gas is expanded from a region with high pressure through a small nozzle into vacuum, see figure 2.11. A nozzle is basically a plate with a hole having a diameter on the order of µm to mm. In the volume with high pressure gas, the velocities of the particles are randomly distributed. The expansion into vacuum occurs as directed beam, reducing the velocity spread of the distribution drastically. The expansion is adiabatic, implying that a very cold environment prevails in the beam, causing first supersaturation and as a consequence condensation of the particles into a cluster. A supersonic jet expansion is only possible if the stagnation pressure is so high that the mean free path of the particles is much smaller than the diameter of the nozzle. Only then will many collisions occur during the expansion which is the necessary condition for cluster formation [14, 51].

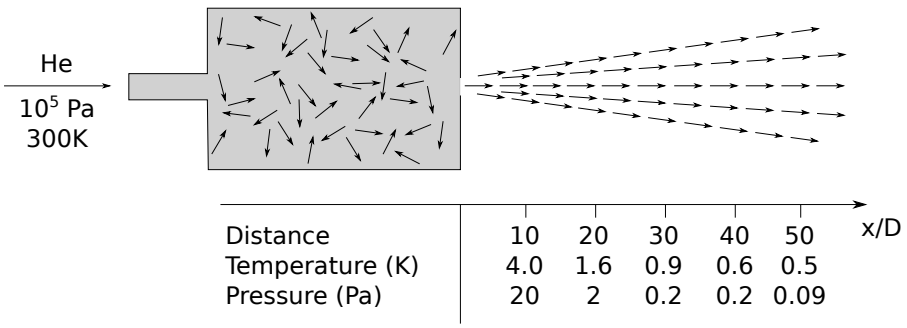

Figure 2.11: Schematics of the formation of clusters via supersonic expansion with conditions for helium given as an example. Adapted from [14].

Expansion of an Ideal Gas

The mechanism requires an aerodynamic treatment and an ideal gas is assumed for simplicity. The enthalpy H_0 of the gas with random molecular motion at the stagnation

pressure p_0 is converted into a directed mass flow with rest enthalpy H. This can be expressed by

$$H_0 = c_p\, T_0 = c_p\, T + \frac{1}{2}\, m\, v^2 = H + \frac{1}{2}\, m\, v^2 \tag{2.43}$$

where c_p is the specific heat capacity at constant pressure, T_0 and T are the temperatures before and during the expansion, respectively, and m and v are the mass and velocity of the particles [14]. Applying energy conservation and thermodynamics, the ratio of the temperatures before and after the expansion can be written as

$$\frac{T}{T_0} = \left(1 + \frac{\gamma - 1}{2}\, M^2\right) \tag{2.44}$$

with $\gamma = c_p/c_v$ the ratio of the specific heat capacities at constant pressure over constant volume and M the Mach number which in turn is defined as

$$M = \frac{v}{c} \tag{2.45}$$

where c is the local speed of sound [14]. The speed of sound can be expressed by

$$c = \sqrt{\frac{\gamma\, k\, T}{m}} \tag{2.46}$$

with k the Boltzmann constant [14]. Applying the Poisson equation for an adiabatic expansion onto equation 2.44, the ratio for the density ρ over initial density ρ_0, and the ratio of the pressure before and during the expansion, p/p_0 can be calculated by

$$\frac{p}{p_0} = \left(\frac{\rho}{\rho_0}\right)^{\gamma} = \left(\frac{T}{T_0}\right)^{\gamma/(\gamma-1)} \tag{2.47}$$

Interpreting equations 2.44 to 2.47, the following conclusions are made: During a supersonic expansion, the pressure decreases drastically. As a consequence, the temperature decreases in accordance to the Poisson equation 2.47. This causes the speed of sound to decrease, see equation 2.46, which in turn increases the Mach number according to equation 2.45. The low temperature implies a narrow spread in the velocity distribution, while the mean velocity of the particles v is only slightly increased compared to the situation during stagnation. The velocity distribution of the effusive molecular beam is given by a Maxwell distribution superimposed with the mean velocity v, giving

$$P(v)\,\mathrm{d}v \propto v^3\, \exp\left(-\frac{m\, v^2}{2\, k\, T}\right) \mathrm{d}v \tag{2.48}$$

[3]. The dependency of the velocity distribution on the Mach number is shown in figure 2.12 a).

Cluster Growth

Once the thermal energy of the particles in the beam is lower than the binding energy of the dimer, it is more energetically favourable for particles to be bound than to be separated. Dimer formation is only possible as a three body initial state process, as the binding energy is released and transformed into kinetic energy (KE) of the final

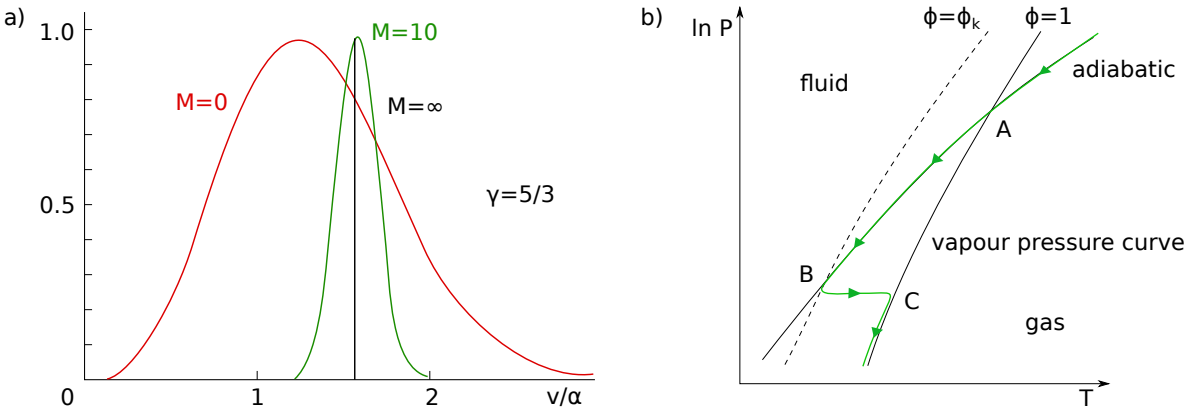

Figure 2.12: a) Velocity distribution $P(v)$ as function of the reduced velocity for different Mach numbers, $\alpha = (2kT/m)^{0.5}$. Adapted from [14]. b) Phase diagram for cluster formation. The green line represents the pathway of cluster condensation, passing the vapour pressure curve (A) before condensation starts once supersaturation is reached (B). The adiabatic curve is left to achieve equilibrium conditions (C). Adapted from [14].

state products according to momentum and energy conservation. The process can be described for an atom or molecule A as

$$\mathrm{A} + \mathrm{A} + \mathrm{A}(KE1) \longrightarrow \mathrm{A}_2 + \mathrm{A}(KE2 > KE1) \tag{2.49}$$

Two processes exist leading to cluster growth. The first is monomer addition. Here, the dimer acts as condensation nucleus and individual atoms are added to it consecutively. This process occurs at the early stage of cluster formation and results in an approximately exponential decay in the cluster size as observed in the mass spectrum. The second mechanism is cluster-cluster aggregation, where two clusters join into one [14, 51]. The two processes can be summarised by

$$\text{monomer addition} \qquad \mathrm{A}_n + \mathrm{A} \longrightarrow \mathrm{A}_{n+1} \tag{2.50}$$

$$\text{cluster-cluster aggregation} \qquad \mathrm{A}_n + \mathrm{A}_m \longrightarrow \mathrm{A}_{n+m} \tag{2.51}$$

A theoretical description of cluster growth is complicated and this thesis is confined to a qualitative explanation based only on classical nucleation theory. The cluster formation can be visualised in a gas-fluid phase diagram as shown in figure 2.12 b) as a transition. The vapour pressure line separates the thermodynamically stable gas and fluid regions and is labelled with $\Phi = 1$. The line of supersaturation is marked with $\Phi = \Phi_k$. As described by the Poisson equations (eq. 2.47), the expansion follows an adiabatic line. The adiabatic and vapour pressure line cross in point A but cluster formation only starts under supersaturated conditions in point B. Since every monomer addition to the growing cluster is associated with the release of the heat of condensation, the production curves leaves the adiabatic line and approaches the vapour pressure line until the equilibrium state C between gas and liquid phase is reached [14].

Cluster Temperature and Stabilisation

The addition of an atom or molecule to the cluster is an exothermic process, implying that the released heat of formation is converted into internal energy of the cluster. As a consequence, the cluster itself can get hot. For rare gases, the temperature is slightly

below their melting points. For molecular clusters, usually a seeding gas is co-expanded which can cool down the molecular cluster to the temperatures only achieved by rare gas clusters [14, 48, 51]. In order to get into a energetically favourable and stable state, the cluster cools down via three different mechanisms:

$$\text{Collisional cooling} \qquad \mathrm{A}_N(T_1) + \mathrm{B}(KE_1) \longrightarrow \mathrm{A}_N(T_2 < T_1) + \mathrm{B}(KE_2 > KE_1) \tag{2.52}$$

$$\text{Evaporative cooling} \qquad \mathrm{A}_N(T_1) \longrightarrow \mathrm{A}_{N-1}(T_2 < T_1) + \mathrm{A}(KE) \longrightarrow ... \tag{2.53}$$

$$\text{Radiative cooling} \qquad \mathrm{A}_N(T_1) \longrightarrow \mathrm{A}_N(T_2 < T_1) + h\nu \tag{2.54}$$

During collisional cooling, the cluster collides with another atom of the same type or with the seeding rare gas. Internal energy from the cluster is passed to the single atom which leaves the interaction with a higher kinetic energy. Since collision partners are required for this process, it is only important in the region of expansion [51]. Evaporative cooling is the reverse process to monomer addition during cluster growth and thus an endothermic, competing process. The activation barrier necessary to break off a single component is overcome by transmitting the excess energy into the according vibrational mode. In contrast to collisional cooling, no particles apart from the cluster are required, making the mechanism accessible for the whole flight path. The process was described by Klots as an evaporative ensemble [55]. The internal energy balance is given by

$$E^*(n) = E^*(n+1) - D(n+1) - \epsilon(n+1) \tag{2.55}$$

where D is the dissociation energy and ϵ is the kinetic energy of the recoiling partners [14, 51]. Radiative cooling is a slow process and is thus rather unimportant on the typical timescale of the mass spectrometry experiments used in this thesis. Here, an infrared photon of energy $h\nu$ is emitted to cool down the cluster. Each cluster cools down to a specific temperature which can also depend on its size. For example, helium droplet can cool down to 0.37 K and neon clusters to around 10 K [54, 56].

Hagena Parameter and Cluster Size

The mean size of a cluster produced by supersonic expansion depends on the type of gas expanded, the stagnation pressure p_0, the temperature of the gas before expansion T_0, and the nozzle diameter d and its geometry. The dependency of expansion conditions under which the cluster mean size is equal is given by the Hagena parameter Γ^*:

$$\Gamma^* = k \cdot \left(\frac{p_0}{\mathrm{mbar}}\right) \left(\frac{d_{eq}}{\mu\mathrm{m}}\right)^b \left(\frac{\mathrm{K}}{T_0}\right)^c \tag{2.56}$$

where k, b, and c are gas dependent factors which require experimental determination [14, 57–60]. For argon, they amount to $k = 1650$, $b = 0.85$, and $c = 2.29$ [59]. The equivalent nozzle diameter d_{eq} is equal to the nozzle diameter for sonic nozzles and otherwise given by

$$d_{eq} = 0.74 \frac{d}{\tan(\alpha)} \tag{2.57}$$

where α is the opening angle [57, 59, 61]. With the Hagena parameter, the mean cluster size is calculated by

$$\overline{n} = a \left(\frac{\Gamma^*}{1000} \right)^u \tag{2.58}$$

where a and u are nozzle geometry dependent factors [59, 60]. They need to be determined experimentally. For a sonic nozzle, the reported values amount to $a = 38.4$ and $u = 1.64$ [59, 60]. In general, the mean cluster size increases with increasing stagnation pressure, increasing nozzle diameter, decreasing opening angle of the nozzle, and decreasing stagnation temperature.

Shock Zones and Skimmer

At some point during the expansion, the pressure of the particle beam p will approach the background pressure p_{bkg}. As a consequence, the atoms or molecules from the directed beam collide with background particles and the narrow velocity distribution broadens. In terms of temperature, this implies a heating of the clusters, which finally leads to evaporation, fragmentation or a complete break up of the cluster. This region is referred to as shock zone and can be divided into barrel shock and Mach disc, see figure 2.13. The barrel shock builds up around the direction of the beam and ends in the second zone, the Mach disc. This is a shock wave perpendicular to the beam. Its position can be calculated by

$$x_m = 0.67\, d \sqrt{\frac{p}{p_{bkg}}} \tag{2.59}$$

with d the nozzle diameter [62]. The volume surrounded by these two shock waves is also classified into two regions. First, the initial expansion region with enough particles to provide sufficient collision partners to maintain an equilibrium of growth and decay. Second, the region of collisionless flow, also referred to as the zone of silence as the speed of sound within the beam approaches zero [62]. To prevent the destruction of the cluster, a skimmer is placed at a position before the shock waves forms. To allow for a maximal region of cluster production, this distance should also be as large as possible [14].

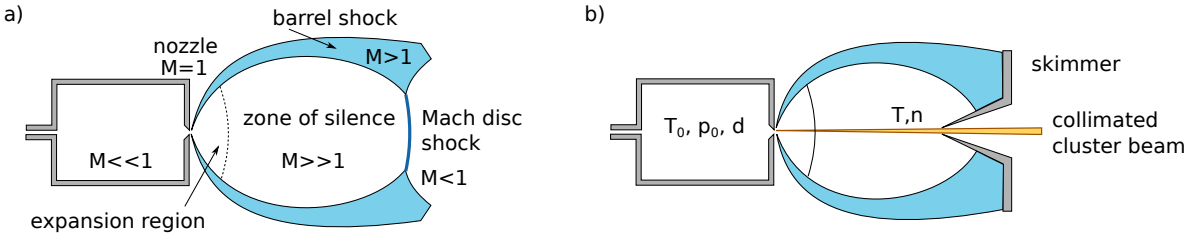

Figure 2.13: Schematics of the shock zones and regions within during a supersonic expansion, a) without a skimmer, and b) with skimmer. Adapted from [63].

Chapter 3

Mass Spectrometry Setups

In order to study the electron interactions with molecules and clusters as described in chapters 2.2 and 2.3, a very sensitive analytical method at molecular level is required. Mass spectrometry experiments offer this tool. For the investigations of this thesis, two different setups were used and are described in the following sections. Each mass spectrometer consists of the following components, see schematics in figure 3.1: 1) An inlet system allows the introduction of the neutral molecules to be analysed into the system. Only gas phase measurements are feasible, thus the state of matter of the compound might have to be changed at this stage. 2) In the ion source the molecule is ionised. As electron interaction processes are studied, electron ionisation sources are used in both setups. 3) A mass analyser separates the ions according to their mass-to-charge (m/z) ratio. 4) A detector measures the current of the electrons which the m/z selected ions hit out of a special surface of the detector. 5) A data acquisition and processing unit enables data readout and analysis. This is the basic working principle each mass spectrometer is based on. For Electrospray-Ionisation (ESI) and Matrix Assisted Laser Desorption Ionization (MALDI) sources, the component 1) and 2) are combined.

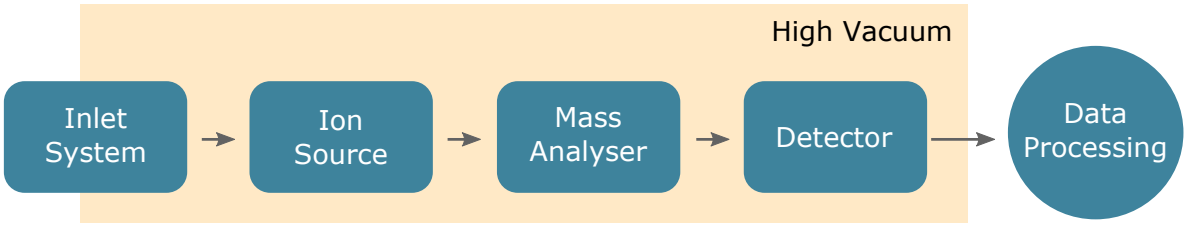

Figure 3.1: Schematics of the components of a mass spectrometer.

For efficient electron-molecule interaction processes with a high signal-to-noise ratio, and for undisturbed ion selection and detection, it is essential to keep the setup under high vacuum conditions. Thus, the mass spectrometer is built inside of airtight chambers. Remaining particles follow a Maxwell-Boltzmann velocity distribution [64]. The mean free path length between two collisions resulting from this movement can be calculated by

$$l = \frac{kT}{\sqrt{2}\pi \cdot p \cdot d^2} \tag{3.1}$$

where k is the Boltzmann constant, T the temperature, p the pressure and d the diameter of the molecules [64]. For high vacuum conditions, i.e. $10^{-3} - 10^{-7}$ mbar, the mean free path length amounts to $10^{-1} - 10^{3}$ m. Typical dimensions within a mass spectrometer range from a few cm to several m, thus high vacuum conditions are required in order to reach collision free conditions.

3.1 Wippi

The Wippi experiment is a typical mass spectrometer comprising the above mentioned components with a crossed-beam setup, see figure 3.2. The neutral beam source is exchangeble. Either an oven with capillary to form an effusive beam or a cluster source can be attached to the experimental setup. In both cases, a neutral particle beam is guided into the direction of the interaction region. Additionally, a gas inlet system is available to introduce calibration gases for energy scale calibration into the chamber. Instead of forming a directed beam, those fill the whole chamber uniformly. A hemispherical electron monochromator (HEM) serves as ion source. Electrons are emitted, formed into a beam with a narrow energy resolution (about 100 meV) and focused onto the interaction point where they cross the neutral beam perpendicularly. Here, the electron interaction processes take place, forming ions via electron attachment or electron ionisation. Subsequently, the ions are extracted by a weak electrostatic field into the quadrupole mass filter which serves as analyser for mass selection. By combining the HEM with the quadrupole, formation efficiency studies of selected fragment and parent ions at varying energies are made feasible. Therefore, the according mass to charge is selected with the quadrupole and at the HEM, the kinetic energy of the electrons is varied by the acceleration potential applied shortly before the interaction region. Conversely, mass spectra can be recorded by keeping the electron energy constant and instead scanning through the mass to charge range of the quadrupole. The quadrupole is aligned with the axis of the neutral beam source. In order to minimise noise effects caused by uncharged particles, the ions are bent out of plane towards the detector by a deflector unit. The ions are detected by a channel electron multiplier and further processed by a preamplifier with analog-to-digital converter unit. Due to pressure-sensitive components in the setup and in order to avoid high background signals, the whole setup is set under high vacuum. Usual background pressures are on the order of 10^{-8} mbar.

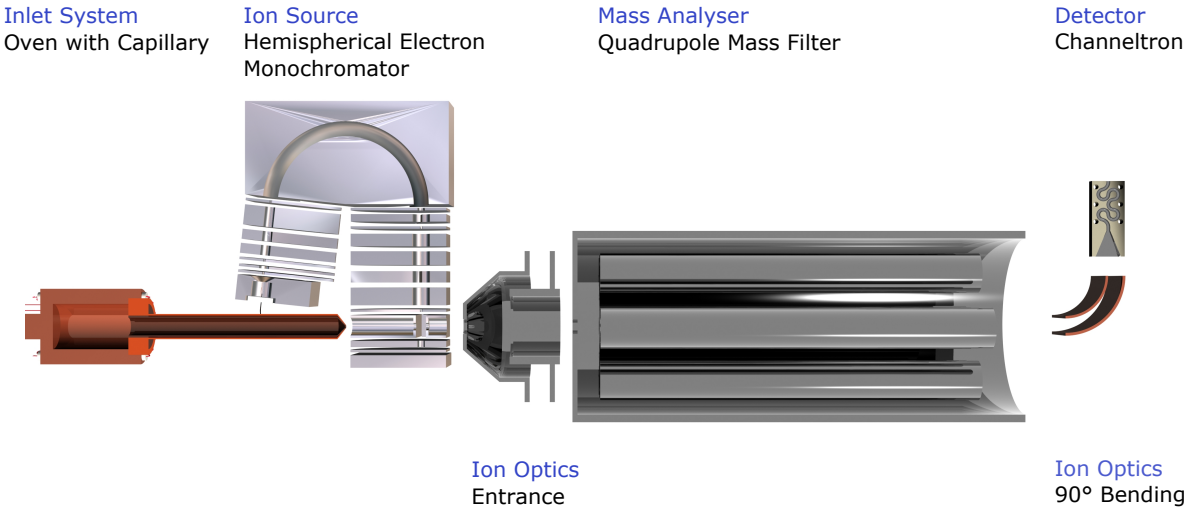

Figure 3.2: Schematic drawing of the Wippi mass spectrometer including the main components within the setup using the oven. Figure credits: P. Scheier, University of Innsbruck.

An estimation of the minimal lifetime of the formed ions is calculated under the condition that they do not interact further on their path s to the detector and that their kinetic energy E_{kin} is given by the extraction potential U. Then, the time-of-flight

t to the detector is a first order linear motion, giving

$$t = \frac{s}{v} = s \cdot \sqrt{\frac{m}{2 \cdot E_{kin}}} = s \cdot \sqrt{\frac{m}{2 \cdot q \cdot U}} \tag{3.2}$$

where m is the mass of the particle and q its charge. Assuming a singly charged ion ($q = e$) with mass $m = 100\,\mathrm{u}$, a typical extraction potential of $U = 3\,\mathrm{V}$ and a flight pass length of $s = 25\,\mathrm{cm}$, a minimal lifetime on the order of $100\,\mu\mathrm{s}$ is required.

3.1.1 Inlet System

The Wippi setup offers the possibility of attaching three different inlet systems for sample introduction. The gas inlet system for calibration compounds is permanently installed as calibration measurements are required at frequent basis. The oven for biomolecules and the cluster source both have to be mounted at the same position perpendicularly to the electron beam. Thus, only one of the sources can be attached at a time.

Gas Inlet System

The gas inlet system is exclusively used for the calibration gases sulfur hexafluoride (SF_6) and carbon tetrachloride (CCl_4) for electron attachment experiments and neon or argon for electron ionisation studies. A permanently installed line connects the containers of the calibration molecules with the Wippi main chamber including a manual flow controller which allows for adjusting the partial pressure of the compound and keeping it at a stable value. Under high vacuum conditions, all compounds are brought into the gas-phase by their vapour pressures. There is no directed molecular beam but rather the whole Wippi main chamber is homogeneously filled with the calibration gas, including the interaction region.

Oven for Biomolecules

Many biomolecules appear in solid state under normal conditions and even under high vacuum at room temperature. Since only compounds in the gas phase can be examined, those molecules need to be sublimated. For this purpose, a custom made oven is available, see figures 3.2 and 3.3. The sample is placed into the copper oven which is screwed onto a heatable holder. This in turn is mounted to a manipulation unit allowing for alignment in x, y, and z positions and can additionally be tilted along x and y. A capillary forms the exit for the sublimated sample towards the interaction region. It is about 7 cm long and has an inner diameter of 1 mm. A ceramic placed on the tip of the capillary electrically isolates the oven from the hemispherical electron monochromator. The temperature of the oven is adjusted by a combination of heat transfer from the holder streaked by heating wires, and light bulbs in the Wippi chamber. The temperature is measured by a Pt100 sensor installed directly on the copper of the oven. The light bulbs additionally heat up the hemispherical electron monochromator and the chamber walls in order to reduce condensation of the sticky biomolecules to cold surfaces within the setup. Overall, an effusive beam is formed in the vicinity of the interaction region.

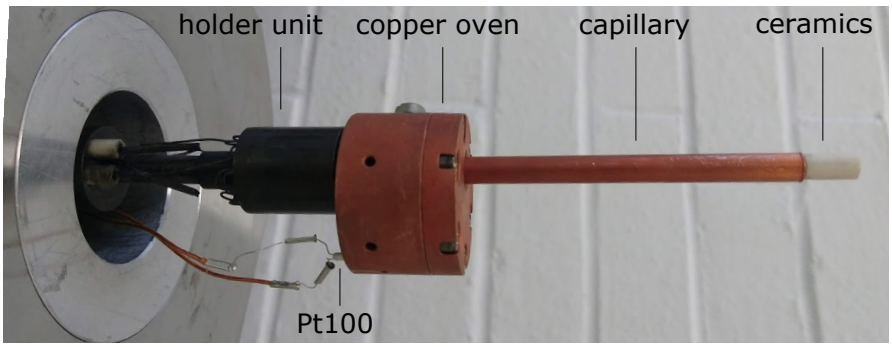

Figure 3.3: Photo of the copper oven from the Wippi experiment.

Cluster Source

Depending on the type of clusters to be formed, two different cluster sources for the Wippi setup are available, a water cluster source and a neon cluster source. For details of the water cluster source design, refer to [65, 66]. Within this thesis, the neon cluster source was implemented in order to consolidate the knowledge about clusters themselves and as preparation for cluster measurements performed at CluB, the second mass spectrometry setup used, see chapter 3.2.

The basic principles of cluster formations are described in chapter 2.4.3.

Wippi Cluster Source

In case of the neon cluster source, the neon gas inlet is introduced into the chamber and the line wind around a two stage liquid Helium cryostat from CTI Cryogenics [67]. Thus, the neon is cooled down. As a cryostat cannot adjust to a specific temperature, a heating wire is wrapped around the second cooling stage. The line ends in a 10 µm or 20 µm pinhole nozzle which is also temperature controlled. Temperature setting occurs by a control loop consisting of a silicon diode sitting directly at the nozzle holder and a Lakeshore 325 temperature controller [68]. Temperatures set should avoid neon freezing which occurs at 24.6 K at ambient pressure [69]. Additionally, a 2 µm filter is assembled within the line and cooled by the first stage to prevent that impurities freeze the nozzle. Typically, the nozzle is held at (40-100) K. For further design details refer to [70]. A photo of the top view of the setup is shown in figure 3.4.

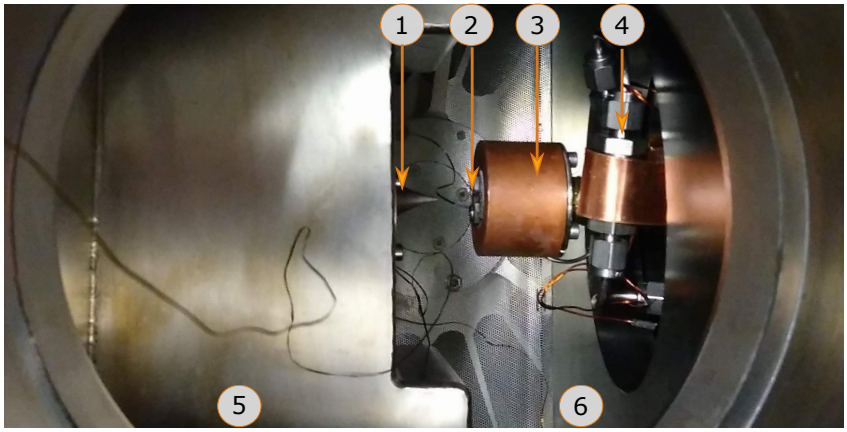

Figure 3.4: Top down view onto the cluster source and the skimmer.

Approximately 1 cm down the cluster beam, a skimmer is placed separating the clus-

ter source chamber from the pick up chamber. Additionally, it prevents that the clusters in the center of the beam hit the Mach disc. The pick up chamber can be filled with a dopand molecule. The cluster beam passes through the approximately 10 cm long chamber collecting the dopants. Subsequently, the (doped) cluster beam passes through a plate with a roughly 1 mm hole into the Wippi main chamber. The separation of the Wippi main chamber, pick up and cluster source chamber is essential for allowing low background signal detection, high dopant pressures and sufficiently high neon pressures for the formation of an initial cluster beam. Differential pumping of the chambers is applied, see chapter 3.1.6. Alignment is achieved by an adjustable perforated plate, skimmer and cluster source in x and y. The source can additionally be tilted and the distance to the skimmer is adjustable.

3.1.2 Hemispherical Electron Monochromator

The ion source of the Wippi setup is a hemispherical electron monochromator (HEM), see figures 3.2 and 3.5. It is custom-made and a detailed description of the function of the individual parts can be found elsewhere [71–73]. Here, the focus lies on providing an overview of the working principle of the HEM. Basically, the HEM comprises a filament for electron emission, a first stack of lenses to form an electron beam and guide it to the energy selective hemisphere, a second set of lenses and the interaction region.

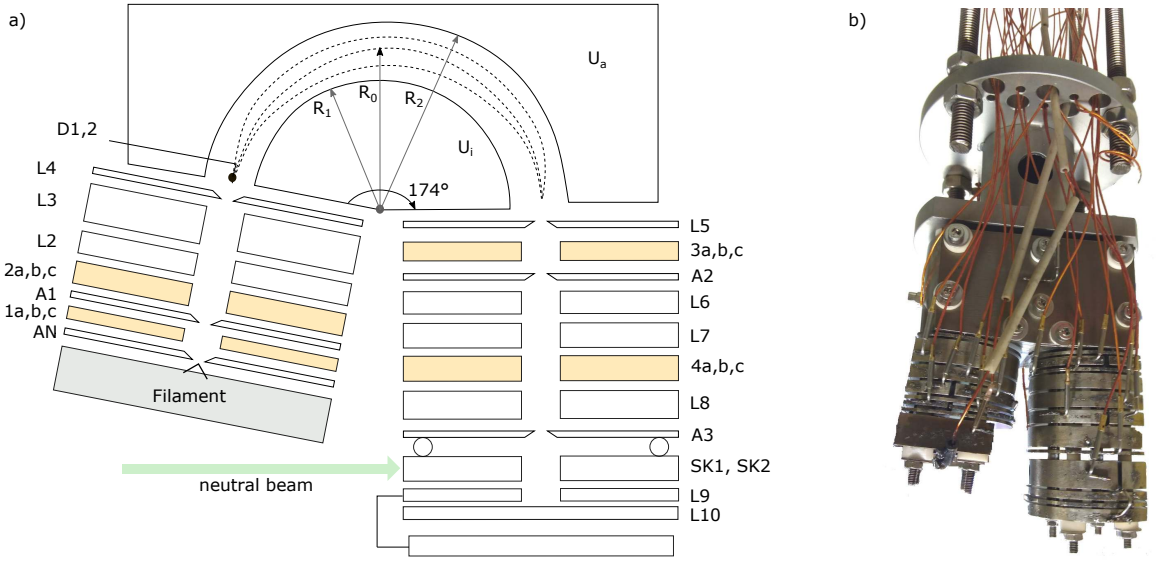

Figure 3.5: The hemispherical electron monochromator (HEM). a) Schematical drawing including the short lens tower (left), the hemisphere and the long tower (right). Segmented lenses are indicated by yellow shaded areas. b) Photograph of the HEM including the electrical connection wires.

The hairpin filament is commercially available from Agar Scientific (model AGA054) [74]. It is a 0.125 mm thick tungsten wire which is heated with typically 2.35 A, such that the emission amounts to a few tens of µA. The thermal electron emission, also known as the Edison effect, results in a typical energy spreads of about 0.7 eV for those types of electron sources [75] and an additional wide angular spread.

In order to form an electron beam and guide the electrons away from the source and towards the HEM spheres, a stack of lenses is implemented. There are principally three different models of lenses, see figure 3.5: 1) Aperture lenses which are thin lenses

with a small orifice. 2) Thick lenses with a larger cylindrical orifice. 3) Segmented lenses which consist of effectively three parts where different voltages can be applied to. Due to the large amount of freedom in lens choice, a detailed review about the path of electrons is refrained here and the interested reader should refer to [72, 73] instead. Basically, each lens has its own power supply. The lens stack functions as set of Einzel lenses and immersion lenses with which the beam can be (de)focused and its energy can be changed [76]. The anode accelerates the emitted electrons from the filament into the lens stack. Additionally, the segmented lenses allow for bending of the beam. All lenses are electrically isolated by Zirconium balls from Swarovski by which the distance between the individual lenses is kept constant at the ball's diameter of 1.55 mm. The last lens before the HEM, L4, defines the maximum width of the beam, similarly to an entrance slit.

The hemispherical electron monochromator is an electrostatic sector comprising of two concentric hemispherical spheres and two deflector wires, D1 and D2, allowing for adjusting the entrance angle of the electron beam. The electrons travel in elliptic orbits through the field and are geometrically focused in first order [76], see figure 3.5. Particles with different kinetic energies are spatially separated. For passing along the ideal radius, R_0, the electron must carry the energy $e \cdot V_0$ with

$$V_0 = \Delta V \frac{R_1 \cdot R_2}{R_2^2 - R_1^2} \tag{3.3}$$

where ΔV is the potential difference applied ($U_a - U_i$, see figure 3.5), $R_1 = 27\,\text{mm}$ and $R_2 = 33\,\text{mm}$ are the inner and outer sphere radii [3]. After the sector, the energy profile is Gaussian like with a resolution narrowed down to a full-width-half-maximum (FWHM) of

$$\Delta T_{\text{FWHM}} = \frac{w}{2R_0} \cdot T_0 \tag{3.4}$$

with $T_0 = e \cdot \Delta V$ the nominal kinetic energy at R_0 and w the width of the entrance slit [76]. Thus, higher resolutions are achieved for lower electron energies which in turn result in larger divergence angles and thus lower transmission [76]. The trade-off must be made individually for each experiment.

For the Wippi setup, usually the hemispheres are set to typical energy resolutions of 100 meV and the lens towers are tuned accordingly. The HEM applied has a deflection angle of 174° to compensate for perturbating fields close to the fringes of the HEM, also known as Herzog correction [77, 78].

In between the HEM and the interaction region, a second set of lenses ensures that the electrons are guided and are locally focused onto the interaction point. Similar to L4, L5 is comparable to an exit slit of the HEM, accelerating the electrons out of the spheres. The final energy definition of the electrons occurs between L8 and A3, see figure 3.5. From A3 onwards, no additional voltage is applied to the lenses in order to keep this region field free. Between A3 and SK1/2 is the only position where Zirkonium balls of diameter 2.5 mm are used. The neutral beam enters the interaction region perpendicular to the electron beam. The point where both cross is the interaction point. To facilitate the extraction of the formed anions or cations, the whole monochromator is floating on a positive or negative potential.

The last lens, L10, forms the Faraday cup. Here, the electron beam stability is controlled. A Faraday cup is a charge detector, i.e. the ion current measured is directly

proportional to the number of electrons impinging it [29]. A shielding end plate prevents dark noise detection from the backside. The Faraday cup is connected to a picoammeter where the current can constantly be checked.

Additionally, the setup contains three pairs of Helmholtz coils with which the magnetic field of Earth can be compensated within the interaction region. Due to non-negligible aberration effects of low energetic electrons ($E < 1\,eV$), the residual magnetic field should be kept in the region of (0.1-1) µT [79]. For the Wippi setup, the field is attenuated down to approximately 0.3 µT [80].

3.1.3 Quadrupole Mass Filter

A quadrupole mass filter comprises four isolated, ideally hyperbolic, electrodes which are arranged in parallel, see figure 3.6. The opposing electrodes are electrically connected. Between the pair of rods, a voltage is applied. It is composed of a time independent DC voltage, U, and a time dependent AC voltage, V. Assuming the rods are aligned with the z axis, the potential at each time t and spacial coordinate (x, y) is described by

$$\phi = [U + V \cdot \cos(\omega t)] \cdot \frac{x^2 - y^2}{2r_0^2} \tag{3.5}$$

where r_0 is the distance to the central axis of the rods and ω is the radio-frequency of oscillation. For practical reasons, the geometry of the rods is commonly changed to a cylindrical design, resulting in a slight change in the potential. Since the system is very sensitive towards mis-alignment or deviations of the field radius r_0, a high precision is required [81].

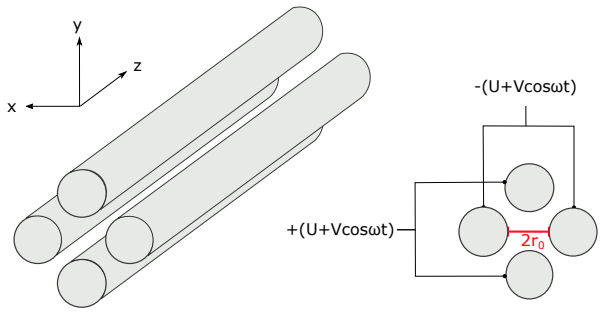

Figure 3.6: Schematics of a quadrupole mass filter. Adapted from [29].

The principle of operation of a quadrupole is similar to a combined low and high pass mass filter [82]. Considering only e.g. the xz plane, the RF potential continuously focuses and de-focuses the ions every half cycle. The added DC voltage lifts the rods to a higher potential around which the AC voltage oscillates. While heavy charged particles are mostly affected by the average field, light ions are influenced by the rapidly changing potential.

If the applied DC voltage carries the same sign as the ion to be analysed, the average of AC and DC field induces a focusing effect and the particle passes the filter. The smaller the mass over charge ratio m/z of the ion, the more intense the effect of the RF field. At a certain m/z, a cycle is long enough to induce an acceleration of the ion which finally leads to the collision with the electrodes and thus neutralises it. Hence, this part of the potential serves as high pass filter [82]. In contrast, the other rod pair

is shifted to an opposite sign potential. The average field seen by higher m/z ions results in a de-focusing trajectory which ultimately does not pass through the filter. Smaller m/z particles experience a correcting RF field, keeping them on a stable path. In the quadrupole, those two effects are superimposed. For an ion to pass through, both trajectories in the xz and in the yz plane must be stable. Thus, the separation is achieved by adjusting the parameters accordingly for a specific mass per charge to path through. Those include the frequency ω, the amplitudes U and V of the DC and AC fields, respectively, and the resolution [82].

Starting from equation 3.5, the equation of motions are derived to

$$\frac{d^2x}{dt^2} + \frac{ex}{mr_0^2} \cdot [U + V \cdot \cos(\omega t)] = \frac{d^2x}{dt^2} + (a_x + 2q_x \cdot cos(2\tau)) \cdot x = 0 \tag{3.6}$$

and similar for the motion in y with the substitutions a_x, q_x and τ

$$a_x = -a_y = \frac{4eU}{mr_0^2\omega^2} \quad q_x = -q_y = \frac{2eV}{mr_0^2\omega^2} \quad \tau = \frac{\omega t}{2} \tag{3.7}$$

[29]. This is the canonical form of the Matthieu equations of which the two-dimensional solution is graphically represented in the stability diagram in figure 3.7 a). For a more detailed description refer to the literature [29, 83].

In the stability diagram, stable trajectories in x and y are illustrated by filled green areas. Overlapping regions of stability in x and y represent bound solutions and thus stable trajectories passing the quadrupole. A detailed view into one of the regions of stability is shown in figure 3.7 b). In first order, a quadrupole is operated at constant a/q or U/V ratio, represented by the mass scan line. By choosing the value of the ratio, the resolution of the quadrupole is set. Each m/z exhibits its specific regions of stability, as can be seen in equation 3.7 and as is shown in figure 3.7 b). Thus, mass spectra are recorded by changing U and V at a constant ratio, moving along the scan line. In figure 3.7 b) it is apparent that with a constant U/V scan line (solid line), the mass peaks of higher masses get broader. As a solution, several commercial quadrupole mass analysers scan at constant mass linewidth instead of constant resolution (dashed line in figure 3.7 b)) [81].

In the Wippi setup, a HiQuad quadrupole mass spetrometry system QMG 700 [86] is used with a high frequency generator QMH 410-2 [87] and QMA 410 analyser [88]. This is a commercial system from Pfeiffer Vacuum with nominal mass range of 2048 u.

In order to achieve a high transmission, it is of advantage to introduce a focused ion beam into the quadrupole. For this purpose, a two lens ion optics from Pfeiffer Vacuum [88] is already built in right in front of the mass filter, see figure 3.8 a). The target region (see figure 3.2) is the interaction region within the monochromator. For anion detection, the whole HEM is set to a negative voltage of about 25-30 V. The first lens of the ion optics (IO_1 in figure 3.8 a)) is set to a positive voltage of about 30-40 V. The difference between those two is the extraction potential for the anions. The second lens (IO_2 in figure 3.8 a)) lies slightly below the floating voltage of the HEM. Thus, a focusing Einzel-lens extracts the anions through the entrance orifice into the rod system. The voltage applied to the latter defines the final kinetic energy of the ions within the quadrupole and thus the number of cycles spent in there, an important parameter for the resolution.

Since neutral particles moving in z-direction with enough kinetic energy to pass the length of the quadrupole are not influenced by the filter, a 90° deflection unit after the

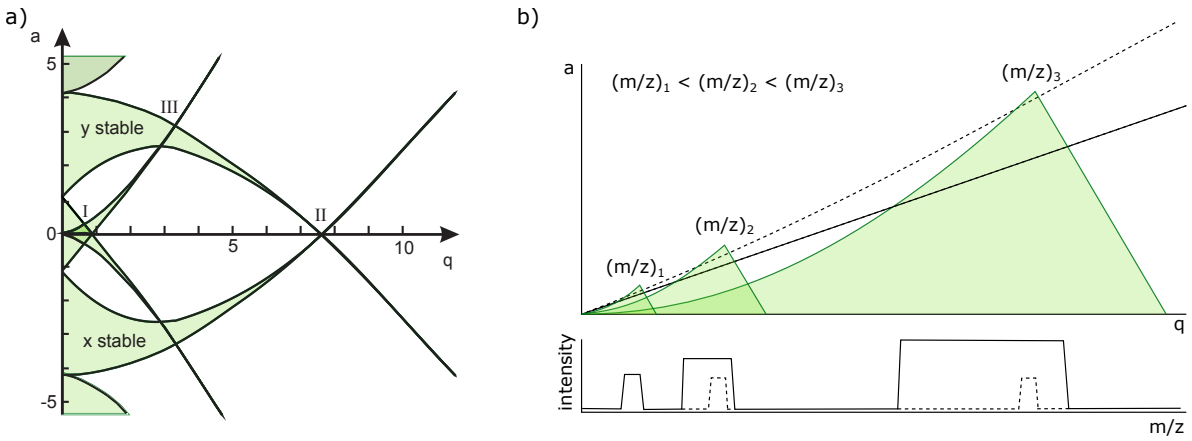

Figure 3.7: Stability regions (green shaded areas) of a quadrupole mass filter. a) Regions marked with I, II and III assign stable trajectories both in x and y. Adapted from [84]. b) Region I for different m/z values. For a scan line with constant a/q (continuous line), the mass resolution is downgraded for higher m/z while the dashed scan line is adapted such that the mass linewidth is constant. Adapted from [29, 85].

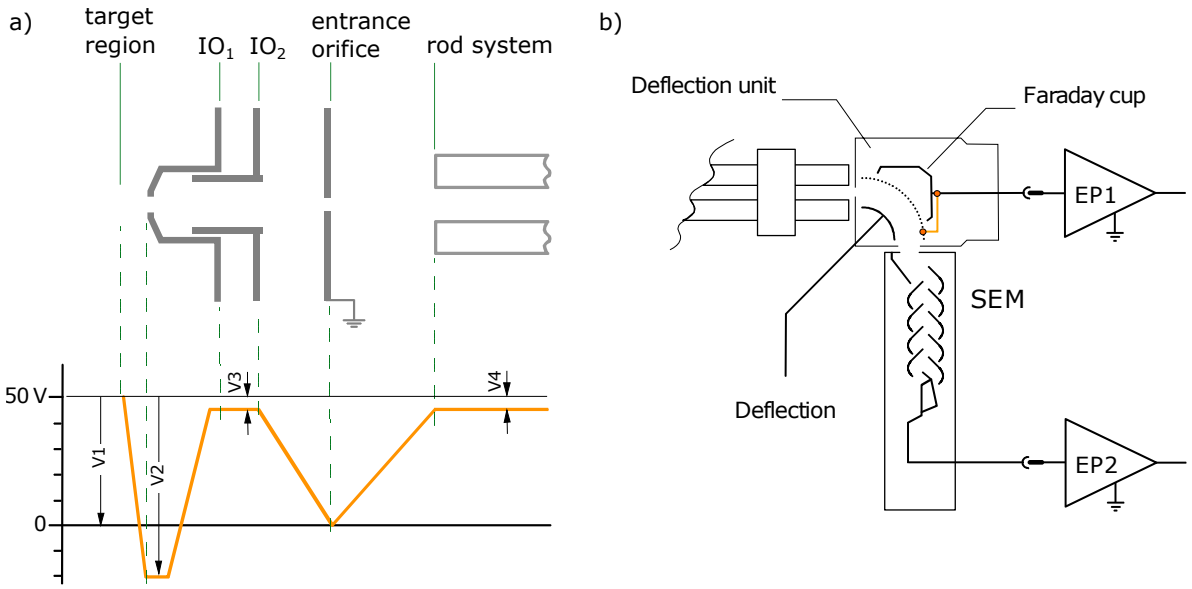

Figure 3.8: Ion optics of the quadrupole mass filter. a) Two lens ion optics for focusing the beam into the quadrupole. b) 90° deflection unit after the quadrupole. Adapted from [88].

rod system bends the ions upwards towards the detector while neutral particles continue straight forward through the deflector grid, see fig. 3.8b. This arrangement reduces the background significantly, depending on the exact ion source setup [88].

3.1.4 Channel Electron Multiplier

For the detection of low electric currents, as is the case in the present setup, a highly sensitive detector is required. Secondary electron multipliers (SEMs) are commonly used for this purpose. The basic working principle is that incoming particles impinge a metal or semiconductor surface and release secondary electrons out of the surface. The amount of electrons depends on the electronic work function of the material applied,

and the velocity and mass of the incoming particles [29]. To achieve a high amplification of the signal, further electrodes, or dynodes, at an increasingly positive potential follow. The electrons are accelerated to the next dynode, impinge the surface and emit further secondary electrons. The initiated cascade of negative charges is collected and read out by the final dynode, or anode as a current [89, 90].

A channel eletron multiplier, short CEM or channeltron, is a SEM with the discrete dynodes being replaced by one continuous dynode [90]. An electrically resistive surface in the shape of a tube forms the dynode to which an electrical gradient is applied. The potential difference between input and anode amounts to about 2 to 2.5 kV, getting increasingly positive towards the output [91]. In order to avoid the creation of a potential barrier for incoming ions, either the output end is set to a high positive voltage or the input of the CEM is set to a high negative voltage for the detection of anions or cations, respectively [91]. Additionally, the channeltron is usually curved as otherwise secondary ionisation of residual gas molecules induces an undesired feedback and reduces the achievable gain of the device [89]. A drawback of channeltrons is the variable gain due to contamination and the dependence of the detection efficiency on the mass and velocity of the incoming particle [81], but the fast response and high sensitivity are advantages outweighing this effect.

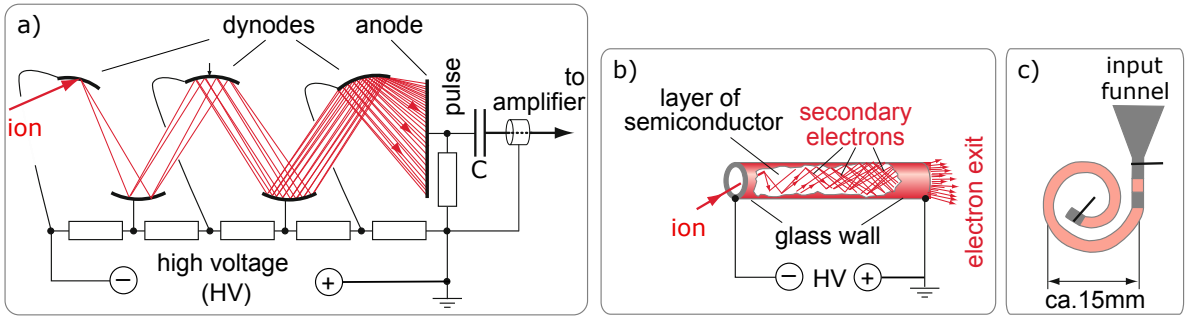

Figure 3.9: Principle of operation of secondary electron multipliers. a) Individual dynodes of a SEM. b) Working principle of a channeltron. c) Typical CEM design. Adapted from [76].

For the Wippi setup, a channeltron from Dr. Sjuts Optotechnik GmbH, model KBL510, is implemented [91]. It consists of a supporting body out of a ceramic material, an active layer made of lead silicated glass and a conductive layer of silver at both ends of the channeltron [91]. The gain amounts to 10^8 and is determined by the length to diameter ratio [92]. Dead time effects occur at count rates of above 10^4 Hz and the channeltron's lifetime amounts to about 10^{10} counts. After that, the gain decreases, an effect which can be compensated for by higher applied voltages for a limited amount of time [91].

3.1.5 Data Processing and Acquisition

The output of the channeltron is a single pulse of collected electrons by the anode. This signal is fed into a pulse preamplifier and detection unit. In the Wippi setup, a WMT PAD 06A from Winkelnkemper Engineering [93] is used which is specifically designed for electron multipliers and processing their fast output pulses. Each signal above a specified threshold level is amplified and transformed into a standard rectangular pulse. Subsequently, a counter is increased by one for each pulse. For readout, a custom-made software based on MATLAB records the data. Two measurement methods are

available: 1) Mass spectra at constant electron energy and varying m/z. 2) Energy scans at constant m/z and variable electron energy.

3.1.6 Vacuum System

The Wippi mass spectrometer is constantly under vacuum for two main reasons. 1) Usually very small amounts of sample are measured. Thus, the background signal due to the detection of or interaction with other compounds like air or water must be decreased to a negligible factor. 2) Some components of the apparatus, especially the hairpin filament (see chapter 3.1.2) and the channeltron (see chapter 3.1.4), are sensitive towards high pressures. In all chambers, two pumping stages are implemented, a pre-vacuum and a high-vacuum pumping stage. The details are listed in table 3.1. Different working pressures are applied in the individual chambers which is possible due to differential pumping. This is required to both have a reasonable cluster beam (in case of cluster measurements) and low background rates in the Wippi chamber. In order to keep the monochromator (see chapter 3.1.2) and the interaction region clean, an oil free diaphragm pump is implemented. Additionally, all surfaces in contact with the pumped media are made of chemically resistant fluoroplastics to avoid damage cause by the measured chemicals [94]. The pressure in all chambers is constantly monitored by type UHV-24 Nude Bayard-Alpert Ionisation Gauges [95]. Those hot cathodes do not possess an additional magnetic field, making them suitable for the Wippi setup. If the pressure gauge of the Wippi main chamber detects pressure values above $6 \cdot 10^{-6}$ mbar, a specially manufactured vacuum security switches off the power to the quadrupole, channeltron and hairpin filament for the protection of the devices. For more details refer to [96]. Hot cathodes are based on the principle of electron ionisation: Since different gases vary in ionisation efficiency, a calibration factor needs to be applied depending on which gas is measured [97]. While pumping, the composition of the gas is modified, as different components are pumped at different efficiencies [92]. While at pre-vacuum pressures the residual gas is dominated by evaporation of water and carbon dioxide from the chamber walls [92], air leaking into the chamber and hydrogen have the main effect at operational pressures [97].

3.2 Cluster Beam Apparatus

The Cluster Beam (CluB) apparatus is the second mass spectrometer used within the course of this thesis. The first version was built at the Max Planck Institute for Dynamics and Selforganization in Göttingen, Germany [99]. Later, it was moved to the J. Heyrovský Institute of Physical Chemistry in Prague where it was extended to its current setup [100–102]. In the present configuration, the setup enables the study of photo- and electron ionisation and dissociation processes of molecules in a cluster environment [100], see figure 3.10. For the study of hydrated biomolecules, only part of the setup is necessary and described in the following sections. A home-built water cluster source with the option of including a dopant molecule is attached as inlet system, see section 3.2.1. An electron gun is used as ionisation source, see section 3.2.2. The ions produced by electron ionisation or attachment processes are mass analysed by a reflectron time-of-flight (RTOF) spectrometer coupled to a multi-channel plate detector, see sections 3.2.3 and 3.2.4.

Chamber	Pre-Vacuum Pump	High-Vacuum Pump	p_{base} / mbar	$p_{working}$ / mbar
Wippi Main	VACUUBRAND MD 4C NT 3.4 m^3/h	Pfeiffer Vacuum TMU 521 P 520 l/s	$10^{-9} - 10^{-8}$	$10^{-7} - 10^{-6}$
Cluster Source	Pfeiffer Vacuum DUO 65 M 70 m^3/h	Pfeiffer Vacuum 1) HiPace 700 685 l/s 2) TPU 2301 P 1900 l/s	10^{-8}	$10^{-4} - 10^{-5}$
Pick-Up	Pfeiffer Vacuum DUO 10 M 12 m^3/h	Pfeiffer Vacuum TMU 261 P 230 l/s	10^{-8}	$10^{-5} - 10^{-3}$

Table 3.1: Details on the vacuum generation in the individual chambers of the Wippi setup, including pre-vacuum and high vacuum pumps, base and working pressure (p_{base} and $p_{working}$). The information of the pumps contain manufacturer, type and pumping speed given for N_2, for more details refer to [94, 98]. All high-vacuum pumps are turbomolecular pumps.

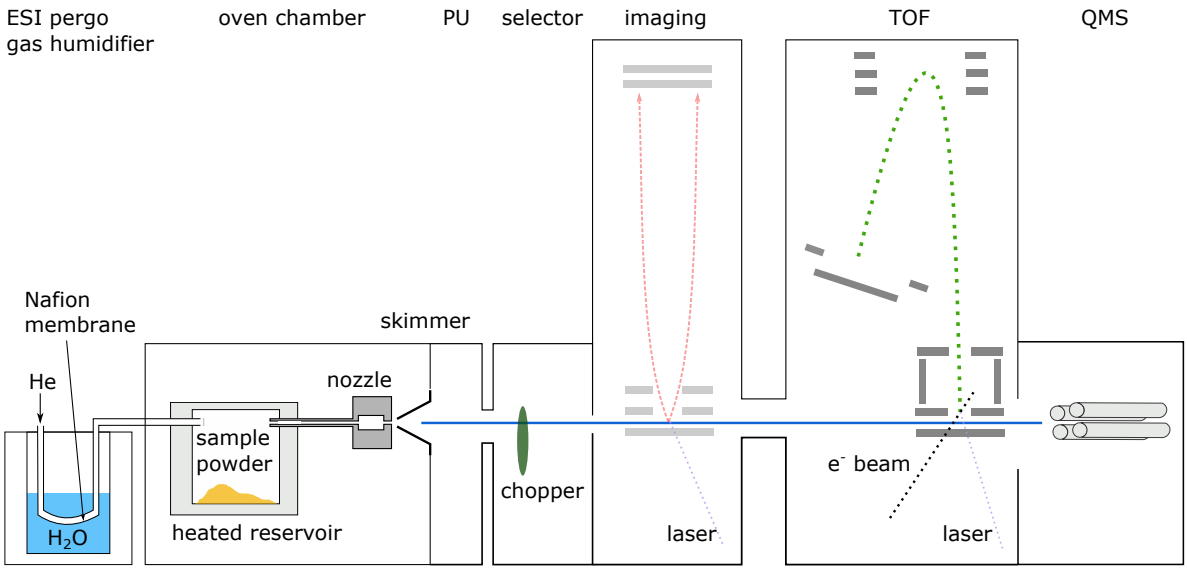

Figure 3.10: Schematic drawing of the CluB mass spectrometer including the main components. For the studies presented within this thesis, the oven chamber (OCI, OCII) and the TOF chamber are actively used. The pickup (PU) chamber remains empty, and the selector chamber contains the chopper which can be inserted into the beam line. Both imaging and QMS chamber remain inactive. Adapted from [103, 104].

3.2.1 Molecular Beam Source

Different inlet systems can be attached to the CluB setup. Here, only the molecular beam source used within the thesis is described. For other application examples, refer to [100–102]. The source was built in order to generate water clusters doped with biomolecular samples and first described in [104]. The basic working principle is as follows: Helium gas is guided through a Pergo Nebulizer Gas Humidifier [105]. This tool was originally developed for the humidification of argon in inductively coupled

plasma mass spectrometry (ICPMS) experiments operating with high concentrations of dissolved solids: It is commercially available from Elemental Scientific [105]. In such a humidifier, the buffer gas passes through a Nafion© membrane tube placed in a water reservoir, see figure 3.10. The membrane is permeable for water vapour but not for argon gas, or, as applied here, neon and helium [105]. The water reservoir is filled with deionised water and kept at constant temperatures between (28-32)°C which enables a high degree of control and stability of hydration [105, 106]. After exiting the humidifier, the buffer gas is introduced into an oven. While the Pergo is working under atmosphere, this is the first component inside of the vacuum system. The sample under investigation is filled into the oven as a powder and heated until evaporation. The humidified gas picks up the gaseous sample compound. At the end of the oven, a conical nozzle with a 90 µm diameter is mounted. Via supersonic expansion, the gas mixture forms a cluster beam, as described in section 2.4.3. In order to avoid condensation of the molecular sample, the nozzle temperature is always kept slightly higher than the temperature of the oven. The mean cluster size can be controlled by adjusting the expansion conditions, specifically the nozzle temperature, the buffer gas pressure and the nozzle geometry, see section 2.4.3. A skimmer is placed approximately 25 mm behind the nozzle. The exact position between nozzle and skimmer can be manipulated from outside as the oven is placed on top of a platform that is movable in height, sideways and back and forth individually.

The next three chambers, all differentially pumped, remain empty during the course of the experiments. The first chamber is an additional pick-up chamber, the second is the so called selector chamber, and the third is the first chamber for analysis with the option of photo-dissociation processes and velocity map imaging (VMI). A pseudo-random chopper is mounted in the selector chamber and allows to chop the beam for background measurements.

3.2.2 Electron Gun

The experimental chamber behind the VMI chamber is equipped with a laser and electron gun as ion sources and a reflectron time-of-flight analyser. Since electron interactions are studied here, the electron gun is applied as ion source. The schematics of the source are shown in figure 3.11. The electron gun is pulsed at 10 kHz, corresponding to a pulse length of 1 µs. The produced electron beam is guided magnetically towards the interaction region improving mass resolution [102]. The electron energies are tunable up to approximately 90 eV, but in the very low energy range between 0 eV and about 1.3 eV the source works sub-optimally since it was optimised for operation at energies on the order of several tens of eV [104]. An earlier study has shown that in the low energy region, the measured current at a Faraday cup behind the interaction region does not correspond to the electron current in the interaction region itself [104]. Data taken in that region requires backup measurements at experimental setups dedicated for those energies, like the Wippi setup. As the electron gun does not comprise a lens system for reducing the energy resolution but is rather designed for maximal electron currents, the energy resolution is limited to 0.6 eV [104]. The cathode heating currents are optimal between (2.3-2.5) A and can be adjusted in order to have a stable emission, which is defined as the sum of all electrons emitted from the filament.

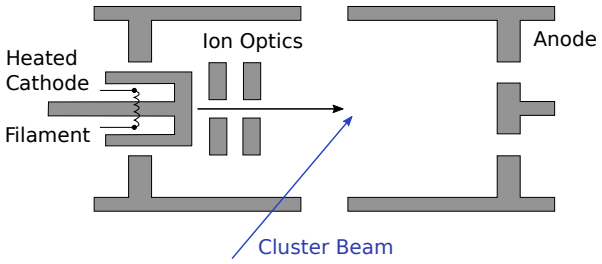

Figure 3.11: Schematics of the electron gun used as ion source. Adapted from [102].

3.2.3 Time-of-Flight Mass Analyser

The cluster beam and the electron beam cross each other perpendicularly. Orthogonal to both beam axis is the mass analyser. In CluB, a reflectron time-of-flight (RTOF) mass analyser is installed. The basic working principle of a TOF in general is illustrated in figure 3.12. Charged particles with different m/z values but with equal kinetic energy E_{kin} differ in their time of flight in a field free region of given length. To apply this effect for mass analysis, the starting point and time of all ions must coincide or at least lie within a narrow interval. Hence, the extraction of a TOF is pulsed.

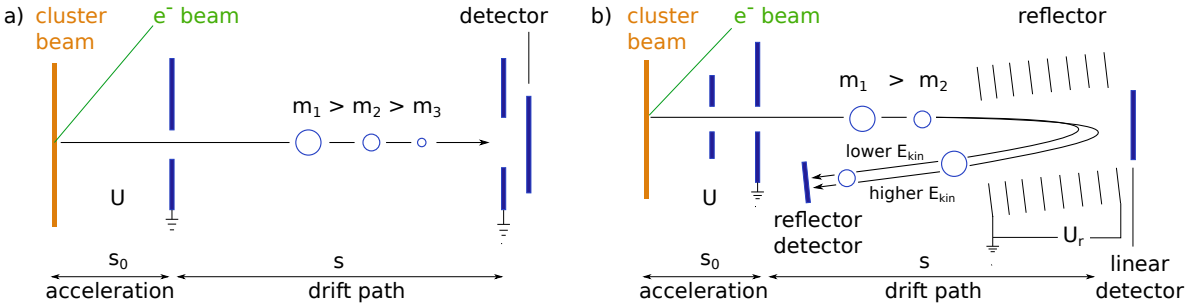

Figure 3.12: Scheme of the working principle of a time-of-flight (TOF) mass spectrometer. Ions of different m/z are separated by their time of flight in a field free region after an initial extraction pulse of voltage U. a) Linear TOF, b) reflectron TOF. Adapted from [29].

The mass spectrum is obtained from the different arrival times of the ions. During the extraction pulse of voltage U, the ion of charge z and mass m acquires the energy of the potential E_{el} which is transformed into kinetic energy

$$E_{\mathrm{kin}} = \frac{1}{2} m v^2 = z\,e\,U = E_{\mathrm{el}} \tag{3.8}$$

Hence, the velocity v of the ion after extraction is

$$v = \sqrt{2\,\frac{z\,e\,U}{m}} \tag{3.9}$$

assuming it was at rest before the pulse. At constant velocity, the ion requires the time

$$t_d = \frac{s}{v} = s\sqrt{\frac{m}{2\,z\,e\,U}} = \frac{s}{\sqrt{2\,e\,U}} \cdot \sqrt{\frac{m}{z}} \tag{3.10}$$

for passing a distance s in a field free region. If multiply charged ions are formed, the

m/z scale is compressed by a factor of z as when compared to singly charged ions. This results in the possibility of overlapping peaks. The time interval Δt_d between the arrival of two ions with different m/z value is given by

$$\Delta t_d \propto s \left(\sqrt{\frac{m_1}{z_1}} - \sqrt{\frac{m_2}{z_2}} \right) \tag{3.11}$$

implying that Δt_d decreases for increasing m/z at constant $\Delta m/z$. This entails two effects. The first is that the mass resolving power decreases. In general, the resolution R is stated as the ratio

$$R = \frac{m}{\Delta m} \tag{3.12}$$

at a certain peak at mass m and full-width half-maximum (FWHM) of Δm [29]. The second effect is that the mass scale is not linear and at least three data points (m/z, t) are required for calibration. Then, the mass scale is calibrated according to

$$m/z = A\,t^2 + B\,t + C \tag{3.13}$$

with A, B, and C as the calibration constants. In case of more calibration points, a least square fit is applied [102].

In a linear TOF, see figure 3.12 a), the ions are produced by e.g. an ionisation event in a time span t_0 typically on the order of nanoseconds [29]. Subsequently, the ions are accelerated into the field region of length s_0

$$s_0 = \frac{1}{2}\,a\,t_a^2 = \frac{1}{2}\,\frac{F}{m}\,t_a^2 = \frac{1}{2}\,\frac{z\,e\,U}{m\,s_0} t_a^2 \tag{3.14}$$

where t_a is the time spent in that region. Thus, the total time from the interaction of the molecular beam with the ion source beam until the detection of the ion is given by

$$t = t_0 + t_a + t_d \tag{3.15}$$

The transmission of a linear TOF is high at approximately 90 % [29]. The main sources of ion losses are due to collisional scattering with the residual gas and poor spatial focusing of the ion source beam [29]. Further advantages of a TOF in general are the basically unlimited mass range, ideal for cluster studies. The only limitation is given by the time between the individual pulses. Additionally, with each pulse a full mass spectrum in recorded, i.e. in about 10 µs [29].

But the linear TOF design also has limitations regarding the mass resolution. Those are mainly due to four effects [29]. 1) The ions are not formed simultaneously but with a finite temporal distribution. As can be seen from equation 3.15, this results in varying total flight times. 2) The formation of ions occurs with a certain spatial distribution, giving them different extraction potentials. 3) The molecules in the cluster beam follow an kinetic energy distribution after the supersonic expansion, influencing the extraction conditions. 4) The initial direction of motion after the ionisation event varies, again resulting in different times of flight [29].

To compensate for those effects, the linear TOF can be replaced by a reflectron time-of-flight (RTOF), see figure 3.12 b). In an RTOF, an ion mirror acts as a reflector for the ions, ultimately resulting in focusing ions of different kinetic energies but equal m/z in the time domain. A retarding electric field is placed behind the field free region,

in form of electrodes of increasing potential. In total, the voltage of the reflectron U_r amounts to 1.05 - 1.10 times the acceleration voltage [29]. The ions penetrate the reflectron until their kinetic energy is zero and exit with the same energy as with which they entered. Thus, ions with higher kinetic energies remain longer in the reflectron and hence, the time of flight is (ideally) unified. Additionally, the flight path depends on E_{kin} which results in a correction of the spatial distribution to a certain amount. These advantages outweigh the disadvantage of a drift length about twice as long as for a linear TOF which at some point diminishes the performance of a TOF due to a reduced transmission [29].

In the CluB setup, a Bipolar Reflectron Time-of-Flight Spectrometer RFT50E from Stefan Kaesdorf is installed [107]. The RTOF is composed of a double stage reflectron system with a Willey McLaren ion extraction region [107]. In the TOF chamber, both photon and electron ionisation studies can be conducted. In order to achieve the highest possible sensitivity, the molecular beam passes directly through the extraction region where it is ionised by the ion source beam [108]. Typical resolution values of $m/\Delta m = 4000$ are achieved. In the case of cluster studies, the kinetic energies of the clusters of different sizes vary over a large range due to their different masses at constant velocity. As has been described above, this results in a diminished mass resolution. In order to compensate for this effect, the extraction pulse voltage is set to a high value of 10 kHz, for details refer to [108]. Afterwards, the ions are accelerated to a final kinetic energy of 8 kV [108]. The effective path length of the RTOF amounts to 0.95 m [107].

3.2.4 Multi-Channel Plate Detector

Detectors commonly placed behind TOF analysers are multi-channel plates (MCPs). They consist of an array of about $10^4 - 10^7$ parallel arranged, interconnected electron multipliers, as described in section 3.1.4, see figure 3.13 a). Typical diameters of the individual multiplier channels are in the range (10-25) µm and the length to diameter ratio amounts to 40-50 [109]. To enhance the conversion efficiency of the primary particle to secondary electrons, the channels are arranged with a bias angle of 5-10° with respect to the entrance and exit axis [109]. The upper and lower surface of the MCP are covered with a thin metal layer serving as electrodes between which a typical voltage of 1000 V is applied. Typical amplification factors are $10^3 - 10^4$ but can be increased by three orders of magnitude by applying a cascade setup of two individual plates [109]. This design is also referred to as Chevron arrangement and is shown schematically in figure 3.13 b). The MCPs are rotated by 180°with respect to each other. Besides significantly enhancing the gain, an additional advantage is that the charged-particle feedback is reduced [109]. MCPs are fast-response detectors with a transit time of the cascade on the order of nanoseconds [109].

In CluB, a MCP detector from Photonics in Chevron configuration is integrated [102]. The water clusters to be detected cover a wide mass range. Since all clusters are emitted with the same velocity during the supersonic expansion their kinetic energies differ widely due to their different masses. As described in the previous section, this has the effect that after the extraction and passage through the TOF analyser, they have a finite local distribution. Thus, a large active area of the detector is important to compensate at least partially for this effect. The active area of the detector implemented in CluB amounts to 4 cm [102].

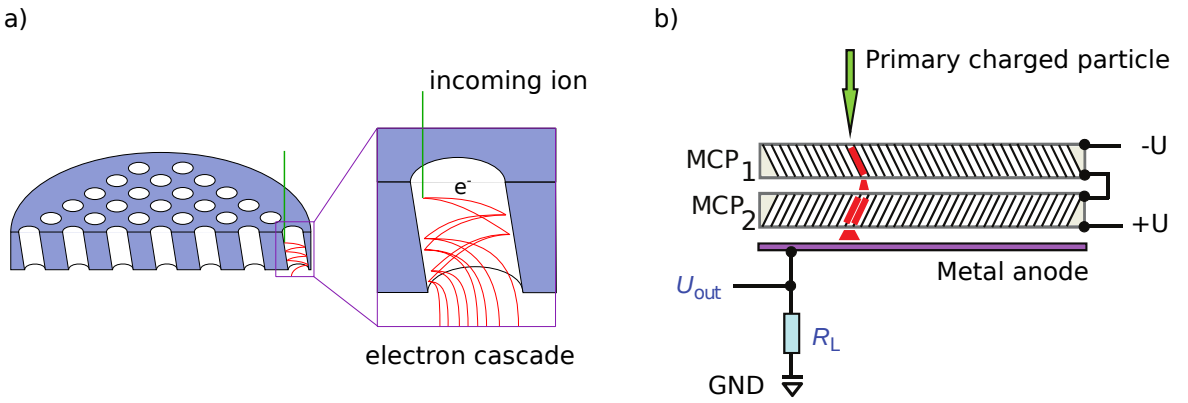

Figure 3.13: Schematics of a microchannel plate, a) in a side view, adapted from [110], and b) in Chevron configuration in a profile view, adapted from [109].

3.2.5 Vacuum System

The CluB setup consists of several vacuum chambers containing the individual parts of the experiments. Essentially, the vacuum protects the sensitive devices, keeps the background rate low and allows the particle and ion beams to pass the rather large distances without large intensity loss due to collisions with the rest gas. All chambers contain a multistage pumping system in order to achieve the required vacuum conditions. For details refer to table 3.2.

In general, the first stage, or pre-vaccum stage, is achieved by rotary vane pumps. Both OKI and OKII feature a high gas load due to the cluster source inlet system and the required volume can be pumped only by using additional piston pumps. For high and ultrahigh vacuum conditions (HV and UHV, respectively), either diffusion and turbomolecular pumps are assembled. Which pumps are installed strongly depends on the purpose of the components within the chamber. The first four chambers are equipped with oil diffusion pumps since they have the advantage of high pumping speeds. In all chambers for mass analysis, namely the TOF, imaging and QMS chambers, turbomolecular pumps are preferred over oil diffusion pumps in order to keep the carbon-containing background at a low level. Some of the chambers also include liquid nitrogen cooled traps in order to freeze rest gas particles and further reduce the background.

Chamber	Pre-Vacuum 1. Stage	Pre-Vacuum 2. Stage	HV- and UHV-Pumps	N_2 Cooled Trap	$p_{working}$ / mbar
OCI	Edwards E2M 175 175 m^3/h	Pfeiffer WKP 1000 1000 m^3/h	Leybold DI 6000 6000 l/s		$4 \cdot 10^{-4}$
OCII	Edwards E1M 175 175 m^3/h	Leybold WS 500 500 m^3/h	Leybold DI 600 E 6000 l/s		$2 \cdot 10^{-4}$
PU	Alcatel T2033 30 m^3/h		Varian VHS 6 2700 l/s	yes	$5 \cdot 10^{-7}$
Selector	Alcatel T2033 30 m^3/h		Varian VHS 6 2700 l/s	yes	$1 \cdot 10^{-7}$
Imaging	Edwards RV 12 14.2 m^3/h		Pfeiffer HiPace700 685 l/s		$1 \cdot 10^{-9}$
TOF	Pfeiffer DUO 10 12 m^3/h		Pfeiffer HiPace700 685 l/s		$2 \cdot 10^{-9}$
QMS	Edwards E2M 18 18 m^3/h		Pfeiffer HiPace700 685 l/s	yes	$2 \cdot 10^{-9}$

Table 3.2: Details on the vacuum generation in the individual chambers of the CluB setup, including the pumping stages and typical working pressures ($p_{working}$). The information of the pumps contain manufacturer, type and pumping speed given for N_2, for more details refer to [98, 111–114]. For chamber abbreviations refer to figure 3.10.

3.3 Analysis and Calibration Methods

Within the analysis of mass spectrometry data, a set of data analysis tools and calibration molecules and methods are applied. Those were applied and are referred to in the results and discussion section.

3.3.1 Data Analysis Software

The main data analysis tools comprise IsotopeFit for the fitting of mass spectra and extraction of cluster series, AEFit for the fitting of ionisation cross sections near threshold and the determination of appearance energies, and resonance onset and area fitting for negative resonance data.

IsotopeFit

IsotopeFit is a software developed by Ralser *et al.* for the analysis and interpretation of high resolution mass spectrometry studies [115]. In complex systems, and especially clusters, a multitude of peaks is observed in the spectra, which can hardly be assigned manually. Additionally, a resolved peak can have contributions from several different types of clusters, including dopants, or even background signals. The isotope distribution featured by some of the compounds only adds to the complexity. IsotopeFit addresses mass spectra rich in peak structures by computationally applying a database containing the exact masses, isotope patterns, and relative abundances onto the data and providing a detailed analysis [115]. For example, the cluster series can be extracted or mass regions can be displayed showing the contributions of individual compounds.

Although the Wippi setup does not provide high resolution data in the mass regime, IsotopeFit can be applied when accepting larger uncertainties in the assignment of peaks to specific compounds. In this thesis, it is mainly used for the extraction of cluster series and identifying stable structures, and to identify the correct compounds contributing to certain peak structures.

AEFit

The behaviour of the ionisation cross section in the threshold region was introduced in chapter 2.2.2. Wigner and Wannier derived an equation (equation 2.22) to determine the ionisation energy or appearance energy from the ion yield curves. The equation is based on a theoretical model and requires and extension when it is applied to experimental data. First, a Heaviside function Θ is multiplied to the equation, since only the behaviour above the threshold region is described. Second, a background contribution b due to noise or other unspecified underlying effects can occur which is superimposed to the signal. Thus, equation 2.22 is extended to

$$f(E) = b + c \cdot (E - \mathrm{AE})^n \cdot \Theta(E - AE) \tag{3.16}$$

This equation is valid for an ideal experimental setup with infinite energy resolution. For all real setups, the energy resolution in finite, usually following a Gaussian profile $g(E)$

$$g(E) = \frac{1}{\sqrt{2\pi}\rho} \cdot \exp\left(-\frac{E^2}{2\rho^2}\right) \tag{3.17}$$

For deriving a function which can be fitted to experimental data acquired with finite energy resolution, $f(E)$ is convoluted with the Gaussian profile $g(E)$, giving

$$\sigma(E) = (f * g)(E) = \int_{-\infty}^{\infty} \mathrm{d}x\, f(x)\, g(E-x) \tag{3.18}$$

$$= \int_{-\infty}^{\infty} \mathrm{d}x\, \left[b + c(E-AE)^n \Theta(E-AE)\right] \frac{1}{\sqrt{2\pi}\rho} \exp\left(-\frac{(E-x)^2}{2\rho^2}\right) \tag{3.19}$$

$$= b + \frac{c}{\sqrt{2\pi}} \rho^n \Gamma(n+1) \exp\left(-\frac{1}{4\rho^2}(AE-E)^2\right) D_{n+1}\left(\frac{1}{\rho}(AE-E)\right) \tag{3.20}$$

where Γ is the gamma function and D_{n+1} is a parabolic cylinder function. A software tool was developed based on this equation and a previous version [116] within the working group with which the experimental data taken at the Wippi apparatus can be fitted. The Chi-Square (χ^2) method is applied and the fit optimised according to a minimisation of the squared sum of the differences of fit and data at each point. The individual uncertainties of each data point are taken into account as a weighting factor. The software tool requires the fitting range and the resolution ρ as input parameters. The output parameters comprise besides the appearance energy (AE) value, the linear background b, the scaling factor c, and the exponent n, including the uncertainties arising from the fitting procedure. Since the input parameters are chosen by the operator and are thus rather arbitrary, this induces an additional uncertainty. Test series of several data sets determined a maximal deviation in the AE value of 50 meV depending on the input parameters, with typical mean values around (10-20) meV deviation. Fitting ranges $\geq$ 3 eV have proven to result in stable AE values. Hence, the square of the quadratic sum of the uncertainty caused by the fit, and the uncertainty caused by the input parameters gives the total statistical error. Since also the calibration molecule is analysed with this fitting tool, the uncertainty on its determined ionisation energy transfers into a systematic error for all cations within an analysis.

Resonance Onset and Area

Dissociative and associative electron attachment to isolated compounds and clusters lead to the formation of resonances as described in chapter 2.3. Those resonances can be described by a Gaussian distribution in first order. In order to extract the peak onset position and the maximum of the distribution, a Gaussian function of the form

$$G(x) = y + A \cdot \exp\left(-\frac{(x-x_c)^2}{2\,w^2}\right) \tag{3.21}$$

can be fitted to the data, where y is the offset, A is the amplitude, x_c the position of the peak maximum, and w the width of the distribution.. In case of several resonances, a multiple Gaussian fit is applied, which basically is a cumulative fit of individual Gaussian distributions. The position of the peak maximum, x_c can directly be extracted as one of the fitted parameters. The area a under the resonance describes the total ion yield of the process and can be calculated by

$$a = 2\,A\,w\,\sqrt{\frac{\pi}{2}} \tag{3.22}$$

The onset of the resonance is a matter of definition and still issue of discussion. Here, a robust and reproducible method was chosen by defining it as the 2σ distance towards

low energies of the position from the peak maximum. This provides a cut-off of 2.1 % of the data which lie before the defined onset. Earlier methods fitted a straight line onto the low energy side of the resonance, which resulted in large uncertainties and depended a lot on the fitting range and person doing the analysis. The new method overcomes these problems by achieving values comparable with the old method, but strongly reducing the arbitrariness. Hence, the onset x_{onset} is given by

$$x_{\text{onset}} = x_c - 2\,\sigma = x_c - 2\,\sqrt{\ln 4}\,w \tag{3.23}$$

3.3.2 Energy Scale Calibration

The energy scale requires a calibration for the acquisition of each data set. The setting of the voltages on the hemispherical electron monochromator (HEM, see section 3.1) and the magnetic field influence the energy which the electrons carry within the interaction region. Since the energy scale is only shifted and otherwise keeps its linear behaviour, a single calibration point is sufficient. For data taking in the region below 10 eV, either the 0 eV resonance from sulfur hexafluoride (SF_6), or from carbon tetrachloride (CCl_4) is used. For the calibration of data taken at higher electron energies, the ionisation energy of neon is determined and compared with the literature value.

Sulfur Hexafluoride

Sulfur hexafluoride (SF_6) is a highly symmetric molecule which features one of the highest electron attachment cross sections σ(EA). The cross section amounts to $\sigma(\text{EA}) \geq 10^{-19}\,\text{m}^2$ and is dominated by the associative attachment and thus the formation of the SF_6^- anion, see figure 3.14 [117]. Below approximately 0.2 eV, the non-dissociative attachment governs the behaviour of the compound. According to theoretical descriptions, an s-wave electron is captured and subsequently, an intramoleuclar vibrational energy redistribution occurs [118, 119]. This leads to lifetimes of the parent anion of $\geq 10\,\mu\text{s}$, which ultimately enable its detection with mass spectrometers [120]. Towards higher energies, the dissociative channels gain importance. Between (0.3-1.5) eV, the formation of SF_5^- is the dominating process and at energies above 2 eV, F^- formation is the most important pathway [117].

Due to the sharp 0 eV peak from SF_6^- of SF_6, the molecule is very suitable both as calibration molecule and for the determination of the energy resolution of the mass spectrometer. The peak position is used to calibrate the energy axis by setting the maximum to 0 eV electron energy, according to the theory, see figure 3.15. Since s-wave attachment results in rapidly decreasing cross-sections, the resonance acquired is a convolution of this s-wave function and the finite electron energy resolution of the beam, typically having a Gaussian shape and dominating the convolution. Hence, the FWHM provides a good measure for the energy resolution of the apparatus.

Carbon Tetrachloride

Carbon tetrachloride (CCl_4) is also a highly symmetric molecule. Electron attachment to the compound leads to the transient negative ion CCl_4^- which has a lifetime of $\approx 30\,\text{ps}$ before autodetachment or dissociation occurs [121, 122]. Thus, it cannot be detected by mass spectrometry experiments. Instead, the most abundant dissociation channel is

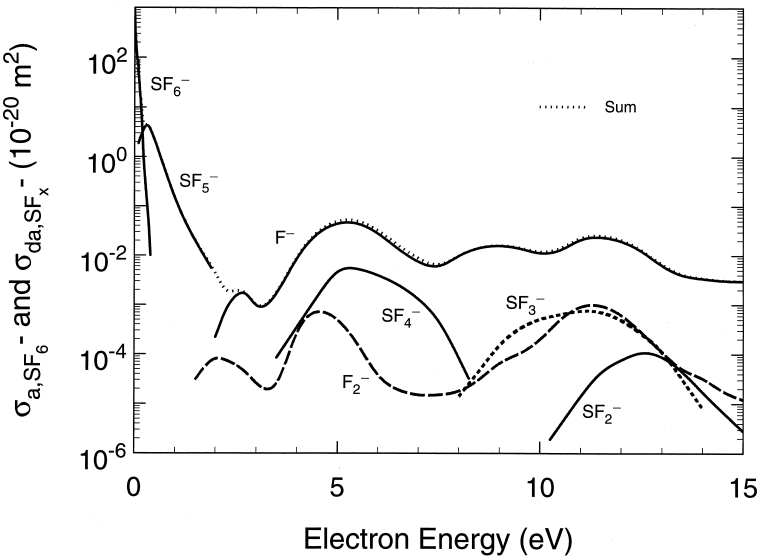

Figure 3.14: Attachment cross section for the associative and dissociative electron attachment to SF_6, leading mainly to the non-dissociative parent anion, SF_6^- after an s-wave electron attachment. Also the dissociative channels are included. Taken from [117].

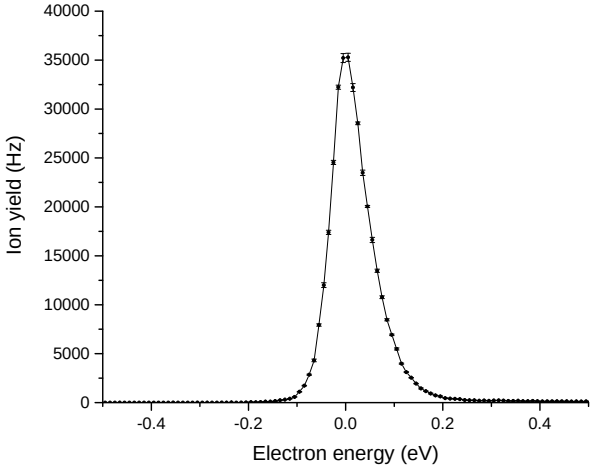

Figure 3.15: SF_6^- from SF_6 calibration measurement example with FWHM $\approx$ 85 meV as measured with the Wippi setup.

observed, leading to the formation of the Cl^- anion via

$$CCl_4 + e^- \rightleftharpoons CCl_4^{-*} \longrightarrow Cl^- + CCl_3 + 0.43\,\text{eV} \tag{3.24}$$

which is an exothermic reaction [123]. The thermodynamic threshold is -0.43 eV and given by the subtraction of the bond dissociation energy of C-Cl_3 (D(Cl-CCl_3)) and the electron affinity of Cl. Thus, electron attachment at 0 eV electron energy is accessible, as can also be seen in the schematic potential energy diagram in figure 3.16. The attachment at 0 eV occurs via s wave electron attachment leading to the symmetric $CCl_4(^2A_1)$ state [124, 125]. Additionally, a second much broader and less intense resonance at 0.8 eV leads to the formation of Cl^-, as can also be seen in figure 3.17 [126]. The TNI assigned to the reaction is the $CCl_4(^2T_2)$ state [127]. Besides the Cl^- anion, also the CCl_2^- and the Cl_2^- anion can be detected at electron energies above 0.6 eV [128].

The electron attachment cross sections for both Cl^- resonances were determined and amount to about $1.3 \cdot 10^{-14}\,cm^2$ and $5 \cdot 10^{-16}\,cm^2$ for the 0 eV and 0.8 eV resonance, respectively [127, 129]. Especially the 0 eV resonance is influenced by the energy resolution of the experimental setup and this is also the reason why the specifications on the ratio of the 0.8 eV to the 0 eV resonance vary in literature between 0.16%-13% [123, 127, 130].

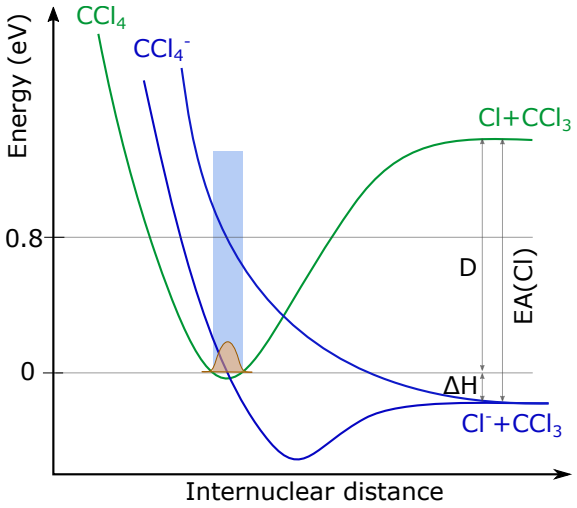

Figure 3.16: Schematics of the potential energy diagram of carbon tetrachloride including two dissociation states leading to the Cl^- anion formation. The electron affinity of Cl (EA(Cl)), the bond dissociation energy D and the thermodynamic threshold ΔH are indicated in the schematics.

For the Wippi experimental setup, carbon tetrachloride is used for three purposes. The first two are the same as for sulfur hexaflouride. They comprise the calibration of the energy scale with the very intense 0 eV peak of Cl^- and the determination of the energy resolution with the FWHM, because again, the s-wave electron attachment results in only a very narrow contribution to the resonance width. The third purpose is the calibration of the magnetic field with the Helmholtz coils of the Wippi apparatus. Since Cl^- has two observable resonances, the peak height ratio and the distance between both peaks can be used to check whether the interaction region is magnetic field free. Since the 0 eV peak is strongly influenced by deviations, a small B-field would already result in a loss of 0 eV electrons, changing the ratio and apparently shifting the peak position to higher energies, since the low energy tail is lost.

Neon

For the calibration of the energy scale of cationic data, mostly a neon calibration is performed. These cationic measurements include appearance energy determination scans and positive mass spectra. The ionisation energy of neon is well known in literature and amounts to IE(neon)=21.56454 eV. Alternatively, also helium gas can be used for calibration with an ionisation energy of IE(helium)=24.58741 eV [131]. The ion yield curve of the rare gases are recorded in an energy range of ±2 eV around the threshold region. Subsequently, the ionisation energy is determined with the AEFit analysis tool as described above. The deviation between the literature value and the determined threshold of the experimental data is equal to the shift of the energy scale. A typical example of such a neon calibration is shown in figure 3.18.

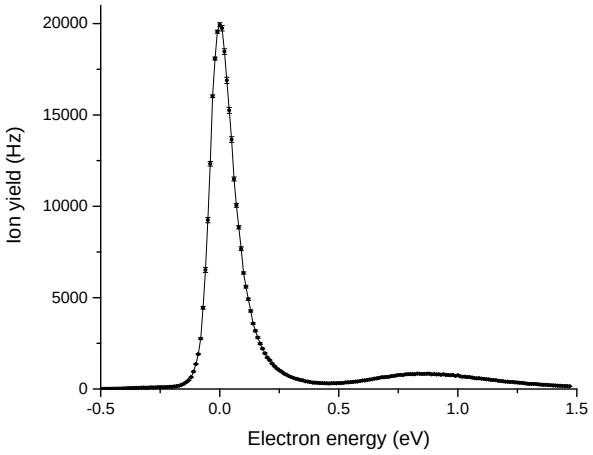

Figure 3.17: CCl_4 calibration measurement example with FWHM $\approx 110\,\text{meV}$ as measured with the Wippi setup.

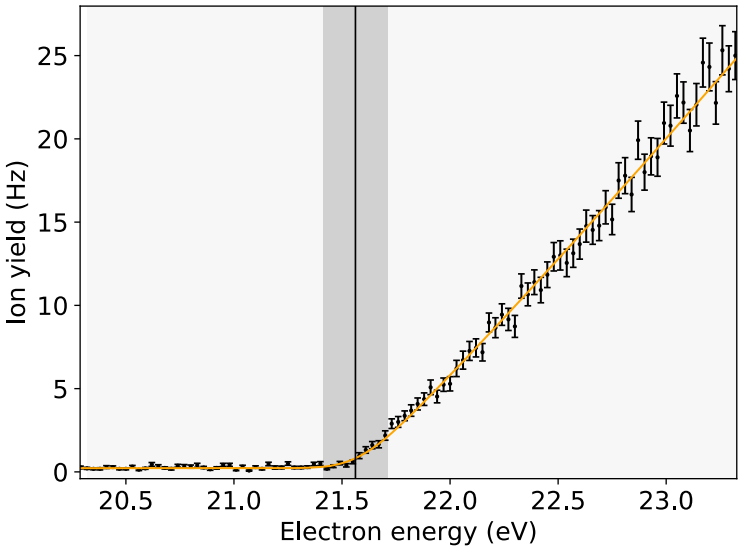

Figure 3.18: Ion yield curve of neon measured for energy scale calibration purposes. The vertical black line represents the determined ionisation energy and the grey region the energy resolution of the hemispherical electron monochromator. The fit from the AEFit analysis tool is shown as an orange line.

Chapter 4

Relevance of Electron Interactions for Radiotherapy

Interactions of (low-energy) electrons with matter are omnipresent and are studied within different background motivations. Those range from plasma and focused electron beam-induced processing (FEBID) to the investigation of the role of low-energy electrons in radiation damage, in atmospheric processes, and in space [6]. Here, the focus lies on the processes induced by low-energy electrons in biologically relevant molecules. As will be reported in this chapter, those electrons arise as secondary particles when matter is irradiated. Irradiation can have both natural sources, like cosmic ray particles, and artificial sources, as is the case for radiotherapy. Radiation is potentially harmful for the human body, leading to DNA mutations and cell death, depending on the energy, the irradiating particle type, and intensity of irradiation. Section 4.1 provides an insight into some of those aspects. In radio-therapy, irradiation is made use of in order to kill malignant cells. It is one out of three traditional cancer therapy methods, along with surgery and chemotherapy. The methods are also commonly combined. Although new methods for cancer treatment arise, radiotherapy remains important with about half of the patients treated for cancer receiving radiotherapy at least once [132]. The physical basis of the treatment is the deposition of energy packages into certain volumes of matter. As a consequence, the atoms and molecules within it are ionised by Compton and photoelectric effects and electrons are released. The biological effects caused depend on several factors, including where, how, and the amount of energy is deposited in the tissue [7]. Since both malignant and healthy tissue is effected by irradiation, efforts are being made to increase the sensitivity of malignant cells towards irradiation. Compounds with this characteristic are referred to as radiosensitisers. They can act via different mechanisms which are reviewed in section 4.2. In this thesis, both biomolecules, for which radiation induced damage is in general unfavourable, and radiosensitisers of different principle of action, are investigated. Experimental consideration for the study of those and a current status of studied compounds are briefly summarised in section 4.3. This chapter only serves as an overview of the radio-physical and radio-biological aspects of electron interactions within radiotherapy. For a complete description, the interested reader is referred to the literature, e.g. references [7, 133] and references therein.

4.1 Radio-Physical Aspects

In the following sections, the radio-physical aspects relevant for radiotherapy are discussed. Those include the primary interaction of radiation with matter, see section 4.1.1, which give rise to secondary particles, see section 4.1.2. The DNA and other macromolecules in a cellular environment can be damaged both directly and indirectly. These concepts are introduced in section 4.1.3. Finally, the possibility of DNA damage by low-energy electrons is summarised in section 4.3.1.

4.1.1 Interactions of Radiation with Matter

Radiation can be classified into either directly ionising, or indirectly ionising. The former comprise charged particles, like electrons, protons, and alpha particles. Those particles interact with the surrounding along their path via the Coulomb force. If the incident particle carries sufficient energy, the atomic structure can be disrupted or electrons are stripped off of the compound, ultimately leading to chemical and biological changes [133]. In contrast, indirectly ionising particles are neutral, such as electromagnetic radiation. In the context of radiotherapy, those especially include γ- and X-rays. Neutral particles act via a two-step process. First, they are absorbed by or scattered from the medium they pass. Second, the energy absorbing compound becomes charged, e.g. by the emission of an electron. These secondary charged particles may further ionise the surrounding in direct processes. Several absorption processes exist for γ- and X-rays, including the photoelectric effect, Compton scattering, and pair production, see figure 4.1 a). The energy of the photon and the chemical composition of the surrounding defines which of the processes dominates [133]. For therapeutic treatments, photons in the energy regime of MeV are applied [7]. Compton scattering accounts for the dominant process between 30 keV and 30 MeV [7] and is thus the relevant process and the only one described here, see figure 4.1 b). The incoming photon is scattered from the compound under irradiation and transfers an energy amount equal to or higher than the binding energy of an electron to the molecule or atom. Subsequently, the photon is deflected into a new direction. The molecule or atom emits an electron carrying some fraction of the photon's initial energy [7]. Compton scattering exhibits only a low dependency on the atomic number of the compound which is also the reason for a similar energy absorption for bone and soft tissue. For the sake of completeness, it should be noted that in contrast to therapeutic irradiation, diagnostic treatment is within the keV photon energy range, making the photoelectric effect the most important ionisation process [7, 133]. The above mentioned ionisation processes continue until the primary and secondary particles are below the energy threshold for further ionisation.

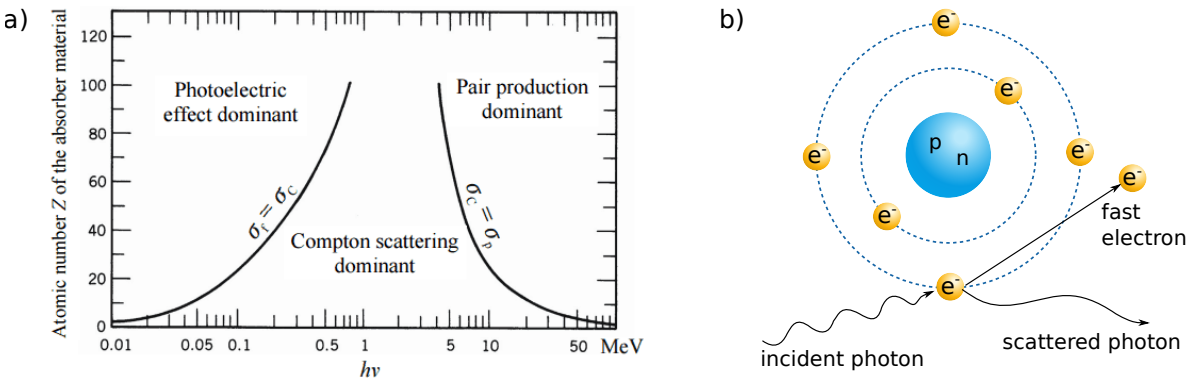

Figure 4.1: Photon interaction processes. a) The relative importance of photoelectric effect, Compton scattering, and pair production depending on the photon energy and the atomic mass number of the absorber. The lines labelled with $\sigma_f = \sigma_c$ and $\sigma_c = \sigma_p$ mark the zone where the cross sections of photoelectric effect (σ_f) and Compton scattering (σ_c), and Compton scattering and pair production (σ_p) are equally high. Taken from [134]. b) Schematics of Compton scattering. Adapted from [133].

4.1.2 Secondary Electrons in Water

Since the human cells consist of about 80% of water, the focus lies on ionisation and electron interaction processes in this medium. Incoming radiation of highly energetic, charged particles deposit about 80% of their energy in ionisation events. The remaining energy is distributed in electronic and vibrational excitation [135, 136]. A Monte Carlo study of protons with kinetic energies between 0.1 and 100 MeV in liquid water simulated the secondary electron energy distribution, see figure 4.2 [137]. The distribution covers an energy range from sub-excitation energies to half of the initial proton energy and peaks at the most probable value of 9-10 eV with only a weak dependence on the energy of the primary ion [137]. The whole reaction chain is discussed in section 4.1.3. The exact distribution is independent of the mass and charge of the incident particle, but depends on the energy of the primary. For higher impact energies, more secondary electrons are produced, corresponding to an increased maximum height of the distribution. Additionally, the maximum is shifted to slightly lower energies, see figure 4.2. Generally, about $4 \cdot 10^4$ electrons are ejected per MeV of deposited energy [138, 139].

It is not the initial energy of the particle defining the physico-chemical consequences, but the energy transferred. A calculated example for an incident 10 MeV proton showed that in 99% of the interactions, the energy transfer is smaller than 100 eV and the mean amounts to 58 eV. The most probable value is 22 eV [137]. The ionisation energy of liquid water amounts to 6.6 eV but the ionisation probability gets only significant from 8-9 eV onwards and reaches unity at above 12.4 eV [137, 140, 141]. Subtracting the latter value as the typical ionisation energy of water from the most probable value of energy transfer, one can calculate the most probable value of electron energy of the secondary electrons, which confirms the aforementioned 9-10 eV, see figure 4.2.

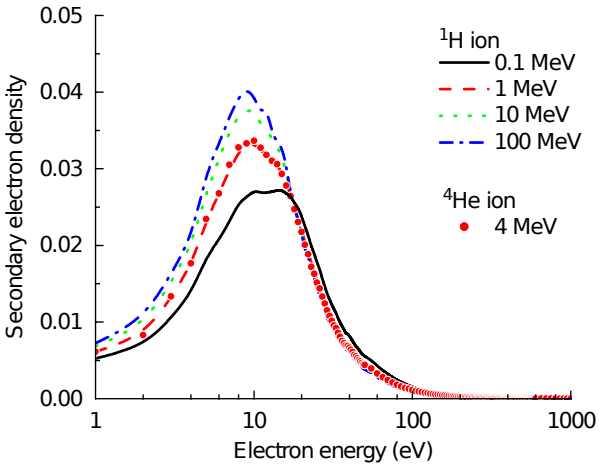

Figure 4.2: Energy distribution of secondary electrons released during primary particle ionisation events in water. Taken from [137].

The secondary electrons produced during the initial ionisation event can themselves carry enough energy for further ionisation or excitation processes. They continue interacting in elastic and inelastic collisions until they are attenuated and lose nearly all of their kinetic energy [142]. Electrons with less than 30 eV are commonly referred to as low-energy electrons (LEEs) [138]. The process of slowing down electrons to close to 0 eV is very fast. The initial ionisation event occurs within 10^{-15} s and is referred to as the physical stage [138]. Subsequently, the electron interacts further, producing ions, excited molecules, and free radicals during the physico-chemical stage on a timescale of 10^{-12} s [138, 143]. At a certain point, the electron will have lost nearly all of its energy,

remaining only with thermal energies of 0.5 - 0.025 eV [138]. Thermalisation occurs at distances of 1 - 10 nm, defining basically the region of energy deposition of the incoming radiation [13, 144, 145] The LEE can be described as polaron which induces dipoles in the surrounding molecules. Within a lifetime of 10 - 20 fs, the electron gets localised by the electrostatic interactions in the conduction band of water [138]. These pre-hydrated electrons have binding energies which amount to about 1 - 1.5 eV and have lifetimes of 200 - 500 fs [145–147]. The state of the electron is further stabilised by dissipating energy into rotational and translational degrees of freedom of the water molecules, until it is finally trapped by a potential well of about 3.2 eV with a lifetime of about 1 ps [138, 146–148]. In that state, the electron is refereed to as solvated or hydrated.

4.1.3 Direct and Indirect Radiation Effects

In general, the primary and secondary radiation particles interact with any molecule in the cell and can potentially damage it. Whether a quantifiable effect arises depends on several factors, including the role of the molecule for the cell's survival and functioning, and how many copies are present in the cell. Since only one DNA molecule is present in every nucleus, it is a critical target and most biological effects involve DNA damage [7, 133]. The origin of damage is classified into direct and indirect effects.

Direct effects arise from an electronic excitation or ionisation of the DNA directly from the incident radiation, or from the recoil electrons released during the ionisation events along the track of those particles, see figure 4.3 a). The highest impact for direct effects carry particles with high linear energy transfer (LET), which is defined as the amount of energy deposited per unit distance. Neutrons and α-particles belong to this group [133]. Since the recoil electrons are solvated on a picosecond timescale, or in a nanometer range, they do only play a minor role for direct DNA damage.

Indirect effects are the result of the interaction between DNA and secondary particles produced in the vicinity of the DNA, see figure 4.3 a). Since the cell mainly consists of water, the processes between primary radiation and the H_2O molecule are of major importance. The dissociation of the molecule is known as radiolysis of water and is summarised in figure 4.3 b), which also includes the secondary species such as free radicals, ions, and low-energy electrons. Additionally, the timescale of events is shown. LEEs are mainly produced by the initial ionisation process of water, described by

$$H_2O + \gamma \longrightarrow H_2O^+ + e^- \tag{4.1}$$

The reactivity of the radiolysis products are very high and if they diffuse far enough to reach the DNA, damage can be induced. It was shown that presolvated electrons account for twice as many DNA strand breaks as the highly reactive OH radical [149]. When compared to the damage induced by direct effects, the indirect actions make up about 2/3 of the total damage [133, 150].

4.2 Radio-Biological Aspects

The main target of radiation therapy when it comes to biological effects is DNA. It represents the carrier of genetic information and alterations in the large molecule can ultimately result in cancer. This section provides a short overview of DNA including its structure and function, cancer as a disease of highly proliferating cells and regions

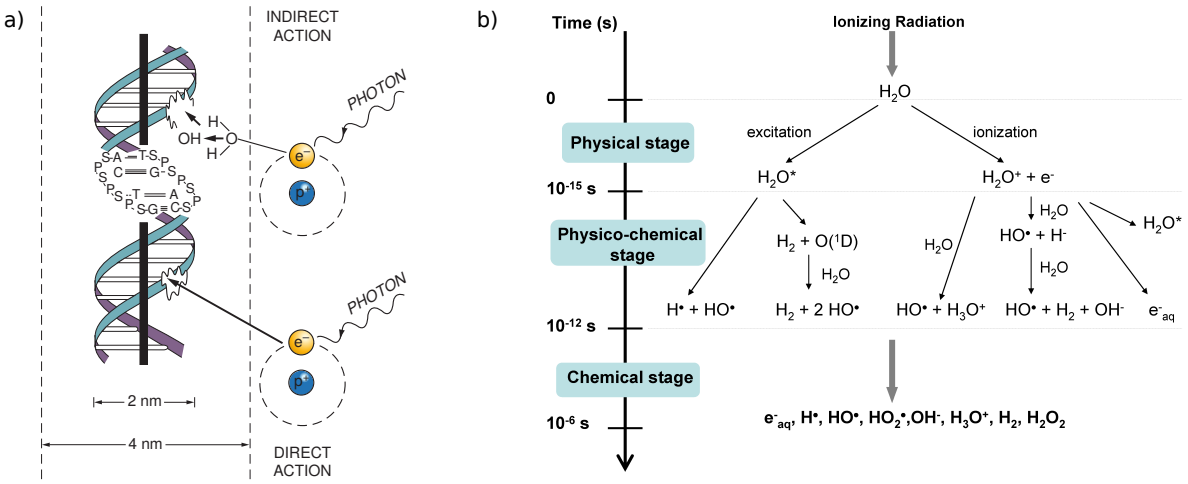

Figure 4.3: DNA damage can be induced by direct and indirect interaction processes, induced by primary radiation and secondary particles. a) Schematics of direct and indirect interactions of radiation with DNA. Taken from [133]. b) Radiolysis of water. All reactive products can potentially induce indirect DNA damage. Taken from [151].

of hypoxia, and radiosensitisers enhancing the killing ratio of malignant cells versus healthy tissue.

4.2.1 DNA, RNA, and Proteins

Deoxyribonucleic acid (DNA) is a molecule of great importance and thus already well studied and described. It consists of two strands which wind into a double helix structure, see figure 4.4 a). Each strand is composed of a backbone of alternating sugar (deoxyribose) and phosphate groups, and four types of nucelobases attached to it. The nucleobases can be differentiated into pyrimidines with a single-ring group, namely thymine (T) and cytosine (C), and purines with a double-ring group, namely adenine (A) and guanine (G). The sequence of the bases defines the genetic code. The two strands are held together by hydrogen bonds. They can only form between the complementary pairs A-T and G-C, see figure 4.4 b), building either two or three hydrogen bonds, respectively [133].

The DNA is located in the cell's nucleus and in mitochondria. The individual genes of the DNA encode the proteins, which each consists of a chain of amino acids. A protein is generated in a two step process. The first step is transcription. Here, the information contained in a part of the DNA is read an transferred to messenger ribonucleic acid (mRNA). It is a complementary copy of the DNA strand. RNA is a single strand similar to an individual DNA strand, but the nucleobase thymine is replaced by uracil. The enzyme RNA polymerase is the catalyser of the formation process. The second step is translation. The mRNA is read in a ribosome. Each group of three bases encodes a specific amino acid. In total, there are 20 which appear in the genetic code. An amino acid is an organic compound consisting of a carboxyl (-COOH), and an amine ($-NH_2$) functional group. Additionally, each amino acid has a characteristic side chain. The specific amino acid sequence encoded in the mRNA results in the formation of a protein [153].

Irradiation can effect the DNA with different lesions ranging widely in severity. For example, irradiation with γ-rays and a dose between (1 - 2) Gy results in more than 1,000 base damages, about 1,000 single strand breaks and around 40 double strand breaks

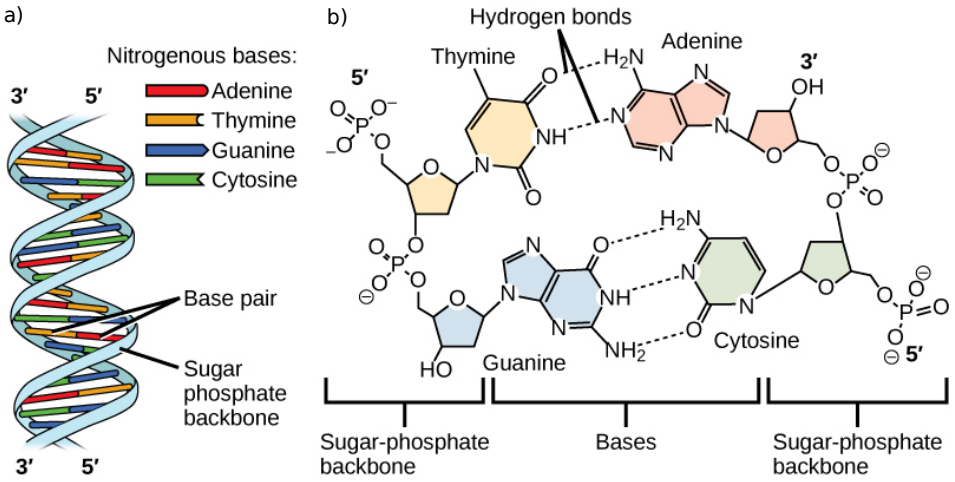

Figure 4.4: Schematic representation of DNA. a) Double strand helix. b) The two DNA strands are hold together by hydrogen bonds between complementary nucleobases. Taken from [152].

[133]. A single strand break can in most cases be repaired by the DNA's own repair mechanism. Here, the second DNA strand serves as template. Double strand breaks are more complex and defined as ruptures of both strands separated by no more than ten bases [154]. The chromatin is ruptured into two pieces and the repair mechanism is only successful in 75% of the cases [155]. Thus, it is believed to be the DNA damage with highest biologically relevant impact. When the DNA's own repair system fails, this can result in the loss, rearrangement, or exchange of DNA segments (bases or entire nucleotides), or even the scission or cross-linkage of the two DNA strands, which means an inappropriate join [7]. During the next mitosis, the damaged DNA either leads to cell death (apoptosis), or the mutations are passed on, which can ultimately result in cancer.

4.2.2 Cancer

Cancer is a broad term for a potentially deadly disease including several different types which can express themselves in very diverse ways. Besides their various forms of appearance and progression, a few critical events are required for the development of cancer. These include mutations which cause an uncontrolled cell growth together with lesions preventing cell death, or apoptosis.

The effects of cancer are diverse, from tumour formation to causing an impaired immune system to further changes which can alter the normal functioning of the body [156–159]. While the cancer starts in a certain area, it can at some point spread to other organs via the lymph nodes. Thus, the malignant cells can advance and invade, subvert, and erode normal tissue [160]. Since the disease is so broad and requires a subject matter expert, the interested reader is referred to the literature, as for example references [156–158] and references therein. At this point, only a short summary to the proliferation of cancer cells and the characteristic oxygen depletion of tumour cells is provided.

Proliferation and Apoptosis

In a proper functioning organism, each cell is regulated regarding its proliferation. Cells are differentiated according to their tasks and at some point or due to certain circumstances they dissolve due to programmed cell death, or apoptosis. All characteristics serve the need of the organism as a whole. In cancer cells, these regulation mechanisms are lost.

The development of cancer can be described as a multistep process. At the beginning, a single cell or a few cells undergo a genetic change which results in the abnormal cellular behaviour. These exhibit an increased proliferation rate, progressing into a region of malignant cells. Additional mutation events provide selective advantages, e.g. quicker growth, which results in even more rapid-growing and increasingly malignant cancer cells [159]. This can extend to the interference with healthy tissue ensuring the functioning of the healthy tissue and organs, or to the spread within the whole body [159].

In healthy cells, the proliferation is regulated by the receipt of appropriate mitogenic signals. In contrast, cancer cells contain one or several lesions which disturb normal growth and division processes. One of them short-circuits the response constraints. As a consequence, the malignant cells do not require external signals for proliferation. Another option for growth-deregulation are mutations which effect the cell cycle directly. Besides influencing cell growth and division, proliferative lesions effect further cell functions, such as their characteristic differentiation. These non specialised cells are immune to the elimination process for progeny cells [160]. Generally, in order for a cell to survive they receive a continuous input signal. In case of the abortion of the signal, apoptosis is induced resulting in the dissolution of the cell. Those signals are only provided within defined somatic environments. If a cell leaves this region, cell death is the automatic consequence. This ensures that the specialised cells remain in the required micro-environment. In cancerous tissue, the region in which the signal can be received is highly extended, thus suppressing apoptosis [160]. Additionally, cell death is triggered in cells under stress, genotoxic damage and depleted survival factors, which is also blocked in malignant cells [160]. A coupling between accelerated proliferation and suppression of apoptosis explains the fast progression of cancer. One type of cancer treatments addresses this point of convergence by e.g. the administration of drugs which are integrated into the DNA of fast proliferating cells [9, 156, 160], see section 4.2.3.

Oxygen Effect

Another effect commonly observed in cancerous tissue is the so called oxygen effect. It describes the dependency of the presence of molecular oxygen in a cell and its response to radiation. As previously described in detail, after the initial absorption of the primary radiation, fast charged particles are produced. These in turn give rise to ion pairs with lifetimes in the order of 10^{-10} s. The subsequent products are highly reactive radicals. Their lifetimes are with 10^{-5} s much longer than those of the ion pairs and play a major role in the chemical damage induced, starting off with chemical bond breakages, and finally resulting in biological damage [133]. Interestingly, the extent of the damage depends both on whether molecular oxygen is present in the irradiated cells or not, and the type of radiation inducing the damage [133]. This can be quantified by the oxygen enhancement ratio (OER). The OER compares the radiation dose administered under hypoxic conditions, i.e. when the cell is deprived of oxygen, and under aerated

conditions. The ratio of both indicates the discrepancy to achieve the same biological effect. While for X- and γ-rays administered with high doses the OER amounts to around 3.5, doses more typical for radiotherapeutic treatment account for OER values of 2.5, see figure 4.5. This means that the treatment of hypoxic tissue with sparsely ionising radiation requires a 2.5 - 3.5 higher dose than well-oxygenated tissue. The effect becomes smaller with higher ionisation degree of the primary radiation and vanishes completely for densely ionising radiation such as α particles [133], see figure 4.5. In order to observe the effect, the oxygen must be present at the moment of, or within miliseconds after the radiation exposure [133]. The similarity in timescales with the free radicals (R) already indicates an interaction with those. When a free radical reacts with the DNA, the complex can usually be reduced into a neutral state by reacting with a sulfhydryl group. While the additional charge is neutralised, an organic peroxide RO_2 is formed which ultimately is a chemical composition change of the DNA. The alteration is permanent, which means that the molecular oxygen fixes the lesion. Hence, the process is also referred to as oxygen fixation hypothesis [133]. In hypoxic cells, the oxygen concentration is too low for those reactions to occur and dedicated repair mechanisms are able to repair most of the lesions.

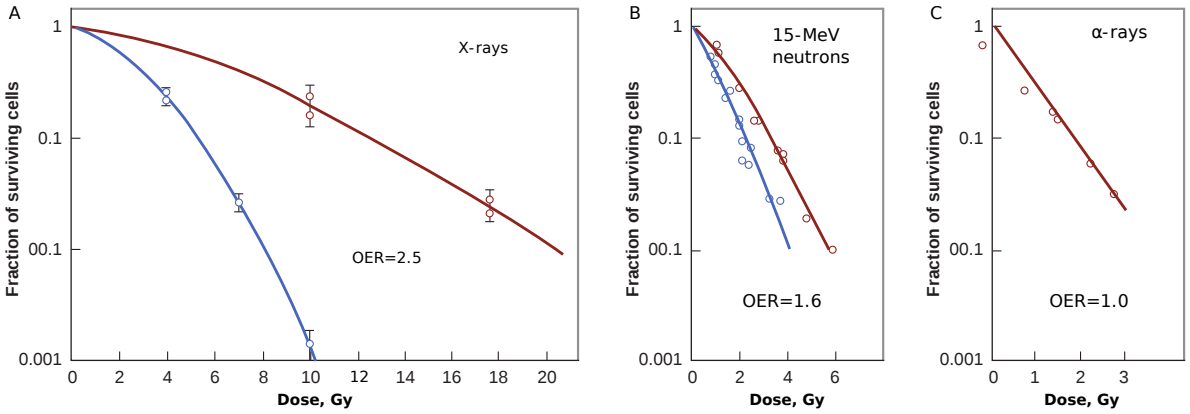

Figure 4.5: The oxygen enhancement ratio for (A) X-rays as scarcely ionising particles, (B) neutrons as medium ionising particles and (C) α-particles as densely ionising particles. Taken from [133].

Two origins of tumour hypoxia are known. The first is chronic hypoxia. Here, the high proliferation rate of malignant cells inhibits the sufficient diffusion of oxygen through the cancerous tissue. The blood vessels are derived from normal tissue and do not meet the requirements of the rapidly growing tissue [156, 161]. The second source is acute hypoxia. The physiological structure of the tumour is less well defined as in healthy tissue and can result in a temporary closing of tumour blood vessels. As a consequence, the tissue is not sufficiently supplied with oxygen [133]. It is important to note that the concentration of oxygen varies among the tumour cells. While the cells at the outer part of the tumour are usually well oxygenated, the concentration decreases with increasing depth into the tumour [161]. In fractionated radiotherapy this is made use of. First the well-oxygenated outer malignant cells are killed by the treatment. Some hours after the treatment, previously hypoxic cells get into the domain of aerated conditions, an effect referred to as reoxygenation. The subsequent treatment leads to further shrinking of the tumour [162]. Unfortunately, this method has limits. Some tumour types cannot be reoxygenated and additionally, surrounding healthy tissue is affected by the irradiation, too.

The therapeutic window is a measure for the range of doses which can be administered resulting in tumour control but avoiding significant adverse health effects, see figure 4.6. To increase the therapeutic window, studies focus on increasing irradiation effects of hypoxic cells without increasing the risks. These methods include inhaling high-oxygen-content gas which enhances the oxygen concentration in nearly all cells, administering cytotoxic drugs that immediately kill hypoxic cells, and administering hypoxic cell radiosensitisers which are drugs selectively improving the sensitivity of hypoxic cells towards radiation [156, 161, 162], see section 4.2.3.

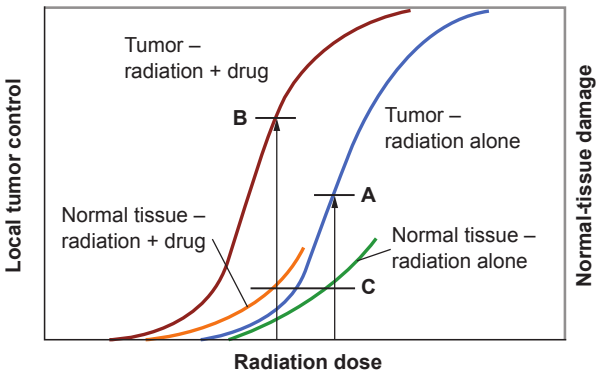

Figure 4.6: The dose-response relationship has a similar shape for tumour and normal tissue. At a given dose, with no additional radiotherapeutic agent, the ratio of tumour control (A) to maximum tolerable level for normal tissue (C) is smaller than with the addition of an appropriate drug (ratio B to C is enhanced). Taken from [133].

4.2.3 Radiosensitisers

Radiosensitisers are one possible component in cancer treatment. At this point, no full review of cancer treatment methods can be provided. This section serves only as short introduction in selected types of radiosensitisers which will be of importance for the compounds studied within this thesis.

Radiosensitisers are chemical and pharmacological agents which address the challenge of increasing the damage of malignant cells compared to healthy cells. They alter the response of DNA to indirect effects as described in section 4.1.3 [133]. Regarding the interaction with electrons, they can basically be divided into agents which enhance the direct electron interaction processes, for example by possessing high electron attachment cross sections, and those which increase the formation of electrons in malignant cells upon radiation, i.e. compounds which strongly interact with the primary radiation and emit secondary electrons for further reactions [6]. In this thesis, the focus lies on the former group. While radiosensitisers increase the cytotoxicity of radiation in tumour cells, radioprotectors save healthy tissue. Ideally, a radiosensitiser is nontoxic and accumulates only in tumour tissue while sparing healthy tissue. Most agents are additionally selective towards tumour type, e.g. they either address highly proliferating cells or hypoxic cells [156]. For a detailed review on radiosensitisers refer to references [8, 9, 133].

Proliferating Cell Radiosensitisers

Most highly proliferating cells seem immune to irradiation, an effect caused by the imbalance of production of new cells towards the death rate of cells induced by the

treatment, resulting in an overall tumour growth. Specialised analogues to the pyrimidine nucleoside thymidine can be incorporated into the DNA due to their structural similarity to the DNA constituent. The most widely tested compounds of this group comprise bromo-, iodo-, and fluoro-deoxyuridine (BrUdR, IUdR, and FUdR) [8]. The halogen atom's dimension is similar to the methyl group of thymidine and the rest of the agent contains the nucleobase uracil, facilitating the incorporation [8].

In combination with radiation therapy, the death rate is significantly increased, with the sensitivity being proportional to the fraction of replaced nucleosides [156]. In order to achieve the best results, the agent should be administered such that several DNA replications occur previous to the irradiation. This guarantees a wider spread of the modified DNA and efficient incorporation into the tumour cell. Since the healthy surrounding cells proliferate at a slower rate, the radiosensitiser spreads more within the tumour cells [8, 156]. The exact action principle remains unclear to a certain degree, but it is likely that the halogen moiety acts as electron capturer. The electron attachment is followed by a bond break between halogen and carbon chain. The resulting carbon containing radical can react with oxygen forming a peroxyl radical which has been shown to induce DNA strand breaks similar to the hydroxyl radical [8]. Proliferating cell radiosensitiser are especially suitable for tumours exhibiting aggressive growth rates which are surrounded by healthy tissue that either has slow or no proliferating characteristics. Examples for such carcinoma are brain tumours and sarcomas [156].

Hypoxic Cell Radiosensitisers

A second group of radiosensitising agents addresses the hypoxia problem. Instead of trying to increase the oxygen concentration in a cell, other compounds which mimic the oxygen fixation effects are administered. The substitutes are designed such that they are not consumed by the metabolism of the cells. This enlarges the diffusion path compared to molecular oxygen and regions even deeper inside of the tumour are reached by the agents [133, 156]. Additionally, high electron affinities are favourable in order to ensure an efficient activity in terms of fixation of DNA damage induced by free radicals [8, 9]. Adams was the first to define four characteristcs a hypoxic radiosensitiser should fulfill. First, the agent is selective to hypoxic cells and the required concentrations are nontoxic to healthy tissue. Second, the radiosensitiser is not decomposed by the metabolism of the cell. Third, the compound must diffuse deeply into the poorly vasculated areas (as far as 200 µm) and is thus either soluble in water or in lipids. Forth, conventional radiotherapy is administered in low doses of a few Gray daily at which the agent must be working efficiently [133, 163].

Nitroimidazoles have emerged as compounds potentially fulfilling these requirements. They consist of a nitroaromatic imidazole ring, a hydrocarbon side chain, and a nitro group. The side chain defines position 1 in the ring labelling, see figure 4.7 a) and b), and is responsible for the lipophilicity of the agent. Unfortunately, it also determines whether or not the drug is toxic, i.e. whether side effects are to be expected. Hence, it is the chemical property limiting the maximum dose to be administered. The nitro group contributes the high electron affinity of the compound. Its position at the imidale ring classifies the agent into a 2-, 4-, or 5-nitroimidazole [8, 9, 133, 156].

The first nitroimidazole to be partly successfully tested was misonidazole, see figure 4.7 b). After encouraging studies were carried out for cells in cultures and in mouse mammary tumours, clinical trial were initiated [133]. While in the laboratory experiments high single doses were administered, the doses had to be reduced for application in humans. The lipophilicity of misonidazole caused the drug to penetrate into the

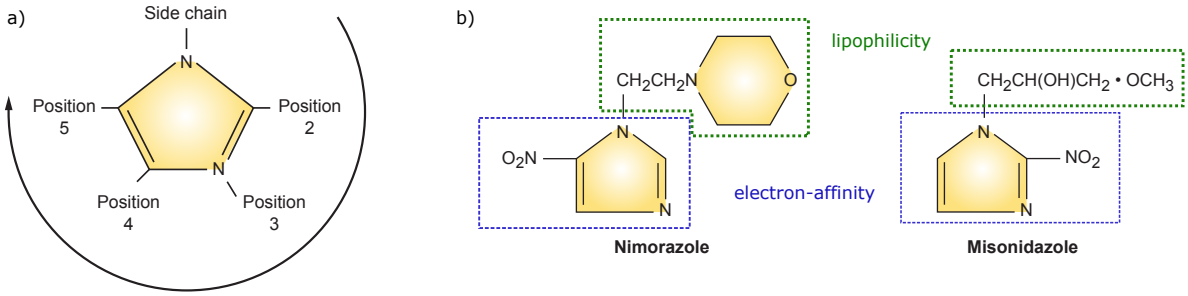

Figure 4.7: Nitroimidazolic compounds. a) General strcuture and numbering. b) Structure of nimorazole and misonidazole. The blue boxes represent the nitroimidazole which is responsible for the high electron affinity and the green boxes represent the side chain which determines the toxicity due to the lipophilicity. Adapted from [133].

nervous system resulting in severe side effects [9]. The Radiation Therapy Oncology Group, USA, found that the consequently lower doses applied were not sufficient to provide statistical advantages in the treatment with misonidazole as a radiosensitiser [164]. A study conducted in Denmark further categorised the patients showing that while an uncategorised group of patients did not show any beneficial effects, the subgroup of males with high hemoglobin levels profited from the administration of misonidazole prior to the treatment of pharynx cancer, doubling the three years tumour control [133, 165], see figure 4.8 b). In order to reduce the toxicity of the drug, further nitroimidazolic derivatives were developed. Even before misonidazole, metronidazole was unsuccessfully tested. Misonidazole proved to be more active and with benefit for a subgroup, but toxic. Etanidazole was less toxic, but did not show any benefits, same as for the pimonidazole which was derived thereafter. Finally, nimorazole was suggested, see figure 4.7 b). While it was less active than its precursors, it was also much less toxic which allowed for the administration of much higher doses. A study of head and neck cancers conducted in Denmark demonstrated benefits for the treatment under the administration of the agent and nowadays it is commonly used for head and neck cancer patients in combination with radiotherapy [133, 166], see figure 4.8 a).

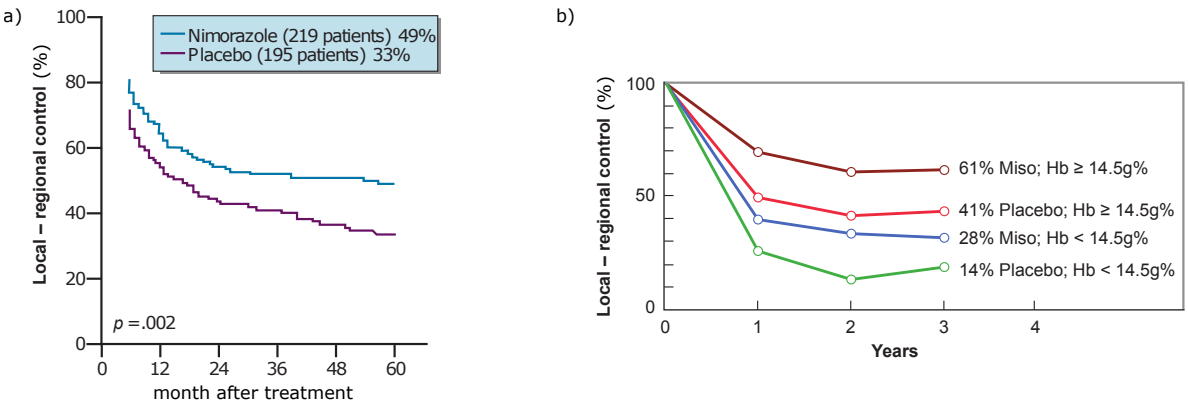

Figure 4.8: Loco-regional control in patients treated for head and neck cancer in Denmark. Results from the DAHANCA protocols from references [165] and [166], for a) nimorazole, taken from [156], and for b) misonidazole, taken from [133].

4.2.4 Time Scale of Events

The last two sections (4.1 and 4.2) can be summarised regarding the time scale of events, see figure 4.9. The initial physical actions of radiation interaction with matter occur within 10^{-15} s. They include the initial ionisation and excitation events. Additionally, it is the timescale at which the electrons are completely solvated. At the physicochemical time regime between $10^{-15} - 10^{-12}$ s, free radical formation takes place. It is followed by the chemical stage in between $10^{-12} - 10^{-6}$ s, which is governed by reactions induced by radicals, e.g. single and double strand breaks induced by the hydroxyl radical, and diffusion controlled reactions. The final classification which follows is the biological stage. It can extend over the whole human lifetime and in the case of mutations in the germ even pass on to future generations. Biological effects such as DNA modifications and subsequent enzyme reactions determine the initial phase. In some cases the DNA is repaired by biochemical reactions but in the case of a faulty or missing repair, the DNA lesion can result in mutations or cell death, which is on the time domain of hours. Follow-up effects are diverse and determine the later phase of that stage, ranging from cancer to inheritable diseases [6, 133, 138].

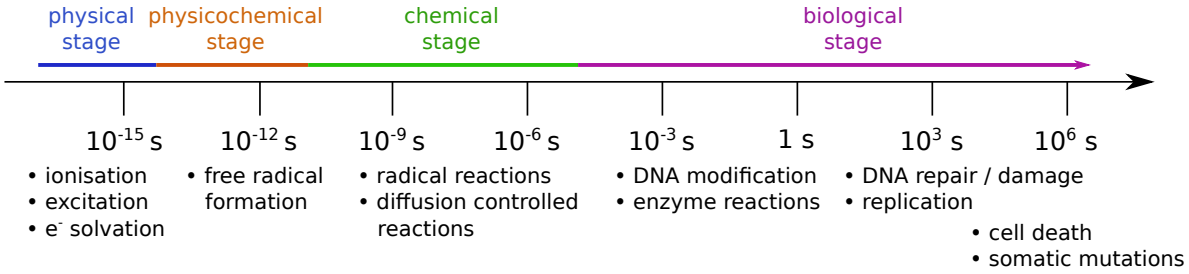

Figure 4.9: Timescale of events during radiotherapeutic treatment divided into physical, physicochemical, chemical, and biological stages.

4.3 Current Scientific Status

The understanding of the importance of electron-driven effects on biologically relevant molecules gained a lot of interest over the last two decades. Several motives for the increasing research efforts can be found. From understanding the basic reactions and working principles of irradiation to developing new chemical agents specifically designed for high electron interaction cross sections. Subsequently, the current scientific knowledge on DNA damaged induced by low-energy electrons will be summarised. Experimental considerations are explained which are important for the planning of new research. Finally, a broader overview of biological building blocks relevant for tissue under irradiation is provided, motivated by the compounds studied within this thesis.

4.3.1 DNA Damage by Low-Energy Electrons

As was discussed in the previous section, DNA possesses highly effective repair mechanisms and mostly the excited states of the DNA nucleobases have very short lifetimes before they de-excite back into their stable form. Nevertheless, not all damage is repaired but some interactions result in photo-physical and -chemical processes, which can ultimately give rise to intermediates for mutagenesis and cancerogenesis [6, 167]. Reducing the considerations to electron induced damage only, direct effects are highly

unlikely due to their solvation and stopping within a nanometer range [145]. In contrast, indirect damage is very important, caused by electrons being produced in the vicinity of the DNA and thus with a sufficient range to interact with the macromolecule [6].

In 2000, it was first demonstrated in an experiment that low energy electrons induce DNA damage. The group of Sanche irradiated plasmid DNA with electrons in an energy range between 3 and 20 eV [168]. Plasmid DNA is a cicular double-stranded DNA containing a few thousands of base pairs. They were able to show that both single and double strand breaks (SSBs, DSBs) are induced by those interactions. The recorded ion yields for SSBs and DSBs feature a distinct peak structure below 15 eV, with a maximum at 8 eV for SSBs and 10 eV for DSBs [168]. As discussed previously, the energy range of produced electrons within radiolysis matches this region, suggesting that these lesions are a possible and realistic scenario during irradiation. The study was extended by the same group, first to the energy range up to 100 eV [169] and later also covering 0 to 4 eV electrons [11]. The latter found that also those electrons induce SSBs efficiently, featuring a global maximum at slightly below 1 eV and another peak structure between around 1.5 and 3 eV [11]. These results are in so far surprising and exciting as they show that DNA damage induced by electrons occurs at energy values even below typical vertical ionisation energies of the DNA nucleobases, which range from 8 to 9 eV [170]. Other processes occurring in that range are electron excitation of the DNA nucleobases at 4 to 5 eV [171], the bond dissociation energy and the vibrational excitation energy of the C-C bond at 3 to 4 eV and 0.1 to 0.5 eV, respectively [6].

The topic of electron interaction with DNA has since gained increasing interest. A few years later, it was shown that besides free electrons with kinetic energy, also those electrons which have lost all their energy within interaction processes in water can induce DNA damage [10, 172]. These presolvated electrons with lifetimes of 1 ps interact with the DNA building blocks forming transient anions which can either relax back or decompose. While the formation of nucleobase anions under dry conditions was known already [10], the study by Wang *et al.* extended the research to a water environment with the main result that presolvated electrons efficiently induce SSBs and DSBs [172]. In a later study by the same group, it was even found that the effectiveness of reductive DNA damage is about twice as high for presolvated electrons as for the hydroxyl radical, which was beforehand believed to be the dominant interaction partner [149]. Most later studies confirmed that presolvated electrons induce DNA damage but exclude DNA lesions caused by solvated electrons. This leaves only a very short time window for electron interaction processes with DNA resulting in measurable effects such as SSBs and DSBs [145, 173–175].

An extended and comprehensive summary of low energy electron damage can be found in reference [176].

4.3.2 Experimental Considerations

Studying the basic principles underlying the interaction of radiation with matter provides several possible experimental systems. One decision concerns the compound to be studied. Basically, two possible approaches exist. In the top-down approach, the complete molecule of interest is investigated and conclusions are made on the individual parts of the compound. In the context of radiation damage leading to biological changes, this mainly includes the DNA or a whole protein. Those compounds are large and thus complex systems. Although giving a complete overview about the occurring reactions, the analysis of data is very complicated and not always unambiguously possible. Sev-

eral reaction products might be assigned to different reactions, obscuring what is going on in detail. Exactly the opposite is followed with the bottom-up approach. Here, the first studies are conducted with the basic building blocks of the macromolecules. The reaction products can be assigned to distinct reaction pathways. In further steps, the complexity of the molecule is increased and the results are compared with the former ones [6].

Besides the complexity of the molecule being studied, different environments can be considered by conducting gas-phase, surface, or cluster (up to solution) experiments. Gas-phase experiments represent the simplest system where the isolated compound interacts with an electron. It is well defined and allows for an unambiguous assignment of reaction pathways and threshold values without interference effects with the surrounding environment. While the main advantage is to describe the basic physical interactions, it does not represent the situation in tissue. Thin films, or surface experiments allow for studying larger molecules than possible in the gas-phase. Additionally, the film can mimic a surrounding material for the compound. The major drawbacks include that film charging effects can occur which change the electric field which ultimately results in a worse energy resolution or systematic shift in energy. Another problem is the discrimination of heavy anions. Energy is required to desorb from the surface, a process which favours light particles and generally shifts the energy axis. Cluster or solution measurements have the advantages of mimicing an environment for the molecules. At the same time, no desorption effects occur. Regarding electron interaction processes, additional pathways are possible, see sections 2.2 and 2.3, and also energy shifts of the reaction channels can occur when compared to gas-phase measurements. That is why cluster measurements are ideally combined with gas-phase measurements to be able to both assign the experimental data to reaction pathways and determine the effects of the environment on the molecule and what changes arise from it [6].

Finally, which approach is chosen and which system is studied depends on the question asked. Shall basic physical principles or a more realistic scenario be described? Or in other words, is it the physical or chemical details of a single compound one is interested in or the overall picture? Different approaches are followed by the individual research groups working in the field of electron interactions.

4.3.3 Electron Interactions with Biological Building Blocks

Probably the most commonly used approach is the bottom-up approach. After experiments demonstrated that DNA is damaged by low energy electrons, several research groups started studying the electron interactions with both the constituents of DNA and further biological building blocks. Regarding constituents of the DNA molecule, one of the interests is the position of the initial electron attachment. This is also an important information for the development of radiosensitisers addressing highly proliferating cells which are built into the DNA strand. If a DNA strand break occurs, a bond in the backbone composed of alternating sugar and phosphate groups cleaves. Experimental studies on direct electron attachment to gas phase model compounds of the phosphate group and sugar unit were conducted. Those include in the case of the phosphate group several phosphoric acid esters [177] and in the case of the sugar unit tetrahydrofuran [178], 2'-deoxyribose [179] and ribose [180]. The investigations conclude that electron attachment to those model compounds is possible at a variety of energies, including close to zero eV energies. Subsequently to the attachment, a considerable amount of dissociation pathways are available which possibly correspond to potential reactions

resulting in strand breaks [6]. Besides the interest in the DNA backbone, studies were conducted with the DNA and RNA nucleobases, thymine, cytosine, uracil, and adenine [181–188]

If the electron initially attaches to a nucleobase instead of the DNA backbone, a charge transfer must follow which ultimately induces the bond cleavage. This process was first theoretically described by the group of Simons [189] and further studies followed [190–195]. Overall, they found that electron attachment to nucleobases is accessible at even lower energies than compared to the phosphate group. Additionally, all nucleotides (nucleobase plus sugar plus phosphate) can capture low energy electrons down to zero eV according to their calculations and subsequently induce DNA strand breaks [6]. Also in the experimental studies the complexity of the complexes was increased gradually and both nucleosides (nucleobase plus sugar) and nucleotides were studied. In 2012, the first study of a nucleotide, namely deoxycytidine monophosphate, confirmed that a phosphodiester bond breakage is likely to arise from direct electron attachment to the nucleobase site of the nucleotide [6, 196]. A detailed review can be found in reference [197]. According to the current scientific status, both the reaction pathway of electrons directly interacting with the backbone and the attachment to the nucleobases can contribute to DNA damage [6].

Besides the study of DNA related model compounds, further biologically relevant building blocks attracted interest. One of them is imidazole. It is present in the amino acid histidine, the hormone histamine, and in antifungal drugs [198]. It consists of a 5-membered planar ring with the formula $C_3N_2H_4$. Imidazole fused with pyrimidine results in purine, the most abundant nitrogen containing heterocyclic aromatic organic compound [199]. Adding a nitro group to the imidazole ring gives nitroimidazole which is present in a series of antibiotics and radiosensitisers addressing tumour hypoxia [200].

Imidazole and nitroimidazoles were studied regarding their electron interaction properties. The electron attachment reactions of imidazole are driven by the cyanocarbon group [201]. The most important channel is described by single hydrogen loss, but also multiple hydrogen loss is observed up to complete dehydrogenation. Additionally, more complex reactions were observed involving the entire molecule [201]. For nitroimidazoles, it was shown that electron attachment reactions are driven by the nitro group. As a consequence, the dissociation channels vary. It was found that a differentiation between the isomers 2-, 4-, and 5-nitroimidazole (2NI, 4NI, 5NI) is required regarding the dissociation channels [202]. While for 2NI the most intense pathway is the formation of neutral H_2O and the according anion, for 4NI and 5NI single hydrogen loss is the dominant reaction [201, 202]. Besides those reactions, also highly reactive products are formed, such as the hydroxyl radical, which again is stronger for 2NI. All isomers additionally fragment further into products such as the NO radical, HNO_2, and CO_2 [202, 203]. When assuming that the action of a radiosensitiser is based on its dissociation into reactive species including radicals, this suggests that the 2NI is a more efficient chemical agent but also more toxic [202]. In another study it was shown that methylation of nitroimidazole stabilises the parent anion and blocks the dissociation reaction completely below 2 eV [203].

Gas-phase experiments are essential to understand the fundamental interactions of the isolated molecule of interest. In order to improve the comparability to the real conditions in the tissue, the surrounding of the compounds need to be simulated. Since the biological environment is dominated by water (with high salt concentrations and surrounded by proteins), water clusters provide a medium which mimics the natural surrounding to the first order. So far, experimental studies on this topic are rare. In

2015, a comparative study of electron attachment to pure and hydrated pyrimidine clusters found evidence that the solvation prevents the ring from fragmenting. Additionally, the anionic monomer was observed in pure pyrimidine clusters while it was unstable under isolated or even hydrated conditions [204]. An electron ionisation study of hydrated and non-hydrated tetrahydrofuran clusters also reported the protective behaviour of the cluster but also discussed new fragmentation channels compared to the isolated compound [205]. Another research group performed electron attachment studies with nucleobases and derivatives of uracil embedded in water clusters [104, 106]. They reported that the dissociation of uracil and thymine was successfully suppressed by the water molecules and ascribed the behaviour to caging-like effects and fast energy transfer [104]. With this observation, they objected theoretical predictions stating that microhydration would enhance the fragmentation processes of uracil [206]. The second study estimated the energy transfer from uracil, 5-fluorouracil, and 5-bromouracil to the surrounding water molecules by quantifying the number of H_2O molecules being evaporated. They found that the average number for 5-bromouracil was much higher, which was also the only compound undergoing DEA reactions under hydration [106]. Only recently, imidazole was measured in a helium cluster environment. Those clusters provide very low temperatures in the few Kelvin range and allow the biomolecules under investigation to aggregate into a cluster themselves which can subsequently be characterised by electron attachment or ionisation [207].

In any case, it is important to define the exact research question in order to chose the appropriate approach, bottom-up, or top-down, and conditions, whether isolated or within a cluster environment.

Chapter 5

Results and Discussion

5.1 Biomolecules and Radiosensitisers

In chapter 4, the importance and relevance of electron interactions for radiotherapy was discussed. It was shown that both healthy and malignant cells are affected by irradiation, justifying also the study of biomolecules present in the healthy organism. In this thesis, some examples for both biomolecules and radiosensitisers are studied. As an example for a biomolecule, the results on histidine are shortly presented in the following section. The compound is based on an imidazole ring structure which is omnipresent in nature and is also used as one possible building block for radiosensitisers. Radiosensitisers were introduced in chapter 4.2.3 as agents which can enhance the effects in cancer treatment during radiotherapy procedures. Depending on their principle of action, they are divided into several groups, two of them are the radiosensitisers addressing highly proliferating cells and the agents designed specifically for hypoxic tumour regions in which they mimic the oxygen effect, see chapter 4.2.3. Within this thesis, examples for both groups were studied. For the group of proliferating cell radiosensitisers, 5-selenocyanato-2'-deoxyuridine, in short SeCNdU, was investigated. It is a uracil derivative and can thus be incorporated into the DNA molecule. It was only recently proposed as possible radiosensitiser [208]. Within the group of hypoxic cell radiosensitisers, two nitroimidazole compounds were studied, as these are known for their electron capturing characteristics. Namely, these are misonidazole and nimorazole, the latter also being studied in a water cluster environment to determine hydration effects on the electron attachment pathways.

5.1.1 Imidazole, 2-Nitroimidazole, Histidine

Imidazole (IMI) is a building block of many biological molecules and thus omnipresent in the human body. It was already introduced in chapter 4.2.3. 2-nitromidazole (2NI) is composed of an imidazole ring to which a nitro functional group is attached. 2NI forms the basis of radiosensitisers such as nimorazole and misonidazole, which are discussed in the subsequent contributions, and in biomolecules such as histidine. Electron interactions with histidine were also studied in the course of this thesis but are not presented in detail. Instead, a short summary is provided at this point, the interested reader is referred to the original paper to be found in reference [209].

Histidine is an aromatic amino acid. It is essential which means that the human body cannot synthesise histidine but it is rather taken up by ingestion [210]. Histidine is required for the synthesis of proteins and the functioning of enzymes [210]. It appears in two isomers, L-, and D-histidine, but only L-histidine is found in the human body. The amino acid consists of a carboxyl group (-COOH), an amine group (-NH_2) and a carbon chain to which an imidazole ring is attached, see figure 5.1. Depending on which nitrogen site of the imidazole ring a hydrogen atom is attached to, the τ and π tautomers are differentiated, see figure 5.1. The molecular formula of histidine is $C_6H_9N_3O_2$ and the molar mass amounts to 155.15 g/mol. In the above mentioned study, electron ionisation and dissociative electron attachment reactions were investigated [209]. The results are supported by quantum chemical calculations conducted at the Institut de Physique Nucléaire de Lyon, Université de Lyon, France. In summary, the ionisation energy of histidine was determined to (8.40 ± 0.04) eV which is in agreement with the calculated vertical ionisation energy. Ionisation energy values from previous studies range from 8.2 eV to 8.72 eV [211–213]. Additionally, the appearance energies of four fragment cations were measured, specifically of $[His\text{-}COOH]^+$, $[C_4N_2H_6]^{\bullet+}$, $[C_4N_2H_5]^+$, and $[NH_3CHCH_2]^+$. The dissociative electron attachment reactions were studied in an energy range of (0 - 18) eV. In total, five fragment anions were observed. Similar to the other aromatic amino acids, no parent anion could be detected. The product anions studied include $[His\text{-}H]^-$, $[His\text{-}COOH]^-$, $[C_4N_2H_5]^-$, OH^-, and O^- / NH_2^-.

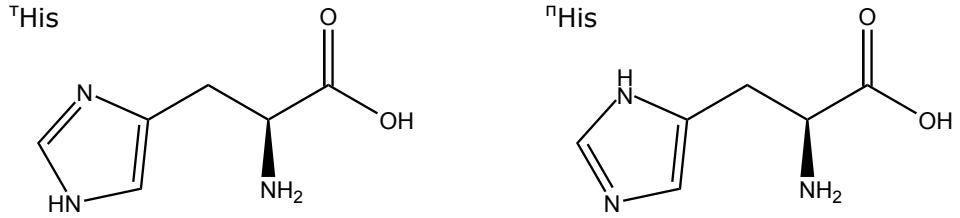

Figure 5.1: Structural formula of L-histidine. The molecule is composed of a carboxyl group, an amine group and a carbon chain to which an imidazole ring is attached. Both the τ and the π tautomer are shown.

My contributions to this article include experimental data taking of both electron attachment and ionisation processes and the analysis of the data. I prepared the figures of the paper showing the experimental results and wrote the section about the experimental setup. The data was interpreted together with Stephan Denifl and Linda Feketeová.

In this section, the main focus lies on electron ionisation studies with IMI and 2NI [214] as they are contained in many of the further studied compounds. The samples were evaporated in the oven of the Wippi experiment as described in chapter 3.1. This includes recording positive mass spectra of both compounds, taken at 70 eV electron

energy, and the determination of the ionisation and appearance energies. Quantum chemical calculations complete the study, which focus on potential energy surfaces, thermodynamic thresholds and transition states within the dissociation channels. The combination of experimental and simulated data enabled the determination of dissociation channels and their thresholds, which were compared to previous photo-ionisation and electron ionisation studies [215, 216]. Briefly summarising the results, the present study revealed positive mass spectra in which the parent cation reached the highest ion yields for both IMI and 2NI. This confirms the previous observation of Klebe *et al.* in their electron ionisation study of imidazole and thus seems to be a characteristic observation for EI [216]. In contrast, the photo-ionisation study of imidazole by Schwell *et al.* revealed a different relative intensity pattern [215]. The study showed that hydrogen loss of imidazole is not accessible *via* a simple bond cleavage, but rather is accompanied by the opening of the ring structure. The hydrogen can then be lost from different positions. Some of the observed cations of electron ionisation to IMI, namely $C_3H_3N_2^+$, $HCCNH^+$, and $HCNH^+$, arise from the same transition state(s). This means that their initial steps of formation are identical. The ionisation energy of IMI was determined to (8.76±0.03) eV and is slightly lower than the calculated value of 8.83 eV, which gives the adiabatic ionisation energy. In case of 2NI, several cations are reported which were also observed for IMI, namely $C_3H_3N_2^+$, $HNCCH^+$, and $HCNH^+$, but their dissociation pathways differ. For example, $C_3H_3N_2^+$ is formed by the loss of the nitro group both in the singlet and in the triplet state. The pathway involves different transient states for singlet and triplet, which also results in characteristic threshold values depending on the final state. Besides those cations, $C_3H_3N_3O^+$, $C_3H_3N_2O^+$, $HNCHCO^+$, and NO^+ were additionally detected for 2NI. The ionisation energy of 2NI was experimentally determined to (9.70±0.02) eV, which is in the 2σ range of the calculated value of 9.74 eV.

My contribution to the paper includes conducting the experiments of the 2NI data. Additionally, I performed the analysis of both IMI and 2NI data and prepared the figures for the paper. I interpreted the results, conducted literature research of previous studies and compared the experimental data to the calculations provided by Linda Feketeová and with the data from previous studies. Finally, I wrote the first draft of the paper and included the remarks of the co-authors.

J. Am. Soc. Mass Spectrom. (2019)
DOI: 10.1007/s13361-019-02337-w

RESEARCH ARTICLE

Electron Ionization of Imidazole and Its Derivative 2-Nitroimidazole

Rebecca Meißner,[1,2] Linda Feketeová,[1,3] Anita Ribar,[1] Katharina Fink,[1] Paulo Limão-Vieira,[2] Stephan Denifl[1]

[1]Institut für Ionenphysik und Angewandte Physik and Center for Molecular Biosciences Innsbruck (CMBI), Universität Innsbruck, Technikerstraße 25, 6020, Innsbruck, Austria
[2]Atomic and Molecular Collisions Laboratory, CEFITEC, Department of Physics, Universidade NOVA de Lisboa, 2829-516, Caparica, Portugal
[3]Institut de Physique des 2 Infinis de Lyon; CNRS/IN2P3, UMR5822, Université de Lyon, Université Claude Bernard Lyon 1, 43 Bd du 11 novembre 1918, 69622, Villeurbanne, France

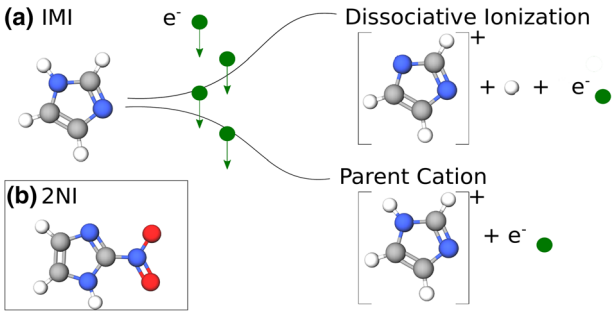

Abstract. Imidazole (IMI) is a basic building block of many biologically important compounds. Thus, its electron ionization properties are of major interest and essential for the comparison with other molecular targets containing its elemental structure. 2-Nitroimidazole (2NI) contains the imidazole ring together with nitrogen dioxide bound to the C2 position, making it a radiosensitizing compound in hypoxic tumors. In the present study, we investigated electron ionization of IMI and 2NI and determined the mass spectra, the ionization energies, and appearance energies of the most abundant fragment cations. The experiments were complemented by quantum chemical calculations on the thermodynamic thresholds and potential energy surfaces, with particular attention to the calculated transition states for the most important dissociation reactions. In the case of IMI, substantially lower threshold values (up to ~ 1.5 eV) were obtained in the present work compared to the only available previous electron ionization study. Closer agreement was found with recent photon ionization values, albeit the general trend of slightly higher values for the case of electron ionization. The only exception for imidazole was found in the molecular cation at *m/z* 40 which is tentatively assigned to the quasi-linear $HCCNH^+$/ $HCNCH^+$. Electron ionization of 2NI leads to analogous fragment cations as in imidazole, yet different dissociation pathways must be operative due to the presence of the NO_2 group. Regarding the potential radiosensitization properties of 2NI, electron ionization is characterized by dominant parent cation formation and release of the neutral NO radical.

Keywords: Electron ionization, Imidazole, Nitroimidazole, Appearance energy, Gas phase, Transition state, Unimolecular dissociation

Received: 10 May 2019/Revised: 2 August 2019/Accepted: 8 September 2019

Introduction

Radiation is a major source of damage for intact cells [1, 2]. It is widely used in radiotherapy to kill tumor cells. The drawback of the radiation is that also healthy tissue may be damaged. The lack of selectivity is addressed by radiosensitizers, increasing the ratio of damage of malignant to healthy cells [3, 4]. One problem is to overcome hypoxia, which is common in many cancerous tissues [5, 6]. The

Electronic supplementary material The online version of this article (https://doi.org/10.1007/s13361-019-02337-w) contains supplementary material, which is available to authorized users.

Correspondence to: Rebecca Meißner; *e-mail:* rebecca.meissner@uibk.ac.at, Linda Feketeová; *e-mail:* l.feketeova@ipnl.in2p3.fr, Stephan Denifl; *e-mail:* stephan.denifl@uibk.ac.at

Published online: 30 October 2019

deprival of oxygen results in a change of metabolism and additionally, those cells show a higher resistance towards radiation [7]. Drugs substituting deprived oxygen in tumor cells are known as oxygen mimetic [5]. Nitric oxide was shown to act highly efficient, even surpassing the effects of oxygen itself [8–12]. 2-Nitroimidazole (2NI) (see Scheme 1) is based on imidazole (IMI). It belongs to the class of nitroimidazole compounds, which have been proven beneficial as oxygen mimetic radiosensitizer in clinical trials and are further used as antibacterial drugs and in antibiotics [11, 13–15]. Imidazole itself is a basic building block in biology, present in the amino acid histidine, the hormone histamine, and the nucleobase purine. It thus serves as model compound for more complex molecular systems present in different environments with particular attention to the biological mediums. It is well established that the physical and chemical properties of a molecule define its role in determining the local interaction with its surrounding molecules. Thus, a detailed knowledge of the chemical and physical properties of IMI and 2NI can help creating novel compounds with relevant impact for medical use and other scientific and even technological applications given their thermal stability, high heats of formation, and good detonation performance [16].

As imidazole is an omnipresent DNA/RNA building block, the ionization energy and fragmentation pathways have been investigated with different methods. Photoelectron spectroscopy (PES) studies provided information about the electronic structure and ionization energy of IMI [17–20] with values similar to the theoretical study of Cuong et al. [21]. Further spectroscopy investigations reported on the electron binding energy of the IMI anion [22], on the vertical electron attachment energy [23], and on the anionic deprotonation pathway [24]. The latter investigation was recently extended by a study of multiple hydrogen loss reactions in neutral IMI upon dissociative electron attachment [25]. Additionally, we note the study from Klebe et al., addressing the loss of the hydrogen atom and the hydrogen cyanide molecule upon electron ionization and reporting the appearance energies of cationic fragments [26]. Later, and apart from the ionization energy, Main-Bobo et al. extended the study by photoionization mass spectrometry and photoelectron photoion coincidence spectroscopy data to the appearance energies of some fragment cations [27]. Another mass-spectrometric photoionization study of Schwell et al. completed this data, proposing fragmentation pathways based on the experimental and calculated values by determining the ionization and appearance energies [28]. Nevertheless, the present study is crucial to examine Main-Bobo et al. findings since electron ionization and photoionization cause a striking different behavior in some fragmentation channels of IMI due to the possibility to excite states by electron impact which are not accessibly by photon excitation [27]. Here we present a complete study of the cationic fragments of IMI upon electron ionization and compare the appearance energies with Klebe et at. [26], improving significantly the precision of the appearance energies and extending the total number of observed fragment channels. Additionally, these results are compared with those obtained from photoionization studies [27, 28].

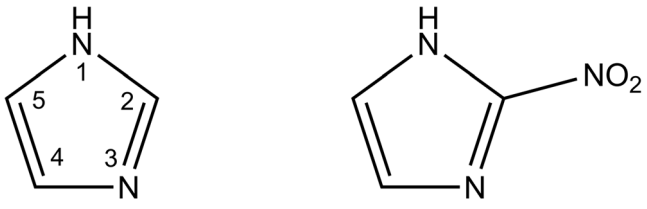

imidazole 2-nitroimidazole

Scheme 1. Structures of imidazole (left) and 2-nitroimidazole (right)

Similarly, nitroimidazoles have been studied by PES to determine their electronic structure [19, 29, 30]. Decomposition products upon photon excitation were reported in [31] with nitric oxide (NO) and nitrogen dioxide (NO_2) as the main fragments. A recent photofragmentation study of doubly charged, core excited 4(5)-nitromindazole (4(5)-NI) showed that methylation at the N1 position (see Scheme 1) suppresses efficiently the NO and NO^+ production [32]. The first mass spectra of electrosprayed nitroimidazolic compounds, like nimorazole, were recorded by Feketeová et al. [33, 34]. They also determined product ions of collision-induced and electron-induced dissociation. Additionally, the isomers 2-NI and 4(5)-NI were studied by dissociative electron attachment experiments; revealing isomer effects regarding the position of the NO_2 group [35] and bond breaking selectivity was achieved upon methylation at the N1 position [36] as well as in electron transfer experiments [37]. Besides, valence ionization of nitroimidazoles was investigated by photoelectron–photoion coincidence (PEPICO) measurements [38]. Recently, two photofragmentation studies investigated the fundamental mechanisms of the bond-breaking, also reporting the ionization and appearance energies of the cationic parent and fragment products [39, 40]. These experimental results were supported by calculations of the fragmentation pathways [40]. In the present study, we also report fragmentation reactions of 2-NI upon electron ionization, derive for the first time ionization and appearance energies, and compare them with the available photoionization studies.

In addition to ionization and appearance energies of IMI and 2NI, mass spectra at the electron energy of 70 eV are presented (Figures 1 and 2) in order to elucidate the most important fragmentation pathways. The experimental results are supported by quantum chemical calculations determining the thermodynamic thresholds of dissociation reactions for both molecular compounds. Finally, for IMI, we also explored potential energy surface and calculated transition states for the most important dissociation reactions, and for 2NI, we propose pathways for the formation of the fragment ion due to the loss of the $–NO_2$ group, which remained an opened question in the previous study using photoionization.

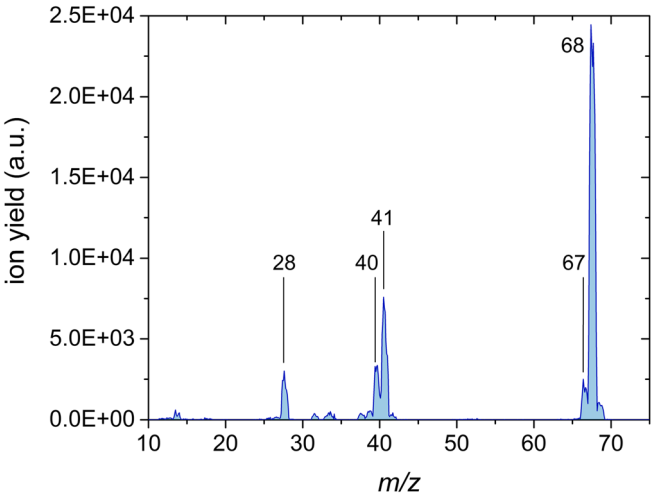

Figure 1. Mass spectrum of imidazole obtained by electron ionization at the electron energy of 70 eV

Experimental Methods

The experimental setup utilized for the present studies consists of a quadrupole mass spectrometer coupled with a high resolution electron monochromator, described in detail elsewhere [41]. Both IMI and 2NI were purchased from Sigma-Aldrich with stated purities of 99.5% and 98%, respectively and were used as delivered.

The compounds under investigation were placed inside of an oven inside of the vacuum chamber. At the typical experimental base pressures of about 10^{-9}–10^{-8} mbar, heating to about 100 °C was required for both compounds in order to achieve sufficient sublimation. An effusive beam of molecules was formed by a capillary with 1 mm diameter which was mounted onto the oven. A hemispherical electron monochromator (HEM) generated an energetically and spatially focused electron beam with a resolution of about 100 meV. The stability of the electron beam was constantly monitored by a picoampere meter connected with a Faraday cup, which was placed after the crossing zone with the neutral beam. In the interaction region, located within the HEM right before the Faraday cup, the IMI or 2NI was ionized. In order to analyze the ionic products, a weak electrostatic field extracted them into a quadrupole mass analyzer with nominal mass range of 2048 u. The mass selected ions were detected with a channel type secondary electron multiplier operated in pulse counting mode and processed by a combined preamplifier and detection unit.

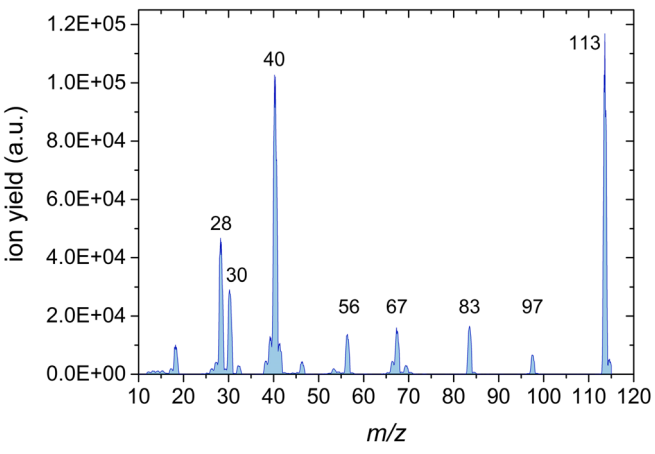

Figure 2. Mass spectrum of 2-nitroimidazole obtained by electron ionization at the electron energy of 70 eV

All ionization efficiency curves were measured within an energy region of minimum ± 1.5 eV around the ionization/appearance energy. For calibration of the energy scale, the ionization efficiency curve of helium or neon was measured and compared to the well-known literature values of 24.587 eV and 21.565 eV, respectively [42].

The statistical uncertainty of the threshold values discussed in the following sections is composed of the shift of the AE value caused by the choice of the input parameter and the uncertainty of the fit. The systematic error is caused by the uncertainty on the neon or helium calibration and amounts to 0.01 eV.

Computational Methods

Determination of Ionization and Appearance Energies

The experimental ionization and appearance energies (IE and AE) were determined by fitting a potential function in a similar form as suggested from Wigner [43] and Wannier [44] for the theoretical ionization cross section close to threshold. Wigner described the cross section behavior at threshold by a simple power law, which depends on the number of outgoing electrons in the exit channel. Specifically for single electron ionization, a linear rise in the cross section was predicted for single ionization processes [43]. Wannier further specified the model to a final state including one ion and two electrons [44], resulting in the function

$$f(E) = b + c\cdot(E-\mathrm{AE})^{n}\cdot\theta\,(E-\mathrm{AE}) \tag{1}$$

with b the background, c a scaling parameter, E the electron energy, AE the appearance or ionization energy, and θ the Heaviside function which is required to model the behavior below threshold. The exponent n was only calculated for hydrogen so far and is in all other cases issue to experimental determination.

Since the experimental setup is subject to a finite energy resolution, we convoluted function $f(E)$ with a Gaussian function to account for the experimental conditions. Thus, the function fitted to the data was

$$\sigma(E) = b + \frac{c}{\sqrt{2\pi}}\rho^{n}\cdot\Gamma\,(n+1)\cdot\exp\left(-\frac{1}{4\rho^{2}}(\mathrm{AE}-E)^{2}\right)\cdot D_{n+1}\left(\frac{1}{\rho}(\mathrm{AE}-E)\right) \tag{2}$$

with Γ the gamma function, D_{n+1} a parabolic cylinder function, and ρ the standard deviation of the Gaussian and energy resolution of the HEM.

Some ionization efficiency curves featured two onsets. In this case, the fitting function was extended by adding a second

power law including a Heaviside function to Eq. (1) and convoluting this formula as for single onsets.

The analysis software, based on a previous version [45], was written in Python using the SciPy, NumPy, and Matplotlib libraries. The required input parameters included the starting values for the free parameters and the fitting range. Then, the ionization efficiency curves were fitted by means of the Chi-square method and as most important output parameter, the appearance and ionization energies were derived.

Quantum Chemical Calculations

Quantum chemical calculations employing M062x/aug-cc-pVTZ level of theory [46, 47] and basis set [48] were carried out with the Gaussian-09D01 program package [49] to calculate vertical ionization energies (VIE), adiabatic ionization energies (AIE), and the free energy of reactions, ΔG. Such energy is calculated for each fragmentation pathway as $\Delta G = \Sigma G(\text{products}) - \Sigma G(\text{reactants})$, where in the currently studied electron ionization processes, the reactant refers to neutral IMI or 2NI.

For all structures, the frequencies were calculated to confirm that those are local minima on the potential energy surface. All energies were corrected for zero-point energies. Transition states (TS) for fragmentation pathways were optimized at the same level of theory and basis set. The frequencies of TS were calculated to confirm that the structures are local maxima on the potential energy surface. Calculations of the intrinsic reaction coordinates (IRC) connected the TS to reactants and products. We estimate an error of less than 2 kcal mol^{-1} (0.09 eV) for the free energies of the reactions from the reported mean unassigned error for M062x thermochemistry [46]. All the considered structures, dissociation pathways, and an example of IRC calculation are summarized in the Electronic Supplementary Material (ESM).

Results and Discussion

Mass Spectra

Electron ionization (EI) is rather a hard ionization method in which an energetic electron interacts with a molecule removing an electron from the neutral compound. Depending on the excess energy deposited, either the parent cation stabilizes or it dissociates into one positively charged fragment and one or more neutral fragments. The ionization method may influence the observed mass spectrum. The possibility of different fragment ions' formation was mentioned by Main-Bobo et al. [27]. The transmission of the mass analyzer and ion collection efficiency can further cause deviations in relative peak intensities, but the number of observed fragments should not be altered. Hence, recording the ionization mass spectra of IMI and 2NI allows the assignment of the cationic fragments and a comparison with photoionization studies [27, 28, 39, 40], together with EI spectra from the NIST database [50] and the Spectral Database for Organic Compounds (SDBS) [51].

Imidazole In the case of the ionization mass spectrum of imidazole (see Figure 1), the most intense ion is assigned to the parent cation at *m/z* 68. This agrees well with the NIST database [50] but represents the major difference to the photoionization mass spectrum recorded at 21 eV by Schwell et al. [28], where the parent cation is very weakly abundant. In contrast, the two most intense ions were reported at *m/z* 41 and *m/z* 40, assigned to $C_2H_3N^+$ and $C_2H_2N^+$, respectively. In the present mass spectrum, these ions form the most dominant fragments, where $C_2H_3N^+$ yields one third the intensity of the parent cation. This cation is formed by HCN loss which was also reported by Klebe at al. [26]. Additionally, two other cationic fragments are observed with considerable yields, *m/z* 28 assigned to $HCNH^+$ and at *m/z* 67 assigned to $[IMI - H]^+$, which corresponds to the dehydrogenated parent cation. Some further weak fragment ions as well as isotopic contributions of abundant fragment ions are also visible in the spectrum. They are of small intensities, and therefore, no appearance energies were determined. From the general point of view, the ionization mass spectrum agrees well with the EI spectrum from NIST [50], Klebe et al. [26], and Schwell et al. [28]. Only as far as the parent cation is concerned, the present yield differs from [28]. Notwithstanding, these authors noted that the low intensity of the parent cation resulted from mass discrimination properties of the quadrupole mass analyzer used in their experiments.

2-Nitroimidazole The ionization mass spectrum of 2NI (see Figure 2) reveals, as expected, some similarities in the product ions when compared to imidazole. Again, the parent cation at *m/z* 113 possesses the strongest yield. In contrast to IMI, no dehydrogenated parent cation is observed. With comparably high intensity, the fragment at *m/z* 40 is assigned to $HCCNH^+$, where losses of NO_2 and HCN from the parent cation are operative. The third most intense cation at *m/z* 28 is assigned to $HCNH^+$. While for the IMI the fragment ion at *m/z* 40 is half of the feature at *m/z* 41, in the case of 2NI the latter is strongly suppressed. At *m/z* 67, we report $C_3H_3N_2^+$, which is formed by the loss of the NO_2 group and is assigned to $[IMI - H]^+$. The peaks at *m/z* 30, 56, 83, and 97 all contain contributions from the nitrogen dioxide group. Here, *m/z* 30 (NO^+) and *m/z* 83 ($C_3H_3N_2O^+$) represent counterparts and stem from the same bond breaking. For *m/z* 56, additionally to the cleavage of the nitro group, HCN loss from the imidazole ring occurs, a process similar to the formation of the fragment cation at *m/z* 40. At *m/z* 97, we report $C_3H_3N_3O^+$ that corresponds to the release of a neutral oxygen atom from the parent cation. Comparing the present mass spectrum to [51], the photoionization data of Bolognesi et al. [39] and Cartoni et al. [40], the detected fragments are identical albeit with different relative peak intensities (which may also be related to different experimental conditions). For example, in the SDBS spectrum [51], the prominent *m/z* 40 peak is a factor of ~1.7 higher than the parent cation, while here and in the work of Cartoni et al. [40], the intensity of both ions is similar. Bolognesi et al. [39] report a

strongly suppressed parent cation and a higher number and abundance of fragment cations. A recent PEPICO study of 2NI by Itälä et al. [38] also reported the mass spectrum at the photon energy of 16 eV. The spectrum featured the parent cations, NO^+ and $[2NI - NO]^+$, at *m/z* 83 as the strongest channels [38].

Ionization and Appearance Energies

The ionization efficiency curves near threshold were measured for the most abundant cations in the mass spectra. The experimental data were fitted by the method described above to determine the experimental ionization and appearance energies. Subsequently, the results are presented, discussed, and compared with both calculations and earlier studies.

Imidazole For IMI, the experimental data and fits are shown in Figure 3 and summarized in Table 1. The energy scale was calibrated by measuring the ion yield curve of helium and determining its onset of formation (see Figure 3a). The mass spectrum indicates that the parent cation forms the most intense channel upon EI of imidazole. We report an experimental ionization energy of 8.76 ± 0.03 eV (see Figure 3f) which is slightly lower than the calculated adiabatic ionization energy (AIE) of 8.83 eV. The vertical ionization energy is also calculated and amounts to 9.08 eV. Calculations on the ring opening (Figure ESM_1 in ESM) and hydrogen transfer (Figure ESM_2) in the ionized IMI^+ cation suggest barriers > 1.69 eV and > 2.39 eV, respectively. Thus, these processes are not possible in the parent cation formed close to threshold. The earlier reported values of the ionization energy of IMI cover a range from 8.66 eV (VUV study of Schwell et al. [28]) up to 9.12 eV (EI study of Klebe et al. [26], who utilized a double-focusing mass spectrometer with a standard ion source, i.e., no monochromatizing element for the electron beam, in contrast to the present study) [17–21, 27].

The combination of the parent cation exhibiting a very high intensity compared to the $[IMI - H]^+$ fragmentation channel and the use of a quadrupole mass spectrometer with limited mass resolution leads to a weak contamination of the ion efficiency curve of $[IMI - H]^+$ which shows two onsets (see Figure 3e). The first onset at 9.5 ± 0.1 eV can be assigned to a background contribution from the IMI^+ ion yield. The disagreement with the IE mentioned above can be explained by the very low ion yield below the second onset. In contrast, the second observed onset is assigned to the appearance energy of $[IMI - H]^+$ at 11.9 ± 0.1 eV. Earlier VUV and EI studies reported values of 11.38 and 12.05 eV and 12.8 eV, respectively [26, 28]. All the calculated $[IMI - H]^+$ ions including triplet states are shown in Figure ESM_3. Based on the thermodynamic threshold, only several ring opened structures could be considered with the observed experimental onset of 11.9 ± 0.1 eV, i.e., no direct hydrogen loss seems to be operative. The H loss with a reverse barrier was already suggested by Main-Bobo et al. [27]. All calculated stable structures with

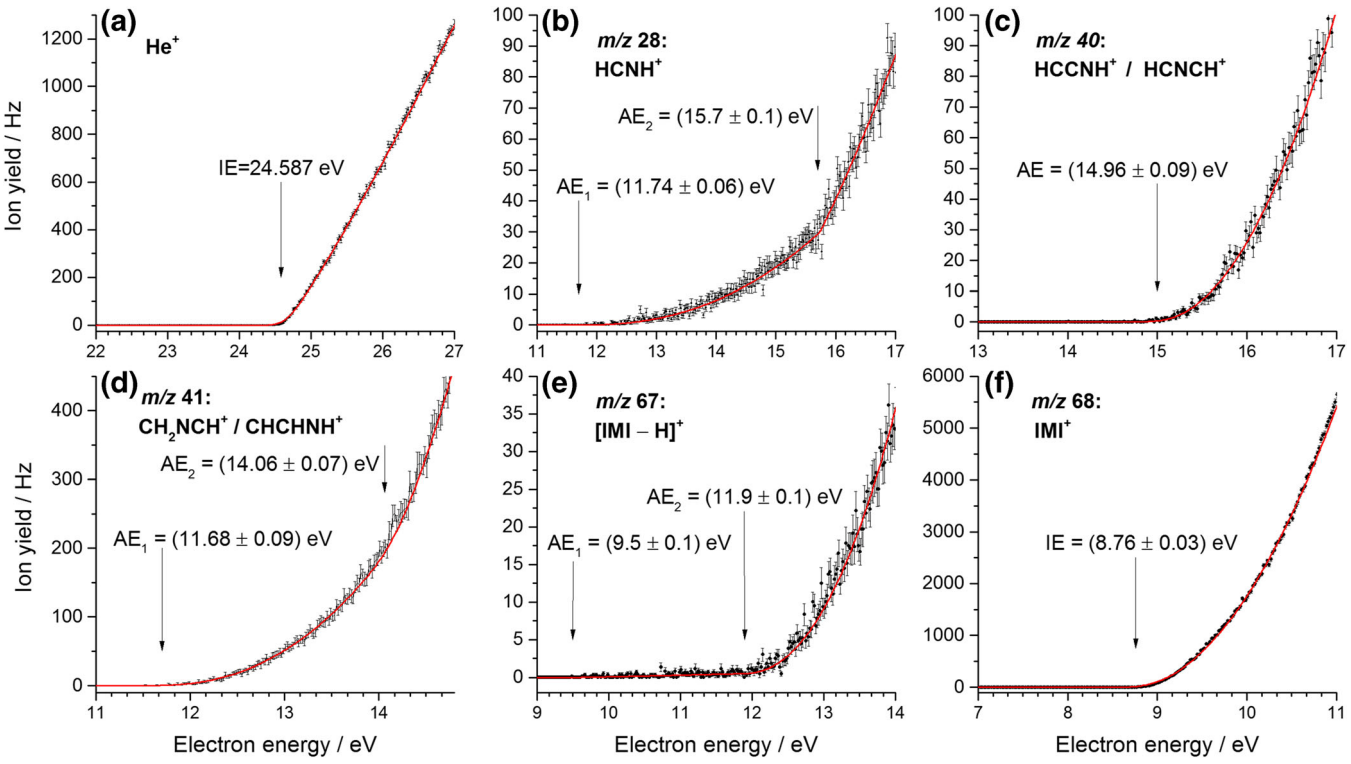

Figure 3. Threshold ionization efficiency curves of imidazole (**b**–**f**). The data is shown as black dots, including the statistical uncertainties as error bars. The red solid lines represent the fitted functions. For each cation, the determined AE is indicated by a black arrow. (**a**) The threshold ionization efficiency of helium which was used for calibration

Table 1. Summary of Observed Cations Upon Electron Ionization of Imidazole, Including *m/z* Value, Assigned Cation and Experimental and Calculated Ionization and Appearance Energy Values, Together with Available Literature Values. All the Calculated Values Refer to the Singlet States of the Respective Cations Unless Marked

m/z	Assignment		IE and AE values (eV)		Previous EI exp.	Previous PI exp.
	Cation	Neutral	Present exp.	Present calc.		
28	$HCNH^+$	CH_2CN	11.74 ± 0.06	11.65		11.67 ± 0.05[a], 11.34 ± 0.05[b]
		CH_2NC	11.74 ± 0.06	11.74		
40	$HCCNH^+$	HCNH	14.96 ± 0.09	15.09		13.83 ± 0.05[b]
	$HCNCH^+$	HCN + H	14.96 ± 0.09	15.07*		
41	CH_2NCH^+	HCN	11.68 ± 0.09	11.80	13.2[c,d]	11.48 ± 0.02[a], 11.41 ± 0.05[b]
	CH_2CNH^+	HCN	11.68 ± 0.09	11.38		
	$CHCHNH^+$	HCN	14.06 ± 0.07	14.02		
67	$[IMI - H]^+$	H	11.9 ± 0.1	11.98, 12.03, 12.04	12.8[c,d]	11.38 ± 0.05[b], 12.05 ± 0.03[b]
68	IMI^+		8.76 ± 0.03	8.83 (AIE)	9.12[c]	8.66–8.96[e]

*Calculated value refers to the triplet state of respective cation
[a]Refer to reference [27]. Their assignment to a specific cationic and neutral structure can be found in the same line, see columns cation and neutral
[b]Refer to reference [28]. Their assignment to a specific cationic and neutral structure can be found in the same line, see columns cation and neutral
[c]Refer to reference [26]
[d]No assignment of the AE to a specific cationic and neutral structure was reported
[e]The range refers to values reported in the references [17–20, 27, 28]

intact ring are energetically not accessible (see Figure ESM_3). This contrasts the suggested cyclic $[IMI - H]^+$ structures by Schwell et al. [28]. Experiments with deuterated IMI by Klebe et al. showed preferential (but not exclusive) hydrogen loss from the C4 and C5 positions [26]. Our calculations on H transfer in the ionized IMI (Figure ESM_2) show that H transfer mechanism is possible with ΔG(barrier) values in the range between 11.22 and 12.18 eV and thus are likely to play a role in the dissociation process. The calculated potential energy surface for H loss and the formation of linear $[IMI - H]^+$ ions that are relevant to the observed experimental threshold are shown in Figure 4. Four pathways are shown. The H transfer from N1 position to C5 through TS1 of 11.80 eV results in cyclic ion 68^+(**1**), where removal of H from C4 results in opening of the ring in the C2–N3 bond resulting in linear 67^+(**1**) with ΔG of 12.03 eV. On the other hand, the H transfer from C5 to C4 through TS2 (11.38 eV) results in cyclic ion 68^+(**2**), where removal of H from the N1 position leads to the opening of the ring and the formation of the same ion 67^+(**1**). However, if the ion 68^+(**2**) opens up the ring through TS3 (11.09 eV), it will lead to linear 68^+(**3**), where the loss of H from the N1 position results in 67^+(**1**), and the loss of H from the C4 results in 67^+(**2**) with ΔG of 12.04 eV. In the latter, this would refer to the loss of H from the C4 or C5, which is the preferred loss observed by Klebe et al. [26]. Considering the dissociation of IMI^+ starting with a ring opening reaction summarized in Figure ESM_1, only one such reaction showed to play a role below 12 eV. The ring opening between N1 and C2 through the TS4 (10.52 eV) leads to 68^+(**4**), where a removal of H from the C5 results in 67^+(**2**). For the ion 68^+(**4**), further H transfer is possible from C5 to C4 through TS5 (10.97 eV) resulting in 68^+(**3**) that, as mentioned above, through H loss can result in 67^+(**1**) or 67^+(**2**). Finally, H transfer from C4 to C5 through TS6 (11.22 eV) forms 68^+(**5**), where removal of an H from N1 leads to the ring opening between C2 and N3 and the formation of 67^+(**1**). If instead the ion 68^+(**5**) opens up the ring between N1 and C5 through TS7 (11.65 eV), the linear ion 68^+(**6**) is formed and H loss from the C2 position leads to the ion 67^+(**3**) with ΔG of 11.98 eV. We note the observation of two thresholds by Schwell et al. [28] at 11.38 eV and a stronger at 12.05 eV, which can be related to two different TS involved in the dissociation rather than a loss of H from different positions.

The fragment ion $C_2H_3N^+$ at *m/z* 41 can arise via multiple fragmentation pathways, leading to different assignments. Two experimental onsets are observed at 11.68 ± 0.09 eV and at 14.06 ± 0.07 eV (see Figure 3d). In the EI study by Klebe et al., an onset value of 13.2 eV is reported, while for the PI study by Main-Bobo et al. of 11.48 eV and for the VUV study by Schwell et al. of 11.41 eV [26–28]. Klebe et al. performed EI measurements with deuterated imidazoles and suggested that neutral HCN loss is preferred over HNC with preference of involving the C2 position and minor contributions of C4 and C5 [26]. Similarly, Main-Bobo et al. reported that HCN loss is the most likely, but with the addition that two fragmentation pathways are to be expected as they observed a bimodal kinetic energy release distribution in the metastable decay of the IMI parent cation on the microsecond time scale [27]. All the calculated structures considered in this study for the *m/z* 41 fragment ion are shown in Figure ESM_4. The potential energy surface for the formation of this ion is shown in Figure 5. It involves the same TS as mentioned above in the formation of the fragment ion at *m/z* 67. It seems reasonable considering the experimental thresholds being close in energy for the formation of these two ions. In Figure 5, the H transfer from N1 to C5 through TS1 (11.80 eV) results in cyclic 68^+(**1**). The following ring opening between C5 and C4 through TS8 (11.33 eV) leads to 68^+(**7**), where further breakage of the C2–N3 bond results in ion 41^+(**1**) with ΔG of 10.85 eV. On the other hand, H transfer from C5 to C4 through TS2 (11.38 eV) followed by ring opening between N1 and C2 through TS3 (11.09 eV) leads to 68^+(**3**), where further excision of the C4–N3 bond results in ion

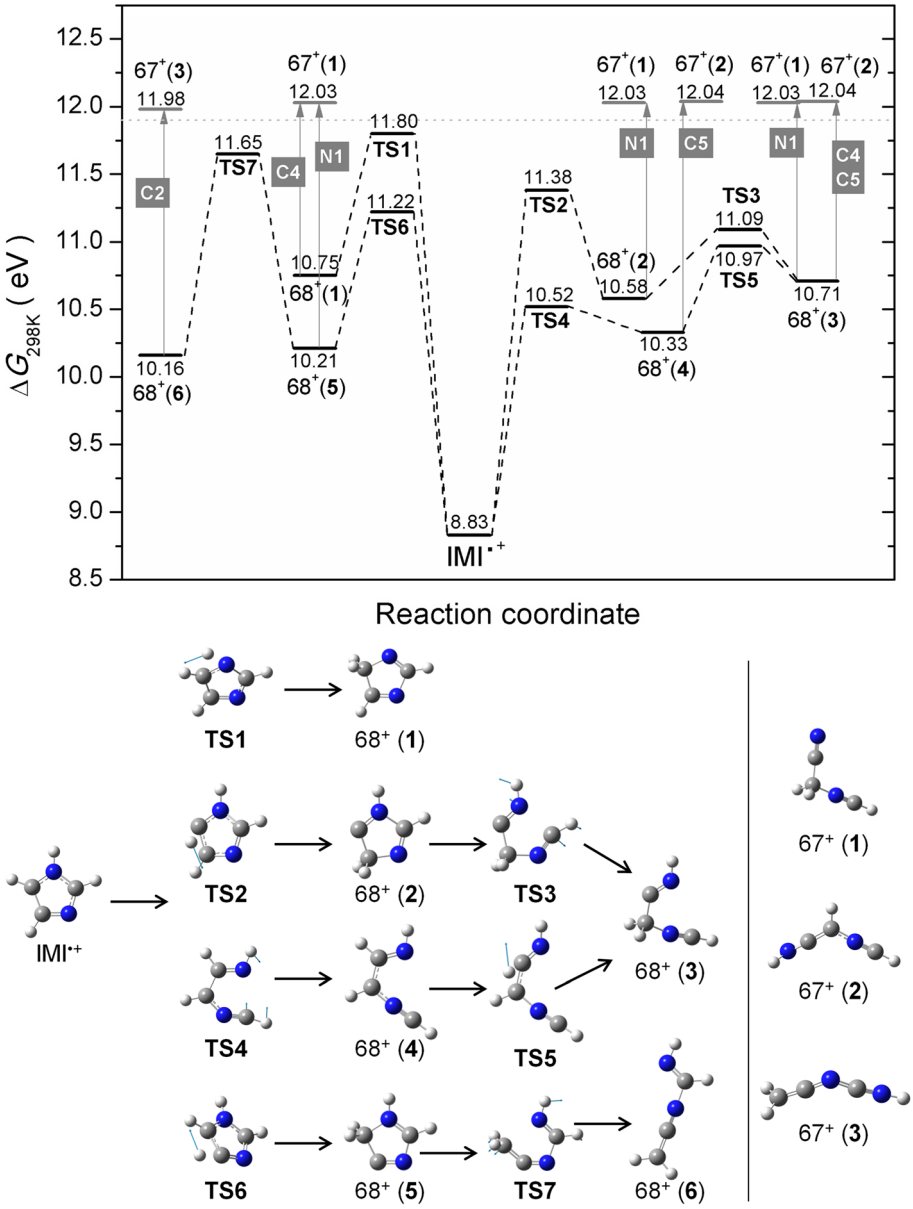

Figure 4. M06-2x/aug-cc-PVTZ calculated potential energy diagram for the decomposition of the IMI^+ leading to the formation of $[IMI - H]^+$ fragment at *m/z* 67 including associated structures shown below. The blue arrows in the respective TS show the displacement vectors. The labels in a gray square refer to the position of the imidazole ring from which the H has been lost. The dotted line corresponds to the experimental value

41^+(**2**) with ΔG of 10.39 eV. This is one of the pathways suggested by Main-Bobo et al. [27]. The ion 41^+(**1**) is assigned to CH_2NCH^+ and a neutral HCN involves the C4 position, while 41^+(**2**) is assigned to CH_2CNH^+ and a neutral HCN involves the C2 position. These fragmentation pathways are governed by the kinetics and thus in good agreement with the first observed threshold. Finally, the ring opening between N1 and C2 through TS4 (10.52 eV) leads to ion 68^+(**4**), followed by a bond breaking between C4 and N3 that results in 41^+(**3**) with ΔG of 14.02 eV. This value is in very good agreement with the second experimental threshold measured here. Our calculations show that the second pathway involves no hydrogen transfer. Again, the neutral fragment is HCN involving the C2 position. We just note that we also considered the pathways suggested by Schwell et al. [28], who reported the AE of 11.41 ± 0.05 eV for the formation of the ion at *m/z* 41. However, the suggestion on the initial rupture of the N3–C4 bond can be excluded due to the TS of 12.96 eV (see Figure ESM_1) that is additionally associated with H transfer from C5 to C4, where further bond breaking between N1 and C2 could also result in the formation of 41^+(**2**), yet, with an apparent AE of 12.96 eV. The second pathway suggested by Schwell et al. [28] starts with the breakage of N1–C2 (related to our TS4; see Figure 4), followed by H transfer C5–C4 (related to TS5) and final breaking of the C4–N3 would lead to an apparent AE of 10.97 eV (TS5), which is too low. Our calculation shows that

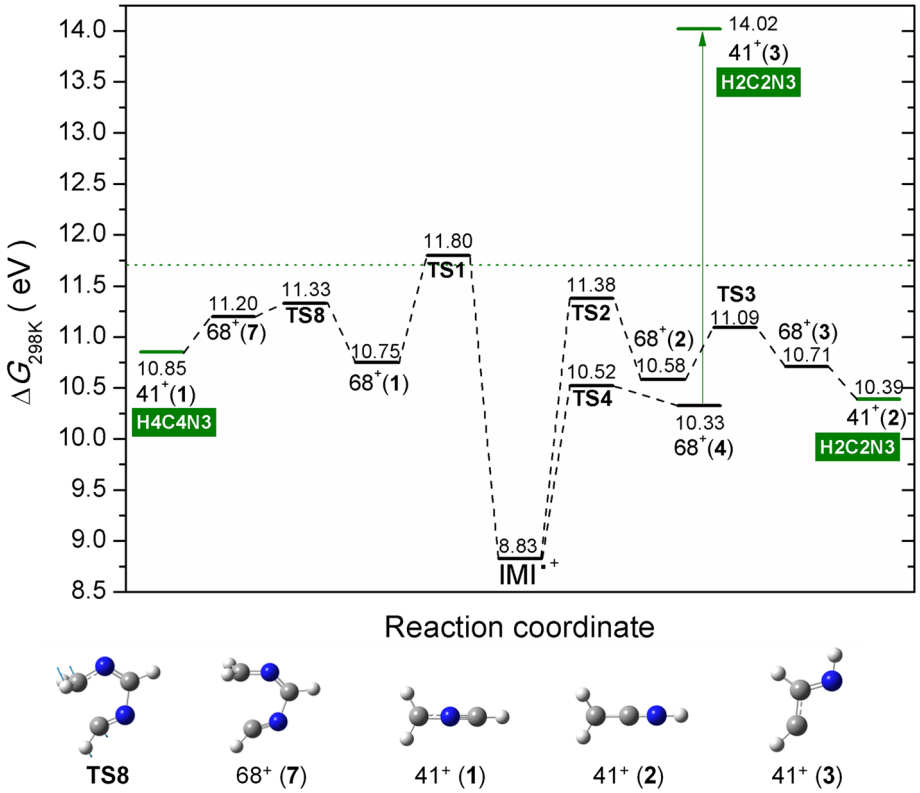

Figure 5. M06-2x/aug-cc-PVTZ calculated potential energy diagram for the decomposition of the IMI^+ leading to the formation of fragment ion at *m/z* 41 including associated structures shown below. The blue arrows in the respective TS show the displacement vectors. The labels in a green rectangle refer to the position of the imidazole ring from which the HCN has been lost. The dotted line corresponds to the experimental value

the H transfer must take place first and is followed by the ring opening as described above and as shown in Figure 5, where the TS2 (11.38 eV) would be in excellent agreement with the AE of 11.41 eV reported by Schwell et al. [28].

The fragment at *m/z* 40 has so far only been reported by Schwell et al. in a VUV study [28]. They reported an appearance energy of 13.83 ± 0.05 eV which is significantly lower than the experimentally determined onset in this study of 14.96 ± 0.09 eV (see Figure 3c). Thus, different dissociation pathways and products are possible. Schwell et al. discussed three possible fragmentation pathways for which we calculated all final states for both singlet and triplet states (see Figures ESM_5–ESM_7). The formation of the ion NCN^+ can be excluded based on the thermodynamic threshold (see Figure ESM_5). The possible potential energy surfaces for the considered processes are shown in Figures ESM_8–ESM_10. Formation of the same fragment *m/z* 40, as a singlet in the VUV study and as a triplet in the EI study, can be excluded, as none of the possible structures shows the 1.13 eV difference expected for such two spin configurations (Figures ESM_5–ESM_7). Thus, it is more likely that a different structure of *m/z* 40 is formed by electron ionization compared to photon ionization. The first proposed pathway describes the loss of HCNH and/or CH_2N from the parent cation IMI^+. The structures are shown in Figure ESM_6, and the potential energy surface considered is shown in Figure ESM_8. However, it does not include formation of all structures present in Figure ESM_6. We considered the simplest path, i.e., breaking of two N–C bonds, followed by ring opening structures that can lead to loss of HCNH. However, these can all be excluded considering the study of Hodges et al. [52] on 1-methylimidazole with a deuterated methyl group showing that CD_3 at the N1 position is not involved in the neutral loss. Thus, other pathways that we have not explored may be possible, like those involving H transfer reactions first before the N–C bond breaking. Based solely on the thermodynamic threshold (Figure ESM_6), the formation of quasi-linear $HCCNH^+$ and HCNH gives a ΔG value of 15.09 eV that is in close agreement with our experiment.

The second suggested channel is the loss of HCN from $[IMI - H]^+$. The structures with thermodynamic thresholds are summarized in Figure ESM_7, and the potential energy surface considered is shown in Figure ESM_9. Here, our calculations show that several fragmentation pathways are accessible and close to the experimentally observed threshold value. Loss of HCN from the 67^+(**1**) yielding CH_2CN^+ is associated with ΔG of 14.77 eV, the loss of HCN from the 67^+(**2**) results in $HCCNH^+$ in a triplet state with a ΔG value of 14.68 eV, and finally the HNC loss from the 67^+(**3**) giving CH_2CN^+ with ΔG of 15.23 eV. These pathways would be all in agreement with the studies on deuterated 1-methylimidazole by Hodges et al.

[52]. However, the deviation from the present AE value of 14.96 ± 0.09 eV is too large.

The third pathway suggested by Schwell et al. is the loss of hydrogen from the *m/z* 41 cation. The structures with thermodynamic thresholds are summarized in Figure ESM_7, and the potential energy surface considered is depicted in Figure ESM_10. Depending on the position from which the hydrogen is stripped off, the 41^+(**1**) could lead to the formation of CH_2NC^+ with Δ*G* of 14.73 eV, or formation of quasi-linear $HCNCH^+$ in a triplet state with Δ*G* of 15.07 eV that is closest to our experimental value, while the 41^+(**2**) can lead to the formation of the triplet $HCCNH^+$ and the singlet CH_2CN^+ with calculated thresholds of 14.68 eV and 14.77 eV, respectively. However, the loss of H from the N position of 41^+(**2**) can be excluded on the base of the 1-methylimidazole study by Hodges et al. [52]. The loss of H from C positions of 41^+(**2**) and 41^+(**3**) can form the same *m/z* 40 $HCCNH^+$ in the triplet state with Δ*G* of 14.68 eV.

Thus, based on our calculations and the thermodynamic thresholds, we suggest that the fragment ion at *m/z* 40 is formed in electron collisions via loss of HCNH from IMI^+ resulting in a quasi-linear ion $HCCNH^+$ in the singlet state with Δ*G* of 15.09 eV and/or via the loss of HCN from 67^+ and/or H loss from 41^+ leading to a quasi-linear ion $HCNCH^+$ in a triplet state with Δ*G* of 15.07 eV. Only one complete pathway has been identified here, namely the loss of H from *m/z* 41. Thus, we cannot exclude pathways that would be governed by the kinetics and not the thermodynamics, i.e., including TSs that we have not explored.

The measured ionization efficiency curve of *m/z* 28 reveals two onsets. In this context, it is worth noting that the N_2^+ cation cannot be separated from CH_2N^+ by its *m/z* due to the limited mass resolution of the quadrupole mass spectrometer. N_2 exhibits an ionization energy of 15.6–15.7 eV as measured by earlier EI experiments [50] which matches our experimentally determined onset for the second threshold of 15.7 ± 0.1 eV (see Figure 3b). Thus, only the first onset is of interest for the fragmentation of imidazole. We derived a value of 11.74 ± 0.06 eV that is in closer agreement with 11.67 ± 0.05 eV reported by Main-Bobo et al. [27] than with the value of 11.34 ± 0.05 eV reported by Schwell et al. [28]. Based on thermodynamic reasons, Schwell et al. suggested that the neutral is lost as a single fragment [28]. We have considered different structures of the neutral (including formation of two neutrals) that are shown in Figure ESM_11. Figure 6 shows two fragmentation pathways, both possible from an energetic point of view. Although Main-Bobo et al. [27] suggested only one pathway based on the single component observed in the kinetic energy release distribution, the experiments with deuterated imidazole by Klebe et al. confirmed that both pathways suggested here are possible [26]. In the first fragmentation channel, which was also suggested by Main-Bobo et al. [27], a hydrogen is transferred from the C4 to the C5 position (TS6 11.22 eV). Subsequently, the N1–C5 bond breaks (TS7 11.65 eV) followed by the C2–N3 bond (10.86 eV). Finally, this results in the $HCNH^+$ 28^+(**1**) cation and a neutral 40(**1**) CH_2CN fragment. In the second pathway, the hydrogen from the C4 position is first transferred to the N3 position (TS9 11.71 eV) forming 68^+(**8**) and then further to the C2 position (TS10 11.74 eV) resulting in 68^+(**9**). Afterwards, the N1–C5 bond breaks (TS11 11.61 eV), the ring opens yielding 68^+(**10**), and the rupture of C4–C5 bond results in the $HCNH^+$ 28^+(**1**) cation and the neutral 40(**2**) CH_2NC fragment. In both pathways, the resulting ion $HCNH^+$ involves the N1 position, whereas the carbon atom involves the C2 in the first pathway and the C5 in the second pathway. Our experimental threshold is in excellent agreement with the calculated transition states involved in the dissociation process.

2-Nitroimidazole For 2-nitroimidazole, the experimental threshold ionization efficiency data and fits are shown in Figure 7 and summarized in Table 2. Here, we used the well-known ionization energy of neon of 21.565 eV to calibrate the electron energy scale (see Figure 7a). Since Cartoni et al. already reported extensive calculations about the reaction mechanisms yielding fragment cations [40], we compare the present results to the thresholds determined in their work. The threshold values listed in Table 2 indicate that our results obtained by electron ionization experiments show in most cases slightly higher appearance energy values than those measured by Cartoni et al. [40] and Bolognesi et al. [39]. We also note that some of the dissociation channels of nitromidazole radical cations were also investigated in our previous work [34].

Like for imidazole, the parent cation forms the most intense channel upon electron ionization. The ionization energy of 2NI is determined to be 9.70 ± 0.02 eV (see Figure 7i). The calculated values are 9.74 eV for the AIE and 9.99 eV for the vertical ionization energy. Similarly to the case of IMI, the measured value is close to the calculated AIE. However, it should be noted that our theoretical method may overestimate ionization potentials. Both the B3LYP calculated IE and the measured value by Cartoni et al. were reported at 9.35 eV and 9.54 ± 0.01 eV, respectively [40]. These authors determined the IE using the outer valence Green's functions (OVGF) and obtained an IE value of 9.70 eV which matches perfectly well our experimental result. Since the OVGF method represents the vertical ionization energy (IE_v), the present results show that during electron ionization no relaxation of the molecules occurs, thus requiring the IE_v for ionization. Regarding the fragmentation channels, one pair of complementary fragments is present: The *m/z* 83 cation is assigned to $C_3H_3N_2O^+$ and thus formed by the loss of a neutral NO group while *m/z* 30 is the charged NO group with a neutral $C_3H_3N_2O$. Bolognesi et al. calculated the fragmentation pathway and showed that both fragment cations are produced via the same transition state with a threshold of 10.60 eV [39]. For the present EI experiment, we determined a fragmentation onset of 11.12 ± 0.02 eV and 11.11 ± 0.04 eV for *m/z* 83 and 30, respectively (see Figures 7g, c), while Cartoni et al. reported 10.86 ± 0.02 eV and 10.94 ± 0.03 eV [40]. Taking our measured IE value of 9.70 ± 0.02 eV and the TS barrier of 1.37 eV [39], which agrees with the barrier calculated in a previous work [34], we obtain

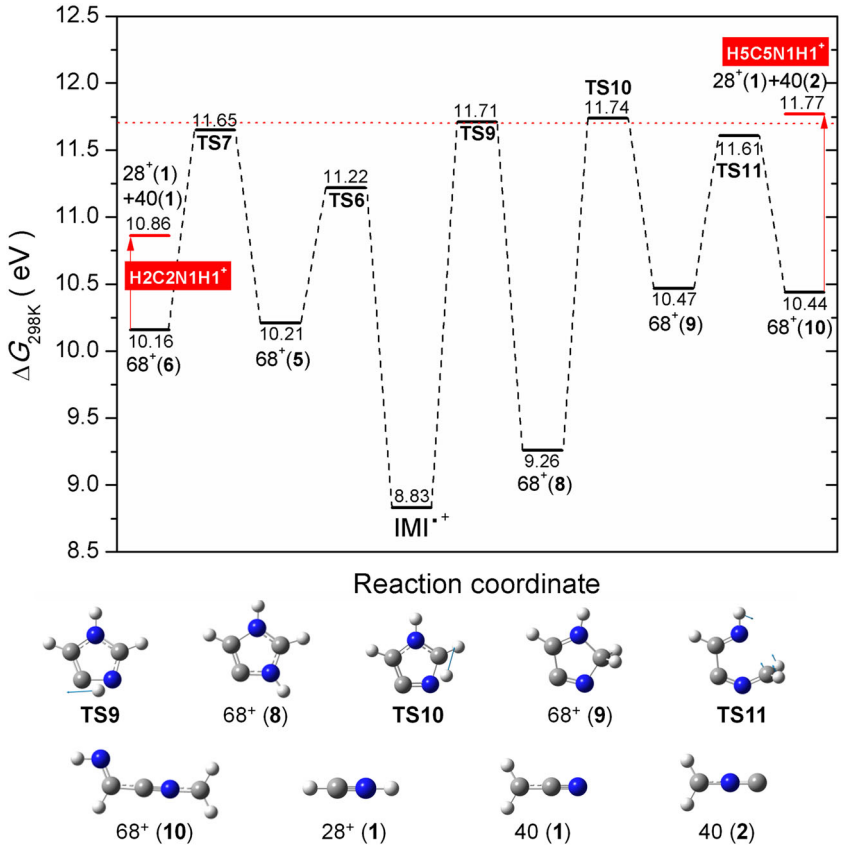

Figure 6. M06-2x/aug-cc-PVTZ calculated potential energy diagram for the decomposition of the IMI^+ leading to the formation of fragment ion $HCNH^+$ at *m/z* 28 including associated structures shown below. The blue arrows in the respective TS show the displacement vectors. The labels in a red rectangle refer to the position of the imidazole ring from which the ion *m/z* 28 has been formed. The dotted line corresponds to the experimental value

the AE of 11.07 eV, in excellent agreement with our experimental finding. The fragment ion at *m/z* 83 $C_3H_3N_2O^+$ further decomposes into two other fragments observed in the mass spectrum, the *m/z* 56 and the *m/z* 28 cations. The detailed description of the fragmentation pathway can be found in [40]. Basically, the imidazole ring breaks at the N1–C2 position and multiple hydrogen transfers occur until finally the hydrogen cyanide molecule, HCN, is released from the complex, forming $HNC(H)CO^+$ at *m/z* 56. The calculated threshold for the reaction is defined by the energetically highest transition state of 11.37 eV. This cation can even fragment further under the release of carbon monoxide, CO, to yield $HNCH^+$ at *m/z* 28. As no higher transition states are involved, the same threshold value holds. Our experimental results are 11.34 ± 0.09 eV and 11.44 ± 0.05 eV, for *m/z* 56 and 28, respectively (see Figures 7e, b) that support the predictions by Cartoni et al., even though their experimental values of 11.14 ± 0.06 eV and 11.16 ± 0.06 eV are slightly lower [40].

At *m/z* 97, we observe $C_3H_3N_3O^+$, the cation formed under the release of an atomic oxygen. We determine an experimental onset of 13.92 ± 0.05 eV (see Figure 7h), which matches the experimental value determined by Cartoni et al. of 13.9 ± 0.2 eV [40]. In their calculations, Cartoni et al. considered different electronic configurations for the pair of cation and neutral fragment formed. It turned out that only for the doublet state of $C_3H_3N_3O^+$ and the singlet state of atomic oxygen, the obtained AE of 13.89 eV agrees energetically with the experiments.

Two fragmentation pathways with relatively high appearance energies lead to the formation of cations *m/z* 67 and *m/z* 40. Additionally, *m/z* 40 features the most intense ion yield among all the fragment ions (see Figure 2). Since both cations are also observed in the EI experiments with imidazole, as discussed above, and in previous studies [26, 28], it is straight forward to explain the formation of *m/z* 40 from the dehydrogenated imidazole at *m/z* 67, $C_3H_3N_2^+$. However, the pathway yielding *m/z* 67 for 2NI must be different from IMI, as formation from 2NI proceeds through the loss of the $–NO_2$ group from the C2 position, which is not the preferential position for the H loss from IMI^+. The likely loss of HCN from *m/z* 67 was computationally investigated by Cartoni et al. who further differentiated between the singlet and triplet states of $C_3H_3N_2^+$. Based on the determined experimental AE values of 13.8 ± 0.1 eV for the fragment at *m/z* 40, they were able to exclude the singlet state of $C_3H_3N_2^+$ with a calculated onset of 15.16 eV and verified the fragmentation pathway via the triplet state with a threshold of 13.69 eV [40]. The AE determined with our EI experiment is 13.74 ± 0.03 eV (see Figure 7d) and,

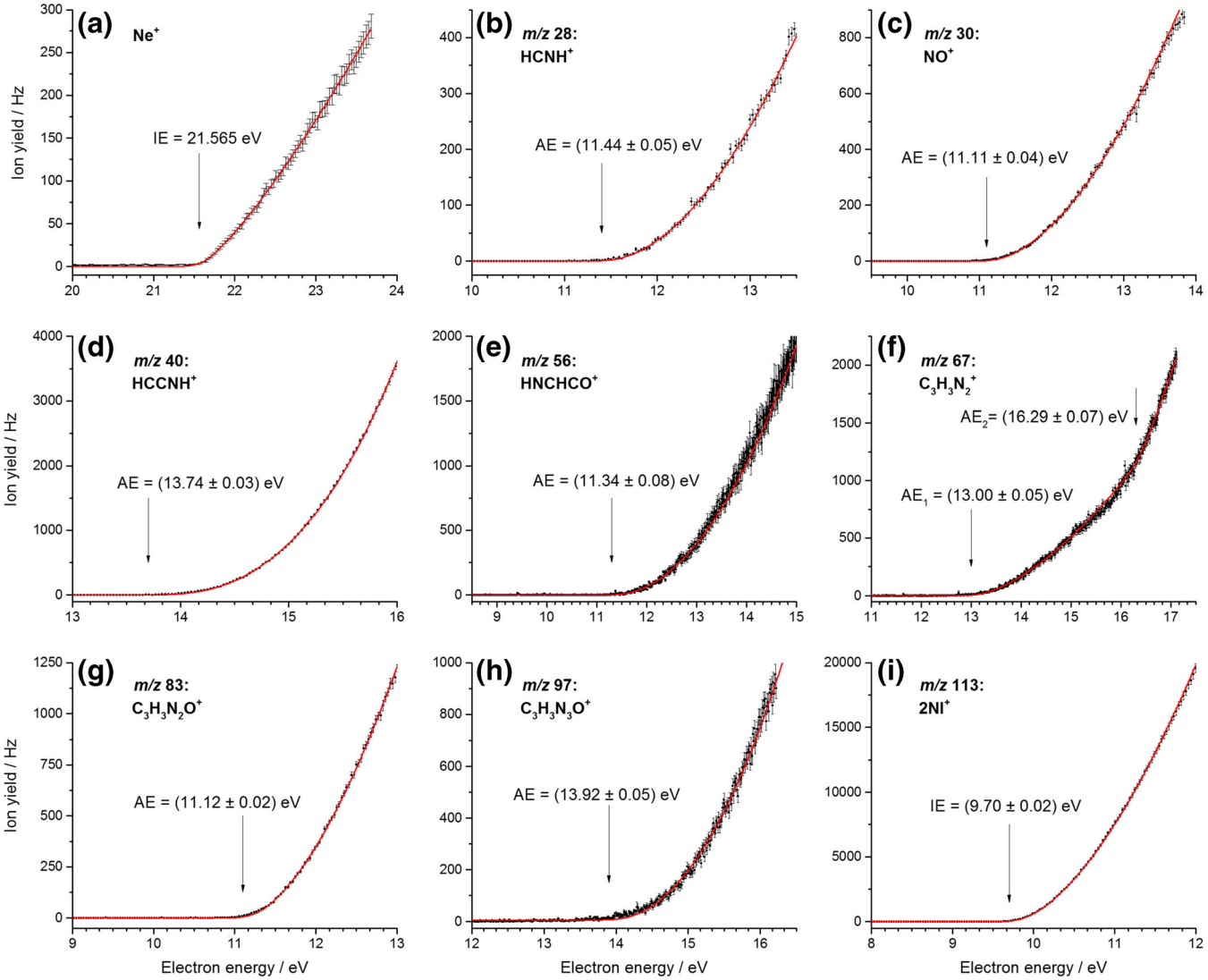

Figure 7. Threshold ionization efficiency curves of 2-nitroimidazole (**b**–**i**). The data is shown as black dots, including the statistical uncertainties as error bars. The red solid lines represent the fitted functions. For each cation, the determined AE is indicated by a black arrow. (**a**) The threshold ionization efficiency of neon which was used for calibration

thus, supports Cartoni et al.'s experimental AE value. The fragmentation pathway for *m/z* 40 was calculated by Cartoni et al. and is summarized here for the triplet state for the sake of completeness. First, the parent cation is ionized and isomerizes

Table 2. Summary of Observed Cations Upon Electron Ionization of 2-Nitroimidazole, Including *m/z* Value, Assigned Cation, and Experimental and Calculated Ionization and Appearance Energy Values

m/z	Assignment		IE and AE values (eV)			
	Cation	Neutral	Present exp.	Present calc.	Previous VUV[a]	Previous calc.[a]
28	$HCNH^+$	NO + HCN + CO	11.44 ± 0.05	–	11.16 ± 0.06	11.37
30	NO^+	$C_3N_2H_3O$	11.11 ± 0.04	–	10.94 ± 0.03	10.60
40	$HCCNH^+$	NO_2 + HCN	13.74 ± 0.03	–	13.8 ± 0.1	13.69*
56	$HNCHCO^+$	NO + HCN	11.34 ± 0.09	–	11.14 ± 0.06	11.37
67	$C_3H_3N_2^+$	NO_2	13.00 ± 0.05	12.77*; 12.92	12.76 ± 0.06	11.64*, 12.09
		NO + O	16.29±0.07	16.22		–
83	$C_3H_3N_2O^+$	NO	11.12 ± 0.02	–	10.86 ± 0.2	10.60
97	$C_3H_3N_3O^+$	O	13.92 ± 0.05	–	13.9 ± 0.2	13.89
113	$2NI^+$		9.70 ± 0.02	9.74 (AIE)	9.54 ± 0.01	9.70

*Calculated value refers to the triplet state of respective cation
[a]Refers to experimental and theoretical values reported in reference [40]

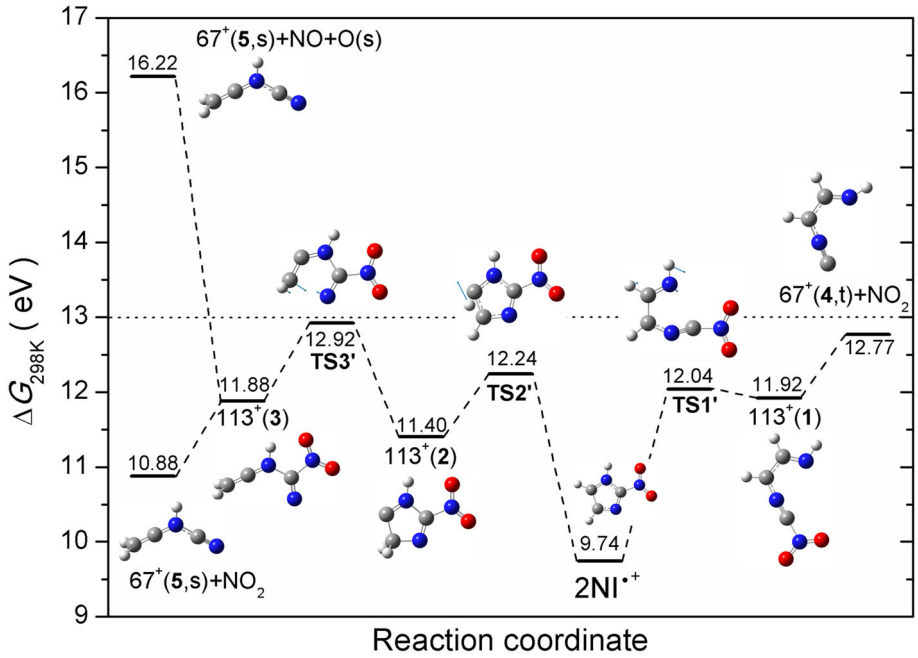

Figure 8. M06-2x/aug-cc-PVTZ calculated potential energy diagram for the decomposition of the $2NI^+$ leading to the formation of fragment ion at *m/z* 67. The blue arrows in the respective TS show the displacement vectors. The resulting cation formed through loss of NO_2 group, 67^+(**4**), is in the triplet state, while 67^+(**5**) is in the singlet state

before it decays into the NO_2 group and the charged dehydrogenated imidazole. This is the step where either the singlet or triplet state is formed. In case of the triplet, the ring opens at the N1–C5 position. The according transition state possesses the highest energy, thus defining the AE of the pathway. Afterwards, the H-N1-C2 moiety shifts position to C5, creating a new bond between C2 and C5. Subsequently, the C4–C5 bond breaks giving rise to the *m/z* 40 fragment $HCCNH^+$ and the neutral HCN. Regarding the *m/z* 67 cation the interpretation remained inconclusive in Cartoni et al.'s discussion. Both calculated AE values, 11.64 eV and 12.09 eV for the triplet and singlet state, respectively, were too low to explain their observed onset at 12.76 ± 0.06 eV. We report two experimentally determined threshold values at 13.00 ± 0.05 eV and at 16.29 ± 0.07 eV (see Figure 7f). For the formation of *m/z* 67 cation, we suggest that either a hydrogen transfer or a ring opening is required before the release of the NO_2. As discussed above in the case of the imidazole molecule, simple bond breaking was insufficient to explain the formation of *m/z* 67. We propose two pathways for the formation of *m/z* 67 shown in Figure 8. The first pathway proceeds through N1–C2 ring opening via the TS1′ of 12.04 eV forming an open chain cation 113^+(**1**), followed by a release of the NO_2 and *m/z* 67 in the triplet state with a Δ*G* of 12.77 eV that is slightly lower than our AE value, though in excellent agreement with Cartoni et al. [40]. The second pathway proceeds with H transfer from C5 to C4 with TS2′ of 12.24 eV forming the cation 113^+(**2**); further, opening of the imidazole ring between C4 and N3 through TS3′ of 12.92 eV leads to the formation of the cation 113^+(**3**). Simple C–NO_2 bond cleavage results in 67^+(**5**) in singlet state with Δ*G* of 10.88 eV; however, the apparent AE is given by the TS3′ of 12.92 eV, which is in excellent agreement with present and previous experimental observation. If the cation 113^+(**3**) dissociates into the same fragment cation 67^+(**5**), however, with the release of NO and O in the singlet state, the respective free energy of reaction Δ*G* of 16.22 eV is in great agreement with the second AE threshold value (16.29 ± 0.07) measured presently.

Conclusions

The present study revealed the reactions in imidazole and 2-nitroimidazole upon electron ionization. Since imidazole is a basic building block of life and dedicated derivatives based on the nitroimidazole group are already used as radiosensitizers in radiation therapy and as antibiotics, this knowledge is crucial to understand the basic reactions occurring under electron interactions mainly those yielding ionization processes. The mass spectra of IMI and 2NI show both the parent cation as the peak with highest intensity, revealing that this ion can be efficiently stabilized upon electron interaction at 70 eV. A comparison to earlier studies demonstrated that electron ionization results in a different relative intensity of product ions when compared to the photoionization spectrum by Schwell et al. [28]. Though it may be also related to different experimental conditions, especially the strong parent cation seems to be a characteristic for electron ionization, which agrees with the EI mass spectrum of Klebe et al. [26]. The observed dissociation channels in IMI yield cations at *m/z* 67, 41, 40, and 28, which we were able to

assign to different structures in agreement with the experimentally measured thresholds. It was shown that *m/z* 67, $[IMI - H]^+$, cannot be formed in a direct loss of H through single bond breaking. Instead, upon ionization of the IMI molecule, an H atom can transfer between various positions of the ring, and further, after ring opening H is lost from different positions with preference for C4 and C5, as suggested from earlier work. Most of the H transfer reactions lie between 11.22 and 11.80 eV, at which electron energy three fragments of IMI appear, namely *m/z* 67, *m/z* 41, and *m/z* 28. Thus, some of the transition states are involved in the formation of several ions. We assigned three different ions to the AEs derived for *m/z* 67, three for *m/z* 41, and only in the case of the fragment at *m/z* 28, it is assigned to a single structure $HCNH^+$. Compared with the assignments from previous PI studies, we predict that more fragmentation pathways are opened. We observed the general trend that in the present study, the AE values are slightly higher than in previous PI studies. The only fragment cation with a mentionable deviation is *m/z* 40. So far, only Schwell et al. [28] reported this cation before at a threshold 1 eV lower than determined by the present EI study. We ascribe this deviation to different dissociation pathways.

We also note that systematically lower values were obtained in comparison to the previous EI values by Klebe et al. [26]. This deviation may be explained by the increased precision of the electron energy scale due to the utilization of an electron monochromator [53] in our study. 2NI exhibits similar fragment cations to IMI, such as, *m/z* 67 $C_3H_3N_2^+$, 40 $HNCCH^+$, and 28 $HCNH^+$. However, they are formed through different dissociation pathways due to the presence of the NO_2 group at the C2 position of the imidazole ring. Additionally, fragment cations are observed with *m/z* 97, 83, 56, and 30. These are assigned to the cations $C_3H_3N_3O^+$ due to O loss from 2NI and $C_3H_3N_2O^+$ due to NO loss from 2NI, $HNCHCO^+$, and NO^+, respectively. For 2NI, the fragment cations with *m/z* 40, 30, and 28 have the highest ion yields. As for IMI, our determined AE values are usually slightly higher than those from PI study. The 2NI dissociation mechanisms were proposed in the earlier photoionization study for all observed cations, with the exception of the formation of ion at *m/z* 67 formed through the loss of the NO_2 group, where proposed pathways did not match the experimentally observed AE threshold value and remained inconclusive. We propose two novel pathways leading to the AE observed in both electron and photon ionization. First pathway involves the ring opening reaction followed by the release of NO_2 and the formation of the *m/z* 67 cation in the triplet state. Second pathway involves H transfer reaction followed by a ring opening and the release of NO_2 forming the *m/z* 67 cation in the singlet state. Additionally, electron ionization showed two thresholds, while PI only one. The second threshold observed in the present study can be associated with the latter pathway proposed forming the *m/z* 67 cation in the singlet state with neutrals NO and O in the singlet state. The main characteristics with radiosensitizing impact of 2NI at the molecular level observed here are the stabilized parent cation and the release of NO as reactive nitrogen species.

Acknowledgements

This work was supported by FWF, Vienna, P30332. R.M. and P.L.-V. received support from the Portuguese National Funding Agency FCT-MCTES through PD/BD/114452/2016 and PTDC/FIS-AQM/31281/2017. This work was also supported by Radiation Biology and Biophysics Doctoral Training Programme (RaBBiT, PD/00193/2012); UID/FIS/00068/2019 (CEFITEC), UID/Multi/04378/2013 (UCIBIO). L.F. received financial support from the University of Innsbruck via grant P7440-035-011, the Institut de Physique Nucléaire de Lyon (Institut de Physique des 2 Infinis de Lyon), and the LABEX Lyon Institute of Origins (ANR-10-LABX-0066) of the Université de Lyon within the program "Investissements d'Avenir" (ANR-11-IDEX-0007) of the French government operated by the National Research Agency (ANR). The crucial computing support from the HPC infrastructures LEO (Austria) and CCIN2P3 (France) is acknowledged gratefully. Open access funding was provided by University of Innsbruck and Medical University of Innsbruck.

Open Access

References

1. Von Sonntag, C.: The Chemical Basis of Radiation Biology, 1st edn. Taylor & Francis, London (1987)
2. Von Sonntag, C.: In: Glass, W.A., Varma, M.N. (eds.) The Chemistry of Free-Radical-Mediated DNA Damage. Springer US (1991)
3. Poggi, M.M., Coleman, C.N., Mitchell, J.B.: Sensitizers and protectors of radiation and chemotherapy. Curr. Probl. Cancer. **25**, 334–411 (2001)
4. Begg, A.C., Stewart, F.A., Vens, C.: Genomic instability in cancer - strategies to improve radiotherapy with targeted drugs. Nat. Rev. Cancer. **11**, 239–253 (2011)
5. Rockwell, S., Dobrucki, I.T., Kim, E.Y., Marrison, S.T., Vu, V.T.: Hypoxia and radiation therapy: past history, ongoing research, and future promise. Curr. Mol. Med. **9**, 442–458 (2009)
6. Weinmann, M., Welz, S., Bamberg, M.: Hypoxic radiosensitizers and hypoxic cytotoxins in radiation oncology. Curr. Med. Chem. Anticancer Agents. **3**, 364–374 (2003)
7. Harrison, L., Blackwell, K.: Hypoxia and anemia: factors in decreased sensitivity to radiation therapy and chemotherapy? Oncologist. **9**(Suppl 5), 31–40 (2004)
8. Howard-Flanders, P.: Effect of nitric oxide on the radiosensitivity of bacteria. Nature. **180**, 1191–1192 (1957)
9. Gray, L.H., Green, F.O., Hawes, C.A.: Effect of nitric oxide on the radiosensitivity of tumour cells. Nature. **182**, 952–953 (1958)
10. Wardman, P., Rothkamm, K., Folkes, L.K., Woodcock, M., Johnston, P.J.: Radiosensitization by nitric oxide at low radiation doses. Radiat. Res. **167**, 475–484 (2007)
11. Oronsky, B.T., Knox, S.J., Scicinski, J.J.: Is nitric oxide (NO) the last word in radiosensitization? A review. Transl. Oncol. **5**, 66–71 (2012)
12. Sonveaux, P., Jordan, B.F., Gallez, B., Feron, O.: Nitric oxide delivery to cancer: why and how? Eur. J. Cancer. **45**, 1352–1369 (2009)

13. Oronsky, B.T., Knox, S.J., Scicinski, J.: Six degrees of separation: the oxygen effect in the development of radiosensitizers. Transl. Oncol. **4**, 189–198 (2011)
14. Adams, G.E., Flockhart, I.R., Smithen, C.E., Stratford, I.J., Wardman, P., Watts, M.E.: Electron-affinic sensitization. VII. A correlation between structures, one-electron reduction potentials, and efficiencies of nitroimidazoles as hypoxic cell radiosensitizers. Radiat. Res. **67**, 9–20 (1976)
15. Mital, A.: Synthetic nitroimidazoles: biological activities and mutagenicity relationships. Sci. Pharm. **77**, 497–520 (2009)
16. Yu, Z.J., Bernstein, E.R.: On the decomposition mechanisms of new imidazole-based energetic materials. J. Phys. Chem. A. **117**, 1756–1764 (2013)
17. Ramsey, B.G.: Substituent effects on imidazole basicity and photoelectron-spectroscopy determined ionization energies. J. Organomet. Chem. **44**, 2093–2097 (1979)
18. Cradock, S., Findlay, R.H., Palmer, M.H.: The molecular energy levels of azoles: a study by photoelectron spectroscopy and ab-initio molecular-orbital calculations. Tetrahedron. **29**, 2173–2181 (1973)
19. Kajfez, F., Klasinc, L., Sunjic, V.: Application of photoelectron-spectroscopy to biologically-active molecules and their constituent parts. 4. Methylnitroimidazoles. J. Heterocyclic Chem. **16**, 529–531 (1979)
20. Tentscher, P.R., Seidel, R., Winter, B., Guerard, J.J., Arey, J.S.: Exploring the aqueous vertical ionization of organic molecules by molecular simulation and liquid microjet photoelectron spectroscopy. J. Phys. Chem. B. **119**, 238–256 (2015)
21. Cuong, N.T., Tai, T.B., Ha, V.T.T., Nguyen, M.T.: Thermochemical parameters of caffeine, theophylline, and xanthine. J. Chem. Thermodynamics. **42**, 437–440 (2010)
22. Carles, S., Lecomte, F., Schermann, J.P., Desfrancois, C.: Gas-phase experimental and theoretical studies of adenine, imidazole, pyrrole, and water noncovalent complexes. J. Phys. Chem. A. **104**, 10662–10668 (2000)
23. Modelli, A., Hajgato, B., Nixon, J.F., Nyulaszi, L.: Anionic states of six-membered aromatic phosphorus heterocycles as studied by electron transmission spectroscopy and ab initio methods. J. Phys. Chem. A. **108**, 7440–7447 (2004)
24. Gianola, A.J., Ichino, T., Hoenigman, R.L., Kato, S., Bierbaum, V.M., Lineberger, W.C.: Photoelectron spectra and ion chemistry of imidazolide. J. Phys. Chem. A. **109**, 11504–11514 (2005)
25. Ribar, A., Fink, K., Li, Z., Ptasinska, S., Carmichael, I., Feketeová, L., Denifl, S.: Stripping off hydrogens in imidazole triggered by the attachment of a single electron. PCCP. **19**, 6406–6415 (2017)
26. Klebe, K.J., Vanhoute, J.J., Vanthuij, J.: Loss of HCN and H from molecular ion of imidazole. Org. Mass Spectrom. **6**, 1363–1168 (1972)
27. Main-Bobo, J., Olesik, S., Gase, W., Baer, T., Mommers, A.A., Holmes, J.L.: The thermochemistry and dissociation dynamics of internal-energy-selected pyrazole and imidazole ions. J. Am. Chem. Soc. **108**, 677–683 (1985)
28. Schwell, M., Jochims, H.W., Baumgartel, H., Leach, S.: VUV photophysics and dissociative photoionization of pyrimidine, purine, imidazole and benzimidazole in the 7-18 eV photon energy range. Chem. Phys. **353**, 145–162 (2008)
29. Jimenez, P., Laynez, J., Claramunt, R.M., Sanz, D., Fayet, J.P., Vertut, M.C., Catalan, J., Depaz, J.L.G., Pfisterguillouzo, G., Guimon, C., Flammang, R., Maquestiau, A., Elguero, J.: The problem of the tautomerism of 4(5)-nitroimidazole - a theoretical and experimental-study. New J. Chem. **13**, 151–156 (1989)
30. Feketeová, L., Plekan, O., Goonewardane, M., Ahmed, M., Albright, A.L., White, J., O'Hair, R.A.J., Horsman, M.R., Wang, F., Prince, K.C.: Photoelectron spectra and electronic structures of the radiosensitizer nimorazole and related compounds. J. Phys. Chem. A. **119**, 9986–9995 (2015)
31. Yu, Z.J., Bernstein, E.R.: Experimental and theoretical studies of the decomposition of new imidazole based energetic materials: model systems. J. Chem. Phys. **137**, 114303 (2012)
32. Itälä, E., Tanzer, K., Granroth, S., Kooser, K., Denifl, S., Kukk, E.: Fragmentation patterns of 4(5)-nitroimidazole and 1-methyl-5-nitroimidazole - the effect of the methylation. J. Mass Spectrom. **52**, 770–776 (2017)
33. Feketeová, L., Albright, A.L., Sorensen, B.S., Horsman, M.R., White, J., O'Hair, R.A.J., Bassler, N.: Formation of radical anions of radiosensitizers and related model compounds via electrospray ionization. Int. J. Mass Spectrom. **365**, 56–63 (2014)
34. Feketeová, L., Postler, J., Zavras, A., Scheier, P., Denifl, S., O'Hair, R.A.J.: Decomposition of nitroimidazole ions: experiment and theory. PCCP. **17**, 12598–12607 (2015)
35. Ribar, A., Fink, K., Probst, M., Huber, S.E., Feketeová, L., Denifl, S.: Isomer selectivity in low-energy electron attachment to nitroimidazoles. Chem. Eur. J. **23**, 12892–12899 (2017)
36. Tanzer, K., Feketeová, L., Puschnigg, B., Scheier, P., Illenberger, E., Denifl, S.: Reactions in nitroimidazole triggered by low-energy (0-2 eV) electrons: methylation at N1-H completely blocks reactivity. Angew. Chem. Int. Ed. **53**, 12240–12243 (2014)
37. Mendes, M., Probst, M., Maihom, T., Garcia, G., Limao-Vieira, P.: Selective bond excision in nitroimidazoles by electron transfer experiments. J. Phys. Chem. A. (2019)
38. Itälä, E., Myllynen, H., Niskanen, J., Gonzalez-Vazquez, J., Wang, Y., Ha, D.T., Denifl, S., Kukk, E.: Controlling NO production upon valence ionization of nitroimidazoles. J. Phys. Chem. A. **123**, 3074–3079 (2019)
39. Bolognesi, P., Casavola, A.R., Cartoni, A., Richter, R., Markus, P., Borocci, S., Chiarinelli, J., Tosic, S., Sa'adeh, H., Masic, M., Marinkovic, B.P., Prince, K.C., Avaldi, L.: Communication: "Position" does matter: the photofragmentation of the nitroimidazole isomers. J. Chem. Phys. **145**, 191102 (2016)
40. Cartoni, A., Casavola, A.R., Bolognesi, P., Castrovilli, M.C., Catone, D., Chiarinelli, J., Richter, R., Avaldi, L.: Insights into 2-and 4(5)-nitroimidazole decomposition into relevant ions and molecules induced by VUV ionization. J. Phys. Chem. A. **122**, 4031–4041 (2018)
41. Denifl, S., Ptasinska, S., Sonnweber, B., Scheier, P., Liu, D., Hagelberg, F., Mack, J., Scott, L.T., Märk, T.D.: Free-electron attachment to coronene and corannulene in the gas phase. J. Chem. Phys. **123**, 104308 (2005)
42. Kaufman, V., Minnhagen, L.: Accurate ground-term combinations in Ne-I. J. Opt. Soc. Am. **62**, 92–95 (1972)
43. Wigner, E.P.: On the behavior of cross sections near thresholds. Phys. Rev. **73**, 1002–1009 (1948)
44. Wannier, G.H.: The threshold law for single ionization of atoms or ions by electrons. Phys. Rev. **90**, 817–825 (1953)
45. Dawley, M.M., Tanzer, K., Cantrell, W.A., Plattner, P., Brinkmann, N.R., Scheier, P., Denifl, S., Ptasinska, S.: Electron ionization of the nucleobases adenine and hypoxanthine near the threshold: a combined experimental and theoretical study. PCCP. **16**, 25039–25053 (2014)
46. Zhao, Y., Truhlar, D.G.: The M06 suite of density functionals for main group thermochemistry, thermochemical kinetics, noncovalent interactions, excited states, and transition elements: two new functionals and systematic testing of four M06-class functionals and 12 other functionals. Theor. Chem. Accounts. **120**, 215–241 (2008)
47. Hehre, W.J., Radom, L., Schleyer, P.V.R., Pople, J.A.: Ab Initio Molecular Orbital Theory. Wiley, New York (1986)
48. Dunning, T.H.: Gaussian-basis sets for use in correlated molecular calculations. 1. The atoms boron through neon and hydrogen. J. Chem. Phys. **90**, 1007–1023 (1989)
49. Frisch, M.J., Trucks, G.W., Schlegel, H.B., Scuseria, G.E., Robb, M.A., Cheeseman, J.R., Scalmani, G., Barone, V., Mennucci, B., Petersson, G.A., Nakatsuji, H., Caricato, M., Li, X., Hratchian, H.P., Izmaylov, A.F., Bloino, J., Zheng, G., Sonnenberg, J.L., Hada, M., Ehara, M., Toyota, K., Fukuda, R., Hasegawa, J., Ishida, M., Nakajima, T., Honda, Y., Kitao, O., Nakai, H., Vreven, T., Montgomery Jr., J.A., Peralta, J.E., Ogliaro, F., Bearpark, M., Heyd, J.J., Brothers, E., Kudin, K.N., Staroverov, V.N., Keith, T., Kobayashi, R., Normand, J., Raghavachari, K., Rendell, A., Burant, J.C., Iyengar, S.S., Tomasi, J., Cossi, M., Rega, N., Millam, J.M., Klene, M., Knox, J.E., Cross, J.B., Bakken, V., Adamo, C., Jaramillo, J., Gomperts, R., Stratmann, R.E., Yazyev, O., Austin, A.J., Cammi, R., Pomelli, C., Ochterski, J.W., Martin, R.L., Morokuma, K., Zakrzewski, V.G., Voth, G.A., Salvador, P., Dannenberg, J.J., Dapprich, S., Daniels, A.D., Farkas, O., Foresman, J.B., Ortiz, J.V., Cioslowski, J., Fox, D.J.: Gaussian 09, Revision D.01. Gaussian, Inc, Wallingford (2013)
50. NIST Chemistry WebBook: Linstrom, P.J., Mallard, W.G. (eds.): NIST standard reference database number 69., p. 20899. National Institute of Standards and Technology, Gaithersburg
51. Spectral Database for Organic Compounds SDBS. National Institute of Advanced Industrial Science and Technology (AIST). Accessed 2019
52. Hodges, R., Grimmett, M.R.: Mass spectra of imidazole and 1-methylimidazole. Aust. J. Chem. **21**, 1085 (1968)
53. Fiegele, T., Mason, N., Foltin, V., Lukac, P., Stamatovic, A., Scheier, P., Märk, T.D.: The energies of the triply excited n=2 intrashell He^- resonances $2s^22p$ and $2s2P^2$ revisited. Int. J. Mass Spectrom. **209**, 23–29 (2001)

5.1.2 SeCNdU

A radiosensitiser studied from the group of compounds which are incorporated into the DNA molecule is 5-selenocyanato-2'-deoxyuridine, SeCNdU. It has the molecular formula $C_{10}N_3O_5H_{11}Se$ and a molar mass of 332.17 g/mol. The structural formula is shown in figure 5.2. SeCNdU is based on a 2'-deoxyuridine molecule (dU) which represents the nucleoside and is as such responsible for the incorporation of the radiosensitiser into the DNA molecule by enzymatic processes. The deoxyuridine molecule is composed of a nucleobase moiety (U-yl) as indicated in green in figure 5.2, and a 2'-deoxyribose moiety as indicated in blue. Attached to the C5 position of the uracil moiety is a selenocyanato (SeCN) side group. It possesses a high electron affinity and is hence the part of the compound capturing low-energy electrons.

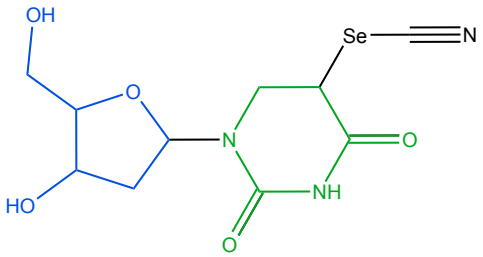

Figure 5.2: Structural formula of SeCNdU. The molecule is composed of a deoxyuridine (which in turn consists of a nucleobase moiety, green, and a 2'-deoxyribose moiety, blue) and a SeCN side chain.

The combination of the 2'-deoxyuridine and an electrophilic SeCN side chain makes SeCNdU a pesudo halouridine. Halouridines have previously been studied extensively, with the most prominent compounds being 5-bromo-2'-deoxyuridine (BrdU) and 5-iodo-2'-deoxyuridine (IdU), [217–219] and references therein. They can efficiently be incorporated into the DNA molecule [220, 221]. Upon dissociative electron interactions, they form the highly reactive uracil-5-yl radical [222–224]. Although these compounds are not applied as radiosensitising compounds for radiation therapy, halouracils are promising radiosensitiser candidates due to their incorporation and electron affinic characteristics. As a consequence, a theoretical model was developed which predicts further (pseudo-)halouracils with electron interaction cross-sections predicted to be beneficial for radiotherapy [225, 226]. One example of such a suggestions is 5-trifluoromethanesulfonyl-uracil [227]. It is a derivative of uracil. An electrophilic triflate group (OTf) is attached to the C5 position of the uracil moiety. The compound was studied at the Wippi setup, described in chapter 3.1, and the results were complemented by quantum-chemical calculations. It was found that, upon dissociative electron attachment, OTfU gives rise to a large variety of fragments, including reactive charged molecules and radicals [227]. The most dominant dissociation channel is described by the formation of the triflate anion and the neutral uracil-5-yl radical as counterpart. For the reaction, the O-C5 bond is broken. The process is most efficient at virtually 0 eV incident electron energy.

To further increase the electrophilicity of this group of compounds, 5-selenocyanato-uracil (SeCNU) was proposed next [228]. The nucleobase derivative was studied in DEA experiments by Sosnovska *et al.*, showing that the degradation yield was by a factor of 1.5 higher than of 5-bromouracil (BrU) at the experimental conditions of 140 Gy of X-rays [228]. The cleavage of the Se-CN bond leads to the most important dissociation channel. As a follow up, the according nucleoside SeCNdU was synthesised [208]. Based

on the observation on SeCNU, it was predicted that the dominant contributions arise from the Se-CN bond cleavage [208]. According to calculations based on the density functional theory, SeCNdU is also expected to be more sensitive than BrdU towards DEA reactions [208].

In the study conducted within the present thesis, the DEA reactions of SeCNdU were investigated in order to verify the predictions made previously by Makurat *et al.* [208] and to identify the most dominant dissociation channels and fragments formed [229]. The sample was synthesised at the Laboratory of Biological Sensitizers at the Faculty of Chemistry at the University of Gdansk [208]. The experiments were carried out utilising the experimental setup Wippi. In order to determine the ideal evaporation conditions of SeCNdU, positive mass spectra were recorded. The occuring peaks were identified by observing the isotope pattern. All fragments including selenium exhibit the characteristic isotope pattern of selenium, which is shown in figure 5.3. Finally, the SeCNdU sample was evaporated at 428.15 K.

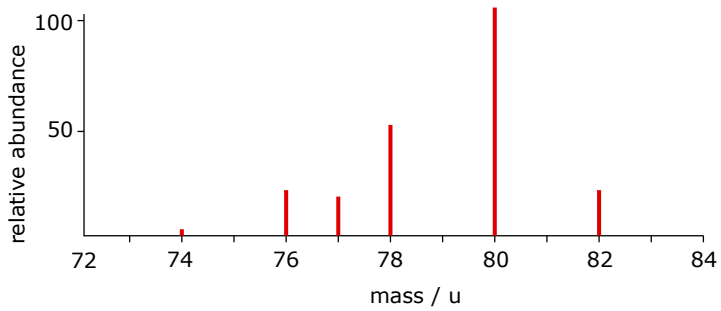

Figure 5.3: Isotope pattern from selenium. Values taken from [230].

Briefly summarising the results, the channel featuring the highest ion yield belongs to the formation of the $(\text{SeU-yl})^{\bullet -}$ radical, or $C_4N_2O_2H_2Se^{\bullet -}$, observed from virtually 0 eV electron energy onwards. This fragment at $m/z = 190$ involves a cleavage of the Se-CN bond during its formation. The fragmentation pathway leading to CN^- is the second most prominent channel and also involves this bond breakage. The heaviest anion observed is $C_9N_2O_5H_{10}Se^{\bullet -}$ with $m/z = 306$. In total, 11 dissociation channels above the detection limit were observed. The product fragments include reactive negatively charged fragments which are directly detected by the experiment, and the neutral counterparts which were identified by the quantum-chemical calculations conducted in the Laboratory of Biological Sensitizers at the Faculty of Chemistry at the University of Gdansk. The fragments arise both from simple bond cleavages and multiple bond cleavages with structural rearrangements. Five out of the eleven channels involve a cleavage of the Se-CN bond, including the two most dominant ones, while only two weak pathways lead to the breakage of the U-SeCN bond. Thus, the experimental data fully supports the predictions.

My contribution to this topic of research includes experimental data taking of the electron interaction results. I analysed this data and prepared the figures for the paper showing the electron attachment data. Additionally, I interpreted the experimental results in combination with the quantum-chemical calculations together with Janusz Rak, Samanta Makurat and Stephan Denifl. I prepared the first paper draft and finalised the manuscript with the comments of all co-authors. Finally, I was responsible for handing in the paper at the journal and was the contact person.

THE JOURNAL OF PHYSICAL CHEMISTRY B

Article

Cite This: J. Phys. Chem. B 2019, 123, 1274−1282

pubs.acs.org/JPCB

Electron-Induced Dissociation of the Potential Radiosensitizer 5-Selenocyanato-2′-deoxyuridine

Rebecca Meißner,*[,†,‡] Samanta Makurat,[§] Witold Kozak,[§] Paulo Limão-Vieira,[‡] Janusz Rak,*[,§] and Stephan Denifl*[,†]

[†]Institut für Ionenphysik und Angewandte Physik and Center for Biomolecular Sciences Innsbruck, Leopold-Franzens Universität Innsbruck, Technikerstrasse 25, A-6020 Innsbruck, Austria

[‡]Atomic and Molecular Collisions Laboratory, CEFITEC, Department of Physics, Universidade NOVA de Lisboa, 2829-516 Caparica, Portugal

[§]Laboratory of Biological Sensitizers, Physical Chemistry Department, Faculty of Chemistry, University of Gdańsk, 80-308 Gdańsk, Poland

Supporting Information

ABSTRACT: 5-Selenocyanato-2′-deoxyuridine (SeCNdU) is a recently proposed radiosensitizer based on 2′-deoxyuridine (dU) with the electron-affinic selenocyanato (−SeCN) side group attached at the C5 position of uracil. Since electron interaction processes may be an important source of DNA damage by ionizing radiation, we have studied low-energy dissociative electron attachment to SeCNdU in the gas phase. Negative ion formation has been obtained by means of mass spectrometry, where a rich fragmentation pattern is observed even at ∼0 eV. The reaction pathways exhibiting the highest ion yields are $C_4N_2O_2H_2Se^{\bullet-}$ and CN^-, both involving a cleavage of the Se−CN bond. The heaviest fragment anion observed is $C_9N_2O_5H_{10}Se^{\bullet-}$, where besides the charged species, the hydrogen and cyano radicals are also formed. Further decomposition channels also yield the highly reactive hydroxyl radical, which possesses a high DNA damage potential. All observed channels have experimentally determined onsets at 0 eV, which are supported by calculations performed at the M06-2X/aug-cc-pVTZ level. The calculations comprise the thermochemical thresholds at standard and experimental (428.15 K, 3×10^{-11} atm) conditions together with the adiabatic electron affinities. The present study shows that low-energy electrons very effectively decompose SeCNdU upon attachment of thermal electrons, producing a large variety of charged fragments and radicals.

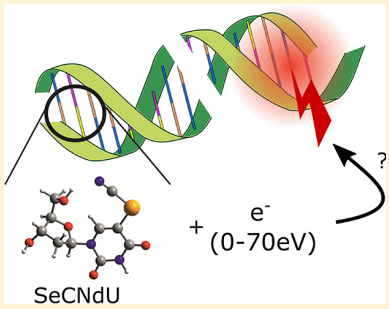

1. INTRODUCTION

In cancer treatment, radiotherapy is one among three established modalities besides surgery and chemotherapy.[1] Within therapeutic irradiation procedures, highly energetic particles interact with biological tissues. In these processes, ionization accounts for about 80% of the energy deposition.[2] The energy distribution of the hereby released electrons peaks at about 9−10 eV in a water environment.[3] Subsequently, the electrons successively loose energy by further ionization or excitation processes until they finally become solvated within a picosecond timescale.[4] It was shown that the electrons have a mean diffusion distance of a few nanometers.[5] Thus, ballistic electrons exhibit a limited chance of direct interaction with DNA from a physical point of view. Solvated electrons can efficiently attach to DNA but remain chemically inactive, that is, no fragmentation, and thus, no significant amount of strand breaks occurs.[6,7] However, base damage can occur, caused via an efficient scavenging of prehydrated and solvated electrons by nucleobases and nucleotides, which increases with concentration.[7,8]

About 80% of the solid tumor cells are hypoxic, that is, they are deprived of oxygen.[9] As oxygen is a highly electrophilic molecule, it attaches to free-radical sites of damaged DNA and makes this damage permanent.[10,11] As a consequence, hypoxic tumors are less sensitive to radiation.[12] To increase the radiosensitivity of tumor cells, chemical agents known as radiosensitizers can be administered.[10] Two different categories are described.[13,14] The first addresses the hypoxia problem with drugs specifically designed to accumulate in hypoxic cells and to mimic the oxygen effect. The second group comprises modified nucleosides, which are incorporated into the DNA. Two necessary conditions must be fulfilled to qualify for such a radiosensitizer. First, the incorporation, via the enzymatic machinery of the cell, must be possible. Because tumor cells mostly have a faster proliferation rate than healthy cells,[15,16] relatively more cancer cells will carry the modification. Second, the compound should be affine toward excess electrons and give rise to reactive radicals inside of the genome upon dissociative electron attachment (DEA).

Received: November 30, 2018
Revised: January 17, 2019
Published: January 18, 2019

DOI: 10.1021/acs.jpcb.8b11523
J. Phys. Chem. B 2019, 123, 1274−1282

5-Substituted-2′deoxyuridine derivatives are 2′-deoxyuridine (dU) analogues, which can be incorporated into DNA because of their structural similarity to the native nucleoside, thus fulfilling the first condition of the above-mentioned second group of radiosensitizers.[17] A higher electron affinity (EA) is achieved by substituting the C5 position of the uracil ring by an electrophilic residue.[18] Until now, several compounds have been proposed as potential radiosensitizers, with 5-bromo-2′-deoxyuridine (BrdU) and 5-iodo-2′-deoxyuridine (IdU) being the best studied among them.[19−21] Upon DEA, BrdU and IdU dissociate into the highly reactive uracil-5-yl radical, enhancing DNA damage.[22−24] It was clearly demonstrated that the compounds are effectively incorporated into the genome,[25,26] although they are not in clinical use.[27] Because 2′-deoxyuridine derivatives are a promising group for potential radiosensitizers, a theoretical model based on quantum chemical calculations was developed and further candidates for hypoxic radiosensitizers were proposed.[18,28] As a result, the modified nucleobase 5-selenocyanatouracil (SeCNU), having an electrophilic residue at the C5 position, was synthesized and experimentally studied with the steady-state X-ray radiolysis.[29] Because a hydroxyl radical scavenger was added to the solution of SeCNU before irradiation, the resulting damage was ascribed to DEA processes. The cleavage of the Se−CN bond was observed as the dominant decomposition channel. When compared to 5-bromouracil under the same experimental conditions (140 Gy of X-rays), SeCNU showed a 1.5-fold higher degradation yield, as indicated by the decay of the substrate, thus demonstrating an improved behavior regarding radiosensitization.[29]

Because SeCNU is a modified nucleobase but nucleosides are incorporated into DNA, the corresponding nucleoside, 5-selenocyanato-2′-deoxyuridine (SeCNdU; see Figure 1 for the molecular structure), was also synthesized.[30] Similarly, density functional theory calculations suggested that SeCNdU is more sensitive toward DEA by solvated electrons than BrdU and the bond breakage of the Se−CN substituent was predicted to be the most prominent one. Minor contributions of the U−SeCN bond breakage were expected.[30] Indeed, first radiolysis studies with SeCNdU proved its susceptibility to damage by ionizing radiation in aqueous solutions and confirmed the predicted bond cleavages.[30]

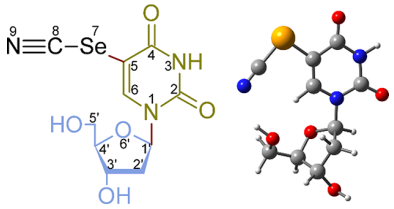

Figure 1. Chemical structure of SeCNdU. The molecule is composed of a −SeCN group, the nucleobase moiety (U-yl; indicated in green), and the 2′-deoxyribose moiety (indicated in blue). The structure is quite rigid, excluding the bonds between C5−Se7 and N1−C1′ (indicated in red), which were subjected to the conformational scan. The lowest energy conformation is also shown in 3D representation.

A similar propensity to be damaged by solvated electrons was found for a sulfur analogue of SeCNdU, namely, for SCNdU.[31] Using low-temperature electron spin resonance, steady-state radiolysis at ambient temperature, and calculations at the M06-2X/6-31++G(d,p) level, it was demonstrated that in an aqueous solution the cleavage of the S−CN bond in the initial π−anion radical $(SCNdU)^{\bullet-}$, leading to the dU-S$^{\bullet}$ radical and CN^- anion, is a preferred pathway of DEA. Moreover, the calculated thermodynamic stimuli and activation barriers for the degradation of both compared anionic systems are comparable.[30,31]

To complete the experimental picture on a physical−chemical stage and gain knowledge on the electron capture abilities of SeCNdU, we have performed DEA studies with this compound in the gas phase. The electron energy ranges from 0 to about 12 eV, covering the range of electron energies where DEA processes are most relevant. Dissociation channels and their energy onsets have been experimentally determined. The measurements have been supported by quantum chemical calculations of the thermodynamic thresholds for the observed anions.

2. EXPERIMENTAL AND COMPUTATIONAL METHODS

2.1. Synthesis of SeCNdU. The synthesis of SeCNdU was already summarized before,[30] and thus, only a brief overview is provided here. For the synthesis of SeCNdU, a modified procedure described by Agenäs[32] was used. A solution of Br_2 (142 μL, 2.76 mmol) in methanol (800 μL) was added to the suspension of KSeCN (100 mg, 0.69 mmol) in anhydrous methanol (166 μL). After 1 h of stirring in a dry ice bath (−80 °C), a suspension of 2′-deoxyuridine (75 mg, 0.34 mmol) in anhydrous methanol (3 mL) was added. After that, the mixture was brought up to −20 °C and stirred for another hour. In the next step, the reaction mixture was evaporated and the crude product was purified with semi-preparative high-performance liquid chromatography (Shimadzu, LC 20AD) equipped with a UV detector (SPD M20A) and a Synergy Polar-RP (Phenomenex) reversed-phase column (10 × 250 mm, 4 μm in particle size and 100 Å in pore size). The linear gradient of 10−25% phase B in 20 min was used (mobile phase A: 0.2% formic acid and B: 80% ACN). The resulting product was obtained as a white solid (20 mg) in a 6.3% yield.

Potassium selenocyanate, bromine, and anhydrous methanol were purchased from Sigma-Aldrich.

^{1}H NMR (Bruker AVANCE III, 500 MHz, CD_3OD): δ 8.72 (s, 1H), 6.25 (t, 1H), 4.40−4.46 (m, 1H), 3.99 (q, 1H), 3.87 (dd, 1H), 3.79 (dd, 1H), 2.33−2.41 (m, 1H), 2.23−2.32 (m, 1H); ^{13}C NMR (125 MHz, DMSO): δ 161.1, 150.4, 147.7, 104.5, 97.5, 88.2, 85.6, 70.4, 61.2, 40.8. HRMS (TripleTOF 5600+, SCIEX), m/z: $[M-H]^-$ calcd for $C_7H_8F_3N_2O_5$ 331.9863, found 331.9293; UV spectrum (water), λ_{max}: 272 nm.

2.2. Experimental Setup. The experimental setup used for the presented study was a crossed electron−molecule beam setup combined with a quadrupole mass spectrometer. A detailed description of the setup can be found in ref 33, and only a brief summary is given here. SeCNdU appeared as powder at standard conditions and was vaporized in a heated oven placed within the vacuum chamber. The oven was heated to about 428.15 K as measured with a Pt100 temperature sensor mounted directly on the oven. The vaporized sample was introduced into the interaction region as an effusive beam through a 1 mm capillary. Perpendicular to it, the electron beam was guided into the interaction region by a hemispherical electron monochromator (HEM). The current of electrons was between 20 and 50 nA. In the collision region, anions were formed via electron attachment processes. The negatively

DOI: 10.1021/acs.jpcb.8b11523
J. Phys. Chem. B 2019, 123, 1274−1282

Table 1. DEA Fragmentation Channels for SeCNdU, Including Mass and Atomic Composition of the Observed Anion, Relative Ion Yield (Rel. Yield) As Determined from the Integrated Area (Int. Area) below the Individual Resonance Profiles, Thermodynamic Reaction Thresholds As Determined in This Experiment (Exp.), and Calculations (Calc.) at the M06-2X/aug-cc-pVTZ Level[a]

mass/u	anion (X^-)	rel. yield/a.u.	reaction channel threshold/eV			AEA/eV
		(int. area)	exp.	calculations		calc.
				1 atm, 298.15 K	3×10^{-11} atm, 428.15 K	
26	CN^-	115	0	−0.28	−1.40	4.08
98	$C_5O_2H_6^{\bullet -}$	0.5	0	−0.52	−2.84	0.54
106	$SeCN^-$	1.8	0	−0.31	−1.42	3.39
110	$C_4N_2O_2H_2^{\bullet -}$	1.2	0	0.47	−0.69	3.98
111	$C_4N_2O_2H_3^-$	0.7	0	0.13	−1.04	3.99
115	$C_5O_3H_7^-$	0.4	0	0.72	−0.51	2.15
136	$C_4N_2O_2H_2CN^-$	1.1	0	−2.12	−3.28	4.47
190	$C_4N_2O_2H_2Se^{\bullet -}$	34	0	−2.03	−3.20	3.48
216	$C_4N_2O_2H_2SeCN^-$	0.2	0	−0.73	−1.92	3.97
270	$C_9N_2O_3H_6Se^{\bullet -}$	0.3	0	−0.42	−3.71	3.33
306	$C_9N_2O_5H_{10}Se^{\bullet -}$	0.9	0	−0.62	−1.66	2.79

[a]The AEA calculated at the same level of theory is also shown.

charged species were extracted by a weak electrostatic field and focused into a quadrupole mass analyzer. The utilized quadrupole had a nominal mass range of 2048 u. After mass analysis, the ions were detected by a channel electron multiplier operating in single ion counting mode and digitalized by a discriminator unit. In order to record the ion yield for a specific anion, the according mass was set constant at the quadrupole and the electron energy was varied with the HEM. The electron energy scale was calibrated with the s-wave electron attachment process to SF_6 or CCl_4,[34,35] which led to a 0 eV resonance in the ion yields of SF_6^- or Cl^-. These calibration gases were introduced into the chamber via a gas inlet system. For an estimate of the energy resolution, the full width at half-maximum of this peak was determined, measuring approximately 100 meV in the present work.

Before starting the DEA measurements, we measured the electron ionization mass spectrum of the compound in order to find optimum vaporization conditions. The resulting mass spectrum from electron impact ionization of SeCNdU at incident electron energies of 70 eV is shown in the Supporting Information (Figure S1) and is briefly discussed. Several mass spectra were recorded while increasing the temperature to check for constant peak ratios. Thereby, thermal decomposition effects were excluded while profiting from a maximal ion yield.

2.3. Computational Model. All calculations were performed using the Gaussian09[36] package with the use of M06-2X[37] functional combined with the aug-cc-pVTZ[38,39] basis set, except the conformational scan that was performed with the aug-cc-pVDZ[39,40] basis set. This methodology was shown to be successful for this kind of calculations,[40] giving results comparable to these from the G4 scheme.[41]

The scan was performed prior to the threshold calculations and consisted of constrained optimizations with two dihedral angles $\varphi_{C6-C5-Se7-C8}$ and $\varphi_{C6-N1-C1'-O6'}$ (for the numbering of atoms, see Figure 1) systematically changed every 30°. After obtaining the potential energy surface, the lowest energy points were subjected to the unconstrained geometry optimizations at higher level of theory. This allowed to calculate the composition of the gas-phase equilibrated mixture in the standard state as well as to choose the most abundant conformer for further studies. The detailed results of the conformational scan and the equilibrated mixture composition are presented in the Supporting Information.

The threshold values were calculated as the difference between the Gibbs free energies ΔG of the products and the SeCNdU substrate in their ground state, as it was performed before,[42] with eq 1

$$\Delta G = G_{\text{products}} - G_{\text{substrate}} \tag{1}$$

The optimized reactants were subjected to the frequency calculations with respect to both standard state (298.15 K, 1 atm) and the experimental conditions (428.15 K, 3×10^{-11} atm). The pressure correction to the G value for the experimental pressure was calculated with eq 2[43]

$$G_{3\times 10^{-11}\text{atm},T} = G_{1\text{atm},T} + T\cdot S_{\text{trans};1\text{atm},T} - T\cdot S_{\text{trans};3\times 10^{-11}\text{atm},T} \tag{2}$$

where $G_{p,T}$ and $S_{\text{trans};p,T}$ are the free enthalpy and the translational entropy, both at pressure p and at temperature T.

For all anionic products, including $SeCNdU^{\bullet -}$, the adiabatic EA, AEA, was calculated as the energy difference of the energies of the optimized neutral, E_{neutral}, and the corresponding anion, E_{anion} (eq 3).

$$\text{AEA} = E_{\text{neutral}} - E_{\text{anion}} \tag{3}$$

Because only the anionic fragment is directly determined by the experiment, various combinations of neutral products are theoretically possible for some of the reactions. In this case, only the lowest reaction energy was taken into account.

3. RESULTS AND DISCUSSION

In DEA, an incoming electron interacts with a neutral molecule forming a transient negative ion (TNI). The electron attachment process follows a vertical transition from the potential energy curve of the neutral to the anionic state following the Franck−Condon principle. Subsequently, the TNI either relaxes back into a neutral state by auto-detachment (eq 4) or forms a fragment anion by DEA (eq 5)[44]

$$e + M \leftrightarrow M^{\#-} \rightarrow M + e \qquad \text{(auto-detachment)} \tag{4}$$

DOI: 10.1021/acs.jpcb.8b11523
J. Phys. Chem. B 2019, 123, 1274−1282

$$e + M \leftrightarrow M^{\#-} \rightarrow [M - X] + X^{-} \quad \text{(DEA)} \qquad (5)$$

with M the molecule—and X^- the fragment anion.

The magnitude of the observed cross section depends on both the overlap of the wave function of neutral and anionic states and the auto-detachment probability of the TNI.[44]

For SeCNdU, having the vertical EA (calculated as the difference between the neutral and anionic SeCNdU, both in the neutral optimized geometry) of 0.23 eV, several fragmentation channels are observable in the energy range for about 0−14 eV within the experimental detection limits (see Table 1); additionally, experimentally determined and calculated thermodynamic thresholds are shown along with the calculated AEA.

In the following discussion, the observed dissociation channels are divided into three parts: (1) channels involving a cleavage of the Se−CN bond; (2) dissociation channels with intact Se−CN bond; and (3) fragment anions without the −SeCN group. The ion yields shown in Figures 2−6 are normalized to the highest detected ion yield of $(SeU\text{-}yl)^{\bullet-}$ at m/z 190.

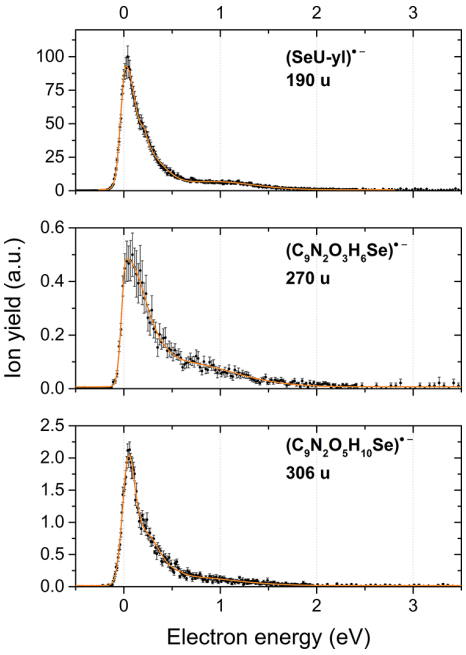

Figure 2. Ion yields (black dots and error bars) and cumulative multiple bi-Gaussian fit (orange line) of the experimentally observed fragment anions, which include the selenium atom and which are formed upon the cleavage of the Se−CN bond.

3.1. Dissociation Channels Involving a Cleavage of the Se−CN Bond. Three dissociation pathways lead to a fragment anion comprising the selenium atom but not the cyano radical. These include $C_4N_2O_2H_2Se^{\bullet-}$ (mass 190 u), $C_9N_2O_3H_6Se^{\bullet-}$ (270 u), and $C_9N_2O_5H_{10}Se^{\bullet-}$ (306 u) (see Figure 2). The first fragment anion $C_4N_2O_2H_2Se^{\bullet-}$ forms in the strongest reaction channel observed. The reaction is shown in Figure 3a as calculated at the M06-2X/aug-cc-pVTZ level of theory. Figure 3 shows all reaction pathways accompanied by multiple bond cleavage reactions (those for single bond cleavage reactions are shown in the Supporting Information). Basically, the anion comprises the U-yl with the attached selenium atom, whereas the cyano and 2′-deoxyribose groups are detached within the process and bind to one neutral reaction product (see Figure 3a). $C_9N_2O_5H_{10}Se^{\bullet-}$, that is, $[M-CN-H]^{\bullet-}$, is the heaviest anion observed and additionally a radical, which as such is highly reactive. During the DEA process, only the cyano and an additional hydrogen atom detach, which form neutral HCN (Figure 3b). In the case of the $C_9N_2O_3H_6Se^{\bullet-}$ anion (Figure 3c), additionally to cyano, three hydrogen and two OH bond cleavages occur. The calculated threshold, listed in Table 1, accounts for the formation of HCN and two water neutrals as final products. Apart from the different amounts and sites of bond breaks, all three fragment anions show striking similar ion yield profiles. A sharp rising edge with 0 eV onset is followed by a peak at roughly 0.4 eV. Then the ion yield decreases slowly with a shoulder, which may indicate another (not resolved) peak feature between about 0.5 and 1.2 eV. This observation suggests that all three fragment anions have the same electronic state of the TNI as a precursor. This formation of the TNI is the starting point for multiple bond cleavage reactions, leading to the observed anions. The negative charge is in all cases bound to the fragment containing SeU-yl. The calculations on the thermochemical threshold confirm the accessibility of the reaction with 0 eV onset, reporting −3.20, −3.71, and −1.66 eV for $C_4N_2O_2H_2Se^{\bullet-}$, $C_9N_2O_3H_6Se^{\bullet-}$, and $C_9N_2O_5H_{10}Se^{\bullet-}$, respectively. All three fragment anions also possess high AEAs, specifically 3.48, 3.33, and 2.79 eV.

The observation of the SeU-yl anion is comparable with earlier studies of halonucleobases[45−47] because the cyano group can be seen as a pseudo-halogen. For halogenated nucleobases, the formation of the U-yl anion turned out to be a highly efficient process. This reaction is in direct competition with the formation of the halogen anion because the cleavage of the same bond is involved. This often leads to comparable ion signals for the halogen anion and U-yl anion. These usually also exhibit 0 eV resonance peaks.[45,46] Also presently, both anions form with intensities in the same order of magnitude in spite of the additional bond to be broken between the nucleobase moiety and sugar moiety. This bond cleavage has been described before in theory and experiments for native nucleosides.[48−53] Additionally, a study of 5-bromouridine also demonstrated that the most abundant anion, BrU^-, is formed under the detachment of the 2′-deoxyribose and exhibits an ion yield higher by an approximate factor of 100.[54] This provides an additional hint for a comparable behavior between well-studied compounds with radiosensitizing properties, such as BrdU, and the proposed SeCNdU.

Channels including −CN but not Se are competing with the dissociation pathways including selenium. Two of those are observed, the cyano anion with mass 26 u and the $C_4N_2O_2H_2CN^-$ anion with mass 136 u (see Figure 4). CN^- shows the second most intense ion yield and is formed in a 0 eV resonance. The resonance tail also reveals a shoulder structure. Two further broad peaks lie between 1−3 and 2.5−8 eV. Above the latter energy, the peak structure devolves into a steadily increasing ion yield. Because the cation HCN^+ was observed in the electron ionization mass spectrum at 70 eV (see S1), the comparison with CN^- upon DEA to HCN is required to reveal any contamination of the ion yield. This shows that the broad peak close to 2 eV is a result of DEA to HCN.[55] As this is the only ion obtained in ref 55, the other two resonance structures presently observed at about 0 and 4.5 eV can be attributed to the SeCNdU compound. The

DOI: 10.1021/acs.jpcb.8b11523
J. Phys. Chem. B 2019, 123, 1274−1282

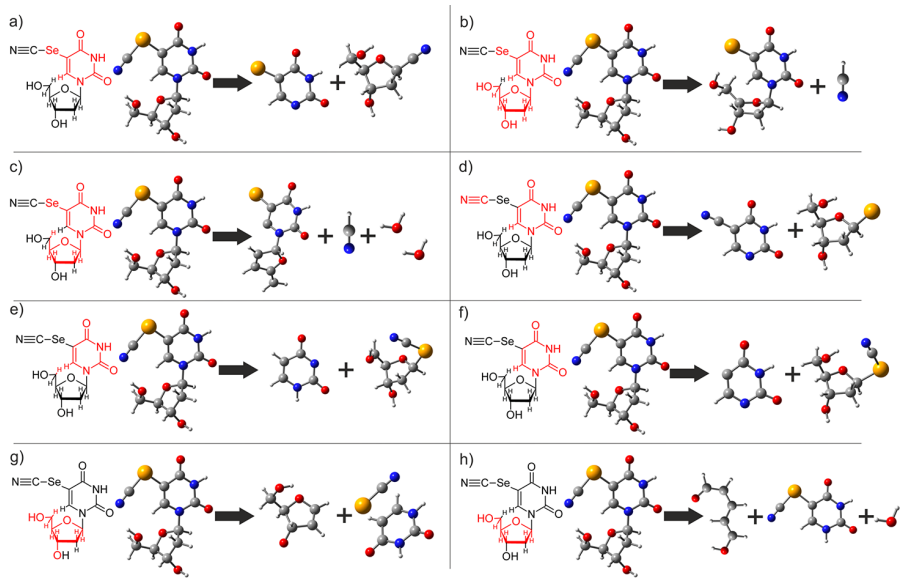

Figure 3. Ball and stick representation of dissociation channels accompanied by multiple bond cleavage reactions: (a) leading to the $C_4N_2O_2H_2Se^{\bullet-}$ or $(SeU\text{-}yl)^{\bullet-}$ anion formation (mass 190 u), (b) $C_9N_2O_5H_{10}Se^{\bullet-}$ (306 u), (c) $C_9N_2O_3H_6Se^{\bullet-}$ (270 u), (d) $C_5N_3O_2H_2^-$ or $(CNU\text{-}yl)^-$ (136 u), (e) $C_4N_2O_2H_3^-$ or $(U\text{-}yl + H)^-$ (111 u), (f) $C_4N_2O_2H_2^{\bullet-}$ or $(U\text{-}yl)^{\bullet-}$ (110 u), (g) $C_5O_3H_7^-$ (115 u), and (h) $C_5O_2H_6^{\bullet-}$ (98 u). Additionally, for each reaction, the schematic SeCNdU structure is presented, where the negatively charged moiety is marked in red.

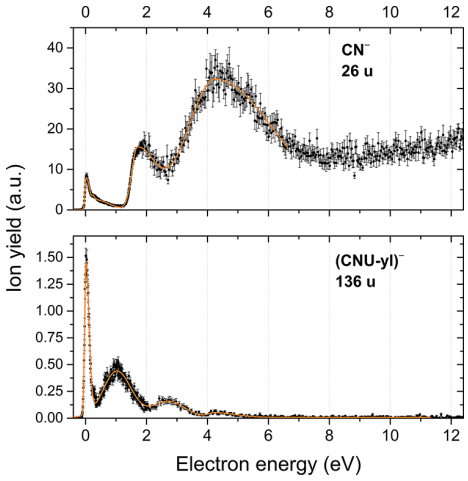

Figure 4. Ion yields (black dots and error bars) and cumulative multiple bi-Gaussian fit (orange line) of the experimentally observed dissociation channels involving the cleavage of the Se−CN bond and including the cyanide in the fragment anion.

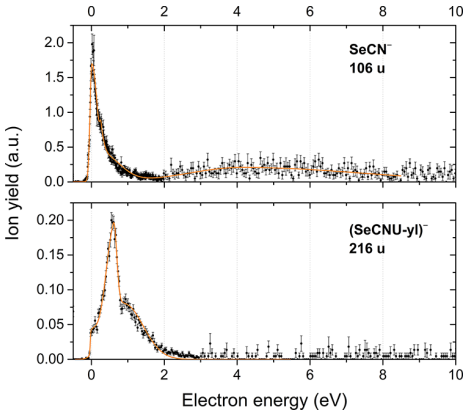

Figure 5. Ion yields (black dots and error bars) and cumulative multiple bi-Gaussian fit (orange line) of the DEA reactions, leading to fragment anions involving the intact SeCN group.

calculated threshold value of −1.40 eV (resulting from the high AEA of 4.08 eV) confirms that the channel is thermodynamically available at 0 eV at the present experimental conditions.

As mentioned above, Rak and coworkers studied the radiolysis of solvated SeCNU.[29] They theoretically predicted and observed the bond cleavage of the Se−CN bond. Only a small kinetic activation barrier of about 50 meV for the release of CN^- was reported, while the reaction is thermodynamically favored with a change in the Gibbs free energy of −0.59 eV between the TNI and the product complex.[30]

The second anion which includes the cyano group is $(CNU\text{-}yl)^-$, that is, $C_4N_2O_2H_2CN^-$. The particularity about this anion is that the selenium atom is cut out in order for the CN radical to bind to U-yl (see Figure 3d). In addition, the bond between the base and sugar moiety is broken. The measured ion yield features a rich peak pattern. The obtained experimental onset is at ∼0 eV and therefore in good agreement with the calculations, which provide a thermochemical threshold of −3.28 eV and an AEA of 4.47 eV.

In summary, a variety of dissociation pathways lead to the cleavage of the Se−CN bond, including the two with the highest ion yields. It is interesting to note that the negatively charged Se^- anion is not observed in the current experiments, though the EA of the selenium atom is positive and amounts to 2.02 eV.[56]

3.2. Dissociation Channels with the Intact Se−CN Bond. In the course of the present DEA study with SeCNdU, we can observe only two reactions which conserve the Se−CN bond. In these cases, $SeCN^-$ and $(SeCNU\text{-}yl)^-$, that is, $C_4N_2O_2H_2SeCN^-$, are formed (see Figure 5). We just note here that an intact Se−CN bond would be required for the observation of the parent anion. However, this anion turned

DOI: 10.1021/acs.jpcb.8b11523
J. Phys. Chem. B 2019, 123, 1274−1282

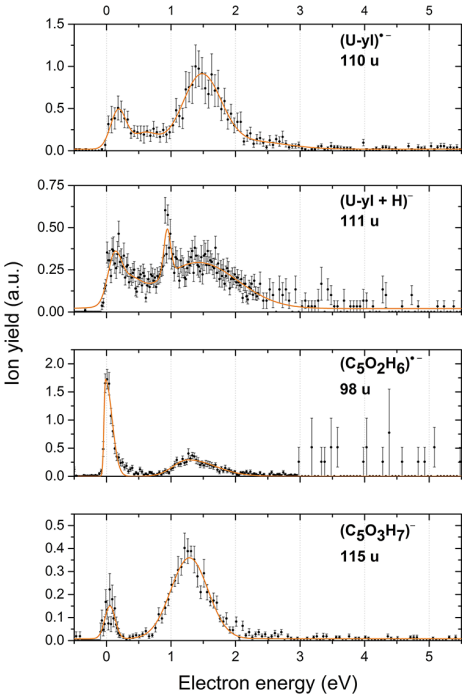

Figure 6. Ion yields (black dots and error bars) and cumulative multiple bi-Gaussian fit (orange line) of the DEA channels, resulting in the anions of the nucleobase and sugar moieties involving (several) H and/or OH losses.

out to be below the detection limit of the present experiments, although we predicted a positive EA of SeCNdU (0.75 eV) in the present calculations. The absence of the parent anion may also be a result of the particular situation that all DEA channels are already energetically open at the electron energy close to 0 eV (see Table 1). In addition, theoretical studies of nucleosides[48,49] reflected a weakening of the C1′−N1 bond strength upon electron attachment, resulting in a drastic geometry change[48] and also promoting dissociation.[49] Indeed, experimental studies with these compounds reinforce the theory by stating the most dominant channel to be a fragment anion.[50−53] Most commonly, the according nucleobase anion forms the strongest channel as it has a higher EA as the 2′-deoxyribose.[49] The present study also shows this characteristic as the dominant channel (SeU-yl) contains the nucleobase moiety.

The $SeCN^-$ fragment anion with the mass 106 u possesses a very low ion yield compared to CN^-. This is in agreement with the theoretical predictions of the former studies of solvated SeCNU[29] and SeCNdU,[30] which predicted and measured the bond cleavage of the Se−CN bond rather than an intact selenocyanate group. The kinetic activation barrier for the release of $SeCN^-$ was determined to be 0.28 eV and thus higher than for CN^- (see above). Moreover, the reaction turned out to be thermodynamically unfavored with a change in the Gibbs free energy of 0.24 eV.[30] As observed in experimental studies of halouracils[45] and 5-bromouridine[54] and simulations of halogenated nucleobases,[57,58] loss of the negatively charged electron-affinic side group from the nucleobase moiety occurs, but for the present compound this process is much less efficient because the cleavage of the Se−CN bond is highly favored. The experimentally obtained onset for $SeCN^-$ formation is at ∼0 eV, which is supported by the calculations. These predict a value of −1.42 eV for the thermochemical threshold. The SeCN fragment also features a high AEA of 3.39 eV. $SeCN^-$ exhibits a sharp rising 0 eV peak with a broader tail of about 2 eV, which is followed by a broad peak with very low intensity from around 2−8 eV.

The only other channel above the detection limit, which preserves an intact SeCN structure in the anion fragment, is $(SeCNU\text{-}yl)^-$ with a mass of 216 u. It is most efficiently formed at around 0.5 eV and features shoulders at each side of the main peak. With a calculated threshold value of −1.92 eV, the thermochemical threshold supports the experimental onset at 0 eV for this anion. The fragment possesses additionally a very high AEA of 3.97 eV. Regarding the intensity of the ion yield, the channel is comparable with $(CNU\text{-}yl)^-$.

Because $SeCN^-$ and $(SeCNU\text{-}yl)^-$ are the only two and rather weak dissociation pathways of the SeCNdU molecule compared to the channels discussed in the first section, the present results confirm that the Se−CN bond cleavage is far more likely to occur upon DEA than the loss of the SeCN fragment.

3.3. Dissociation Channels without SeCN. Besides the fragment anions discussed in the two previous sections, further channels were observed (see Figure 6). These build two subgroups: the first contains the hydrogenated U-yl anion (see Figure 3e) and the U-yl anion (see Figure 3f) with masses 111 and 110 u, respectively. The second group consists of components of the 2′-deoxyribose moiety, $(C_5O_2H_6)^{\bullet-}$ with mass 98 u and $(C_5O_3H_7)^-$ with mass 115 u. The corresponding reactions are shown in Figure 3g,h.

The $(U\text{-}yl)^-$ and $(U\text{-}yl + H)^-$ anions both exhibit two broad peak structures, one peaking around 0.2 eV and the other at about 1.5 eV. An additional sharp peak is observed for $(U\text{-}yl + H)^-$ at about 0.95 eV (see Figure 6). We note that earlier studies of uracil[59,60] and thymidine[50,51] showed a similar structure of the sharp peak at 0.95 eV and the broad feature centering around 1.5 eV for the fragment anion obtained at mass 111 u (corresponding to the dehydrogenated parent anion of the nucleobase). In one of the thymidine studies,[50] it was argued from the study of the ion yields at different sample evaporation temperatures that those peaks originate from thermal decomposition because they showed a far stronger increase with temperature compared to another peak structure found between about 5 and 10 eV. In addition, they also resembled resonances found for thymine, while the peak structure at higher energies was only found for thymidine. However, the second[51] study excluded thermal decomposition completely. The 0 eV is not observed for uracil[59] and can thus be assigned to the intact SeCNdU molecule. The calculations are in agreement with our experimental findings for 0 eV thresholds for both channels, specifically resulting in values of −0.69 and −1.04 eV for $(U\text{-}yl)^-$ and $(U\text{-}yl + H)^-$, respectively. Those exothermicities are among the lowest ones within the present study. In contrast, the AEAs of both U-yl and (U-yl + H) are among the highest with 3.98 and 3.99 eV, respectively. In a DEA study with uridine,[53] both fragment anions at m/z 110 and 111 were observed. However, the ion yield curves differ notably with the main difference that resonance structures in the range of 5−10 eV were also present and found with higher intensities than at low electron energies. We note that within the detection limit of the present apparatus, no ion yields can be observed in the range of higher electron energies in the present study with SeCNdU.

DOI: 10.1021/acs.jpcb.8b11523
J. Phys. Chem. B 2019, 123, 1274−1282

The two channels representing anionic fragments of the 2′-deoxyribose moiety have peak features at similar electron energies. Both show a peak between 0 and 0.05 eV. The channel thus exhibits a 0 eV threshold, which is in agreement with calculations stating thermochemical thresholds of −2.84 and −0.51 eV for $C_5O_2H_6^{\bullet-}$ (mass 98 u) and $C_5O_3H_7^-$ (mass 115 u), respectively. The AEA of $C_5O_2H_6$ is rather moderate and with 0.54 eV the smallest for the measured fragments obtained with an excess charge. $C_5O_3H_7$ exhibits a higher AEA of 2.15 eV. We can also observe a second broader peak between 0.5 and 2 eV. While the peak positions and the broadness coincide, the ratios differ. Earlier studies of uridine,[53] thymidine,[50,51] and 2′-deoxyribose[61] also observed resonance structures at m/z 98[53,61] and m/z 115.[50,51,61] The 2′-deoxyribose study revealed abundant 0 eV peaks for both masses.[61] The studies with thymidine observed an additional second broad resonance occurring roughly between 0.5 and 2 eV. These studies pointed out a possible thermal decomposition and, while Abdoul-Carime et al.[51] excluded thermal decomposition based on NMR analyses performed before and after heating the thymidine sample to 430 K, Ptasinka et al.[50] argued that the 0 eV peak results from thermal decomposition, while the second broad structure results from a resonance formed by the intact molecule. Like for the anions of the nucleobase moiety, the uridine study[53] differs noticeably from the former ones concerning the detection of fragment anions from the sugar moiety. Only a fragment anion at m/z 98 was observed with two resonance structures, the first as a small bump at around 0 eV and the second one, about 20 times more intense, between about 5 and 10 eV. However, it should be noted that the data of ref 53 were recorded with a standard ion source combined with a magnetic mass spectrometer. Therefore, ion yields at low electron energies may be discriminated because of space charge effects of the intense slow beam of electrons. In the present ion yields, we did not observe resonance at higher electron energies for $C_5O_2H_6^{\bullet-}$ and $C_5O_3H_7^-$.

4. CONCLUSIONS

In this work, the reaction pathways upon DEA were studied for the potential radiosensitizer SeCNdU. The results indicate that SeCNdU can be considered as a pseudo-halouridine composed of an electron-affinic −SeCN side group and a nucleobase moiety. Eleven dissociation channels were observed within the detection limit of the experiment. The highest ion yield was obtained for $(SeU\text{-}yl)^{\bullet-}$, which is a radical and thus highly reactive. A comparable ion yield was observed for the cyano anion. The yields of the other fragment anions are at least 1 order of magnitude smaller. Besides the negatively charged fragments directly obtained in the experiments, neutral counterparts were investigated by calculations. These include radicals such as SeU-yl$^{\bullet}$ and molecules such as H_2O and HCN. One of the main questions, whether a bond cleavage of the Se−CN bond or the C5−Se bond occurs more efficiently, was solved because the Se−CN bond was far more efficiently cleaved with 5 out of 11 fragmentation pathways and the 2 most intense dissociation channels among them. Cleavage of the C5−Se bond also occurs upon DEA; however, only two channels were observed with low ion yields. Remarkably, all reactions exhibit a 0 eV threshold in the experimental data, which is in full agreement with the calculated thermochemical thresholds. The calculations showed that all DEA channels are exothermic at the present experimental conditions. Few reactions have exothermicities of more than 3 eV. Such behavior also results from the exceptionally high EA of most of fragments released with an excess electron. The anion $(SeU\text{-}yl)^-$ with the most intense ion yield is formed upon simple cleavage reactions. The formation of CN^-, the other abundant anion, is based on simple bond cleavage, while two bonds have to be cleaved and one formed to produce $(SeU\text{-}yl)^-$. Most other dissociation processes involve multiple bond cleavages, which are also accompanied by structural rearrangement. The formation of $C_4N_2O_2H_2CN^-$ represents such a process because the selenium must be cut out of the molecule in order to form a U-yl−CN bond. Moreover, the resonance profiles of $C_4N_2O_2H_2Se^{\bullet-}$, $C_9N_2O_3H_6Se^{\bullet-}$, and $C_9N_2O_5H_{10}Se^{\bullet-}$ showed a very similar structure, suggesting one common electronic state of the TNI.

Overall, this study fully supports recent suggestions that SeCNdU may be a potential radiosensitizer on the physicochemical stage of radiation damage. Similar to the recently studied 5-trifluoromethanesulfonyl-uracil,[40] DEA to SeCNdU is characterized through a large variety of very efficient dissociation processes, which can already be induced by low-energy electrons with thermal kinetic energies. Reactive charged particles and radicals are formed upon DEA, which may lead to subsequent DNA damage. As a next step, the compound should be studied in water clusters. It is expected to observe a diminished fragmentation pattern, possibly favoring different channels than observed in this study. For example, we expect that the $(SeU\text{-}yl)^{\bullet-}$ anion production will be suppressed as it involves two bond breakages (see Figure 3a). Instead, the CN^- anion is likely to be formed more efficiently along with the according radical SedU$^{\bullet}$.

Indeed, the previous study on SeCNdU,[30] which employed steady-state radiolysis in water solution containing a hydroxyl radical scavenger, demonstrates the dUSe−SedU dimer and SeO_2HdU as the major stable products, which proves that DEA to SeCNdU primarily leads to the SedU$^{\bullet}$ radical and CN^- anion.

■ ASSOCIATED CONTENT

Supporting Information

The Supporting Information is available free of charge on the ACS Publications website at DOI: 10.1021/acs.jpcb.8b11523.

Cation mass spectrum, conformational scan, mixture composition, and visualization of calculated reaction pathways (PDF)

■ AUTHOR INFORMATION

Corresponding Authors

*E-mail: rebecca.meissner@uibk.ac.at (R.M.).
*E-mail: janusz.rak@ug.edu.pl (J.R.).
*E-mail: stephan.denifl@uibk.ac.at (S.D.).

ORCID

Rebecca Meißner: 0000-0003-3928-8964
Paulo Limão-Vieira: 0000-0003-2696-1152
Janusz Rak: 0000-0003-3036-0536
Stephan Denifl: 0000-0001-6072-2070

Notes

The authors declare no competing financial interest.

DOI: 10.1021/acs.jpcb.8b11523
J. Phys. Chem. B 2019, 123, 1274−1282

■ ACKNOWLEDGMENTS

This work was supported by FWF, Vienna, P30332. R.M. and P.L.-V. acknowledge the Portuguese National Funding Agency FCT-MCTES through PD/BD/114452/2016 and research grants UID/FIS/00068/2013 and PTDC/FIS-AQM/31281/2017. This work was also supported by Radiation Biology and Biophysics Doctoral Training Programme (RaBBiT, PD/00193/2012); UID/Multi/04378/2013 (UCIBIO). J.R. also acknowledges the financial support by the Polish National Science Center (NCN) under the grant no. UMO-2014/14/A/ST4/00405. Calculations have been carried out in Wroclaw Center for Networking and Supercomputing (wcss.wroc.pl), grant no. 209 and at a local cluster.

■ ABBREVIATIONS

DEA, dissociative electron attachment; TNI, transient negative ion; LEE, low-energy electron; DNA, deoxyribonucleic acid; AEA, adiabatic electron affinity; SeCNdU, 5-selenocyanato-2′-deoxyuridine; SeCNU, 5-selenocyanatouracil; IdU, 5-iodo-2′-deoxyuridine; BrdU, 5-bromo-2′-deoxyuridine; BrU, 5-bromouridine

■ REFERENCES

(1) Joiner, M. C.; van der Kogel, A. *Basic Clinical Radiobiology*, 4 ed.; CRC Press: London, U.K., 2009.
(2) Hatano, Y.; Inokuti, M. *Photoabsorption, Photoionization and Photodissociation Cross Sections*; International Atomic Energy Agency: Vienna, Austria, 1995.
(3) Pimblott, S. M.; LaVerne, J. A. Production of Low-Energy Electrons by Ionizing Radiation. *Radiat. Phys. Chem.* **2007**, *76*, 1244−1247.
(4) Alizadeh, E.; Sanche, L. Precursors of Solvated Electrons in Radiobiological Physics and Chemistry. *Chem. Rev.* **2012**, *112*, 5578−5602.
(5) Kai, T.; Yokoya, A.; Ukai, M.; Fujii, K.; Higuchi, M.; Watanabe, R. Dynamics of Low-Energy Electrons in Liquid Water with Consideration of Coulomb Interaction with Positively Charged Water Molecules Induced by Electron Collision. *Radiat. Phys. Chem.* **2014**, *102*, 16−22.
(6) Westphal, K.; Wiczk, J.; Miloch, J.; Kciuk, G.; Bobrowski, K.; Rak, J. Irreversible Electron Attachment - a Key to DNA Damage by Solvated Electrons in Aqueous Solution. *Org. Biomol. Chem.* **2015**, *13*, 10362−10369.
(7) Kumar, A.; Adhikary, A.; Shamoun, L.; Sevilla, M. D. Do Solvated Electrons (eaq-) Reduce DNA Bases? A Gaussian 4 and Density Functional Theory-Molecular Dynamics Study. *J. Phys. Chem. B* **2016**, *120*, 2115−2123.
(8) Ma, J.; Wang, F.; Denisov, S. A.; Adhikary, A.; Mostafavi, M. Reactivity of Prehydrated Electrons toward Nucleobases and Nucleotides in Aqueous Solution. *Sci. Adv.* **2017**, *3*, No. e1701669.
(9) Visvader, J. E.; Lindeman, G. J. Cancer Stem Cells in Solid Tumours: Accumulating Evidence and Unresolved Questions. *Nat. Rev. Cancer* **2008**, *8*, 755−768.
(10) Zeman, E. M. Biological Basis of Radiation Oncology. In *Clinical Radiation Oncology*, 4 ed.; Gunderson, L. L., Tepper, J. E., Eds; Elsevier Inc.: Philadelphia, USA, 2016; pp 3−42.
(11) Linam, J.; Yang, L. X. Recent developments in radiosensitization. *Anticancer Res* **2015**, *35*, 2479−2485.
(12) Rockwell, S.; Dobrucki, I.; Kim, E.; Marrison, S.; Vu, V. Hypoxia and Radiation Therapy: Past History, Ongoing Research, and Future Promise. *Curr. Mol. Med.* **2009**, *9*, 442−458.
(13) Hall, E. J.; Giacca, A. J. *Radiobiology for the Radiologist*, 7 ed.; Lippincott Williams & Wilkins: Philadelphia, USA, 2012.
(14) Wardman, P. Chemical Radiosensitizers for Use in Radiotherapy. *Clin. Oncol.* **2007**, *19*, 397−417.
(15) Evan, G. I.; Vousden, K. H. Proliferation, Cell Cycle and Apoptosis in Cancer. *Nature* **2001**, *411*, 342−348.
(16) López-Sáez, J. F.; de la Torre, C.; Pincheira, J.; Giménez-Martín, G. Cell proliferation and cancer. *Histol. Histopathol.* **1998**, *13*, 1197−1214.
(17) Eidinoff, M. L.; Cheong, L.; Rich, M. A. Incorporation of Unnatural Pyrimidine Bases into Deoxyribonucleic Acid of Mammalian Cells. *Science* **1959**, *129*, 1550−1551.
(18) Chomicz, L.; Zdrowowicz, M.; Kasprzykowski, F.; Rak, J.; Buonaugurio, A.; Wang, Y.; Bowen, K. H. How to Find out Whether a 5-Substituted Uracil Could Be a Potential DNA Radiosensitizer. *J. Phys. Chem. Lett.* **2013**, *4*, 2853−2857.
(19) Lawrence, T. S.; Davis, M. A.; Maybaum, J.; Stetson, P. L.; Ensminger, W. D. The Effect of Single versus Double-Strand Substitution on Halogenated Pyrimidine-Induced Radiosensitization and DNA Strand Breakage in Human Tumor Cells. *Radiat. Res.* **1990**, *123*, 192−198.
(20) Watanabe, R.; Nikjoo, H. Modelling the Effect of Incorporated Halogenated Pyrimidine on Radiation-Induced DNA Strand Breaks. *Int. J. Radiat. Biol.* **2002**, *78*, 953−966.
(21) Webb, C. F.; Jones, G. D. D.; Ward, J. F.; Moyer, D. J.; Aguilera, J. A.; Ling, L. L. Mechanisms of Radiosensitization in Bromodeoxyuridine-Substituted Cells. *Int. J. Radiat. Biol.* **1993**, *64*, 695−705.
(22) Dextraze, M.-E.; Wagner, J. R.; Hunting, D. J. 5-Bromodeoxyuridine Radiosensitization: Conformation-Dependent DNA Damage. *Biochemistry* **2007**, *46*, 9089−9097.
(23) Dextraze, M.-E.; Cecchini, S.; Bergeron, F.; Girouard, S.; Turcotte, K.; Wagner, J. R.; Hunting, D. J. Reaching for the Other Side: Generating Sequence-Dependent Interstrand Cross-Links with 5-Bromodeoxyuridine and γ-rays. *Biochemistry* **2009**, *48*, 2005−2011.
(24) Park, Y.; Polska, K.; Rak, J.; Wagner, J. R.; Sanche, L. Fundamental Mechanisms of DNA Radiosensitization: Damage Induced by Low-Energy Electrons in Brominated Oligonucleotide Trimers. *J. Phys. Chem. B* **2012**, *116*, 9676−9682.
(25) Iliakis, G.; Kurtzman, S.; Pantelias, G.; Okayasu, R. Mechanism of Radiosensitization by Halogenated Pyrimidines: Effect of BrdU on Radiation Induction of DNA and Chromosome Damage and Its Correlation with Cell Killing. *Radiat. Res.* **1989**, *119*, 286−304.
(26) Kinsella, T. J.; Dobson, P. P.; Mitchell, J. B.; Fornace, A. J. Enhancement of X ray induced DNA damage by pre-treatment with halogenated pyrimidine analogs. *Int. J. Radiat. Oncol., Biol., Phys.* **1987**, *13*, 733−739.
(27) Prados, M. D.; Scott, C.; Sandler, H.; Buckner, J. C.; Phillips, T.; Schultz, C.; Urtasun, R.; Davis, R.; Gutin, P.; Cascino, T. L.; et al. A Phase 3 Randomized Study of Radiotherapy Plus Procarbazine, CCNU, and Vincristine (PCV) with or without BUdR for the Treatment of Anaplastic Astrocytoma: A Preliminary Report of RTOG 9404. *Int. J. Radiat. Oncol., Biol., Phys.* **1999**, *45*, 1109−1115.
(28) Makurat, S.; Chomicz-Mańka, L.; Rak, J. Electrophilic 5-Substituted Uracils as Potential Radiosensitizers: A Density Functional Theory Study. *ChemPhysChem* **2016**, *17*, 2572−2578.
(29) Sosnowska, M.; Makurat, S.; Zdrowowicz, M.; Rak, J. 5-Selenocyanatouracil: A Potential Hypoxic Radiosensitizer. Electron Attachment Induced Formation of Selenium Centered Radical. *J. Phys. Chem. B* **2017**, *121*, 6139−6147.
(30) Makurat, S.; Zdrowowicz, M.; Chomicz-Mańka, L.; Kozak, W.; Serdiuk, I. E.; Wityk, P.; Kawecka, A.; Sosnowska, M.; Rak, J. 5-Selenocyanato and 5-trifluoromethanesulfonyl derivatives of 2′-deoxyuridine: synthesis, radiation and computational chemistry as well as cytotoxicity. *RSC Adv.* **2018**, *8*, 21378−21388.
(31) Zdrowowicz, M.; Chomicz, L.; Żyndul, M.; Wityk, P.; Rak, J.; Wiegand, T. J.; Hanson, C. G.; Adhikary, A.; Sevilla, M. D. 5-Thiocyanato-2′-deoxyuridine as a possible radiosensitizer: electron-induced formation of uracil-C5-thiyl radical and its dimerization. *Phys. Chem. Chem. Phys.* **2015**, *17*, 16907−16916.
(32) Agenäs, L.-B.; Uldall, I.; Samuelsson, B.; Sjövall, J.; Munch-Petersen, J. Selenium Derivatives in the Indole Series. I. On the

DOI: 10.1021/acs.jpcb.8b11523
J. Phys. Chem. B 2019, 123, 1274−1282

Synthesis of 3-Selenocyanatoindole and 3,3'-Diindolyl Diselenide. *Acta Chem. Scand.* **1963**, *17*, 268−270.
(33) Denifl, S.; Ptasińska, S.; Sonnweber, B.; Scheier, P.; Liu, D.; Hagelberg, F.; Mack, J.; Scott, L. T.; Märk, T. D. Free-Electron Attachment to Coronene and Corannulene in the Gas Phase. *J. Chem. Phys.* **2005**, *123*, 104308.
(34) Matejcik, S.; Eichberger, P.; Plunger, B.; Kiendler, A.; Stamatovic, A.; Märk, T. D. Dissociative Electron-Attachment to SF_6^- Production of SF_5^- at Temperatures Below 300 K. *Int. J. Mass Spectrom. Ion Processes* **1995**, *144*, L13−L17.
(35) Scheunemann, H.-U.; Illenberger, E.; Baumgärtel, H. Dissociative Electron-Attachment to CCl_4, $CHCl_3$, CH_2Cl_2 and CH_3Cl. *Ber. Bunsen-Ges. Phys. Chem.* **1980**, *84*, 580−585.
(36) Frisch, M. J.; Trucks, G. W.; Schlegel, H. B.; Scuseria, G. E.; Robb, M. A.; Cheeseman, J. R.; Scalmani, G.; Barone, V.; Petersson, G. A.; Nakatsuji, H.; et al. *Gaussian 09*, revision D.01; Gaussian, Inc.: Wallingford CT, 2013.
(37) Zhao, Y.; Truhlar, D. G. The M06 Suite of Density Functionals for Main Group Thermochemistry, Thermochemical Kinetics, Noncovalent Interactions, Excited States, and Transition Elements: Two New Functionals and Systematic Testing of Four M06-Class Functionals and 12 Other Functionals. *Theor. Chem. Acc.* **2008**, *120*, 215−241.
(38) Kendall, R. A.; Dunning, T. H.; Harrison, R. J. Electron affinities of the first-row atoms revisited. Systematic basis sets and wave functions. *J. Chem. Phys.* **1992**, *96*, 6796−6806.
(39) Woon, D. E.; Dunning, T. H. Gaussian basis sets for use in correlated molecular calculations. III. The atoms aluminum through argon. *J. Chem. Phys.* **1993**, *98*, 1358−1371.
(40) Ameixa, J.; Arthur-Baidoo, E.; Meißner, R.; Makurat, S.; Kozak, W.; Butowska, K.; Ferreira da Silva, F.; Rak, J.; Denifl, S. Low-Energy Electron-Induced Decomposition of 5-Trifluoromethanesulfonyl-Uracil: A Potential Radiosensitizer. *J. Chem. Phys.* **2018**, *149*, 164307.
(41) Curtiss, L. A.; Redfern, P. C.; Raghavachari, K. Gaussian-4 Theory. *J. Chem. Phys.* **2007**, *126*, 084108.
(42) Ribar, A.; Huber, S. E.; Śmiałek, M. A.; Tanzer, K.; Neustetter, M.; Schürmann, R.; Bald, I.; Denifl, S. Hydroperoxyl Radical and Formic Acid Formation from Common DNA Stabilizers Upon Low Energy Electron Attachment. *Phys. Chem. Chem. Phys.* **2018**, *20*, 5578−5585.
(43) Ochterski, J. W. *Thermochemistry in Gaussian*; Gaussian, Inc., 2000; pp 1−19.
(44) Fabrikant, I. I.; Eden, S.; Mason, N. J.; Fedor, J. Recent Progress in Dissociative Electron Attachment. *Adv. At., Mol., Opt. Phys.* **2017**, *66*, 545−657.
(45) Abdoul-Carime, H.; Huels, M. A.; Illenberger, E.; Sanche, L. Sensitizing DNA to Secondary Electron Damage: Resonant Formation of Oxidative Radicals from 5-Halouracils. *J. Am. Chem. Soc.* **2001**, *123*, 5354−5355.
(46) Denifl, S.; Matejcik, S.; Gstir, B.; Hanel, G.; Probst, M.; Scheier, P.; Märk, T. D. Electron Attachment to 5-Chloro Uracil. *J. Chem. Phys.* **2003**, *118*, 4107−4114.
(47) Schürmann, R.; Tanzer, K.; Dąbkowska, I.; Denifl, S.; Bald, I. Stability of the Parent Anion of the Potential Radiosensitizer 8-Bromoadenine Formed by Low-Energy (< 3 eV) Electron Attachment. *J. Phys. Chem. B* **2017**, *121*, 5730−5734.
(48) Richardson, N. A.; Gu, J.; Wang, S.; Xie, Y.; Schaefer, H. F. DNA Nucleosides and Their Radical Anions: Molecular Structures and Electron Affinities. *J. Am. Chem. Soc.* **2004**, *126*, 4404−4411.
(49) Li, X.; Sanche, L.; Sevilla, M. D. Base Release in Nucleosides Induced by Low-Energy Electrons: A DFT Study. *Radiat. Res.* **2006**, *165*, 721−729.
(50) Ptasinska, S.; Denifl, S.; Gohlke, S.; Scheier, P.; Illenberger, E.; Märk, T. D. Decomposition of Thymidine by Low-Energy Electrons: Implications for the Molecular Mechanisms of Single-Strand Breaks in DNA. *Angew. Chem., Int. Ed.* **2006**, *45*, 1893−1896.
(51) Abdoul-Carime, H.; Gohlke, S.; Fischbach, E.; Scheike, J.; Illenberger, E. Thymine Excision from DNA by Subexcitation Electrons. *Chem. Phys. Lett.* **2004**, *387*, 267−270.
(52) Muftakhov, M. V.; Shchukin, P. V. Destruction of Peptides and Nucleosides in Reactions with Low-Energy Electrons. *Tech. Phys.* **2018**, *63*, 747−758.
(53) Muftakhov, M. V.; Shchukin, P. V. Resonant Electron Capture by Uridine. *J. Anal. Chem.* **2013**, *68*, 1200−1204.
(54) Denifl, S.; Candori, P.; Ptasińska, S.; Limão-Vieira, P.; Grill, V.; Märk, T. D.; Scheier, P. Positive and Negative Ion Formation Via Slow Electron Collisions with 5-Bromouridine. *Eur. Phys. J. D* **2005**, *35*, 391−398.
(55) May, O.; Kubala, D.; Allan, M. Absolute Cross Sections for Dissociative Electron Attachment to HCN and DCN. *Phys. Rev. A* **2010**, *82*, 010701.
(56) Mansour, N. B.; Edge, C. J.; Larson, D. J. Laser photodetachment spectroscopy of Se− and S−. *Nucl. Instrum. Methods Phys. Res., Sect. B* **1988**, *31*, 313−316.
(57) Chomicz, L.; Rak, J.; Storoniak, P. Electron-Induced Elimination of the Bromide Anion from Brominated Nucleobases. A Computational Study. *J. Phys. Chem. B* **2012**, *116*, 5612−5619.
(58) Li, X.; Sanche, L.; Sevilla, M. D. Dehalogenation of 5-Halouracils after Low Energy Electron Attachment: A Density Functional Theory Investigation. *J. Phys. Chem. A* **2002**, *106*, 11248−11253.
(59) Hanel, G.; Gstir, B.; Denifl, S.; Scheier, P.; Probst, M.; Farizon, B.; Farizon, M.; Illenberger, E.; Märk, T. D. Electron Attachment to Uracil: Effective Destruction at Subexcitation Energies. *Phys. Rev. Lett.* **2003**, *90*, 188104.
(60) Scheer, A. M.; Aflatooni, K.; Gallup, G. A.; Burrow, P. D. Bond Breaking and Temporary Anion States in Uracil and Halouracils: Implications for the DNA Bases. *Phys. Rev. Lett.* **2004**, *92*, 068102.
(61) Ptasinska, S.; Denifl, S.; Scheier, P.; Märk, T. D. Inelastic Electron Interaction (Attachment/Ionization) with Deoxyribose. *J. Chem. Phys.* **2004**, *120*, 8505−8511.

DOI: 10.1021/acs.jpcb.8b11523
J. Phys. Chem. B 2019, 123, 1274−1282

Supporting Information for

Electron-Induced Dissociation of the Potential Radiosensitizer 5-Selenocyanato-2'-Deoxyuridine

Rebecca Meißner[1,2*], Samanta Makurat[3], Witold Kozak[3], Paulo Limão-Vieira[2], Janusz Rak[3*] and Stephan Denifl[1*]

[1] Institut für Ionenphysik und Angewandte Physik and Center for Biomolecular Sciences Innsbruck, Leopold-Franzens Universität Innsbruck, Technikerstrasse 25, A-6020 Innsbruck, Austria

[2] Atomic and Molecular Collisions Laboratory, CEFITEC, Department of Physics, Universidade NOVA de Lisboa, 2829-516 Caparica, Portugal

[3] Laboratory of Biological Sensitizers, Physical Chemistry Department, Faculty of Chemistry, University of Gdańsk, 80-308 Gdańsk, Poland

1) Cation formation upon dissociative electron ionization

In order to find optimum vaporization conditions and to identify possible impurities present in the sample or the vacuum chamber, we measured electron ionization mass spectra of the compound. Electron ionization (EI) is a hard ionization technique where an incoming electron knocks out an electron from a neutral molecule. The parent cation either stabilizes or dissociates forming neutral and positively charged fragments. The EI spectrum of SeCNdU is shown in Figure S1. It was recorded at an electron energy of about 70 eV and an oven temperature of about 428.15K.

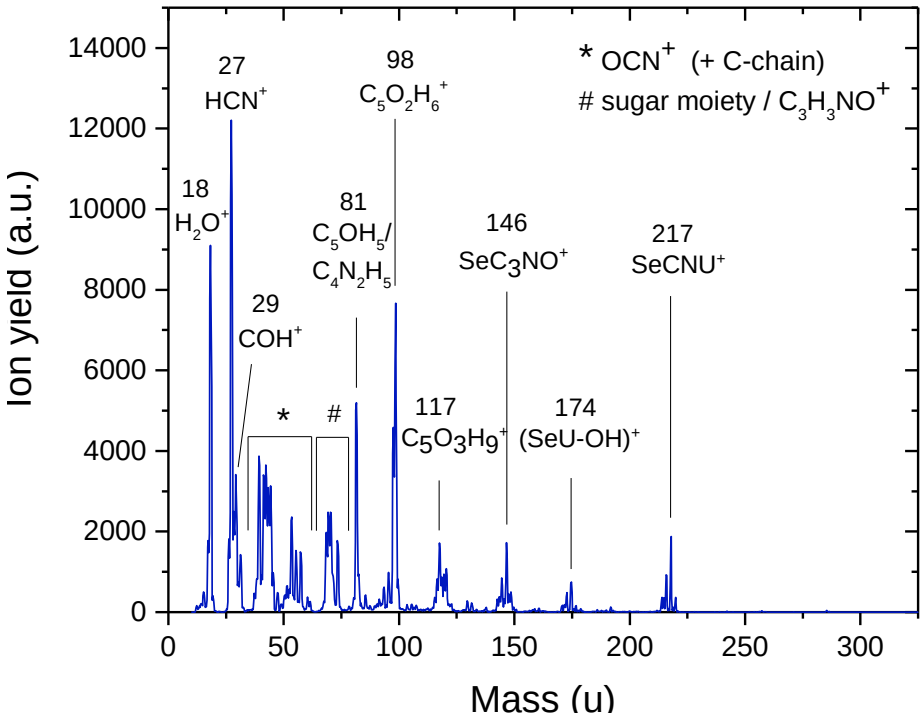

Figure S1. Mass spectrum resulting from electron ionization of SeCNdU at incident electron energies of 70 eV.

For the possible future comparison with other measurements, we note that both observed fragments and relative peak heights may vary with the ionization method. Further experimental sources for deviations in the relative peak heights are the electron energy applied for ionization, the mass analyzer since quadrupoles have a decreasing mass transmission to higher m/z ratios,

and the ion collection efficiency of fragments, which is reduced if those are formed with high initial kinetic energy. The observed fragments within EI studies should always be the same. The parent cation at m/z 333 is not observed. This characteristic varies from earlier nucleobase studies[59-63] and a recent study of OTfU,[37] also a 5-substituted-2'deoxyuridine derivative. Simple amino acids and sugar molecules are more fragile and as a consequence break up easily and do not show a parent anion, either[59, 64]. The heaviest fragment cation observed in the shown mass spectrum is SeCNU-yl$^+$ at m/z 217, representing the loss of the sugar moiety. The peak structures at m/z 174 and 146 show the typical selenium isotope pattern and can thus be assigned to (SeU-yl - OH)$^+$ and SeC_3NO^+, respectively. At around m/z 117, the sugar moiety ($C_5O_3H_9^+$) results in a number of peaks caused by the loss of a variable number of hydrogen atoms. One of the strongest fragmentation channels appears at m/z 98 ($C_5O_2H_6^+$), resulting of the break-off of the SeCNU group and an OH radical. For the fragment cation observed at m/z 81, two possible dissociation paths exist, one leading to the sugar moiety without the two side chains, $C_5OH_5^+$, and the other to the uracil ring without attached oxygen, $C_4N_2H_5^+$. Towards lower m/z values, three peak groups are observed, at around m/z 69, 53 and 42. Those are likely to arise from the breakage of the uracil ring. Previous measurements of uracil taken at the same experimental setup under comparable conditions[60] showed formation of $C_3H_3NO^+$ (m/z 69) and OCN^+ (m/z 42). The structure peaking around m/z 55 could result from OCN^+ with an additional carbon and hydrogen attached. Fragment channels at low m/z are COH^+ (m/z 29) and HCN^+ (m/z 27). The water peak observed at m/z 18 results from the background as measurements without oven filling have shown.

2) The conformational scan and mixture composition

The conformational scan, see Figure S2, and further unconstrained optimizations of the lowest-energy points lead to five local minima of different geometry and energy, see Figure S3. The difference in the Gibbs free energies between these allowed to calculate the composition of the gas-phase equilibrated mixture. The lowest energy conformer was set as a reference structure *R* and for every structure *N* other than the reference structure R the equilibrium constant K_N was determined with

$$K_N = \mathrm{e}^{-\Delta G/RT}$$

The fraction of *N* in the equilibrated sample is given by

$$X_N = \frac{K_N}{1 + K_1 + K_2 + \cdots}$$

where the sum in the denominator goes through all the considered conformations.

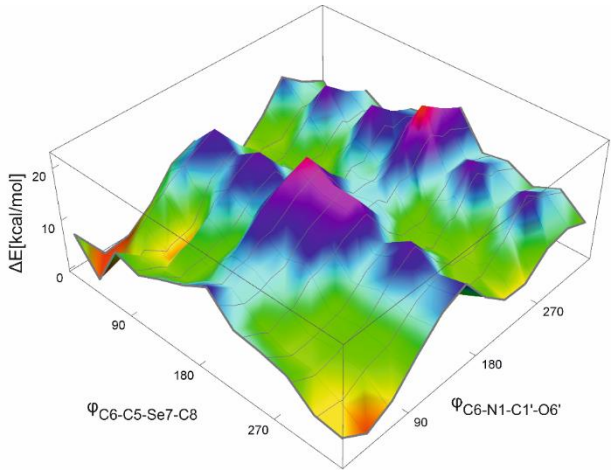

Figure S2. Scan results over the two dihedrals rotation $\varphi_{C6\text{-}C5\text{-}Se7\text{-}C8}$ and $\varphi_{C6\text{-}N1\text{-}C1'\text{-}O6'}$. The scan was performed at the M06-2X/aug-cc-pVDZ level of theory, and only the local minima were later optimized with larger aug-cc-pVTZ basis set of triple-zeta quality.

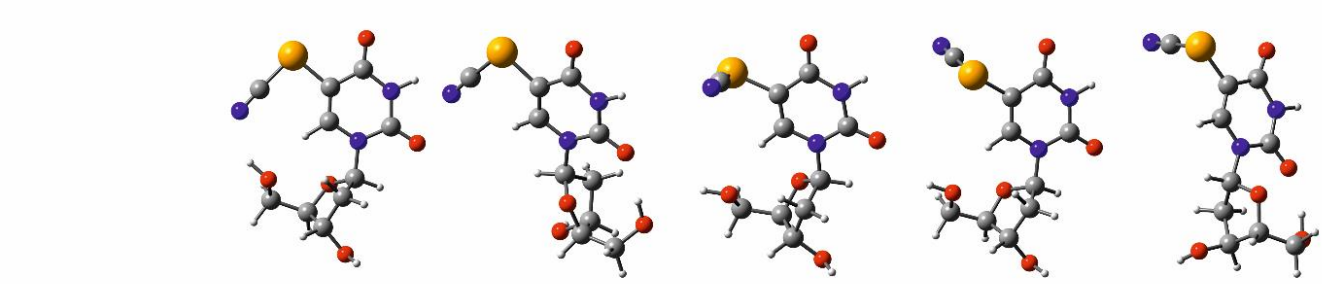

ΔG[kcal/mol]	0	3.7	4.7	5.1	5.6
$\varphi_{C6-C5-Se7-C8}$	-3	0	99	-99	-98
$\varphi_{C6-N1-C1'-O6'}$	46	124	45	50	-115
% in the mix.	98.8	0.8	0.2	0.1	0.1

Figure S3. The most stable conformations chosen from PES scan, optimized at M06-2X/aug-cc-pvtz level of theory. The angles as well as free energy difference between the geometries along with their representation in mixture (%, standard state) are shown.

3) Visualization of calculated reaction pathways for single bond cleavage reactions

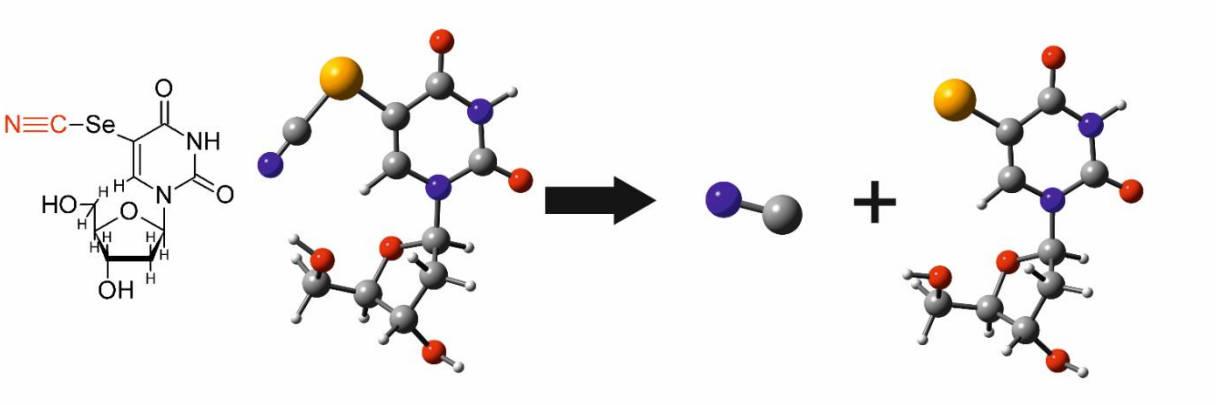

Figure S4. Ball and stick representation for the dissociation channel leading to CN^- anion formation (identified mass of 26u). Additionally schematic SeCNdU structure is presented, where the part that leaves as an anion is marked red.

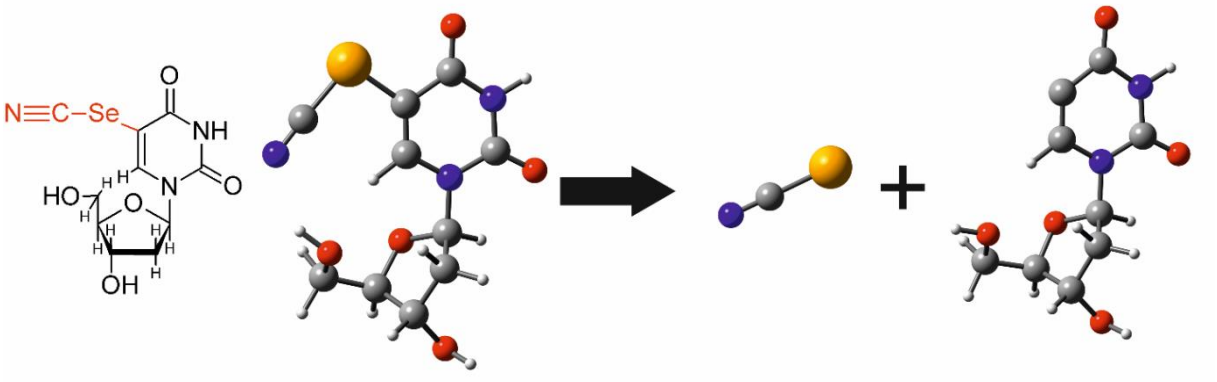

Figure S5. Ball and stick representation for the dissociation channel leading to $SeCN^-$ anion formation (identified mass of 106u). Additionally, the schematic SeCNdU structure is presented, where the part that leaves as an anion is marked red.

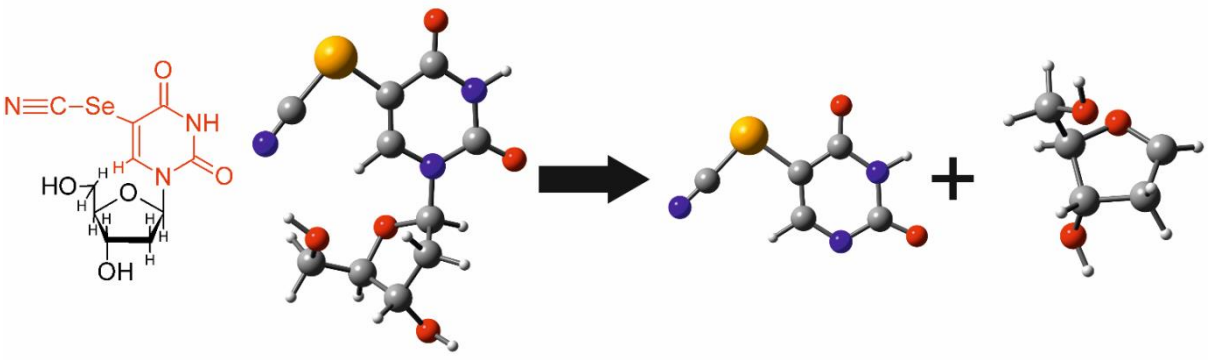

Figure S6. Ball and stick representation for the dissociation channel leading to $C_5N_3O_2H_2Se^-$ anion formation (identified mass of 216u). Additionally, the schematic SeCNdU structure is presented, where the part that leaves as an anion is marked red.

Supplementary References

62. Center, N. M. S. D., Mass Spectra. In *NIST Standard Reference Database Number 69*, Linstrom, P. J.; Mallard, W. G., Eds. Gaithersburg MD.

63. Denifl, S.; Sonnweber, B.; Hanel, G.; Scheier, P.; Märk, T. D., Threshold Electron Impact Ionization Studies of Uracil. *Int. J. Mass Spectrom.* **2004**, *238*, 47-53.

64. Dawley, M. M.; Tanzer, K.; Cantrell, W. A.; Plattner, P.; Brinkmann, N. R.; Scheier, P.; Denifl, S.; Ptasinska, S., Electron Ionization of the Nucleobases Adenine and Hypoxanthine near the Threshold: A Combined Experimental and Theoretical Study. *PCCP* **2014**, *16*, 25039-25053.

65. Rahman, M. A.; Krishnakumar, E., Electron Ionization of Adenine. *XXIX International Conference on Photonic, Electronic, and Atomic Collisions (ICPEAC2015), Pts 1-12* **2015**, *635*.

66. Wang, H.; Mu, X.; He, H.; Zhang, X. D., Cancer Radiosensitizers. *Trends Pharmacol Sci* **2018**, *39*, 24-48.

67. Papp, P.; Shchukin, P.; Kočišek, J.; Matejčik, Š., Electron Ionization and Dissociation of Aliphatic Amino Acids. *J. Chem. Phys.* **2012**, *137*.

5.1.3 Misonidazole

A large group of radiosensitisers, both already in use and under intense study, are the nitroimidazoles. They were introduced in chapter 4.3.3 as agents addressing hypoxic tumour cells [166, 231]. Nitroimidazoles accumulate in these cells and efficiently capture low energy electrons. The subsequent associative or dissociative electron attachment reactions yield reactive species, both charged and neutral. These can either further interact with the cell's components and induce DNA damage or act as species fixing previously induced DNA damage similar to oxygen. Misonidazole is such a nitroimidazole derivative. It is composed of an imidazole ring with a nitro group attached to the C2 position of the ring, making it more specifically a 2-nitroimidazole derivative. Additionally, a side chain is attached to the N1 position. The structural formula is shown in figure 5.4. The molecular formula is $C_7H_{11}N_3O_4$ resulting in a molar mass of 201.18 g/mol. Misonidazole was already clinically tested. Although it was found to be a very efficient radiosensitiser, its neurotoxicity prevented the application of the required doses during the treatment and hence the application was stopped [12, 231].

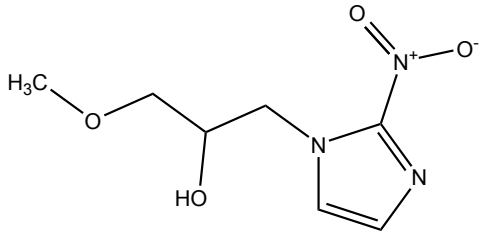

Figure 5.4: Structural formula of misonidazole. The molecule is composed of an imidazole ring with an attached nitro group and a characteristic carbon side chain.

In the present study, misonidazole was studied upon associative and dissociative electron attachment (AA, DEA) in order to identify the operation mechanisms on a molecular scale by determining the reactions and products of nitroimidazolic radiosensitisers. The importance of low energy electrons was discussed in chapter 4. For data taking, the experimental setup Wippi was used. The sample was heated gradually while acquiring positive mass spectra in order to prevent thermal decomposition. Once the compound thermally decomposes, low mass fragments increase in their relative ion yields in the mass spectra. An example spectrum is shown in figure 5.5 taken at 75°C which is the temperature found with yet no thermal degradation and the highest ion yields.

Briefly summarising the results of the present study, it was shown that misonidazole efficiently captures low energy electrons [232]. The initial reduction of the radiosensitiser is required for the uptake in hypoxic tumour cells. The dominant channel is the associative attachment resulting in the reduced parent molecule, the non-decomposed $C_7H_{11}N_3O_4^-$. This anion is formed within a very narrow energy range close to 0 eV electron energy. Additionally, DEA pathways are observed in the measured electron energy range from (0-10) eV. The formation processes include single bond cleavages, such as for the formation of NO_2^-, multiple bond cleavages, as for CN^-, and even complex rearrangements, as for the release of neutral H_2O. Among the DEA channels, the formation of the NO_2^- anion is the most dominant, accessible from virtually 0 eV electron energy onwards. An overview of all anions above the detection limit for the energy range between (0-10) eV is shown in figure 5.6 with a logarithmic scale applied to the ion yield. Besides the charged fragments, highly reactive neutral radicals are released, too. The

identification of those was enabled by quantum mechanical calculations conducted at the Institut de Physique Nucléaire de Lyon, Université de Lyon, France. These also provide data on the free reaction energies and the energetically favourable structures of the anions. Experimental and theoretical data combined allowed revealing details of the molecular mechanisms of how misonidazole works as a radiosensitizer [232].

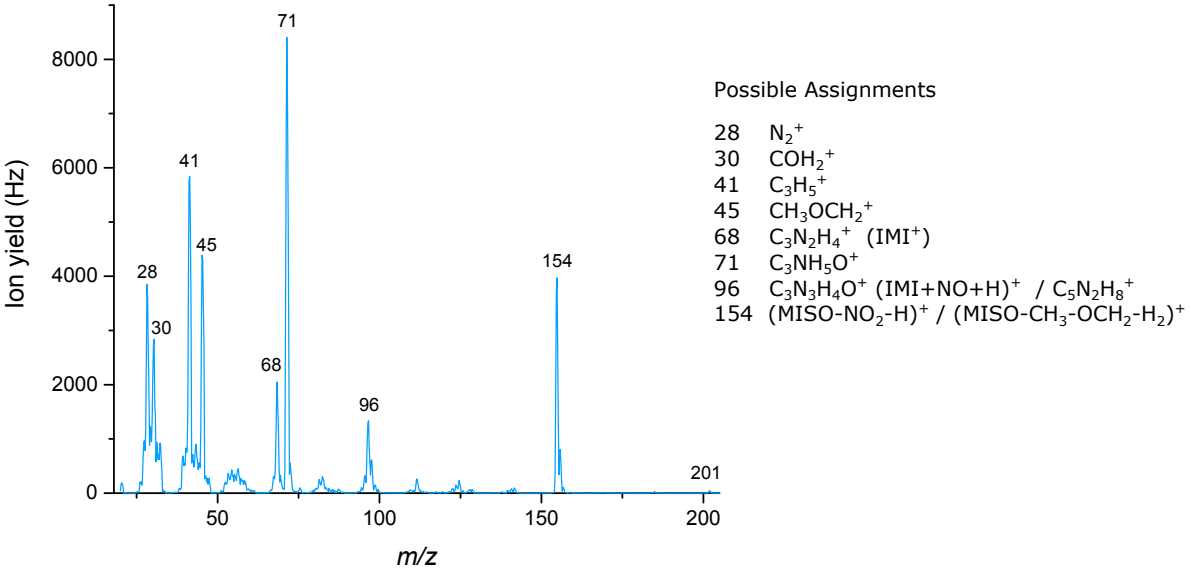

Figure 5.5: Cationic mass spectrum resulting from electron ionisation of misonidazole at incident electron energies of 70 eV and the possible assignment of fragments.

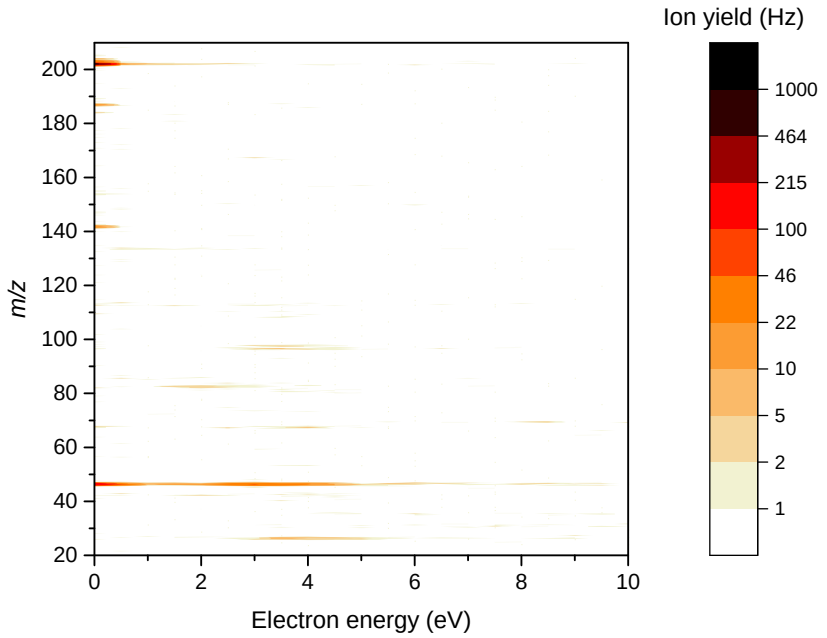

Figure 5.6: Intensity map of anions formed upon associative and dissociative electron attachment to misonidazole. The ion yields are shown on a logarithmic scale. The parent anion at $m/z = 201$ forms the dominant channel, followed by the NO_2^- anion.

My contribution to this study includes the experimental data taking, the analysis of this data and the preparation of the according figures in the paper. The interpretation of results was done by all authors together. Finally, I wrote the experimental setup part of the paper.

International Journal of
Molecular Sciences

MDPI

Article

Reactions in the Radiosensitizer Misonidazole Induced by Low-Energy (0–10 eV) Electrons

Rebecca Meißner [1,2], Linda Feketeová [3], Eugen Illenberger [1,4] and Stephan Denifl [1,*]

1 Institut für Ionenphysik und Angewandte Physik and Center for Molecular Biosciences Innsbruck, Leopold-Franzens Universität Innsbruck, Technikerstrasse 25, A-6020 Innsbruck, Austria
2 Atomic and Molecular Collisions Laboratory, CEFITEC, Department of Physics, Universidade NOVA de Lisboa, 2829-516 Caparica, Portugal
3 Université de Lyon; Université Claude Bernard Lyon1; Institut de Physique Nucléaire de Lyon, CNRS/IN2P3 UMR 5822, 69622 Villeurbanne CEDEX, France
4 Institut für Chemie und Biochemie-Physikalische und Theoretische Chemie, Freie Universität Berlin, Takustrasse 3, 14195 Berlin, Germany
* Correspondence: stephan.denifl@uibk.ac.at; Tel.: +43-(0)512-507-52662

Received: 27 June 2019; Accepted: 11 July 2019; Published: 16 July 2019

Abstract: Misonidazole (MISO) was considered as radiosensitizer for the treatment of hypoxic tumors. A prerequisite for entering a hypoxic cell is reduction of the drug, which may occur in the early physical-chemical stage of radiation damage. Here we study electron attachment to MISO and find that it very effectively captures low energy electrons to form the non-decomposed molecular anion. This associative attachment (AA) process is exclusively operative within a very narrow resonance right at threshold (zero electron energy). In addition, a variety of negatively charged fragments are observed in the electron energy range 0–10 eV arising from dissociative electron attachment (DEA) processes. The observed DEA reactions include single bond cleavages (formation of NO_2^-), multiple bond cleavages (excision of CN^-) as well as complex reactions associated with rearrangement in the transitory anion and formation of new molecules (loss of a neutral H_2O unit). While any of these AA and DEA processes represent a reduction of the MISO molecule, the radicals formed in the course of the DEA reactions may play an important role in the action of MISO as radiosensitizer inside the hypoxic cell. The present results may thus reveal details of the molecular description of the action of MISO in hypoxic cells.

Keywords: electron attachment; misonidazole; radiosensitizer; mass spectrometry; fragmentation; nitroimidazoles; reduction

1. Introduction

A variety of nitroimidazole derivatives have been under investigation for their potential use in cancer therapy [1,2]. Here we study free electron attachment to the gas phase nitroimidazolic derivative misonidazole (MISO) ($C_7H_{11}N_3O_4$; see Figure 1a for the molecular structure) which was clinically tested in trails as radiosensitizer for the treatment of hypoxic tumors [2]. Such tumors are characterized by a significant low oxygen state compared to the normal cell tissue. As radiosensitizer, MISO should be preferentially cytotoxic to hypoxic cells. The molecular mechanisms how radiosensitizers like MISO operate, have not been proven yet. Previously it was suggested that this cellular effect is only produced after reduction of the drug [3]. In cancer therapy, reduction of MISO is performed with zinc, ammonium, or by radiolysis by high-energy quanta (particles or photons in the MeV range). The subsequent action of radiosensitizers should ideally result in a selective death of the tumor cells without damage of healthy tissue [4–6]. In particular, within the complex processes which finally

lead to cell damage, reactions induced by low-energy electrons with kinetic energies between ~0 and 10 eV may play an important role in the early time window (<ps) after energy deposition [4–7]. This hypothesis comes from the fact that in the first step the action of high-energy quanta (photons or particles) with living cells removes electrons from the molecular network of the cell by various ionization mechanisms [8]. These ballistic secondary electrons are quickly slowed down and can initiate the reduction of a radiosensitizer as well as effective chemical reactions before they enter some stage of solvation and become a chemically inactive species. The estimated quantity is 10^4–10^5 secondary electrons per 1 MeV primary quantum [9]. In the very low energy domain (0–3 eV) and before reaching some stage of solvation, these ballistic secondary electrons can initiate chemical reactions via dissociative electron attachment (DEA) which lead to the formation of negatively charged fragment ions and radicals [10–14]. Due to their potentially high cross sections, it was believed that DEA reactions occurring at low energies (0–3 eV) within the ps time window after energy deposition are significant and decisive steps towards cell apoptosis [4–6].

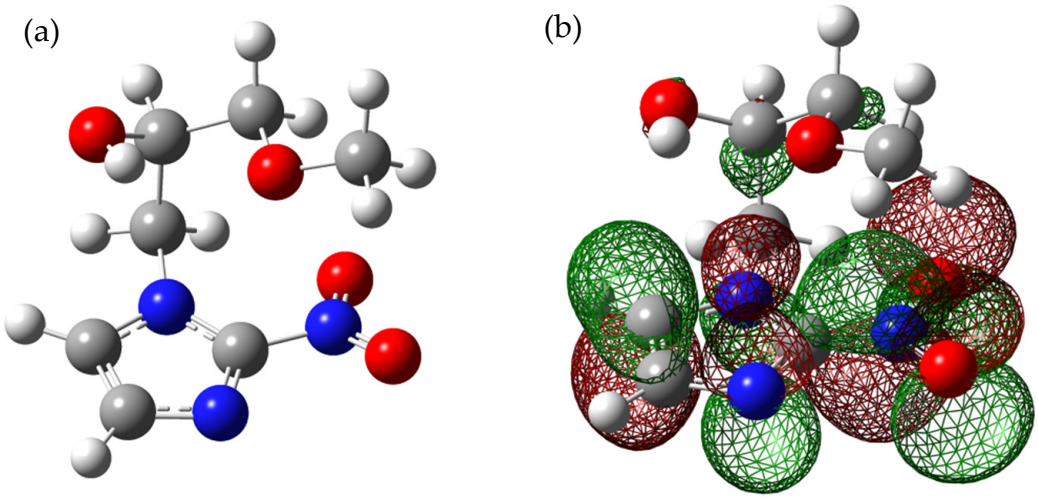

Figure 1. (**a**) Optimized molecular structure of misonidazole (MISO), (**b**) singly occupied molecular orbital of the MISO anion.

Radiation damage can involve any of the cell components like DNA, water, and/or proteins. Ionization of water leads to the formation of highly reactive OH radicals which may attack important cell components. It is estimated that damage of the genome in a living cell by high energy radiation is about one third direct and two third indirect [15]. Direct damage is related to the energy deposition directly in the DNA and closely bound water molecules. In contrast, indirect damage is caused by energy deposition in the nearer vicinity of DNA. Since this mainly involves ionization of water, indirect damage is mainly ascribed to the action of the above-mentioned OH radicals [16].

Previous studies showed that DEA can be an effective process in breaking bonds and hence generates radicals at electron energies considerably below typical bond dissociation energies [10–14]. Such behavior was also observed in DEA studies with radiosensitizers like modified nucleobases [5,6,17–20]. By modification of the native nucleobase by highly electron affinic side groups, an increase of the DEA cross section can be achieved. It is thus likely that in the course of radiotherapy treatment, radicals from the radiosensitizer damage the tumor cells. Therefore, for the characterization of a radiosensitizer it is of particular significance to know its response towards low-energy electrons.

As member of the class of 2-nitroimidazoles (the NO_2 group binds to the imidazole ring at the C2 position), MISO was previously tested in clinical trials as radiosensitizer for hypoxic tumors. Though considered to be a highly efficient radiosensitizer, the trials turned out to be unsuccessful due to the high neurotoxicity of MISO [21]. This side effect does not allow the application of the drug in the required doses. In order to gain knowledge on mechanisms of radiosensitizers on the molecular level upon irradiation, we have studied electron attachment to the MISO compound. As will be shown

below, MISO is in fact very effectively reduced by capturing low energy electrons. This proceeds via (a) formation of the intact molecular anion at very low energies (close to 0 eV) and (b) in the range 0–10 eV, by generating NO_2^- and a variety of further fragment anions via DEA thus revealing in detail the possible reduction processes. In addition, the radicals generated in the course of the DEA reactions are presumably relevant in the action of MISO as radiosensitizer inside the hypoxic cell.

2. Results and Discussion

2.1. General Features of Associative (AA) and Dissociative Electron Attachment (DEA) and Characterization of the Involved Resonances

The dominant process in electron attachment to MISO is the very effective formation of the non-decomposed parent anion which is exclusively formed within a very narrow resonance close to 0 eV (Figure 2). We further observe a large variety of negatively charged fragment ions generated within pronounced resonances, which are the result of dissociative electron attachment (DEA, Figures 3–5), among them the prominent DEA reaction yielding NO_2^- representing a simple (C–NO_2) bond cleavage (Figure 3a). Further DEA reactions involve multiple bond cleavages (simultaneous loss of a neutral NO_2 and a CH_2 unit) (Figure 3c), complex reactions associated with rearrangement in the transitory negative ion (TNI), followed by multiple bond cleavages and formation of new molecules (loss of a neutral H_2O molecule) (Figure 4a), excision of a CN^- and OCN^- unit (Figure 4b,c) and formation of the dehydrogenated nitroimidazole anion (Figure 5a). All these DEA reactions are observed in the electron energy range 0–10 eV and at significant lower cross sections compared to the associative attachment process generating the parent anion.

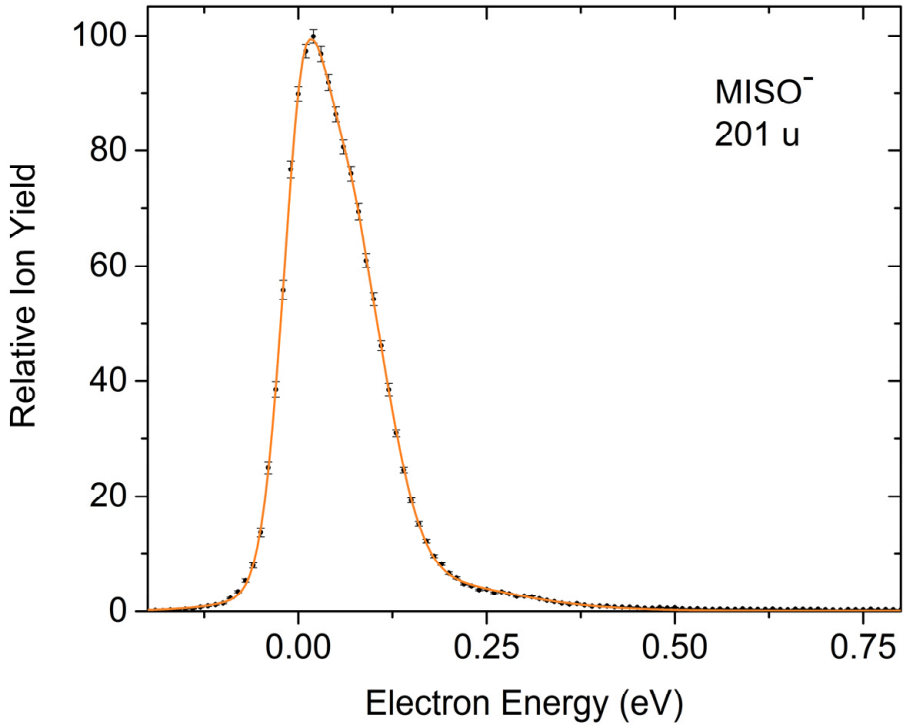

Figure 2. Relative ion yield for the associative attachment (AA) process generating the non-decomposed molecular anion.

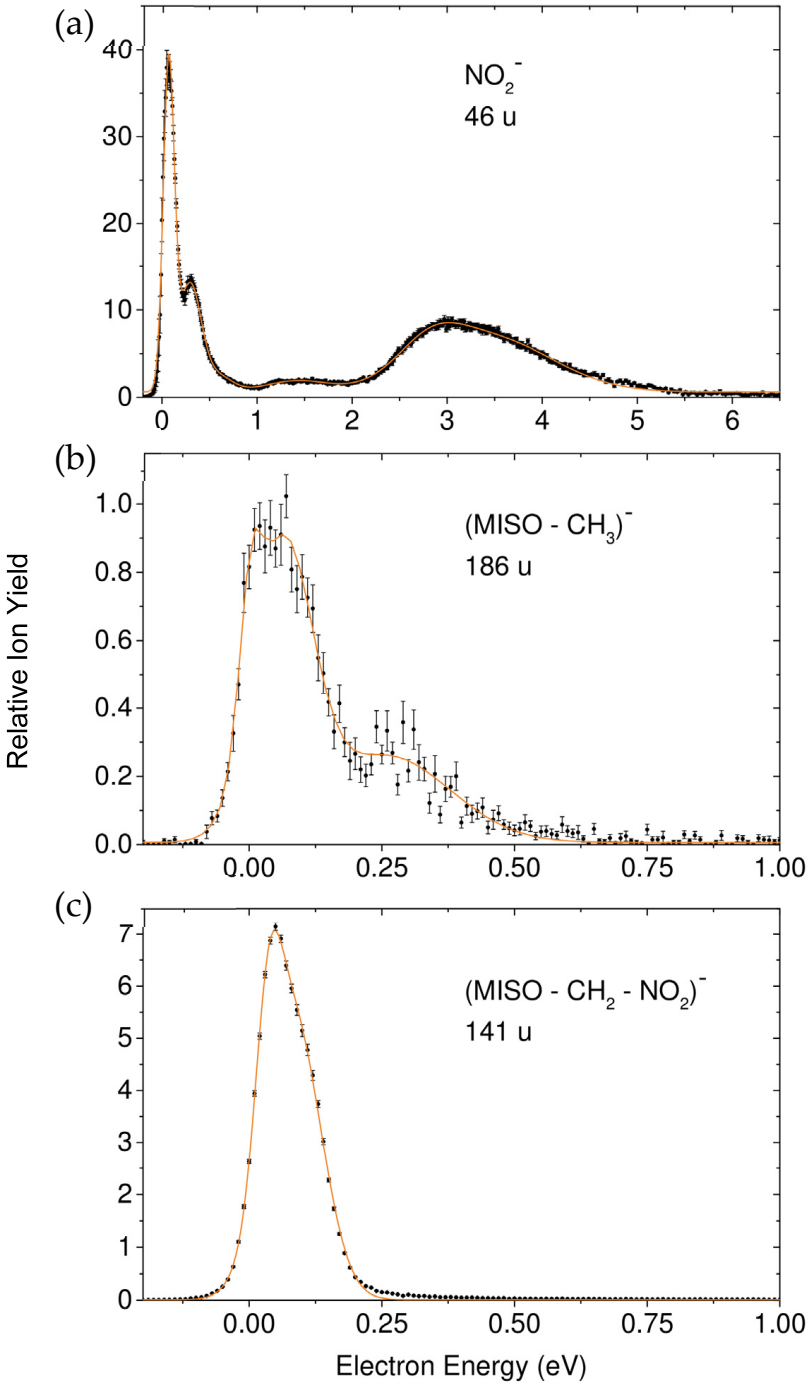

Figure 3. Relative ion yields for the dissociative electron attachment (DEA) reactions generating the NO_2^- fragment ion (**a**), the fragment ion arising from the loss of a neutral CH_3 unit $(M - CH_3)^-$ (**b**), and the fragment ion due to the loss of the two neutral units CH_2 and NO_2 $(M - CH_2 - NO_2)^-$ (**c**).

The formation of a non-decomposed parent anion by capture of a free electron in the gas phase under collision free conditions requires that the excess energy deposited by the attachment (comprised of the initial kinetic energy of the incoming electron and the electron affinity of the molecule) is effectively dispersed over the vibrational degrees of freedom in the TNI. In such case, autodetachment is delayed and the resulting lifetimes are in the μs regime and longer, which allow observation by mass spectrometry [13]. MISO has a positive electron affinity of 1.33 eV [22]. The Singly Occupied Molecular Orbital (SOMO) of the MISO anion is shown in Figure 1b and clearly indicates the delocalization of the excess electron over the whole nitroimidazole group. In contrast, resonant (dissociative) electron

attachment beyond 0 eV is usually described as accommodation of the extra electron into one of the normally unoccupied molecular (valence) orbitals (MOs) thus forming the temporary negative ion (TNI) or synonymously, the resonance which then decomposes. In terms of localized Born–Oppenheimer (BO) potential energy surfaces, DEA is then described as a vertical transition between the potential energy surface of the neutral and that of the anion followed by dissociation into a stable fragment anion and the neutral counterpart [10,13]. It should be emphasized that AA close to 0 eV is a non-BO phenomenon which cannot be described as a transition between localized potential energy surfaces.

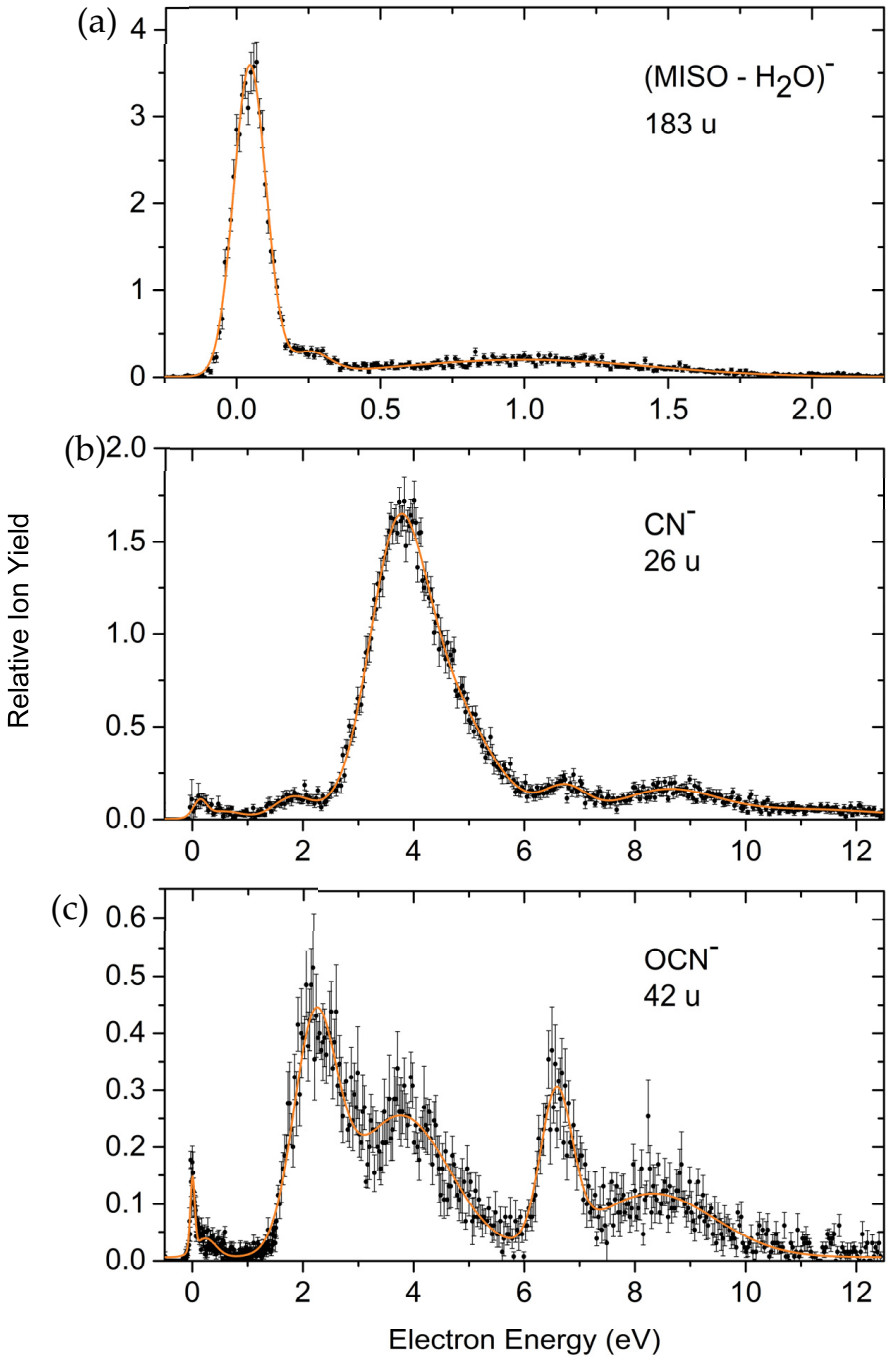

Figure 4. Relative ion yields for the ion appearing from the loss of a neutral water unit $(M - H_2O)^-$ (**a**), relative cross section for the excision of CN^- (**b**) and the excision of OCN^- (**c**).

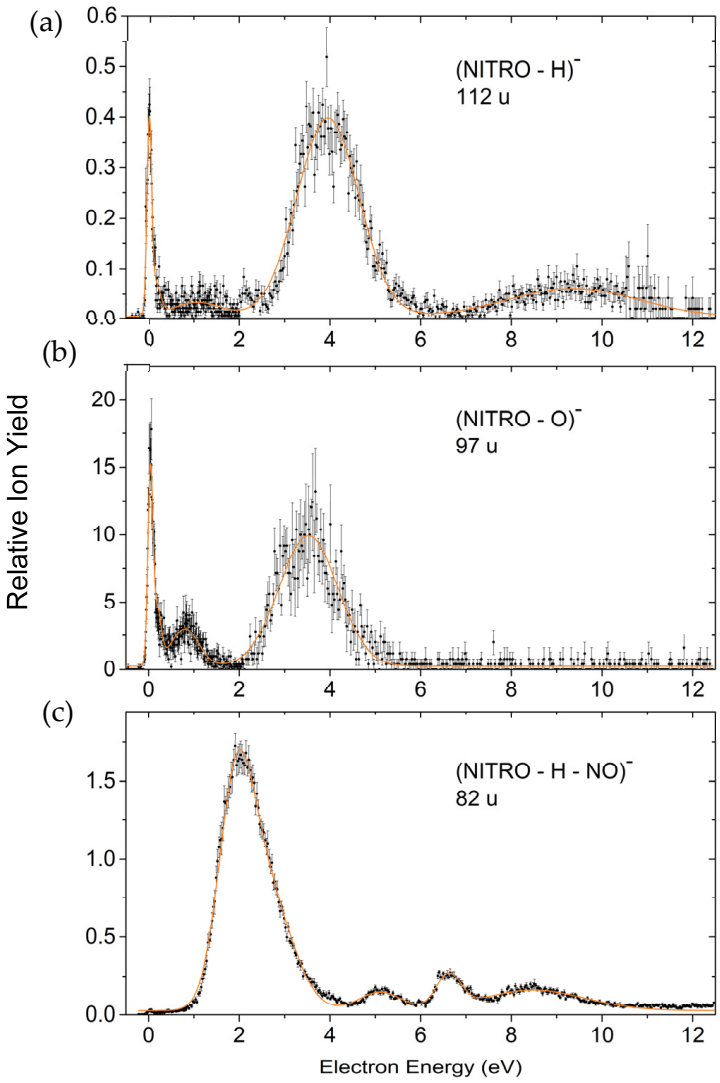

Figure 5. Relative ion yields for the formation of the dehydrogenated closed shell nitroimidazole anion (**a**), the nitroimidazole anion subjected to the additional loss of a neutral O unit (**b**), and the nitroimidazole anion subjected to the additional loss of a neutral NO unit (**c**).

2.1.1. Formation of the Non-Decomposed Parent Anion

As mentioned above, the intact molecular anion of MISO is the most abundant anion observed in the present experiment. Though we did not explicitly determine the absolute cross section for this AA reaction, we estimate from the relative ion yields recorded at the corresponding partial pressures that the cross section has a similar order of magnitude as the well-known electron scavengers like SF_6 (formation of SF_6^-) [23] and CCl_4 (Cl^- formation) [24]. SF_6 has one of the highest electron attachment cross sections known [23]. One of the main reasons for this behavior is the fact that all DEA channels are endothermic and therefore not available at electron energies close to 0 eV. Together with the high symmetry of the molecule, the conditions for the formation of a metastable parent anion are fulfilled, where spontaneous autodetachment is the only competitive channel. Additionally, many other examples of molecules creating a metastable parent anion have been already reported. Their ion signal is usually characterized by an exclusive narrow peak at the electron energy of ~0 eV [13,25,26] or in combination with another peak at slightly higher electron energies [27–29]. The only remarkable exception is the C_{60}^- ion yield formed upon electron attachment to C_{60} [30,31]. This anion is formed over a wide range of electron energies extending up to about 12 eV. C_{60} is of high symmetry and the

binding energies for each C atom are equal. This provides ideal conditions for delayed autodetachment and the absence of DEA [30,31].

In contrast, MISO is of low symmetry but the appreciable number of 69 vibrational degrees of freedom apparently provides an effective means for energy redistribution making the observation of an intense parent anion possible. We note that MISO exhibits a similar behavior towards attachment of a single electron like the 5-nitroimidazolic molecule nimorazole. The latter compound is utilized as radiosensitizer for the treatment of pharyngeal and supra-glottic carcinoma in Danish radiotherapy centers [1]. A recent electron attachment study showed that the parent anion is the most abundant anion for nimorazole, and DEA plays a minor role [32]. Due to its morpholine ring linked by a short hydrocarbon chain to the nitroimidazole moiety, even more excess energy could be stored than in the case of MISO. Therefore, one may be tempted to conclude that just a large number of vibrational degrees is required to cause sufficient stabilization of the transient negative anion. However, in that context we also mention that in a recent study by our laboratory with the considerable smaller methylated nitroimidazoles 1-methyl-4-nitroimidazole and 1-methyl-5-nitroimidazole (36 vibrational degrees of freedom) the non decomposed molecular anion was also observed in both compounds appearing at a narrow resonance right at threshold [33,34]. Since for the non-methylated nitroimidazoles no parent anion is observable on μs-timescales, the replacement of the hydrogen at the N1 position of the imidazole ring by the methyl group closes DEA channels at threshold and allows the stabilization of the molecular anion to mass spectrometric time scales.

2.1.2. Dissociative Electron Attachment (DEA)

The ion yields due to the different dissociative attachment reactions appear, depending on the ion under observation, within resonances extending from threshold (0 eV) to about 10 eV (Figures 3–5). The evolution of these resonances finally results in simple bond cleavages (formation of NO_2^-) but also much more complex reactions in the TNI finally leading to the loss of a neutral H_2O unit, excision of CN^-, etc.

In cases when DEA is operative already at threshold, we have to assume that vibrational Feshbach resonances (VFRs) are involved. This is in particular the case in the DEA reaction leading to NO_2^- which shows two overlapping narrow peaks at very low electron energies (vide infra).

Formation of NO_2^-, Loss of the Neutral Unit CH_3, and Loss of the Two Neutral Units NO_2 + CH_2

Figure 3 presents the ion yields of the corresponding DEA reactions. NO_2^- (Figure 3a) is the dominant DEA product representing the cleavage of a C–NO_2 bond

$$e^- + MISO \rightarrow MISO^{\#-} \rightarrow (MISO - NO_2) + NO_2^-, \quad (1)$$

with $MISO^{\#-}$ as the transitory negative ion of MISO formed upon electron attachment.

The NO_2^- fragment anion is formed via two narrow and overlapping features close to threshold, a further resonance centered around 1.5 eV and a broad and unstructured feature in the energy range between 2.5 and 4.5 eV. We assign the resonances off 0 eV as shape resonances (with possible contributions of low-lying core excited resonances in the broad feature peaking at ~3 eV [35]) and the narrow features close to 0 eV as vibrational Feshbach resonances (VFRs) in analogy to the situation previously described in DEA to nitroimidazoles [33,34]. Such VFRs can in fact couple to dissociative valence configurations, thereby acting as effective doorways for DEA [36].

Our quantum chemical calculations on the thermodynamics of NO_2^- formation upon DEA to MISO indeed indicate a more complex DEA mechanism. At first, we calculated the free reaction energy for the DEA Reaction (1), where a simple bond cleavage reaction is assumed. In this case, the reaction is endothermic with a free energy of +0.339 eV. Since the ion yield of NO_2^- is observed already at threshold, such simple bond cleavage reaction does not lead to the observed threshold peak. Therefore, we computationally investigated rearrangement reactions and found that NO_2 loss with H transfer to

C2 position of the imidazole moiety (see Figure 6) gives an exothermic reaction with a free energy of −0.341 eV.

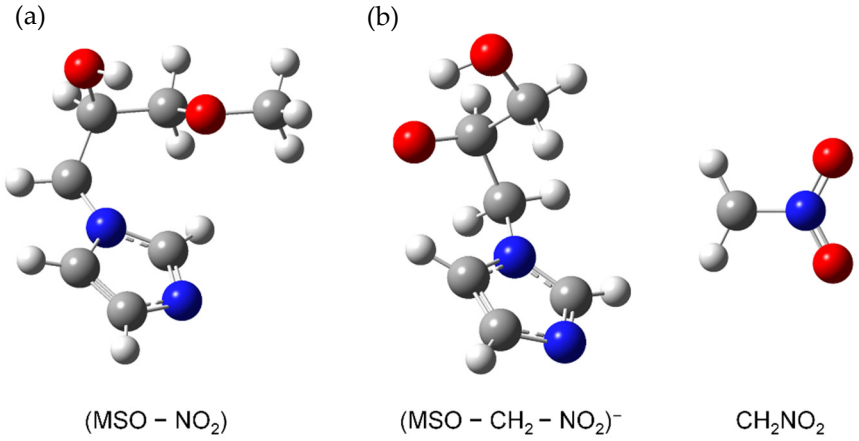

Figure 6. (**a**) Calculated structure of the neutral product of the DEA Reaction (1). (**b**) Calculated structure of the charged and neutral products of the DEA Reaction (3).

For the NO_2^- peaks at the electron energy of about 1.5 and 3 eV a single bond cleavage is energetically possible. We note that the ion yield is similar to the NO_2^- ion yield formed upon DEA to nitroimidazole [33]. Kossoski and Varella performed theoretical calculations of low-energy resonances in 4- and 5-nitroimidazole (NI) and 1-methyl-nitroimidazoles [37]. They suggest an indirect dissociation mechanism for the NO_2^- fragment anion, where coupling of π* states and the repulsive σ^*_{CN} state occurs. By the analogy of the ion yield we may therefore assume also an indirect dissociation mechanism for MISO, which involves the coupling of the π* state and the repulsive σ^*_{CN} state.

Figure 3b shows the fragment anion which is formed by the loss of a neutral CH_3 unit according to

$$e^- + MISO \rightarrow MISO^{\#-} \rightarrow (MISO - CH_3)^- + CH_3, \quad (2)$$

and hence the cleavage of the O–CH_3 bond with the excess charge finally localized on the large imidazole containing unit. This negatively charged fragment is only observed within the two very narrow features close to threshold assigned as VFRs, indicating that the evolution of the shape resonances leading to NO_2^- does not result in Reaction (2).

This observation mirrors the possibility to distribute the excess energy which is different for the two DEA Reactions (1) and (2). The excess energy in a DEA reaction amounts to the electron energy above the thermodynamic threshold energy of the respective process and is distributed among the formed fragments.

In Reaction (1), the light fragment ion NO_2^- is detected while the excess energy in the large neutral fragment (M–NO_2) may lead to further and even multiple decompositions. In contrast, in Reaction (2) from stoichiometry we know that the neutral fragment is CH_3 (provided that further decompositions can be excluded) but for the large ionic fragment the ability to carry excess energy is limited by the decomposition threshold with respect to both, detachment of the extra charge and dissociation. This fact apparently restricts the observation of the large ionic fragment to the very low energy domain.

Figure 3c finally shows the yield for the ionic fragment with mass 141 u, formed in the DEA reaction formally associated with the loss of CH_2 + NO_2.

$$e^- + MISO \rightarrow MISO^{\#-} \rightarrow (MISO - CH_2 - NO_2)^- + CH_2NO_2. \quad (3)$$

The corresponding ion yield shows only one asymmetric resonance feature close to threshold, which is in contrast to Reactions (1) and (2), where the related ion yields close to threshold are characterized by a structure with two distinct peaks. We note that the loss of a methyl group and the

NO_2 would only require two simple bond cleavages. However, the loss of CH_2 as observed in the present experiment is only possible by a rearrangement reaction. We computationally investigated various rearrangement reactions and found as lowest possible free reaction energy a value of +0.11 eV, which involves migration of the hydrogen to the C2 carbon site and formation of neutral CH_2NO_2 (see Figure 6). Experimentally, a peak maximum at 0.05 ± 0.01 eV is obtained (the stated error corresponds to the step width of the electron energy scan), which is slightly below the predicted onset. Therefore, this ion yield may be interpreted as hot band transition which can play a significant role in DEA in particular at elevated temperatures as is the case in the present experiment. The considerable intensity of such hot band transitions is due to the peculiarities of DEA like increasing cross section with decreasing electron energy, etc. [38,39].

Loss of Neutral H_2O and Excision of the Pseudohalogens CN^- and OCN^-

The ion yields due to the rather complex DEA reactions resulting in the loss of a neutral water unit and the excision of the ions CN^- and OCN^- are presented in Figure 4. Formation of a neutral water unit following electron attachment to the target compound (Figure 4a) may occur at different sites of the target compound and proposing a detailed reaction mechanism would be rather speculative. A likely site is the linear chain outside the imidazole unit at the [-H_2C-(CH-OH)-CH_2-] unit. In this case, the reaction would require the cleavage of a C–H and a C–OH bond followed by the formation of the H_2O molecule. As is obvious from Figure 4a, this reaction is already operative at threshold (zero electron energy) and additionally within the weak resonances at around 0.25 and 1 eV. We note that the loss of a water molecule upon DEA turned out to be an isomer selective process for NIs [40]. The DEA reaction with formation of H_2O was only abundant for the 2-NI isomer, while for the 4-NI molecule this channel was very weak. Indeed, a pathway for H_2O loss was found during the computational exploration of the relevant potential energy surfaces for the 2-NI isomer. The found reaction was exothermic in agreement with the experimental data. The present results also indicate an exothermic reaction for the loss of water. However, the abundance of $(MISO - H_2O)^-$ is rather minor, which may be explained by the efficient stabilization of the MISO parent anion in competition to DEA reaction. In contrast, for 2-NI no parent anion was observable within the detection limit of the experimental apparatus.

Figure 4b represents the ion yield due to the excision of CN^- and Figure 4c that of OCN^- formation. Both CN and OCN are well known pseudohalogens having electron affinities (EAs) exceeding even those of the halogen atoms (EA (CN) = 3.86 eV, EA (OCN) = 3.61 eV [41]). On the other hand, a large EA does not necessarily lead to a high cross section for the formation of CN^- via DEA. For example, CN^- formation from compounds like (amino)acetonitrile or benzonitrile [42–44] was comparatively weak due to the underlying decomposition mechanism. Although it is also formed for these compounds via a single C–CN bond cleavage, the dissociation mechanism was suggested to be indirect in the way that the excess electron initially resides in a π^* (CN) antibonding MO and decomposition into CN^- requires transfer of the available energy from CN into the C–CN coordinate (vibrational predissociation).

Both pseudohalogenide ions appear within resonance features above 2 eV. It is likely that the C–NO_2 site is involved in the corresponding DEA reaction. While there is no established thermochemical data available for the present system it should be mentioned that DEA to MISO leading to CN^- can be accompanied by a more or less complete degradation of the entire target molecule as, besides CN^-, stable neutral counterparts like N_2, CO_2 and hydrocarbons can be formed. It has in fact been demonstrated in DEA to the comparably smaller system acetamide, that excision of CN^- observed within a resonance at 2 eV is accompanied by a complete degradation of the entire target molecule [45]. Similar complex decomposition processes are likely accompanied with the formation of OCN^-, as shown previously for the pyrimidine nucleobases [46].

Formation of Nitroimidazolic Anions

Figure 5 finally presents ion yields of three DEA reactions associated with the cleavage of the N–C bond and hence formation of nitroimidazolic anions $(C_3H_2N_3O_2)^-$, $(C_3H_3N_3O)^-$ and $(C_3H_2N_2O)^-$. More precisely, Figure 5a shows the ion yield recorded at 112 u which we assign to the dehydrogenated closed shell anion of NI ($(C_3H_2N_3O_2)^-$), a prominent DEA product from the NIs previously studied in our laboratory [33,34]. The ion yield recorded at 96 u, Figure 5b, corresponds to a further loss of a neutral O unit ($(C_3H_3N_3O)^-$) and that recorded at 82 u, Figure 5c, to a loss of a neutral NO unit from the (dehydrogenated) NI anion ($(C_3H_2N_2O)^-$). While this could lead to anions with an imidazole structure, we cannot exclude that in the course of these DEA reactions the cyclic structure deteriorates.

3. Materials and Methods

3.1. Experiment

The electron attachment experiments were performed with a crossed-beam experiment recently described in [32]. The setup comprises a molecular beam source consisting of an oven with capillary with 1 mm inner diameter, a hemispherical electron monochromator (HEM), a quadrupole mass analyzer, and a channel electron multiplier with pulse counting system. Since only gas phase studies can be conducted by mass spectrometric means, the crystalline MISO was evaporated in the oven at around 75 °C. The resulting pressure in the vacuum chamber amounts to 5×10^{-7} mbar. The effusive beam crosses the electron beam in the interaction region at the end of the HEM. The energy resolution is a compromise over a high electron current and was set to about 100 meV for the current study. The resolution is determined by the full width at half maximum from the well known sharp 0 eV resonance of SF_6^- (AA) and Cl^- from CCl_4 (DEA). Those ion yield curves additionally serve for calibration of the energy scale. The electron current is monitored by a Faraday cup detector placed behind the interaction region to ensure stable conditions. After the anions were formed by electron attachment, they were extracted by a weak electric field between HEM and quadrupole. Subsequently, they were detected and recorded by a preamplifier and detection unit [34].

The misonidazole sample was purchased from Toronto Research Chemicals Canada with a stated purity of 98% and was used as received.

The utilization of the HEM enabled stable electron beam conditions in the measured electron energy range. Therefore, the intensities of the peaks measured for a mass selected anion are comparable. The only exception occurs for peaks at 0 eV electron energy, where the height of the peaks is underestimated due to the experimental limit in the production of electrons with energies approaching 0 eV as well as the finite energy resolution of the electron beam [24]. The ion yields of the mass selected anions shown in Figures 2–5 were recorded at identical conditions (same pressure, electron current etc.) and are presented on a relative scale. However, they were not corrected by the mass transmission of the quadrupole mass analyzer and detection efficiency of the channeltron. This leads to an error in the comparison of relative ion intensities, as discussed in [32]. We further note that for the comparison of the $MISO^-$ anion yield with the ion yields from SF_6 and CCl_4 (see Section 2.1.1.) an additional error in the determination of the corresponding partial pressures in the chamber arises, see [32].

3.2. Calculations

Quantum chemical calculations employing the density functional M062x [47,48] were carried out to calculate free energies of reactions, ΔG. The thermodynamic threshold for a DEA reaction, considering the precursor molecule M and a release of a neutral fragment X, can be expressed by $\Delta G([M - X]^-) = DE(M–X)–EA(M - X)$, where DE(M–X) is the bond dissociation energy and EA(M – X) is the electron affinity of the corresponding fragment. The threshold energy for the experimental observation of $[M - X]^-$ in electron attachment experiments coincides with $\Delta G([M - X]^-)$ if the fragments are formed with no excess energy. For the MISO we used the lowest structure reported previously [22]. All structures where optimized at the M062x/6-311+G(d,p) level of theory and basis set with the

Gaussian-09D01 programme package [49]. Frequencies were calculated in all cases to confirm that the structures are local minima on the potential energy surface and not the transition states.

4. Conclusions

Free electron attachment to the radiosensitizer misonidazole (MISO) in the gas phase predominantly creates the non-decomposed anion which is exclusively formed from a very narrow resonance near zero electron energy. In addition, a large variety of fragment anions are observed from resonance features in the energy range from 0 to 10 eV. These DEA reactions involve simple bond cleavages (formation of NO_2^-, loss of CH_3, etc.) and considerable complex reactions (loss of a neutral water unit, excision of the pseudohalogenide ions CN^- and OCN^-). All these electron attachment processes represent initial reduction of the radiosensitizer, which is necessary for its uptake by a hypoxic tumor cell. The present results hence reveal details of the intrinsic reduction process in MISO. In addition, the various neutral radicals formed along the DEA reactions may represent important components in the description of the molecular mechanisms how the radiosensitizer MISO acts within a hypoxic cell. While the present results reveal intrinsic properties of gas phase MISO, the question is on the relevance of the present results for the action of MISO as radiosensitizer in vivo. Extended electron attachment studies to molecules embedded in clusters and in the condensed phase demonstrated [32,50] that in bound molecules, the intrinsic electron attachment properties are preserved. In other words, electron attachment to bound molecules can still be pictured on a molecular site, i.e., attachment to an individual molecule, which is coupled to a particular environment. In light of that, we conclude that the present results can help to reveal details of the molecular mechanisms, how MISO acts as radiosensitizer in hypoxic tumor cells. Future studies with misonidazole in water clusters may show which reactions observed here will sustain in solution, since energy transfer to the water medium will likely modify the dissociation processes.

Author Contributions: Measurements and data analysis, R.M.; quantum chemical calculations, L.F.; preparation of manuscript, R.M., L.F., E.I. and S.D.

Funding: This work was supported by the FWF, Vienna (P30332). R.M. acknowledges the Portuguese National Funding Agency FCT-MCTES through PD/BD/114452/2016 and research grant UID/FIS/00068/2019 (CEFITEC). This work was also supported by the Radiation Biology and Biophysics Doctoral Training Programme (RaBBiT, PD/00193/2012) and UID/Multi/04378/2013 (UCIBIO). L.F. is grateful to the funding support of the LABEX Lyon Institute of Origins (ANR-10-LABX-0066) of the Université de Lyon for its financial support within the program "Investissements d'Avenir" (ANR-11-IDEX-0007) of the French government operated by the National Research Agency (ANR).

Acknowledgments: The crucial computing support from CCIN2P3 (France) is gratefully acknowledged.

Conflicts of Interest: The authors declare no conflict of interest.

Abbreviations

MISO	Misonidazole
NI	Nitroimidazole
AA	Associative attachment
DEA	Dissociative electron attachment
DNA	Deoxyribonucleic acid
SOMO	Singly occupied molecular orbital
MO	Molecular orbital
BO	Born–Oppenheimer
TNI	Transitory negative ion
VFR	Vibrational Feshbach resonance
EA	Electron affinity
HEM	Hemispherical electron monochromator

References

1. Overgaard, J.; Hansen, H.S.; Overgaard, M.; Bastholt, L.; Berthelsen, A.; Specht, L.; Lindeløv, B.; Jørgensen, K. ARandomized Double-Blind Phase IIIStudy of Nimorazole as a Hypoxic Radiosensitizer of Primary Radiotherapy in Supraglottic Larynx Pharynx, C.a.r.c.i.n.o.m.a. Results of the Danish Head Neck Cancer Study (DAHANCA) Protocol, 5.-8.5. *Radiother. Oncol.* **1998**, *46*, 135–146. [CrossRef]
2. Overgaard, J. Hypoxic Modification of Radiotherapy in Squamous Cell Carcinoma of the Head and Neck—A Systematic Review and Meta-Analysis. *Radiother. Oncol.* **2011**, *100*, 22–32. [CrossRef] [PubMed]
3. Edwards, D.I. Nitroimidazole drugs—Action and Resistance Mechanisms I. Mechanisms of Action. *J. Antimicrob. Chemother.* **1993**, *31*, 9–20. [CrossRef] [PubMed]
4. Park, Y.; Polska, K.; Rak, J.; Wagner, J.R.; Sanche, L. Fundamental Mechanisms of DNA Radiosensitization: Damage Induced by Low-Energy Electrons in Brominated Oligonucleotide Trimers. *J. Phys. Chem. B* **2012**, *116*, 9676–9682. [CrossRef] [PubMed]
5. Baccarelli, I.; Bald, I.; Gianturco, F.A.; Illenberger, E.; Kopyra, J. Electron-Induced Damage of DNA and Its Components: Experiments and Theoretical Models. *J. Phys. Rep.* **2011**, *508*, 1–44. [CrossRef]
6. Abdoul-Carime, H.; Huels, M.A.; Brüning, F.; Illenberger, E.; Sanche, L. Dissociative Electron Attachment to Gas-Phase 5-Bromouracil. *J. Chem. Phys.* **2000**, *113*, 2517–2521. [CrossRef]
7. Boudaïfffa, B.; Cloutier, P.; Hunting, D.; Huels, M.A.; Sanche, L. Resonant Formation of DNA Strand Breaks by Low-Energy (3 to 20 eV) Electrons. *Science* **2000**, *287*, 1658–1660.
8. Ren, X.G.; Al Maalouf, E.J.; Dorn, A.; Denifl, S. Direct Evidence of two Interatomic Relaxation Mechanisms in Argon Dimers Ionized by Electron Impact. *Nat. Commun.* **2016**, *7*, 11093. [CrossRef]
9. Zimbrick, J.D. Radiation Chemistry and the Radiation Research Society: A History from the Beginning. *Radiat. Res.* **2002**, *158*, 127–140. [CrossRef]
10. Illenberger, E. Electron Attachment Processes in Molecules and Molecular Aggregates. In *Gaseous Molecular Ions. An Introduction to Elementary Processes Induced by Ionization*; Baumgärtel, H., Franck, E.U., Grünbein, W., Eds.; Steinkopff Verlag, Darmstadt/Springer-Verlag: New York, NY, USA, 1992; Volume 2, pp. 291–337.
11. Hotop, H.; Ruf, M.-W.; Allan, M.; Fabrikant, I. Resonance and Threshold Phenomena in Low-Energy Electron Collisions with Molecules and Clusters. *Adv. At. Mol. Opt. Phys.* **2003**, *49*, 85–216.
12. Christophorou, L.G.; Olthoff, J.K. Fundamental Electron-Molecule Interactions and Their Technological Significance. In *Fundamental Electron Interactions with Plasma Processing Gases*; Kluwer Academic: New York, NY, USA, 2004; pp. 1–59.
13. Langer, J.; Balog, R.; Stano, M.; Abdoul-Carime, H.; Illenberger, E. Low Energy Electron Driven Reactions in Free and Bound Molecules: From Unimolecular Processes in the Gas Phase to Complex Reactions in a Condensed Environment. *Int. J. Mass Spectrom.* **2004**, *233*, 267–291.
14. Gorfinkiel, J.; Ptasinska, S. Electron Scattering from Molecules and Molecular Aggregates of Biological Relevance. *J. Phys. B At. Mol. Opt. Phys.* **2017**, *50*, 182001. [CrossRef]
15. Michael, B.D.; O´Neill, P.A. A Sting in the Tail of Electron Tracks. *Science* **2002**, *287*, 1603–1606. [CrossRef] [PubMed]
16. von Sonntag, C. Formation of Reactive Free Radicals in an Aqueous Environment. In *Free Radical Induced DNA Damage and Its Repair*; Springer-Verlag: Berlin, Germany, 2006; pp. 7–46.
17. Ferreira da Silva, F.; do, N.; Varella, M.T.; Jones, N.C.; Vrønnin Hoffmann, S.; Denifl, S.; Bald, I.; Kopyra, J. Electron-Induced Reactions in 3-Bromopyruvic Acid. *Chem. Eur. J.* **2019**, *25*, 5498–5506. [CrossRef] [PubMed]
18. Schürmann, R.; Tanzer, K.; Dąbkowska, I.; Denifl, S.; Bald, I. Stability of the Parent Anion of the Potential Radiosensitizer 8-Bromoadenine Formed by Low-Energy (<3 eV) Electron Attachment. *J. Phys. Chem. B* **2017**, *121*, 5730–5734.
19. Meißner, R.; Makurat, S.; Kozak, W.; Limão-Vieira, P.; Rak, J.; Denifl, S. Electron-Induced Dissociation of the Potential Radiosensitizer 5-Selenocyanato-2′-deoxyuridine. *J. Phys. Chem. B* **2019**, *123*, 1274–1282. [CrossRef] [PubMed]
20. Ameixa, J.; Arthur-Baidoo, E.; Meißner, R.; Makurat, S.; Kozak, W.; Butowska, K.; Ferreira da Silva, F.; Rak, J.; Denifl, S. Low-energy Electron-Induced Decomposition of 5-trifluoromethanesulfonyl-uracil: A Potential Radiosensitizer. *J. Chem. Phys.* **2018**, *149*, 164307. [CrossRef]
21. Overgaard, J. Hypoxic Radiosensitization: Adored and Ignored. *J. Clin. Oncol.* **2007**, *25*, 4066–4074. [CrossRef]

22. Feketeová, L.; Albright, A.L.; Sørensen, B.S.; Horsman, M.R.; White, J.; O'Hair, R.A.J.; Bassler, N. Formation of Radical Anions of Radiosensitizers and Related Model Compounds via Electrospray Ionization. *Int. J. Mass Spectrom.* **2014**, *365–366*, 56–63. [CrossRef]
23. Klar, D.; Ruf, M.-W.; Hotop, H. Attachment of Electrons to Molecules at meV Resolution. *Aust. J. Phys.* **1992**, *45*, 263–291. [CrossRef]
24. Klar, D.; Ruf, M.-W.; Hotop, H. Dissociative Electron Attachment to CCl_4 Molecules at Low Electron Energies with meV Resolution. *Int. J. Mass Spectrom.* **2001**, *205*, 93–110. [CrossRef]
25. Sulzer, P.; Rondino, F.; Ptasinska, S.; Illenberger, E.; Märk, T.D.; Scheier, P. Probing Trinitrotoluene (TNT) by Low-Energy Electrons: Strong Fragmentation Following Attachment of Electrons Near 0 eV. *Int. J. Mass Spectrom.* **2008**, *271*, 149–153. [CrossRef]
26. Sulzer, P.; Mauracher, A.; Denifl, S.; Probst, M.; Märk, T.D.; Scheier, P.; Illenberger, E. Probing Di-Nitrobenzene by Low Energy Electrons Identification of Isomers via Resonances in Dissociative Electron Attachment. *Int. J. Mass Spectrom.* **2007**, *266*, 138–148. [CrossRef]
27. Pshenichnyuk, S.A.; Vorob'ev, A.S.; Asfandiarov, N.L.; Modelli, A. Molecular Anion Formation in 9,10-anthraquinone: Dependence of the Electron Detachment Rate on Temperature and Incident Electron Energy. *J. Chem. Phys.* **2010**, *132*, 244313. [CrossRef] [PubMed]
28. Khvostenko, O.G.; Shchukin, P.V.; Tuimedov, G.M.; Muftakhov, M.V.; Tseplin, E.E.; Tseplina, S.N.; Mazunov, V.A. Negative Ion Mass Spectrum of the Resonance Electron Capture by Molecules of p-Benzoquinone. *Int. J. Mass Spectrom.* **2008**, *273*, 69–77. [CrossRef]
29. Ómarsson, B.; Ingólfsson, O. Stabilization, Fragmentation and Rearrangement Reactions in Low-Energy Electron Interaction with Tetrafluoro-Para-Benzoquinone: A Combined Theoretical and Experimental Study. *Phys. Chem. Chem. Phys.* **2013**, *15*, 16758. [CrossRef]
30. Matejcik, S.; Märk, T.D.; Spanel, P.; Smith, D.; Jaffke, T.; Illenberger, E. Formation and Decay of C_{60}^- Following Free-Electron Capture by C_{60}. *J. Chem. Phys.* **1995**, *102*, 2516–2521. [CrossRef]
31. Ptasińska, S.; Echt, O.; Denifl, S.; Stano, M.; Sulzer, P.; Zappa, F.; Scheier, P.; Märk, T.D. Electron Attachment to Higher Fullerenes and to $Sc_3N@C_{80}$. *J. Phys. Chem. A* **2006**, *110*, 8451–8456. [CrossRef]
32. Meißner, R.; Kočišek, J.; Feketeová, L.; Fedor, J.; Fárník, M.; Limão-Vieira, P.; Illenberger, E.; Denifl, S. Low-Energy Electrons Transform the Nimorazole Molecule into a Radiosensitiser. *Nat. Commun.* **2019**, *10*, 2388. [CrossRef]
33. Tanzer, K.; Feketeová, L.; Puschnigg, B.; Scheier, P.; Illenberger, E.; Denifl, S. Reactions in Nitroimidazole Triggered by Low-Energy (0–2 eV) Electrons: Methylation at N1-H Completely Blocks Reactivity. *Angew. Chem. Int. Ed. Engl.* **2014**, *53*, 12240–12243. [CrossRef]
34. Tanzer, K.; Feketeová, L.; Puschnigg, B.; Scheier, P.; Illenberger, E.; Denifl, S. Reactions in Nitroimidazole and Methylnitroimidazole Triggerd by Low Energy (0–8 eV) Electrons. *J. Phys. Chem. A* **2015**, *119*, 6668–6675. [CrossRef] [PubMed]
35. Modelli, A.; Venuti, M. Empty Level Structure and Dissociative Electron Attachment in Gas-Phase Nitro Derivatives. *Int. J. Mass Spectrom.* **2001**, *205*, 7–16. [CrossRef]
36. Sommerfeld, T. Coupling Between Dipole-Bound and Valence States: The Nitromethane Anion. *Phys. Chem. Chem. Phys.* **2002**, *4*, 2511–2516. [CrossRef]
37. Kossoski, F.; Varella, M.T.D.N. How Does Methylation Suppress the Electron-Induced Decomposition of 1-Methyl-Nitroimidazoles? *J. Chem. Phys.* **2017**, *147*, 164310. [CrossRef] [PubMed]
38. Hahndorf, I.; Lehr, L.; Illenberger, E.; Manz, J. Temperature Effects in Dissociative Electron Attachment to CF_3Cl. *Chem. Phys. Lett.* **1994**, *231*, 460–466. [CrossRef]
39. Hahndorf, I.; Illenberger, E. Temperature Effects in Dissociative Electron Attachment. *Int. J. Mass Spectrom. Ion Proc.* **1997**, *167/168*, 87–101. [CrossRef]
40. Ribar, A.; Fink, K.; Probst, M.; Huber, S.E.; Feketeová, L.; Denifl, S. Isomer Selectivity in Low-Energy Electron Attachment to Nitroimidazoles. *Chem. Eur. J.* **2017**, *23*, 12892–12899. [CrossRef]
41. NIST Chemistry WebBook. Available online: http://webbook.nist.gov/chemistry (accessed on 10 November 2019).
42. Pelc, A.; Huber, S.E.; Matias, C.; Czupyt, Z.; Denifl, S. Formation of Negative Ions upon Dissociative Electron Attachment to the Astrochemically Relevant Molecule Aminoacetonitrile. *J. Phys. Chem. A* **2016**, *120*, 903–910. [CrossRef]

43. Lentz, D.; Heni, M.; Illenberger, E. The Isomers CF_3CN and CF_3NC: Formation and Dissociation of the Anions Formed on Electron Attachment. *Int. J. Mass Spectrom. Ion Proc.* **1986**, *71*, 199–210.
44. Heni, M.; Illenberger, E. Electron Attachment by Saturated Nitriles, Acrylonitrile (C_2H_3CN and Benzonitrile (C_6H_5CN). *Int. J. Mass Spectrom. Ion Proc.* **1986**, *73*, 127–144. [CrossRef]
45. König-Lehmann, C.; Kopyra, J.; Dabkowska, I.; Kosicek, J.; Illenberger, E. Excision of CN^- and OCN^- from Acetamide and Some Amide Derivatives Triggered by Low Energy Electrons. *Phys. Chem. Chem. Phys.* **2008**, *10*, 6954–6961. [CrossRef] [PubMed]
46. da Silva, F.F.; Matias, C.; Almeida, D.; García, G.; Ingólfsson, O.; Flosadóttir, H.D.; Omarsson, B.; Ptasinska, S.; Puschnigg, B.; Scheier, P.; et al. NCO^-, a Key Fragment Upon Dissociative Electron Attachment and Electron Transfer to Pyrimidine Bases: Site Selectivity for a Slow Decay Process. *J. Am. Soc. Mass Spectrom.* **2013**, *24*, 1787–1797. [CrossRef] [PubMed]
47. Zhao, Y.; Truhlar, D.G. The M06 Suite of Density Functionals for Main Group Thermochemistry, Thermochemical Kinetics, Noncovalent Interactions, Excited States, and Transition Elements: Two New Functionals and Systematic Testing of Four M06-class Functionals and 12 Other Functionals. *Theor. Chem. Acc.* **2008**, *120*, 215–241.
48. Zhao, Y.; Truhlar, D.G. Density Functionals with Broad Applicability in Chemistry. *Acc. Chem. Res.* **2008**, *41*, 157–167. [CrossRef] [PubMed]
49. *Gaussian 09, Revision D.01*; Frisch, M.J.; Trucks, G.W.; Schlegel, H.B.; Scuseria, G.E.; Robb, M.A.; Cheeseman, J.R.; Scalmani, G.; Barone, V.; Mennucci, B.; Petersson, G.A.; et al. (Eds.) Gaussian, Inc.: Wallingford, CT, USA, 2013.
50. Illenberger, E. Electron Attachment Reactions in Molecular Clusters. *Chem. Rev.* **1992**, *92*, 1589–1610. [CrossRef]

5.1.4 Hydrated Misonidazole

Additionally to the study of electron interaction processes with misonidazole in the gas phase (as presented in the previous section), misonidazole was investigated in a water cluster environment. The water cluster mimics the cell's environment into which the radiosensitiser would be embedded into in the case of an application within radiotherapeutic treatment, see chapter 4.2.3. The experimental study was conducted at the J. Heyrovský Institute of Physical Chemistry in Prague together with the local researchers at the CluB experiment, see chapter 3.2. Quantum chemical calculations performed by the first author of the here presented paper provide a theoretical model which backs up the experimental data and show i.a. the structure and reaction pathways of the compound and products. Briefly summarising the results, it was shown that under hydration, the fragmentation pathways of misonidazole are suppressed with the exception of the dissociation channel leading to OH^- formation [233]. The quantum mechanical model showed that hydration of OH^- is energetically more favourable than the hydration of NO_2^- byproducts. Besides, the calculation demonstrated that the high reaction energy of the OH^- channel is likely to give rise to an additional new C-N bond ultimately leading to a ring formation. The results are of importance for the understanding of the action of bio-reductive drugs which may be tested further on substitutes of nitro-compounds with long hydrocarbon chains.

My contribution to the presented study includes conducting the measurements at the experimental setup in Prague together with Jaroslav Kočišek. I also contributed to the data analysis and data interpretation.

International Journal of
Molecular Sciences

MDPI

Article

Ring Formation and Hydration Effects in Electron Attachment to Misonidazole

Milan Ončák [1,*], Rebecca Meißner [1,2], Eugene Arthur-Baidoo [1], Stephan Denifl [1,3], Thomas F. M. Luxford [4], Andriy Pysanenko [4], Michal Fárník [4], Jiří Pinkas [4] and Jaroslav Kočišek [4,*]

1 Institut für Ionenphysik und Angewandte Physik, Leopold-Franzens Universität Innsbruck, Technikerstrasse 25, Innsbruck A-6020, Austria
2 Atomic and Molecular Collisions Laboratory, CEFITEC, Department of Physics, Universidade Nova de Lisboa, 2829-516 Caparica, Portugal
3 Center for Biomolecular Sciences Innsbruck, Leopold-Franzens Universität Innsbruck, Technikerstrasse 25, Innsbruck A-6020, Austria
4 J. Heyrovský Institute of Physical Chemistry v.v.i., The Czech Academy of Sciences, Dolejškova 3, 18223 Prague, Czech Republic
* Correspondence: Milan.Oncak@uibk.ac.at (M.O.); jaroslav.kocisek@jh-inst.cas.cz (J.K.)

Received: 22 August 2019; Accepted: 3 September 2019; Published: 6 September 2019

Abstract: We study the reactivity of misonidazole with low-energy electrons in a water environment combining experiment and theoretical modelling. The environment is modelled by sequential hydration of misonidazole clusters in vacuum. The well-defined experimental conditions enable computational modeling of the observed reactions. While the NO_2^- dissociative electron attachment channel is suppressed, as also observed previously for other molecules, the OH^- channel remains open. Such behavior is enabled by the high hydration energy of OH^- and ring formation in the neutral radical co-fragment. These observations help to understand the mechanism of bio-reductive drug action. Electron-induced formation of covalent bonds is then important not only for biological processes but may find applications also in technology.

Keywords: misonidazole; clusters; low-energy electron; bond formation; electron attachment

1. Introduction

Low-energy electrons, which can be formed as secondary species after the interaction of radiation with living matter, are well known reactive species. Reactions of low-energy electrons with DNA can result in severe damage [1], especially when taking into account their large quantity [2,3] and different processes of their formation [4]. The most studied process of DNA damage by low-energy electrons is dissociative electron attachment (DEA):

$$AB + e^- \rightarrow A + B^-$$

Radiation damage by DEA is unique, in that it can break covalent bonds at sub-excitation energies. Even hydrated electrons, with solvation free energies of ∼1.5 eV [5], can break the bonds if the energy gained due to electron affinity of one of the fragments is enough to overcome the dissociation barriers. This unique feature of DEA was proposed to be a key for the development of novel radiosensitizers—molecules enhancing the combined action of concurrent chemo-radiation treatment of tumors [6]. However, other processes induced by low-energy electrons may also be important in this manner, including inelastic electron scattering [3] and associative electron attachment [7,8]. Identification of the processes importance in radiosensitization requires systematic studies of DEA to molecules with known radiosensitizing effects. An example of such a molecule is misonidazole ((RS)-1-Methoxy-3-(2-nitroimidazol-1-yl)propan-2-ol, MISO), which is studied in the present work.

Misonidazole is a prototypical system of a bio-reductive agent. The bio-reductivity can be used for targeted action of the molecule in a hypoxic environment [9] in imaging [10,11] or radiosensitizing [12,13] applications. The bio-reduction may work on several different time scales. On the shortest scale, a single electron reduction can occur as known for other nitro substituted compounds [14] and as was recently also proposed for nimorazole [7]. The single electron reduction may be important in radiosensitization occurring immediately after irradiation [15,16] or for molecular transport within the cell structures [7]. On longer timescales, reduction by several electrons can occur, which results in formation of free radicals, radical anions or complex metabolites with DNA segments [17]. Most of these reduction products were, however, shown to be further biologically inactive [18].

In this work, we focus on the single electron reduction and processes that immediately follow this step in a water environment. The study was performed under vacuum conditions, colliding free electrons with model clusters consisting of MISO and a controlled number of water molecules. These well-defined experimental conditions enable us to experimentally study the DEA energetics and perform computational modelling of the processes immediately following the dissociation. The study is a continuation of our systematic exploration of low-energy electron induced chemistry of nitro-imidazolic radiosensitizers [19,20]. In the present issue, we also report on the electron induced chemistry of isolated MISO [21].

We show that while the nitro group dissociation is suppressed upon the hydration of MISO, the hydroxyl group dissociation channel remains open in a water environment. A reasonable explanation for the hydroxyl group dissociation for low-energy incident electrons is based on the formation of a covalent C-N bond following the DEA. The structures enabling covalent bond formation and synthesis under the action of low-energy electrons attracted significant interest in recent years due to possible technological applications and understanding of fundamental astrochemical reaction mechanisms [22–24]. Apart from a very low energy input for inducing the reaction, also the site selectivity and possible catalytic action makes the low-energy electron an attractive trigger of reactivity [25]. The formation of C-N bonds under the action of low-energy electrons was formerly predicted also for azabenzene.$(CO_2)_n$ clusters [26]. Here, we show that the C-N bond formation occurs on a single molecule and creates a neutral cyclic π-bonded system.

2. Materials and Methods

2.1. Experiment

We used a source of microhydrated clusters [27] and a reflectron time-of-flight mass spectrometer (RTOF) [28], which are parts of the complex CLUster Beam (CLUB) setup [29]. The beam of microhydrated MISO was prepared by co-expanding a mixture of a buffer He or Ne gas, humidified by the Pergo gas humidifier system, together with sublimed MISO (98% purity, Toronto Research Chemicals) through a 90 µm nozzle into vacuum (10^{-4} mbar range during the experiment). The beam was skimmed and, 1.5 m

downstream, it entered the interaction region of the RTOF (10^{-8} mbar during the experiment) where it was crossed by a beam of low-energy electrons. The electrons were produced by thermal emission from a tungsten cathode with an energy distribution width of ~0.7 eV. Electrons were then accelerated to the required kinetic energy in the range of 0.6–5.6 eV in the interaction region. Product anions were extracted directly from the interaction zone into the RTOF where they were separated according to their mass to charge ratio. The ion signal was acquired using a time to digital conversion method.

The MISO sublimation temperature was 363 K, which is high for a biomolecule. Therefore, we checked thermal decomposition of the molecule by prolonged heating (8 h) at an elevated temperature (390 K) and NMR analysis of the original and heated sample. The NMR analysis of both samples (as solutions in DMSO-d_6) showed nearly identical spectra, indicating a reasonable thermal stability of MISO.

2.2. Theory

The MISO.$(H_2O)_n$ clusters and their fragments were first optimized at the B3LYP/6-31+g* level of theory along with D2 dispersion correction as proposed by Grimme [30]. The resulting structures were then re-optimized at both B3LYP+D2/aug-cc-pVDZ and M06/aug-cc-pVDZ levels of theory to assess the error of calculations. For scanning possible fragment isomers, we used molecular dynamics at the semi-empirical PM6 level and at various temperatures, with a time step of 40 a.u. (~0.96 fs). The Gaussian program [31] was used for all quantum chemical calculations reported, molecular dynamics was performed in the Abin code [32]. Supplementary material: Cartesian coordinates of structures optimized in the present study.

3. Results and Discussion

3.1. Molecular Fragmentation

Anion mass spectra for MISO at different hydration conditions are depicted in Figure 1. The anion formation has a resonant character as can be seen from Figure 2, which shows electron energy dependent ion yields. Therefore, we are showing cumulative spectra, which are obtained by summing individual spectra taken at energies ranging from 0.6 to 5.6 eV with a step of 0.25 eV.

The top panel of Figure 1 represents "dry" conditions when pure He, without humidification, was used as a buffer gas. These data may be compared to the results for isolated MISO [21] (see Table 1). Isolated MISO fragments primarily to $m/z = 46$ (NO_2^-; 100), $m/z = 201$ (M^-; 50) and $m/z = 141$ (25) anions, with numbers in parentheses representing the integrated yield of the anion. In the present experiment, the four most intense anions are $m/z = 141$ (100), M^-(75), NO_2^-(30), OH^-(22). The $m/z = 141$ anion can be assigned to either [MISO-CH_2NO_2]$^-$ or [MISO-$C_2H_4O_2$]$^-$ as discussed below.

Table 1. Relative ion yields for the main anions observed after electron attachment to MISO integrated over the studied electron energy range. (i) isolated molecule from Ref. [21], (ii) expansion without hydration and (iii) highest hydration conditions. The values are scaled to 100 for the most intense ion yield, $m/z = 141$ fragment may result from sample impurity. The ion yields at hydrated conditions are sums of yields of anion and its hydrated clusters.

m/z	Ion	Relative Ion Yield		
		(i) isolated [21]	(ii) dry	(iii) hydrated
201	$MISO^-$	50	75	100
141	[MISO-CH_2NO_2]$^-$ or [MISO-$C_2H_4O_2$] $^-$	25	100	50
46	NO_2^-	100	30	3
17	OH^-	-	22	20

In the present molecular beam experiment at dry conditions, we observe (i) lower relative intensity of the $m/z = 46$ anions; (ii) higher relative intensity of $m/z = 141$ anions; (iii) OH^- anions that have not been investigated for the isolated molecule. There are two possible reasons for the observed differences:

(i) *Differences in the experimental approaches.*

The first difference is the used mass spectrometer. Transmission efficiency of the quadrupole mass spectrometer, used in the isolated molecule study, may be lower for high mass fragments.

Second, the electron source in Ref. [21] is dedicated to electron attachment spectroscopy, with excellent performance at low electron energies. The simple electron gun at the CLUB setup cannot produce reliable results at electron energies below ~1.2 eV [33], this region is therefore hatched in Figure 2. We can see that this discrepancy may result in lowering the anion signal of resonances at incident electron energies near 0 eV.

The third important difference is in the used molecular beams, which was effusive in the gas phase study and adiabatic expansion in the present experiment. In the beam experiment, the sublimed molecules are cooled down by buffer gas collisions, which may result in much lower neutral precursor temperature during the electron attachment. This may be a reason for the higher parent anion M^- signal in the present experiments, despite the mentioned low efficiency of our electron gun at low electron energies.

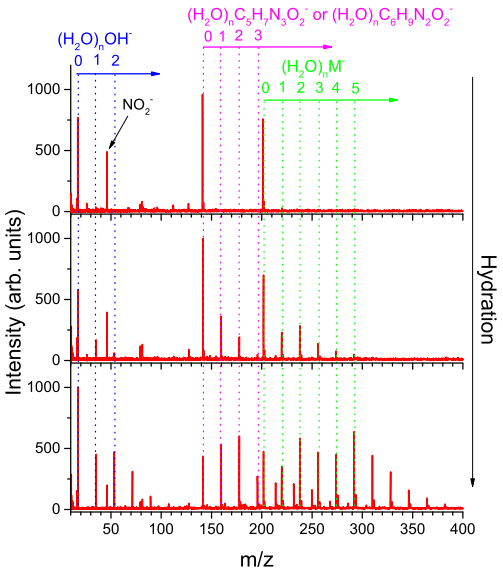

Figure 1. Cumulative mass spectra for negative ion formation after interaction of electrons in the 0.6–5.6 eV range with MISO in a molecular beam without hydration and at two different levels of hydration. The number of water molecules attached to misonidazole in the neutral precursor cluster increases from top to bottom.

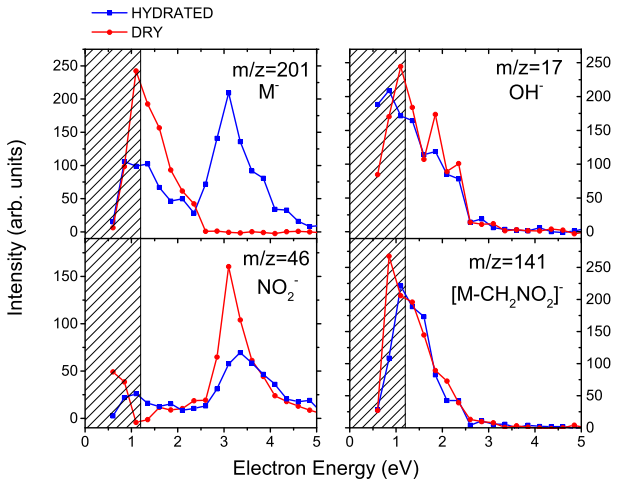

Figure 2. Ion yields for the formation of selected anions from misonidazole as a function of the energy of the incident electron. Red and blue curves show a molecular beam of MISO without and with hydration, respectively ("dry" and "hydrated"). The region of a strong decrease in the electron current is hatched.

(ii) *Different neutral precursor.*

We analyzed the sample by ^{1}H NMR spectroscopy in DMSO-d_6. Besides the MISO signals, we have found low-abundant signals of byproducts (in total ca 1 mol % with respect to MISO, which is consistent with stated purity of the sample, 98%). Among them, 1-ethyl-2-nitroimidazole (around 0.5 mol % with respect to MISO) was determined as the main species. The ^{1}H NMR spectrum showed a triplet at 1.39 and quartet at 4.40 ppm (with a mutual coupling constant $^{3}J_{HH}$ = 7.2 Hz), corresponding to the methyl and methylene groups of the ethyl substituent. In addition, heterocycle protons were found at 7.22 and 7.87 ppm, respectively. These signals correspond to previously published data for 1-ethyl-2-nitroimidazole and its derivatives [34]. The mass of the 1-ethyl-2-nitroimidazole is 141, therefore the $m/z = 141$ anion may be formed by direct electron attachment to a neutral 1-ethyl-2-nitroimidazole molecule. Despite its low mol % in the solid sample, the higher vapour pressure of 1-ethyl-2-nitroimidazole could lead to a higher partial pressure in the gas phase, explaining the intense peak observed in the cumulative mass spectra.

The 1-ethyl-2-nitroimidazole could be a sample impurity or it could be formed by thermal decomposition of MISO. This is suggested by our theoretical calculations, showing that a strongly exothermic channel exists, where MISO decomposes into a neutral fragment with the mass of 141, which is the neutral analogue of isomer **I** in Figure 3. The corresponding reaction is (as calculated at the B3LYP+D2/aug-cc-pVDZ level of theory):

$$\text{(N1) MISO} \rightarrow [\text{MISO} - C_2H_4O_2] + CH_4 + CO_2 + 1.32 \text{ eV}$$

Note that the respective energy might reach up to 2.2 eV if a ring is formed. The fact that this channel may be a thermal decomposition product of the sample does not decrease its importance for the combined chemo-radiation therapy. Activation barriers for the decomposition may be easily overcome by the action of ionizing radiation [35]. Also, thermal and photothermal therapies are of increasing interest [36]. However, as already stated, the comparison of ^{1}H NMR spectra of the sample before and after heating is not significantly different, which may indicate that the decomposition products, including the 1-ethyl-2-nitroimidazole, sublime at the decomposition temperature.

Several more fragment anions with low intensities were observed for the isolated molecule in [21], below the detection sensitivity of our instrument. Only $m/z = 26, 97$ and 112 anions are revealed in the present spectra.

3.2. Water Solvent Effects

We will focus here on the effect of the water solvent on the main dissociation channels. Examples of mass spectra obtained for two hydration conditions are shown in the middle and bottom panel of Figure 1.

First, we can see that M^-, $[MISO\text{-}CH_2NO_2]^-$/$[MISO\text{-}C_2H_4O_2]^-$ and OH^- bind strongly to water as revealed by the presence of hydrated clusters in the spectrum. Particularly interesting are the intensity enhancements for the $(H_2O)_nM^-$ anions with $n = 2$ and $n = 5$ or a significant intensity drop for $(H_2O)_n[M\text{-}CH_2NO_2]^-$/$[MISO\text{-}C_2H_4O_2]^-$ anions above $n = 2$.

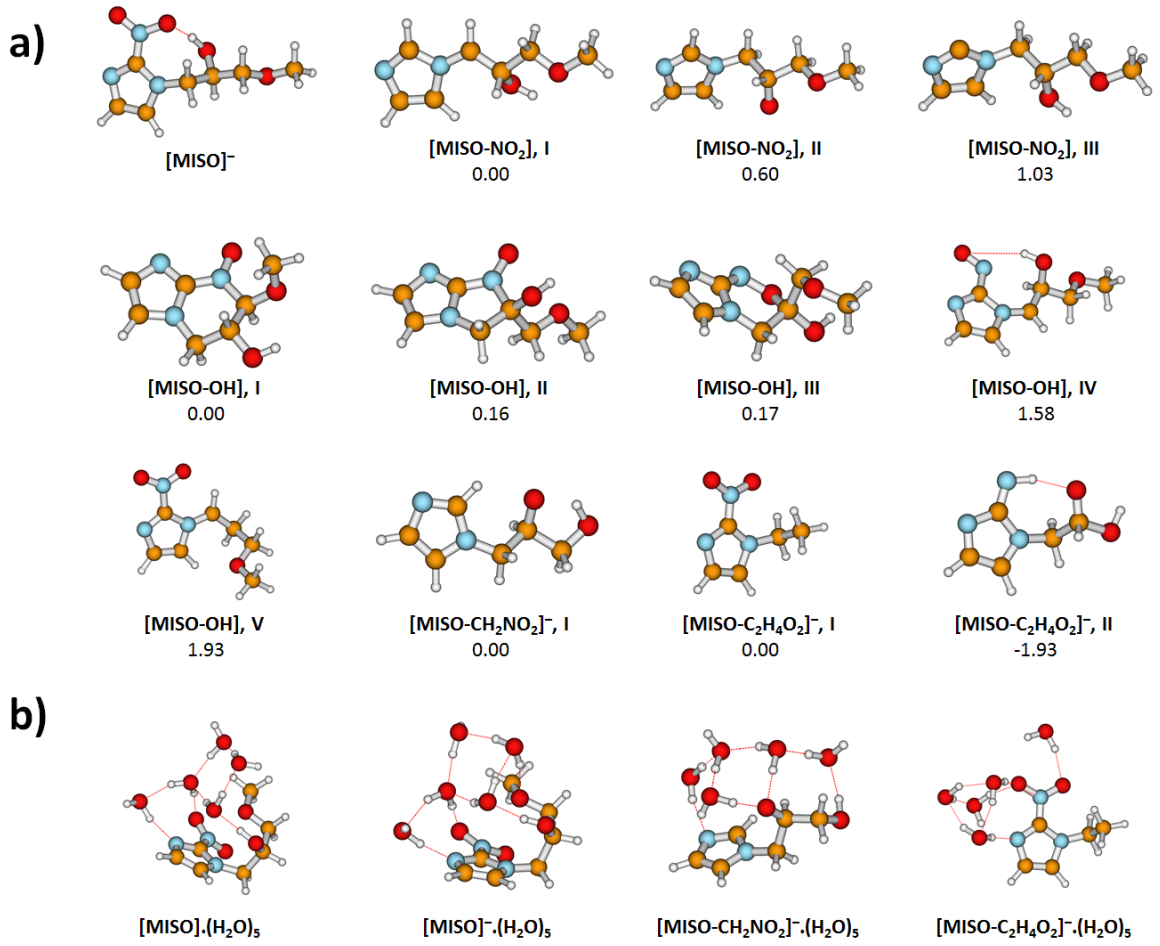

Figure 3. Optimized structures of MISO clusters and dissociation fragments, calculated at the B3LYP+D2/aug-cc-pVDZ level. (**a**) Various isomers of non-hydrated dissociation products, along with relative energy (in eV). (**b**) Selected hydration structures for five water molecules.

Generally, a water solvent reduces DEA fragmentation of biomolecules [7,8,27]. This effect can be seen also for the NO_2^- channel from MISO in Figure 4, which shows that the branching ratio of the NO_2^- fragment ions with respect to the total intensity of $(H_2O)_nM^-$ decreases at higher levels of hydration. The decrease of the fragmentation is not as steep as for the previously studied radiosensitizer nimorazole [7].

If we compare the decrease for hydration conditions characterized by in average $n = 3$ water molecules in $(H_2O)_nM^-$ hydrated parent anion clusters, the NO_2^- signal decreases 10 times in comparison to the parent ion signal while the decrease in the case of nimorazole is 100 times. The observation may be influenced by a different number of water molecules evaporating from the cluster after electron attachment and, consequently, different neutral precursor cluster sizes. We have shown that the number of evaporated water molecules depends on the adiabatic electron affinity of the molecule [8]. The adiabatic electron affinity of nimorazole is $\sim$ 1.3 eV [7] and that of MISO is 1.33 eV [37]. Therefore, we do not expect significant differences in the hydration levels of the two molecules.

The slowly disappearing NO_2^- fragmentation channel will probably not be closed completely in solution and may be the cause of the higher toxicity of MISO in comparison to nimorazole [38]. The interconnection of DEA to biological activity and toxicity has been reviewed recently [39].

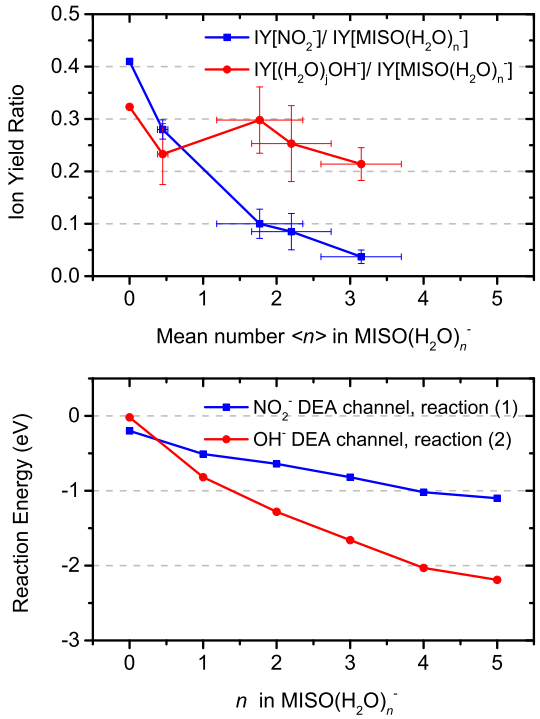

Figure 4. Evolution of relative ion yields for OH^- and NO_2^- fragments as a function of hydration (**top**) and computed reaction energies for respective DEA reaction channels (**bottom**).

The closing of the NO_2^- DEA channel can be observed also in the energy dependent ion yields, shown at the left panels of Figure 2. After hydration, the NO_2^- total intensity decreases and a resonance at $\sim$3 eV starts to appear in the spectrum of the parent anion clusters.

In contrast to the NO_2^- signal, intensity of the OH^- fragment seems to be independent of hydration. While there may be some decrease, this decline lies within the error bars of the present experiment. The $(H_2O)_nOH^-$ signal is not caused by direct electron attachment to water, as water does not have any low-lying DEA resonances [40]. Also, the OH^- signal has not been observed after electron attachment to other types of clusters of water with biological molecules [27] or nitro compounds [7]. On the other hand, a similar behavior was observed for deoxycytidine monophosphate [41]. In the following section, we will show that the OH^- release in water environment is caused by a large hydration energy of OH^- and illuminate the complex process that drives its dissociation from MISO at low energies.

3.3. Theoretical Model for DEA from MISO

We performed quantum chemical calculations of gas phase and hydrated molecules and ions, with results shown in Figures 3 and 4 and Table 2.

After electron attachment, the electron is located at the NO_2 group, see Figure 5. Starting with the vertical electron affinity (VEA), it can be seen that water molecules stabilize the anionic state more than the neutral one, from 0.84 eV for MISO to about 1.4 eV for MISO.$(H_2O)_5$. The adiabatic electron affinity is by about 0.6 eV higher, with the reorganization energy mainly accounting for more efficient hydration of the negatively charged NO_2 group. For example, an OH...NO_2 hydrogen bond is formed in $[MISO]^-$, see Figure 3. However, the spin density distribution stays very similar (Figure 5). Among possible dissociative channels, we considered the following reactions:

(1) $MISO^-.(H_2O)_n \rightarrow NO_2^-.(H_2O)_n + [MISO\text{-}NO_2]$
(2) $MISO^-.(H_2O)_n \rightarrow OH^-.(H_2O)_n + [MISO\text{-}OH]$
(3a) $MISO^-.(H_2O)_n \rightarrow [MISO\text{-}CH_2NO_2]^-.(H_2O)_n + CH_2NO_2$
(3b) $MISO^-.(H_2O)_n \rightarrow [MISO\text{-}C_2H_4O_2]^-.(H_2O)_n + CH_3OH + CO$

The NO_2^- channel (1) produces a [MISO-NO_2] radical. If a simple NO_2 dissociation is considered, isomer **III** in Figure 3 is formed. However, the carbon atom to which the NO_2 group was connected now carries the odd electron. If a proton is transferred from the CH_2 group attached to the imidazole ring (isomer **I**), stabilization by about 1 eV is observed, as already noted elsewhere [21].

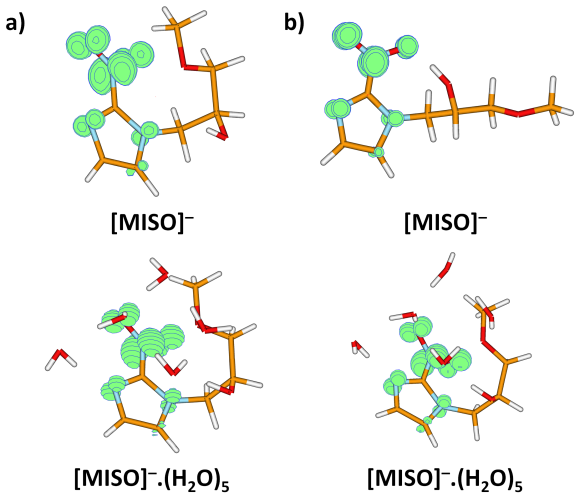

Figure 5. Spin density for the misonidazole anion (**a**) in the structure of the neutral molecule; (**b**) for the minimum located after optimization in the anionic state. Both $MISO^-$ and $MISO^-.(H_2O)_5$ were considered. Calculated at the B3LYP+D2/aug-cc-pVDZ level.

In the case of the OH^- channel (2), the situation is more complicated. Here, a simple dissociation reaction leads to a high-lying [MISO-OH] isomer, making reaction (2) endothermic by about 2 eV, isomer **V**. The dissociation energy can be reduced by about 0.4 eV when the dissociating oxygen comes from the NO_2 group, isomer **IV**. However, the most stable structures found for [MISO-OH] are the ones including ring formation, e.g., isomers **I-III**. The most stable configuration found has a six-membered ring (**I**), with a structure with a five-membered ring being close in energy (**II**). The respective rings can be formed with

only small structural rearrangements from isomer **IV**. Only when the ring formation is accounted for, the low energy of the respective resonances in Figure 2 can be explained.

The stochiometry of $m/z = 141$ can correspond either to $[\text{MISO-CH}_2\text{NO}_2]^-$ or $[\text{MISO-C}_2\text{H}_4\text{O}_2]^-$. In both cases, a considerable structural rearrangement is needed to form the respective anion. In the first case, the NO_2 group along with a CH_2 from the alkyl chain has to dissociate, leading to an overall endothermic reaction (3a) with the reaction energy of about 0.4 eV. In the second case, CH_3OH and CO might dissociate from the imidazole substituent after substantial rearrangement. In this case, however, an exothermic reaction with the energy of about −0.8 eV is predicted. Note that even a more stable isomer **II** can be formed, its formation would however require more substantial changes in bonding. At the same time, about 1.7 eV more energy can be obtained if CH_4 and CO_2 dissociate instead of CH_3OH and CO, making the reaction exothermic even in the neutral state (see Equation (N1)).

The $m/z = 141$ anions can be therefore formed by direct electron attachment to the $m/z = 141$ impurity of the sample (0.5% mol) or as a thermal decomposition product of MISO or by DEA to MISO. In all cases, the most probable structure is the 1-ethyl-2-nitroimidazole anion ($[\text{MISO-C}_2\text{H}_4\text{O}_2]^-$, **I** depicted in Figure 3).

In the gas phase, reaction (3b) is the only one that is markedly exothermic, reactions (1) and (2) are almost thermoneutral and reaction (3a) is endothermic. Upon hydration, reaction (2) is most markedly influenced due to the efficient hydration of OH^- compared to other ions and becomes more exothermic than reaction (1) already for hydration with one water molecule. This can explain the experimentally observed increase in the OH^-/NO_2^- ratio in Figure 4. Reactions (3a,b) are less influenced, with each water molecule shifting the DEA energy by about 0.2 eV.

Let us stress here that energy gained by hydration of OH^- is characteristics of hydroxyl anion, independent of the precursor molecule. This energy gain may therefore enable dissociation after electron attachment in water environment to many other molecules containing hydroxyl functional groups.

Table 2. Reaction energies (in eV) for electron attachment and DEA reactions for $\text{MISO}(\text{H}_2\text{O})_n$ clusters in dependence on the number of hydrated water molecules. Reaction energies are given with respect to isomers **I** shown in Figure 3. Calculated at the B3LYP+D2/aug-cc-pVDZ (M06/aug-cc-pVDZ) level.

n	VEA	AEA	R. (1)	R. (2)	R. (3a)	R. (3b)
0	0.84 (0.81)	1.45 (1.42)	−0.20 (−0.06)	−0.02 (0.13)	0.41 (0.49)	−0.83 (−0.76)
1	1.01 (0.96)	1.63 (1.66)	−0.51 (−0.43)	−0.82 (−0.73)	0.05 (0.23)	−1.09 (−1.05)
2	1.09 (0.97)	1.84 (1.77)	−0.64 (−0.49)	−1.28 (−1.13)	−0.12 (0.07)	−1.33 (−1.23)
3	1.22 (1.19)	2.07 (1.99)	−0.82 (−0.70)	−1.66 (−1.55)	−0.27 (−0.09)	−1.45 (−1.33)
4	1.48 (1.45)	2.17 (2.08)	−1.02 (−0.92)	−2.03 (−1.94)	−0.62 (−0.41)	−1.71 (−1.61)
5	1.35 (1.33)	2.14 (2.06)	−1.10 (−1.04)	−2.19 (−2.14)	−0.58 (−0.32)	−1.81 (−1.71)

4. Conclusions

We have demonstrated how the molecular environment influences interactions of low-energy electrons (0–5 eV) with a model bio-reductive therapeutics molecule, MISO. Negative ion mass spectra show the suppression of fragmentation, except for the OH^- dissociation channel. Quantum chemical calculations show that hydration of OH^- is much more energetically favourable than hydration of the proposed NO_2^- reaction byproducts. The mechanism may be important also in other OH-containing biomolecules, such as the previously studied dCMP [41]. At the same time, the reaction energy of the simple OH^- dissociation is high and only the formation of a new covalent bond in the neutral by-products may explain its observation at very low electron energies. Here, the most probable ring formation occurs after a loss of an oxygen atom from the nitro group and subsequent formation of a new C-N bond. The proposed behavior may be tested on further nitro- compounds substituted by long hydrocarbon chains.

Supplementary Materials: Supplementary materials can be found at http://www.mdpi.com/1422-0067/20/18/4383/s1.

Author Contributions: Experimental measurements and analysis R.M., T.F.M.L., J.K., A.P.; NMR measurements and analysis J.P.; theoretical modeling M.O.; writing–draft preparation J.K., M.O.; writing–review and editing, all authors; funding acquisition S.D., J.K., M.F.

Funding: This research was funded by CZECH SCIENCE FOUNDATION grant number 19–01159S; Czech Ministry of Education Youth and Sports via OP RDE Grant no.CZ.02.2.69/0.0/16_027/0008355; S.D. acknowledges funding from the FWF, Vienna (P30332).

Acknowledgments: R.M. acknowledges the Portugese National Funding Agency FCT-MCTES through PD/BD/114452/2016 and research grant UID/FIS/00068/2019(CEFITEC). This work was also supported by Radiation Biology and Biophysics Doctoral Programme (RaBBIT, PD/00193/2012) and UID/Multi/04378/2013(UCIBIO).

Conflicts of Interest: The authors declare no conflict of interest.

Abbreviations

The following abbreviations are used in this manuscript:

DEA	Dissociative Electron Attachment
RTOF	Reflectron Time of Flight Mass Spectrometer
MISO	Misonidazole
DMSO	dimethyl sulfoxide

References

1. Alizadeh, E.; Orlando, T.M.; Sanche, L. Biomolecular Damage Induced by Ionizing Radiation: The Direct and Indirect Effects of Low-Energy Electrons on DNA. *Annu. Rev. Phys. Chem.* **2015**, *66*, 379–398. [CrossRef] [PubMed]
2. Gomez-Tejedor, G.G.; Fuss, M.C. *Radiation Damage in Biomolecular Systems*; Springer: Dordrecht, The Netherlands, 2012.
3. Alizadeh, E.; Sanche, L. Precursors of Solvated Electrons in Radiobiological Physics and Chemistry. *Chem. Rev.* **2012**, *112*, 5578–5602. [CrossRef] [PubMed]
4. Mucke, M.; Braune, M.; Barth, S.; Förstel, M.; Lischke, T.; Ulrich, V.; Arion, T.; Becker, U.; Bradshaw, A.; Hergenhahn, U. A hitherto unrecognized source of low-energy electrons in water. *Nat. Phys.* **2010**, *6*, 143. [CrossRef]
5. Kumar, A.; Walker, J.A.; Bartels, D.M.; Sevilla, M.D. A Simple ab Initio Model for the Hydrated Electron That Matches Experiment. *J. Phys. Chem.* **2015**, *119*, 9148–9159. [CrossRef]
6. Chomicz, L.; Zdrowowicz, M.; Kasprzykowski, F.; Rak, J.; Buonaugurio, A.; Wang, Y.; Bowen, K.H. How to Find Out Whether a 5-Substituted Uracil Could Be a Potential DNA Radiosensitizer. *J. Phys. Chem. Lett.* **2013**, *4*, 2853–2857. [CrossRef]
7. Meißner, R.; Kočišek, J.; Feketeová, L.; Fedor, J.; Fárník, M.; Limao-Vieira, P.; Illenberger, E.; Denifl, S. Low-energy electrons transform the nimorazole molecule into a radiosensitiser. *Nat. Commun.* **2019**, *10*, 2388. [CrossRef]
8. Poštulka, J.; Slavíček, P.; Fedor, J.; Fárník, M.; Kočišek, J. Energy Transfer in Microhydrated Uracil, 5-Fluorouracil, and 5-Bromouracil. *J. Phys. Chem.* **2017**, *121*, 8965–8974. [CrossRef]
9. Workman, P.; Strafford, I.J. The experimental development of bioreductive drugs and their role in cancer therapy. *Cancer Metastasis Rev.* **1993**, *12*, 73–82. [CrossRef]
10. Liu, J.n.; Bu, W.; Shi, J. Chemical Design and Synthesis of Functionalized Probes for Imaging and Treating Tumor Hypoxia. *Chem. Rev.* **2017**, *117*, 6160–6224. [CrossRef]
11. Lopci, E.; Grassi, I.; Chiti, A.; Nanni, C.; Cicoria, G.; Toschi, L.; Fonti, C.; Lodi, F.; Mattioli, S.; Fanti, S. PET radiopharmaceuticals for imaging of tumor hypoxia: A review of the evidence. *Am. J. Nucl. Med. Mol. Imaging* **2014**, *4*, 365–384.

12. Paterson, I.; Dawes, P.; Henk, J.; Moore, J. Pilot study of radiotherapy with misonidazole in head and neck cancer. *Clin. Radiol.* **1981**, *32*, 225–229. [CrossRef]
13. Fu, K.K.; Cooper, J.S.; Marcial, V.A.; Laramore, G.E.; Pajak, T.F.; Jacobs, J.; Al-Sarraf, M.; Forastiere, A.A.; Cox, J.D. Evolution of the radiation therapy oncology group clinical trials for head and neck cancer. *Int. J. Radiat. Oncol. Biol. Phys.* **1996**, *35*, 425–438. [CrossRef]
14. Mason, R.P.; Holtzman, J.L. Mechanism of microsomal and mitochondrial nitroreductase. Electron spin resonance evidence for nitroaromatic free radical intermediates. *Biochemistry* **1975**, *14*, 1626–1632. [CrossRef]
15. Knox, R.J.; Knight, R.C.; Edwards, D.I. Studies on the action of nitroimidazole drugs: The products of nitroimidazole reduction. *Biochem. Pharmacol.* **1983**, *32*, 2149–2156. [CrossRef]
16. Wardman, P. The mechanism of radiosensitization by electron-affinic compounds. *Int. J. Radiat. Appl. Instrum. Part Radiat. Phys. Chem.* **1987**, *30*, 423–432. [CrossRef]
17. Varghese, A.J.; Whitmore, G.F. Modification of Guanine Derivatives by Reduced 2-Nitroimidazoles. *Cancer Res.* **1983**, *43*, 78–82. [PubMed]
18. Edwards, D.I. Reduction of nitroimidazoles in vitro and DNA damage. In *Bioreduction in the Activation of Drugs*; Alexander, P., Gielen, J., Sartorelli, A.C., Eds.; Pergamon Press Ltd.: Oxford, UK, 1986; p. 53.
19. Tanzer, K.; Feketeová, L.; Puschnigg, B.; Scheier, P.; Illenberger, E.; Denifl, S. Reactions in Nitroimidazole Triggered by Low-Energy (0–2 eV) Electrons: Methylation at N1-H Completely Blocks Reactivity. *Angew. Chem. Int. Ed.* **2014**, *53*, 12240–12243. [CrossRef]
20. Ribar, A.; Fink, K.; Probst, M.; Huber, S.E.; Feketeová, L.; Denifl, S. Isomer Selectivity in Low-Energy Electron Attachment to Nitroimidazoles. *Chem. Eur. J.* **2017**, *23*, 12892–12899. [CrossRef]
21. Meißner, R.; Feketeová, L.; Illenberger, E.; Denifl, S. Reactions in the Radiosensitiser Misonidazole Induced by Low-Energy (0–10 eV) Electrons. *Int. J. Mol. Sci.* **2019**, *20*, 3496. [CrossRef]
22. Böhler, E.; Warneke, J.; Swiderek, P. Control of chemical reactions and synthesis by low-energy electrons. *Chem. Soc. Rev.* **2013**, *42*, 9219–9231. [CrossRef]
23. Lafosse, A.; Bertin, M.; Azria, R. Electron driven processes in ices: Surface functionalization and synthesis reactions. *Prog. Surf. Sci.* **2009**, *84*, 177–198. [CrossRef]
24. Sajeev, Y. Cycloaddition of molecular dinitrogens: formation of tetrazete anion (N4-; D2h) through associative electron attachment. *Mol. Phys.* **2019**, *117*, 2162–2166. [CrossRef]
25. Davis, D.; Sajeev, Y. Low energy electron catalyst: the electronic origin of catalytic strategies. *Phys. Chem. Chem. Phys.* **2016**, *18*, 27715–27720. [CrossRef] [PubMed]
26. Lee, S.H.; Kim, N.; Ha, D.G.; Kim, S.K. "Associative" Electron Attachment to Azabenzene-(CO2)n van der Waals Complexes: Stepwise Formation of Covalent Bonds with Additive Electron Affinities. *J. Am. Chem. Soc.* **2008**, *130*, 16241–16244. [CrossRef] [PubMed]
27. Kočišek, J.; Pysanenko, A.; Fárník, M.; Fedor, J. Microhydration Prevents Fragmentation of Uracil and Thymine by Low-Energy Electrons. *J. Phys. Chem. Lett.* **2016**, *7*, 3401–3405. [CrossRef] [PubMed]
28. Kočišek, J.; Lengyel, J.; Fárník, M. Ionization of large homogeneous and heterogeneous clusters generated in acetylene–Ar expansions: Cluster ion polymerization. *J. Chem. Phys.* **2013**, *138*, 124306. [CrossRef]
29. Fárník, M.; Lengyel, J. Mass spectrometry of aerosol particle analogues in molecular beam experiments. *Mass Spectrom. Rev.* **2018**, *37*, 630–651. [CrossRef]
30. Grimme, S. Semiempirical GGA-type Density Functional Constructed with a Long-Range Dispersion Correction. *J. Comput. Chem.* **2006**, *27*, 1787–1799. [CrossRef] [PubMed]
31. Frisch, M.J.; Trucks, G.W.; Schlegel, H.B.; Scuseria, G.E.; Robb, M.A.; Cheeseman, J.R.; Scalmani, G.; Barone, V.; Petersson, G.A.; Nakatsuji, H.; et al. *Gaussian 16 Revision A.03, 2016*; Gaussian Inc.: Wallingford, CT, USA, 2016.
32. Hollas, D.; Svoboda, O.; Ončák, M.; Slavíček, P. ABIN, Source Code. Available online: https://github.com/PHOTOX/ABIN (accessed on 1 September 2019).
33. Kočišek, J.; Grygoryeva, K.; Lengyel, J.; Fárník, M.; Fedor, J. Effect of Cluster Environment on the Electron Attachment to 2-Nitrophenol. *Eur. Phys. J.* **2016**, *70*, 98. [CrossRef]
34. Smiglak, M.; Hines, C.C.; Reichert, W.M.; Vincek, A.S.; Katritzky, A.R.; Thrasher, J.S.; Sun, L.; McCrary, P.D.; Beasley, P.A.; Kelley, S.P.; et al. Synthesis, limitations, and thermal properties of energetically-substituted,

protonated imidazolium picrate and nitrate salts and further comparison with their methylated analogs. *New J. Chem.* **2012**, *36*, 702–722. [CrossRef]
35. Solov'yov, A.V.; Surdutovich, E.; Scifoni, E.; Mishustin, I.; Greiner, W. Physics of ion beam cancer therapy: A multiscale approach. *Phys. Rev. E* **2009**, *79*, 011909. [CrossRef]
36. Zou, L.; Wang, H.; He, B.; Zeng, L.; Tan, T.; Cao, H.; He, X.; Zhang, Z.; Guo, S.; Li, Y. Current Approaches of Photothermal Therapy in Treating Cancer Metastasis with Nanotherapeutics. *Theranostics* **2016**, *6*, 762–772. [CrossRef] [PubMed]
37. Feketeová, L.; Albright, A.L.; Sørensen, B.S.; Horsman, M.R.; White, J.; O'Hair, R.A.; Bassler, N. Formation of radical anions of radiosensitizers and related model compounds via electrospray ionization. *Int. J. Mass Spectrom.* **2014**, *365–366*, 56–63. [CrossRef]
38. Overgaard, J.; Overgaard, M.; Nielsen, O.S.; Pedersen, A.K.; Timothy, A.R. A comparative investigation of nimorazole and misonidazole as hypoxic radiosensitizers in a C3H mammary carcinoma in vivo. *Br. J. Cancer* **1982**, *46*, 904–911. [CrossRef] [PubMed]
39. Pshenichnyuk, S.A.; Modelli, A.; Komolov, A.S. Interconnections between dissociative electron attachment and electron-driven biological processes. *Int. Rev. Phys. Chem.* **2018**, *37*, 125–170. [CrossRef]
40. Fedor, J.; Cicman, P.; Coupier, B.; Feil, S.; Winkler, M.; Głuch, K.; Husarik, J.; Jaksch, D.; Farizon, B.; Mason, N.J.; et al. Fragmentation of Transient Water Anions Following Low-Energy Electron Capture by H2O/D2O. *J. Phys. At. Mol. Opt. Phys.* **2006**, *39*, 3935. [CrossRef]
41. Kočišek, J.; Sedmidubská, B.; Indrajith, S.; Fárník, M.; Fedor, J. Electron Attachment to Microhydrated Deoxycytidine Monophosphate. *J. Phys. Chem.* **2018**, *122*, 5212–5217. [CrossRef] [PubMed]

5.1.5 (Hydrated) Nimorazole

Nimorazole is another example for a radiosensitiser based on a nitroimidazole. Hence, it also belongs to the group of compounds which were developed to mimic the oxygen effect, thus addressing hypoxic tumour cells [8, 9]. Nimorazole has the molecular formula $C_9H_{14}N_4O_3$, a molecular weight of 226.23 g/mol and is depicted in figure 5.7. The molecule consisists of a nitromidazole with attached carbon side chain to which in turn a morpholine ring is attached. Out of the nitroimidazole derivatives, nimorazole is the only one which is currently applied in the treatment of cancer combined with radiotherapy. In Denmark, patients receive the agent during the treatment of pharyngeal and supra-glottic carcinomas [234]. Compared to the other compounds of this class, nimorazole turned out to have the minimal side effects which allow for the administration of a sufficiently high dose to achieve beneficial effects [235]. Many studies investigated the compound at different levels, reaching from the physical and chemical properties to medical benefits [166, 236–241].

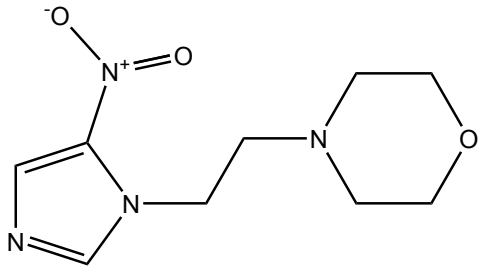

Figure 5.7: Structural formula of nimorazole. The molecule is composed of an imidazole ring with an attached nitro group and a carbon side chain ending in a morpholine ring.

In the present study, nimorazole (NIMO) is studied upon electron attachment, both as isolated molecule and within a micro-hydration environment [242]. While the gas-phase studies are conducted at the Wippi setup, the water cluster studies were performed at the CluB setup. Previous studies of nucleobases and halogenated uracils embedded into water clusters showed that in most cases, the dissociation pathways were suppressed as when compared to the isolated molecules [104, 106]. In order to quantify the level of hydration in the present study, the mean number $< n >$ in the $\mathrm{NIMO}(H_2O)_n^-$ anions was derived from the recorded mass spectra. It is important to note that this describes the situation after ionisation but is a reasonable measure to compare the hydration conditions before electron attachment, too. A previous study at the CluB experiment evaluated a method to estimate the number of ejected water molecules during electron attachment and it was shown that while the number of evaporated water molecules increases for larger clusters at the same electron energy, the anionic cluster size distribution still reflects the distribution of neutral clusters [106]. In case of the isolated molecule it became apparent that the electron attachment cross sections are high. With the Wippi setup, an assessment of the order of magnitude of the cross section is possible by comparing the ion yield of the nimorazole parent anion with the ion yield of the 0.8 eV peak of the Cl^- anion from CCl_4, under consideration of the partial pressures and otherwise constant experimental conditions. The cross section of the Cl^- anion ($\sigma_{Cl^-(0.8\,eV)}$) is well-known, see chapter 3.3.2, and can hence be used as a reference.

Thus, the cross section can be determined with

$$\sigma_{\mathrm{NIMO}^-} = \sigma_{\mathrm{Cl}^-(0.8\,\mathrm{eV})} \cdot \frac{I_{\mathrm{NIMO}^-}}{I_{\mathrm{Cl}^-(0.8\,\mathrm{eV})}} \cdot \frac{p_{\mathrm{NIMO}}}{p_{\mathrm{CCl_4}}} \tag{5.1}$$

where I_{NIMO^-} and $I_{\mathrm{Cl}^-(0.8\,\mathrm{eV})}$ are the ion yields of the nimorazole parent anion and the Cl^- anion, respectively, and p_{NIMO} and $p_{\mathrm{CCl_4}}$ the partial pressures of nimorazole and carbon tetrachloride, respectively. Uncertainties in the determination of the partial pressure determination and the quadrupole mass filter transmission and resolution effects limit the accuracy of the calculated value such that only the order of magnitude can be evaluated.

Briefly summarising the results, the study shows that associative attachment is the key process among electron attachment [242]. It occurs very efficiently at 0 eV electron energy and for the isolated molecule a cross section of about $3 \cdot 10^{-18}\,\mathrm{m}^2$ was determined. In contrast, DEA processes exhibit cross sections which are at least one order of magnitude smaller. In the case of hydrated nimorazole, the effect is enhanced and the quenching of DEA channels grows with the size of the water cluster. The only observable DEA fragment anion is NO_2^- with a resonance peaking at around 3 eV. With increased hydration levels (measurement with up to $< n >= 15$ water molecules were recorded) and further suppression of the DEA channel, this resonance disappears for NO_2^-. Instead, a new resonance structure forms out at 3 eV for the parent anion. It is concluded that the nimorazole anion is stabilised in water, which is also supported by calculation performed at the J. Heyrovský Institute of Physical Chemistry v.v.i., Czech Academy of Science, Prague.

My contribution to the presented study includees performing the experimental measurements in the gas phase, analysing the data, and the figure preparation for the paper. The cluster measurements were conducted by me together with Jaroslav Kočišek. We shared the analysis of the cluster data. Additionally, all authors contributed in the interpretation of the data. Finally, I also wrote the experimental section of the paper.

nature COMMUNICATIONS

ARTICLE

https://doi.org/10.1038/s41467-019-10340-8 OPEN

Low-energy electrons transform the nimorazole molecule into a radiosensitiser

Rebecca Meißner [1,2], Jaroslav Kočišek[3], Linda Feketeová [4], Juraj Fedor[3], Michal Fárník [3], Paulo Limão-Vieira [2], Eugen Illenberger[1,5] & Stephan Denifl [1]

While matter is irradiated with highly-energetic particles, it may become chemically modified. Thereby, the reactions of free low-energy electrons (LEEs) formed as secondary particles play an important role. It is unknown to what degree and by which mechanism LEEs contribute to the action of electron-affinic radiosensitisers applied in radiotherapy of hypoxic tumours. Here we show that LEEs effectively cause the reduction of the radiosensitiser nimorazole via associative electron attachment with the cross-section exceeding most of known molecules. This supports the hypothesis that nimorazole is selectively cytotoxic to tumour cells due to reduction of the molecule as prerequisite for accumulation in the cell. In contrast, dissociative electron attachment, commonly believed to be the source of chemical activity of LEEs, represents only a minor reaction channel which is further suppressed upon hydration. Our results show that LEEs may strongly contribute to the radiosensitising effect of nimorazole via associative electron attachment.

[1] Institut für Ionenphysik und Angewandte Physik and Center for Biomolecular Sciences Innsbruck, Leopold-Franzens Universität Innsbruck, Technikerstrasse 25, A-6020 Innsbruck, Austria. [2] Atomic and Molecular Collisions Laboratory, CEFITEC, Department of Physics, Universidade NOVA de Lisboa, 2829-516 Caparica, Portugal. [3] J. Heyrovský Institute of Physical Chemistry v.v.i., The Czech Academy of Sciences, Dolejškova 3, 18223 Prague, Czech Republic. [4] Université de Lyon; Université Claude Bernard Lyon1; Institut de Physique Nucléaire de Lyon, CNRS/IN2P3 UMR 5822, 69622 Villeurbanne, Cedex, France. [5] Institut für Chemie und Biochemie-Physikalische und Theoretische Chemie, Freie Universität Berlin, Takustrasse 3, 14195 Berlin, Germany. Correspondence and requests for materials should be addressed to S.D. (email: Stephan.Denifl@uibk.ac.at)

Ballistic electrons with kinetic energies below about 12 eV are formed as abundant secondary species in the interaction of high-energy quanta (particles or photons in the MeV range) with cellular components[1,2]. After their formation, they lose kinetic energy by a series of elastic or inelastic collisions before they reach some stage of solvation and become chemically inactive[3,4]. In the course of this collision sequence, they can initiate very effective chemical reactions via dissociative electron attachment (DEA), thereby generating negatively charged fragment ions and neutral radicals at electron energies significantly below the corresponding bond dissociation energy[5]. DEA can be a highly selective process in the cleavage of certain chemical bonds within a molecule[6]. This unique property compared to processes induced by high-energy radiation, is based on the resonant nature of DEA, i.e., the incoming electron with a specific low-energy forms a specific transient anion state. Since about 10^4–10^5 secondary low-energy electrons are formed in biological matter per 1 MeV deposited primary quantum, the relevance of low-energy electrons for radiation damage of critical targets such as DNA was recognised[7]. Indeed, the importance of the DEA processes for the induction of strand breaks in dry plasmid DNA by low-energy electrons was shown by Sanche et al.[8] and very recently bond cleavage upon electron attachment was also observed for ribothymidine in the solution phase[9]. DEA was also suggested as the operative mechanism for the action of modified pyrimidines acting as radiosensitisers in tumour cells[10–12]. For example, 5-bromouracil (BrU) is a well-known radiosensitiser with a bromine atom attached at the C5 position of the pyrimidine ring. The DEA cross section for the formation of Br^- (accompanied by formation of the corresponding neutral radical) turned out to be two orders of magnitude larger than the cross section for the most abundant DEA reaction in thymine, the formation of the dehydrogenated parent anion by emission of a neutral H radical[11]. When BrU is incorporated into DNA due to its structural analogy to thymine (CH_3 group at C5 position) and uracil (H atom at C5 position), the radical sites in the DNA formed upon DEA may lead to strand breaks by subsequent local chemistry[13].

Here we study the prototype compound, nimorazole (NIMO), of the class of nitroimidazolic (NI) radiosensitisers. For few decades, NIs have been investigated in biochemical and oncologic studies. Those compounds have been considered to mimic the well-known oxygen effect which is absent in hypoxic cells due to their anaerobic environment[13,14]. The chemical structure of NIMO is included in Fig. 1. The compound is characterized by its NI ring interconnected to a morpholine ring by a carbon chain. NIMO turned out to be the only successful compound to overcome tumour hypoxia with reasonable side effects for patients[15] and therefore is used as standard chemical compound for pharyngeal and supra-glottic carcinoma in Danish radiotherapy centers[16].

In our study we obtain that dissociation plays a minor role when an electron attaches to NIMO. Instead, the formation of the parent radical anion by associative electron attachment to NIMO is a very efficient process, in particular, when the molecule is hydrated. In this case, the only notable fragment anion NO_2^- becomes strongly quenched which is not related to a change in the probability of spontaneous electron emission (autodetachment). Our quantum chemical calculations for NIMO clustered with one or two water molecules fully support these experimental results. The calculations show that electron attachment to hydrated NIMO is stabilized by the presence of water. Ultimately, these results show that free radical anion formation by attachment of a low-energy electron could be the key process for radiosensitisation of hypoxic tumour cells by the electron-affinic NI radiosensitisers.

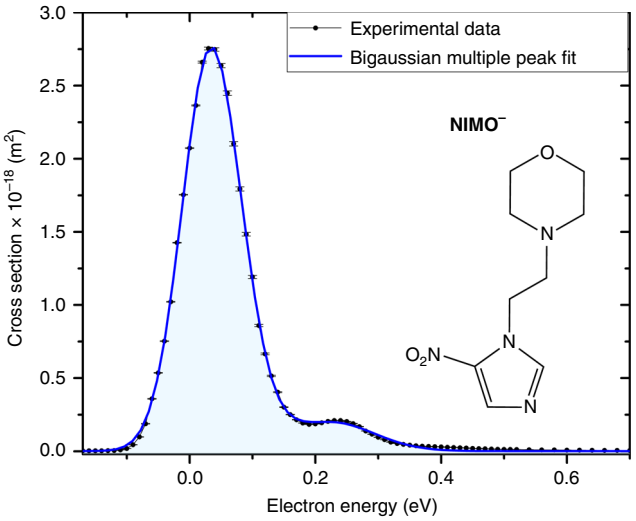

Fig. 1 Cross-section of the nimorazole radical anion and molecular composition. The black dots (connected by the black line as guide for the eye) represent the experimentally determined cross-section values as a function of the electron kinetic energy. Statistical error margins are included for each data point and refer to the standard error of the mean, see data analysis section for details. The blue line shows a bigaussian (sum of two Gauss peaks) multiple peak fit of the experimental data. In addition, the skeletal formula of nimorazole ($C_9H_{14}N_4O_3$) with its nitroimidazole moiety and the morpholine ring is shown. Source data are provided as a Source Data file

Results

Formation of the NIMO radical anion upon electron attachment. The present results indicate that *free* low-energy electrons are very effectively captured by NIMO. In contrast to halouracils, the dominant feature in electron attachment to NIMO is the very effective formation of the non-dissociated (metastable) parent anion, $NIMO^-$, without the cleavage of chemical bonds. This anion is observed within a very narrow main peak close to zero eV electron energy as shown in Fig. 1. We determined the absolute cross-section of this associative attachment (AA) process to be $\sim 3 \times 10^{-18}$ m^2 (with an uncertainty of one order of magnitude, see "Methods" for the discussion on possible systematic errors). This cross-section is an extraordinary high value which exceeds the geometrical cross-section of the target molecule (about 0.5×10^{-18} m^2).

Attachment of free electrons is accompanied with often significant energy release comprising the kinetic energy of the incoming electron and the electron affinity of the molecule, which was calculated to be 1.31 eV (at the M062x/6-311 + G(d,p) level of theory)[17]. The anion lifetime is typically short due to electron autodetachment or molecular dissociation[5]. The formation of (metastable) parent anions with high cross-sections on a microsecond detection time scale, as for the present case, is therefore restricted to only two types of molecular systems. The first enables effective redistribution of the excess energy over the vibrational degrees of freedom such as the sulphur hexafluoride molecule SF_6[18] or fullerenes like C_{60}[19]. These two compounds are characterised by the high symmetry of the molecule (e.g., in the former case there are six equal S–F bonds), which provides favourable conditions for the formation of a metastable parent anion. The second provides an effective sink for the excess energy via intramolecular bond breakage and rearrangement[20]. Though NIMO is of low symmetry, we suppose its appreciable number of 84 vibrational degrees of freedom

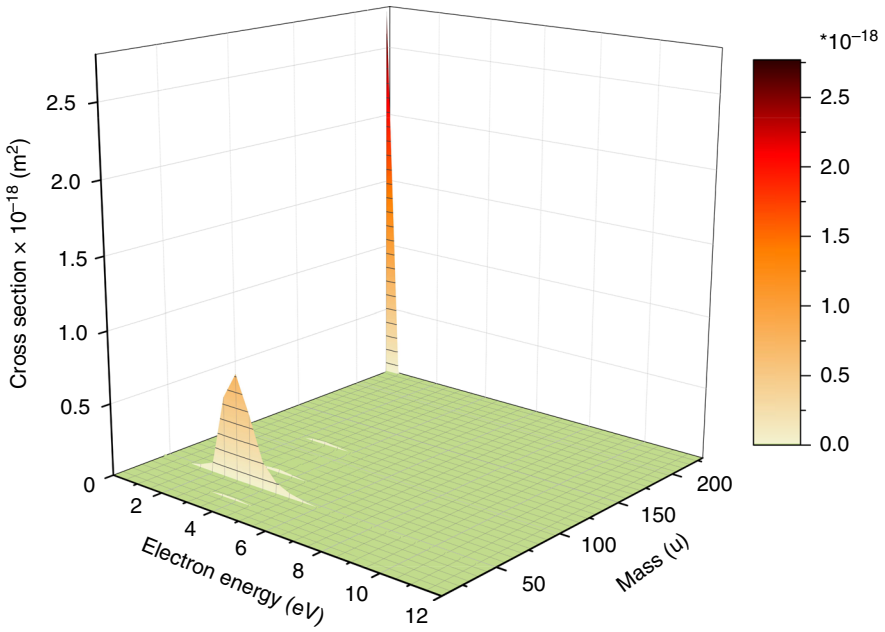

Fig. 2 Intensity map of (fragment) anions formed upon electron attachment to nimorazole. The map shows cross-sections derived from negative ion mass spectra recorded in the interval of 0.5 eV for the electron energy range between ~0 and 12 eV. Only two abundant anions can be observed, (i) the radical anion at mass 226 u close to zero eV (see Fig. 1), and (ii) the nitrite NO_2^- at mass 46 u, which is abundantly formed only in the region between 2 and 4 eV. Source data are provided as a Source Data file

provides an effective means for energy redistribution making the observation of an intense $NIMO^-$ within our observation time window of few hundred microseconds possible.

Dissociative electron attachment to NIMO. The only observable relevant DEA reaction is the formation of NO_2^-. Figure 2 shows that the cross-section for this channel is about one order of magnitude lower than that for $NIMO^-$, occurring in the electron energy range between ~2–4 eV. Other observed fragment anions have cross-sections even two orders of magnitude lower than that for the parent anion and therefore they will not be discussed here. The electron energy dependence of their cross-sections is shown in the Supplementary Figs. 1–3. The formation of NO_2^- can formally be expressed as,

$$e^- + \mathrm{NIMO} \leftrightarrow (\mathrm{NIMO}^-)^{\#} \rightarrow (\mathrm{NIMO} - \mathrm{NO_2}) + \mathrm{NO_2^-} \quad (1)$$

with $(NIMO^-)^{\#}$ representing the intermediate molecular anion. Reaction (1) represents the simple cleavage of the C–NO_2 bond after initial formation of a repulsive shape resonance of σ^*(C–NO_2) character. In this case, the DEA reaction is expected as direct electronic dissociation along the repulsive C–N potential energy surface. We calculated the thermochemical threshold (free energy of reaction ΔG) for this process at the M062x/6–311+G(d,p) level of theory and obtained a value of +0.53 eV (release of the intact neutral fragment, as mentioned in reaction (1)). Since we can also observe a weak NO_2^- signal at electron energies close to 0 eV (see Supplementary Fig. 3), we investigated other dissociation pathways, which may lead to this anion yield. The only exothermic reaction found corresponds to the release of $C_3H_3N_2 + C_6H_{11}NO$ with $\Delta G = -0.26$ eV. The formation of NO_2^- is driven by the appreciable adiabatic electron affinity (AEA) of NO_2 (present value 2.40 eV). However, the weak NO_2^- ion yield at zero eV indicates a barrier on this reaction pathway. Therefore, autodetachment can effectively compete with the DEA channel of $(NIMO^-)^{\#}$ at this energy. We further note that though our calculations for the (NIMO–NO_2) fragment predict an appreciable AEA of +2.07 eV, and a DEA threshold of +0.85 eV for the release of NO_2+ $(NIMO–NO_2)^-$, we do not observe this simple reaction channel leading to the reactive nitrogen species NO_2[21].

Solvation effects upon DEA to NIMO. It is important to note that the outcome of DEA reactions may be influenced by the presence of an environment. In order to elucidate this point, we performed electron attachment experiments with hydrated NIMO, i.e. $NIMO(H_2O)_n$ clusters with $\langle n \rangle \leq 14$. We chose this approach since intense research in such finite cluster systems and in the condensed phase over the last years demonstrated that in bound molecules DEA can usually still be described on a molecular site, i.e., electron attachment proceeds to an *individual* molecule which is coupled to an environment. The latter affects both, the initial attachment process and the decomposition of the intermediate molecular anion[22]. The results for clustered NIMO indicate that DEA becomes suppressed in favour of AA. The ion yield ratio of $NO_2^-/(NIMO(H_2O)_n)^-$ (which can also be interpreted as the overall ratio DEA/AA) for different solvation conditions is shown in Fig. 3. A decrease by three orders of magnitude can be observed, indicating that DEA is reduced for solvated NIMO. This behaviour is within the general trend when going from the gas phase over microsolvation into solution[23] and it is caused by parent anion stabilization via energy dissipation to the environment[24]. The detailed mechanism of the anion stabilization can be caused by (i) caging of dissociation products[25,26] and (ii) ultrafast quenching of the transient anion[27].

In view of the strong decrease of the ion yield ratio of $NO_2^-/(NIMO(H_2O)_n)^-$, one could also speculate about option (iii), a change in the autodetachment probability which leads to the decrease of the NO_2^- channel. This process will lead to a change of the position and the width of the resonance with the hydration[28]. To elucidate this question, we performed electron energy dependent ion yield measurements for the NO_2^- and the parent anion at different hydration conditions. The yields are shown in Fig. 4. As already discussed, in the isolated molecule the parent anion is formed at near zero energies and NO_2^- at around 3 eV. With increased hydration, the intensity of the low-energy

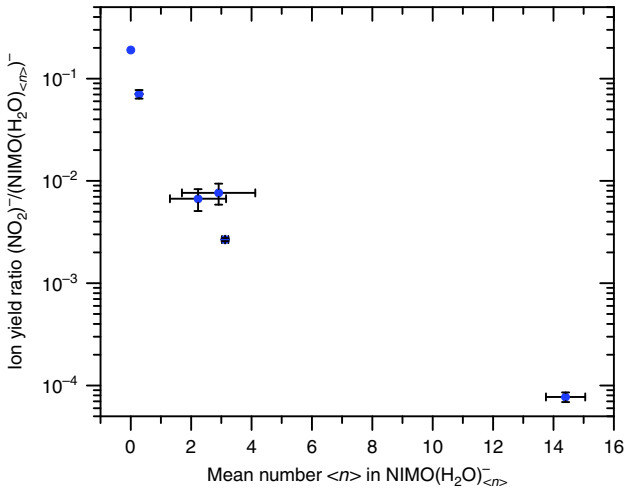

Fig. 3 Closing of the most intense DEA channel with hydration—total ion intensity. The relative intensity of DEA to AA (blue data points) is expressed as the ratio of total yields of NO_2^- to $NIMO(H_2O)_n^-$ parent ions at different hydration conditions (see Supplementary Fig. 4). The level of hydration is characterised by the mean number <n> of water molecules attached to the parent anion in $NIMO(H_2O)_n^-$ clusters. The number <n> is lower, but directly proportional to the number of water molecules in the neutral precursor cluster (see ref. [24] for details). The statistical uncertainty described by the standard deviation is shown as error bars, see data analysis section for more details. Source data are provided as a Source Data file

peak in the spectrum of the parent anion decreases. This is caused by the fact that the attachment at low electron energies results into formation of $NIMO(H_2O)_n^-$ anions instead of bare $NIMO^-$. The new feature is that when the molecule is hydrated with only few water molecules, the parent anion signal appears at around 3 eV. Therefore, the 3 eV resonance, which normally results in the dissociation, is now stabilized and the excess energy is presumably released by evaporation of water. Such evaporation then results in the formation of the parent anion. The 3 eV resonance shape weakly depends on the hydration degree: at lower hydration conditions (I, II) only the lower energy part of the resonance is stabilized, at higher hydration conditions (III, IV) the parent anion curve practically resembles that of the NO_2^- curve of the isolated molecule. Finally, at the highest hydration conditions (V), the 3 eV resonance practically disappears for both NO_2^- and the parent anion. Both resonances now result in the formation of larger $NIMO(H_2O)_n^-$ cluster anions. The energy acquired by the attachment process is not enough to dissociate the molecule, nor to evaporate all the water monomers from the cluster.

On the basis of the aforementioned observation, we can clearly exclude option (iii) from the explanation of the NIMO stabilisation against DEA. If mechanism (iii) is operative, one would expect only the disappearance of the 3 eV resonance but no formation of the parent anions at the same energy. The data also demonstrates the important fact that the primary electron attachment target at low energies is still the NIMO molecule, despite of the possible electron attachment to the surrounding water network[29]. This effect can be ascribed to the large de-Broglie wavelength of the impinging low-energy electron, which is about 0.7 nm at the electron energy of 3 eV and to the positive electron affinity of NIMO.

Moreover, we have also calculated structures of anionic NIMO hydrated by one and two water molecules. The anions were optimized at M062x/6–31 + G(d,p) level of theory and basis set. The lowest energy conformers are shown in Fig. 5, while all the different binding motifs investigated are summarized in Supplementary Figs. 5 and 6. From all the structures found for the anionic NIMO hydrated by water, we can conclude that the anion is more and more stabilized with the increasing number of water molecules present. The AEAs of NIMO hydrated by one water molecule increases to 1.36–1.76 eV (see Supplementary Fig. 5), while for the NIMO hydrated by two water molecules increases to the range of 1.53–1.96 eV (Supplementary Fig. 6). Additionally, the vertical detachment energy (VDE) of the NIMO anion also increases with the increasing number of water molecules. While for the bare NIMO anion, the VDE is 1.68 eV, addition of one water molecule increases the VDE to 1.83–2.32 eV (see Supplementary Fig. 5), and the presence of two water molecules increases the VDE to 2.11–2.64 eV (Supplementary Fig. 6). Notably, for the most stable conformers of the hydrated NIMO anion in Fig. 5, the water molecules seem to cluster around the $-NO_2$ group, however, this is not the case for neutral structures. It can be seen in Supplementary Fig. 5 that the preference for water binding to neutral NIMO are, e.g., the O atom of the morpholine ring or the N atom of the imidazole ring. Nevertheless, the relative energies of these neutrals within the error of the calculation can be assumed to be isoenergetic.

Discussion

Together with the remarkably high electron attachment cross-section, the quenching of DEA in the solvated molecule is the second key outcome of our studies. The calculations for NIMO clustered with one or two water molecules indicate that the attachment of an electron to hydrated NIMO is stabilized by the presence of water, the attraction of water molecules to the $-NO_2$ group and a fast dissipation of the excess energy due to the strong interactions between the O−H oscillators of water molecules[30,31] and their evaporation, while the increased VDE makes the autodetachment also less probable. Though very simplified systems are studied here compared to the complex cellular environment, the time evolution of radiation damage and the peculiar features of electron attachment mentioned above may allow nonetheless some predictions on the action of NIMO as radiosensitiser in vivo. Due to the favourable adiabatic electron affinity of NIs, it was previously suggested that NIs become only active after the reduction[13,32], where the rate of the reduction determines the uptake of the radiosensitiser by the cell. Therefore, free radical anion formation by low-energy electrons seems to be the key process for radiosensitisation of hypoxic tumour cells by NIs. This conclusion is further supported by the result that NIs have to be present at the instant of radiation for a radiosensitising effect, while when adding them at a later stage (after few ms) the effect vanished[13].

After the reduction process of NIs in a cellular environment, it was suggested that the intact anion itself is not the cytotoxic species which attacks DNA. Instead, the NI radical anion may become protonated in hypoxic cells[32,33], and then the neutralised radical compound could bind to DNA. In such case, chemical reaction schemes exist, which lead to strand breaks in DNA[34,35]. These schemes rely on the binding of neutral NIs at DNA sites attacked by hydroxyl radicals. The latter radicals are formed simultaneously by radiolysis processes. Therefore, NIs were suggested to mimic the oxygen effect in hypoxic tumours.

Finally, we note that hypoxic cells without a radiosensitiser usually require two to three times higher radiation dose for cell death compared to normally-oxygenated cells[13]. Electron-affinic radiosensitisers such as NIs may significantly lower the doses and consequently the side effects of the therapy[36]. Here, we demonstrate a fundamental mechanism of their accumulation in tumour

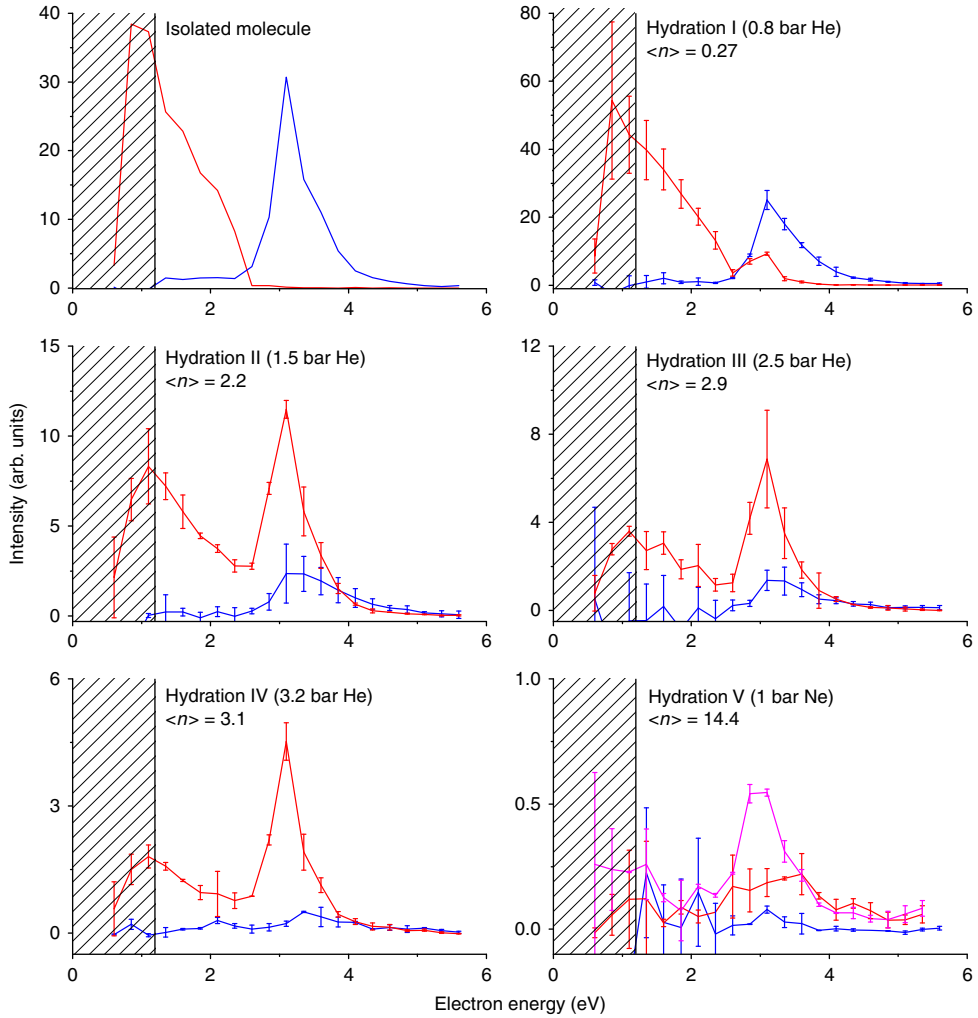

Fig. 4 Closing of the most intense DEA channel with hydration—energy dependence. Energy dependent ion yields for the formation of NO_2^- (blue) and parent $NIMO^-$ (red) ions at different hydration conditions. The level of hydration is characterised by the mean number <*n*> of water molecules attached to the parent anion in $NIMO(H_2O)_n^-$ clusters. At the highest hydration conditions, we are showing also the yield for $m/z = 280$ $NIMO(H_2O)_3^-$ anion (pink). The shape of the ion yield curve in the patterned part of the spectra (below about 1.2 eV) is influenced by the decrease of the electron current in the cluster beam setup, see ref. [40] for details. The statistical uncertainty described by the standard deviation is shown as error bars, see data analysis section for more details. Source data are provided as a Source Data file

cells, which may be used in further improvement of these important therapeutic agents.

Methods

Experimental design. The present study was carried out at two different crossed electron-molecular/cluster beam setups. The single-molecule data was collected at the Wippi apparatus in Innsbruck, a detailed description can be found in ref. [37]. An oven serves as inlet for the NIMO sample. A capillary of 1 mm diameter is mounted onto it to guide the evaporated sample towards the interaction region. As ionisation source serves a hemispherical electron monochromator (HEM). It provides electrons with a narrow energy distribution (~100 meV) with Gaussian profile. The attachment processes take place in the region where molecular beam and electrons cross. Measurements at different electron energies are enabled by applying an appropriate acceleration potential in the HEM shortly before the interaction region. The negatively charged parent and fragment ions formed are subsequently extracted into a quadrupole mass analyser by a weak electrostatic field. The quadrupole has a nominal mass range of 2048 u and is utilised for mass selection. Thus, combining the HEM and the mass filter, the formation efficiency of selected fragments at varying energies can be studied. The ions are detected by a channel electron multiplier and counted by a preamplifier with analog-to-digital converter unit. The mass spectrometer is operated under high vacuum ($\sim 10^{-8}$ mbar background pressure).

For cluster experiments, the CLUster Beam (CLUB) apparatus in Prague was used, for a detailed review refer to ref. [38]. In the present study, the configuration of the experiment was identical to that one described in ref. [25]. For cluster production, helium or neon gas is humidified by a Pergo gas humidifier. A Nafion tubing gas line passes through a water bath and its membrane selectively permeate water vapour. The humidified gas is introduced into a heated oven filled with NIMO. At the opposite end a 90 µm conical nozzle is mounted. The mixture of humidified buffer gas and NIMO is co-expanded through the nozzle, which leads to the formation of $NIMO(H_2O)_n$ clusters. The cluster beam is skimmed after a distance of ~2.5 cm and crossed by an electron beam in the interaction region ~1.5 m downstream. The electron energy can be varied by an accelerating potential. The created anions are extracted by a 2 µs long high-voltage pulse into a reflectron time-of-flight (RTOF) mass analyser with a mass resolution of $\sim 5 \times 10^3$. A delay of 0.5 µs between electron pulse and ion extraction excludes any effects caused by those. With each extraction pulse, all anions are analysed, detected by a multichannel plate and recorded as mass spectrum.

Materials. The NIMO used in both experiments was purchased from Toronto Research Chemicals (Canada) with a stated purity of ≥99%. For the doped water cluster study, type II pure water was prepared by reverse osmosis. Helium 4.6 and neon 5.0 served as buffer gases.

Experimental procedures. NIMO appears as powder but the focus lies on interactions with single molecules or molecules in a microhydration environment, the sample reservoirs of both experiments are heated to evaporate the sample. For Wippi, the oven was heated to about 95 °C, for CLUB between 80 and 110 °C. The

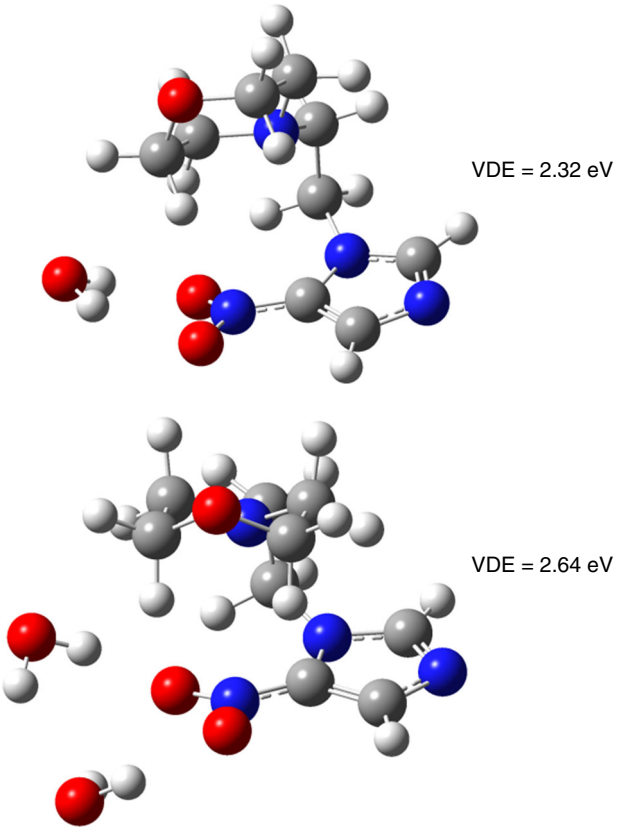

Fig. 5 Lowest energy conformers of hydrated anionic nimorazole. The calculations were performed for one (top) and two (bottom) water molecules. The anions were optimized at M062x/6–31 + G(d,p) level of theory and basis set. The corresponding vertical detachment energy (VDE) is shown respectively. Colour coding: Carbon (grey), hydrogen (white), nitrogen (blue), oxygen (red)

temperatures were set carefully avoiding thermal decomposition of the sample but having reasonable signal rates. At CLUB, the mean cluster sizes are controlled by the pressure of the buffer gas. Here, higher pressures lead to higher humidification conditions and thus larger cluster sizes.

Additionally, background spectra were taken at identical experimental conditions to exclude both background gas and instrumentally caused peaks. For Wippi this includes both measurements with empty oven and at random masses, for CLUB measurements at empty oven and during a blocked cluster beam. Background data was subtracted from the signal traces.

For both setups, an energy calibration is required. At Wippi, the well-known 0 eV resonance positions in the ion yields of SF_6^-/SF_6 [18] and Cl^-/CCl_4[39] arising from s-wave electron attachment processes are used. Additionally, the energy resolution is determined based on the full-width at half maximum (FWHM) of this peak to be ~100 meV. At CLUB, electrons below 1.3 eV are strongly suppressed due to the design of the electron gun (see ref. [40] for details). Thus, the 4.4 eV resonance in the ion yield of O^-/CO_2[41] is used for the calibration of the energy scale. The energy resolution amounts to ~0.7 eV. Cross-sections were determined with the data taken at Wippi by comparing the ion yields of NIMO and the well-known cross-sections of the 0.8 eV peak of Cl^-/CCl_4[39] measured under the same conditions. Pressure calibrations caused by different sample introduction methods were implemented based on earlier experiments. Partial pressures were taken into account by normalizing the signal traces according to the related values. Only the order of magnitude can be derived due to systematic uncertainties. Two main influencing factors exist. First, the partial pressure determination arises uncertainties as the partial pressure cannot be measured directly but can only be evaluated by subtracting the pressures with and without presence of NIMO in the vacuum chamber. Additionally, the correction factor of the hot cathode used as pressure gauge for different gases must be estimated since it is not available (O(30%)). Second, resolution and transmission effects of the used quadrupole mass analyser result in varying signal heights (O(30%)).

Data analysis for Figs. 1 and 2. Statistical significance and reproducibility were verified by repeating each measurement several times (Figs. 1 and 2). In case of Wippi data (Figs. 1 and 2), this includes data obtained at different days for various oven fillings, making up to about 200–300 set of measurements for the NIMO and nitrogen dioxide anion each, with gate times of 1 s/mass step and step size of 0.01 u. The figures in the main text show the mean of the according measurements already converted into cross-sections. Error bars refer to the statistically caused standard error of the mean which is calculated as $s/\sqrt{m}$ with s the standard deviation of the mean and m the number of averaged measurements. Here, the individual curves are normalised for error calculations to exclude systematic uncertainties caused by the quadrupole and pressure determination described before and hence only refer to the statistical variation of the shape of the resonance.

Data analysis for Figs. 3 and 4. The ratios and mean number of water molecules $<n>$ in the mixed clusters $NIMO(H_2O)_n^-$ were determined from the mass spectra depicted in the Supplementary Fig. 4 (Figs. 3 and 4). The mass spectra were obtained by averaging the values of cumulative mass spectra obtained in three independent measurements for every hydration condition except of the mass spectrum for the isolated molecule taken only once. The isolated molecule was studied in detail using the Wippi apparatus introduced above. The individual cumulative spectra used for averaging were taken at different days and different spectrometer settings. To avoid systematic errors, we performed the set of measurements at the experimental setting preferring the detection of high m/z's in the present TOF setup and the standard deviation of these measurements was used for estimation of error bars in Fig. 3. Every individual cumulative mass spectrum was obtained as a sum of 21, background subtracted, and electron current divided, mass spectra measured at electron energies from 0.6 to 5.6 eV with step size 0.25 eV. The dynamic range of the single measured mass spectrum was 2×10^6.

Quantum chemical calculations. The thermodynamic threshold (free energy of reaction ΔG) for a DEA reaction, considering precursor molecule M and a release of a neutral fragment X (see e.g., reaction (1)), can be expressed by $\Delta G([M - X]^-) = DE(M{-}X) - EA(M - X)$, where $DE(M - X)$ is the bond dissociation energy and $EA(M - X)$ the electron affinity of the corresponding fragment. The threshold energy for the experimental observation of $[M - X]^-$ in electron attachment experiments coincides with $\Delta G([M - X]^-)$ if the fragments are formed with no excess energy. Fragmentation reactions with kinetic energy release occur at electron energies above the thermodynamic threshold $\Delta G([M - X]^-)$. Quantum chemical calculations employing the density functional M062x[42,43] were carried out to calculate free energies of reactions, dissociation energies (including the zero-point energy correction), and adiabatic electron affinities. For NIMO we used the lowest structure reported in ref. [17]. All structures where optimized at the M062x/6–311 + G(d,p) level of theory and basis set with the Gaussian-09D01 program package[44]. Structures of NIMO hydrated by one and two water molecules were optimized at M062x/6–31 + G(d,p) level of theory and basis set. We determined AEAs and vertical electron affinities of the neutrals, and VDEs of the anions. Frequencies were calculated in all cases to confirm that the structures are local minima on the potential energy surface and not the transition states.

Data availability

All data that led to the present findings are available upon request to the corresponding author. The source data underlying Fig. 1–4 and Supplementary Figs. 1–4 are provided as a Source Data file.

Received: 17 October 2018 Accepted: 3 May 2019
Published online: 03 June 2019

References

1. Gokhberg, K., Kolorenč, P., Kuleff, A. I. & Cederbaum, L. S. Site- and energy-selective slow-electron production through intermolecular Coulombic decay. *Nature* **505**, 661–663 (2014).
2. Ren, X. G., Al Maalouf, E. J., Dorn, A. & Denifl, S. Direct evidence of two interatomic relaxation mechanisms in argon dimers ionized by electron impact. *Nat. Commun.* **7**, 11093 (2016).
3. Westphal, K. et al. Irreversible electron attachment - a key to DNA damage by solvated electrons in aqueous solution. *Org. Biomol. Chem.* **13**, 10362–10369 (2015).
4. Ma, J., Wang, F., Denisov, S. A., Adhikary, A. & Mostafavi, M. Reactivity of prehydrated electrons toward nucleobases and nucleotides in aqueous solution. *Sci. Adv.* **3**, e1701669 (2017).
5. Baccarelli, I., Bald, I., Gianturco, F. A., Illenberger, E. & Kopyra, J. Electron-induced damage of DNA and its components: Experiments and theoretical models. *Phys. Rep.* **508**, 1–44 (2011).
6. Ptasinska, S., Denifl, S., Scheier, P., Illenberger, E. & Märk, T. D. Bond- and site-selective loss of H atoms from nucleobases by very-low-energy electrons (<3 eV). *Angew. Chem. - Int Ed.* **44**, 6941–6943 (2005).

7. Michael, B. D. & O'Neill, P. Molecular biology. A sting in the tail of electron tracks. *Science* **287**, 1603–1604 (2000).
8. Boudaïfffa, B., Cloutier, P., Hunting, D., Huels, M. A. & Sanche, L. Resonant formation of DNA strand breaks by low-energy (3 to 20 eV) electrons. *Science* **287**, 1658–1660 (2000).
9. Ma, J. et al. Observation of dissociative quasi-free electron attachment to nucleoside via excited anion radical in solution. *Nat. Commun.* **10**, 102 (2019).
10. Chomicz, L. et al. How to find out whether a 5-substituted uracil could be a potential DNA radiosensitizer. *J. Phys. Chem. Lett.* **4**, 2853–2857 (2013).
11. Abdoul-Carime, H., Huels, M. A., Illenberger, E. & Sanche, L. Sensitizing DNA to secondary electron damage: resonant formation of oxidative radicals from 5-halouracils. *J. Am. Chem. Soc.* **123**, 5354–5355 (2001).
12. Schürmann, R. et al. Resonant formation of strand breaks in sensitized oligonucleotides induced by low-energy electrons (0.5-9 eV). *Angew. Chem. Int Ed. Engl.* **56**, 10952–10955 (2017).
13. Wardman, P. Chemical radiosensitizers for use in radiotherapy. *Clin. Oncol.* **19**, 397–417 (2007).
14. Wang, H., Mu, X., He, H. & Zhang, X. D. Cancer radiosensitizers. *Trends Pharm. Sci.* **39**, 24–48 (2018).
15. Baumann, M. et al. Radiation oncology in the era of precision medicine. *Nat. Rev. Cancer* **16**, 234–249 (2016).
16. Henk, J. M., Bishop, K. & Shepherd, S. F. Treatment of head and neck cancer with CHART and nimorazole: phase II study. *Radio. Oncol.* **66**, 65–70 (2003).
17. Feketeová, L. et al. Formation of radical anions of radiosensitizers and related model compounds via electrospray ionization. *Int J. Mass Spectrom.* **365-366**, 56–63 (2014).
18. Klar, D., Ruf, M. W. & Hotop, H. Attachment of electrons to molecules at meV resolution. *Aust. J. Phys.* **45**, 263–291 (1992).
19. Matejčík, Š. et al. Formation and decay of C_{60}^- following free-electron capture by C_{60}. *J. Chem. Phys.* **102**, 2516–2521 (1995).
20. Sommerfeld, T. & Davis, M. C. Ring-opening attachment as an explanation for the long lifetime of the octafluorooxolane anion. *J. Chem. Phys.* **149**, 084305 (2018).
21. Cerón-Carrasco, J. P., Requena, A., Zúñiga, J. & Jacquemin, D. Mutagenic effects induced by the attack of NO_2 radical to the guanine-cytosine base pair. *Front. Chem.* **3**, 13 (2015).
22. Neustetter, M., Aysina, J., da Silva, F. F. & Denifl, S. The effect of solvation on electron attachment to pure and hydrated pyrimidine clusters. *Angew. Chem. Int Ed.* **54**, 9124–9126 (2015).
23. Bald, I., Langer, J., Tegeder, P. & Ingólfsson, O. From isolated molecules through clusters and condensates to the building blocks of life. A short tribute to Prof. Eugen Illenberger's work in the field of negative ion chemistry. *Int J. Mass Spectrom.* **277**, 4–25 (2008).
24. Poštulka, J., Slavíček, P., Fedor, J., Farník, M. & Kočišek, J. Energy transfer in microhydrated uracil, 5-fluorouracil, and 5-bromouracil. *J. Phys. Chem. B* **121**, 8965–8974 (2017).
25. Kočišek, J., Pysanenko, A., Farník, M. & Fedor, J. Microhydration prevents fragmentation of uracil and thymine by low-energy electrons. *J. Phys. Chem. Lett.* **7**, 3401–3405 (2016).
26. Kohanoff, J., McAllister, M., Tribello, G. A. & Gu, B. Interactions between low energy electrons and DNA: a perspective from first-principles simulations. *J. Phys. -Condens Mat.* **29**, 383001 (2017).
27. Zawadzki, M., Ranković, M., Kočišek, J. & Fedor, J. Dissociative electron attachment and anion-induced dimerization in pyruvic acid. *PCCP* **20**, 6838–6844 (2018).
28. Fabrikant, I. I. Electron attachment to molecules in a cluster environment: suppression and enhancement effects. *Eur. Phys. J. D.* **72**, 96 (2018).
29. Barnett, R. N., Landman, U., Scharf, D. & Jortner, J. Surface and internal excess electron-states in molecular clusters. *Acc. Chem. Res* **22**, 350–357 (1989).
30. Cowan, M. L. et al. Ultrafast memory loss and energy redistribution in the hydrogen bond network of liquid H_2O. *Nature* **434**, 199–202 (2005).
31. Zhang, Z., Piatkowski, L., Bakker, H. J. & Bonn, M. Ultrafast vibrational energy transfer at the water/air interface revealed by two-dimensional surface vibrational spectroscopy. *Nat. Chem.* **3**, 888–893 (2011).
32. Edwards, D. I. Nitroimidazole drugs - Action and resistance mechanisms I. Mechanisms of action. *J. Antimicrob. Chemother.* **31**, 9–20 (1993).
33. Wardman, P. Electron transfer and oxidative stress as key factors in the design of drugs selectively active in hypoxia. *Curr. Med. Chem.* **8**, 739–761 (2001).
34. Wardman, P. The mechanism of radiosensitization by electron-affinic compounds. *Radiat. Phys. Chem.* **30**, 423–432 (1987).
35. von Sonntag C. *Free-Radical-Induced DNA Damage and Its Repair, A Chemical Perspective*, 1 edn. (Springer-Verlag, Berlin Heidelberg, 2006).
36. Adams, G. E. et al. Electron-affinic sensitization. VII. A correlation between structures, one-electron reduction potentials, and efficiencies of nitroimidazoles as hypoxic cell radiosensitizers. *Radiat. Res.* **67**, 9–20 (1976).
37. Denifl, S. et al. Free-electron attachment to coronene and corannulene in the gas phase. *J. Chem. Phys.* **123**, 104308 (2005).
38. Kočišek, J., Lengyel, J. & Farnik, M. Ionization of large homogeneous and heterogeneous clusters generated in acetylene-Ar expansions: Cluster ion polymerization. *J. Chem. Phys.* **138**, 124306 (2013).
39. Gallup, G. A., Aflatooni, K. & Burrow, P. D. Dissociative electron attachment near threshold, thermal attachment rates, and vertical attachment energies of chloroalkanes. *J. Chem. Phys.* **118**, 2562–2574 (2003).
40. Kočišek, J., Grygoryeva, K., Lengyel, J., Farnik, M., & Fedor, J. Effect of cluster environment on the electron attachment to 2-nitrophenol. *Eur. Phys. J. D.* **70**, 98 (2016).
41. Dressler, R. & Allan, M. Energy partitioning in the O^-/CO_2 dissociative attachment. *Chem. Phys.* **92**, 449–455 (1985).
42. Zhao, Y. & Truhlar, D. G. The M06 suite of density functionals for main group thermochemistry, thermochemical kinetics, noncovalent interactions, excited states, and transition elements: two new functionals and systematic testing of four M06-class functionals and 12 other functionals. *Theor. Chem. Acc.* **120**, 215–241 (2008).
43. Hehre, W. J., Radom, L., Schleyer, PvR, Pople, JA. *Ab Initio Molecular Orbital Theory*. (Wiley, Hoboken, NJ, 1986).
44. Frisch, M. J. et al. Gaussian 09, Revision D.01. (Gaussian Inc., Wallington CT, 2013).

Acknowledgements

This work was supported by FWF, Vienna (P30332). R.M. and P.L.V. acknowledge the Portuguese National Funding Agency FCT-MCTES through PD/BD/114452/2016 and research grants UID/FIS/00068/2019 (CEFITEC) and PTDC/FIS-AQM/31281/2017. This work was also supported by Radiation Biology and Biophysics Doctoral Training Programme (RaBBiT, PD/00193/2010); UID/Multi/ 04378/2019 (UCIBIO). J.K. acknowledges the support by the Czech Science Foundation Grant 19–01159S. L.F. is grateful to the LABEX Lyon Institute of Origins (ANR-10-LABX-0066) of the Université de Lyon for its financial support within the program "Investissements d'Avenir" (ANR-11-IDEX-0007) of the French government operated by the National Research Agency (ANR). The crucial computing support from CCIN2P3 (France) is acknowledged gratefully. S.D. thanks Ass. Prof. Dr. Andreas Seppi from the Medical University Innsbruck for discussions.

Author contributions

R.M. and J.K.: data aquisition experiment, data analysis; L.F.: quantum chemical calculations; R.M., J.K., L.F., J.F., M.F., P.L.-V., E.I. and S.D.: interpretation of data and manuscript preparation.

Additional information

Supplementary Information accompanies this paper at https://doi.org/10.1038/s41467-019-10340-8.

Competing interests: The authors declare no competing interests.

Reprints and permission information is available online at http://npg.nature.com/reprintsandpermissions/

Journal peer review information: *Nature Communications* thanks the anonymous reviewers for their contribution to the peer review of this work. Peer reviewer reports are available.

Publisher's note: Springer Nature remains neutral with regard to jurisdictional claims in published maps and institutional affiliations.

Supplementary Information to

Low-energy electrons transform the nimorazole molecule into a radiosensitiser

Rebecca Meißner[1,2], Jaroslav Kočišek[3], Linda Feketeová[4], Juraj Fedor[3], Michal Fárník[3], Paulo Limão-Vieira[2], Eugen Illenberger[1,5], Stephan Denifl[1]*

[1]Institut für Ionenphysik und Angewandte Physik and Center for Biomolecular Sciences Innsbruck, Leopold-Franzens Universität Innsbruck, Technikerstrasse 25, A-6020 Innsbruck, Austria

[2]Atomic and Molecular Collisions Laboratory, CEFITEC, Department of Physics, Universidade NOVA de Lisboa, 2829-516 Caparica, Portugal

[3]J. Heyrovský Institute of Physical Chemistry v.v.i., The Czech Academy of Sciences, Dolejškova 3, 18223 Prague, Czech Republic

[4]Université de Lyon; Université Claude Bernard Lyon1; Institut de Physique Nucléaire de Lyon, CNRS/IN2P3 UMR 5822, 69622 Villeurbanne Cedex, France

[5]Institut für Chemie und Biochemie-Physikalische und Theoretische Chemie, Freie Universität Berlin, Takustrasse 3, 14195 Berlin, Germany

*Corresponding author. E-Mail: Stephan.Denifl@uibk.ac.at

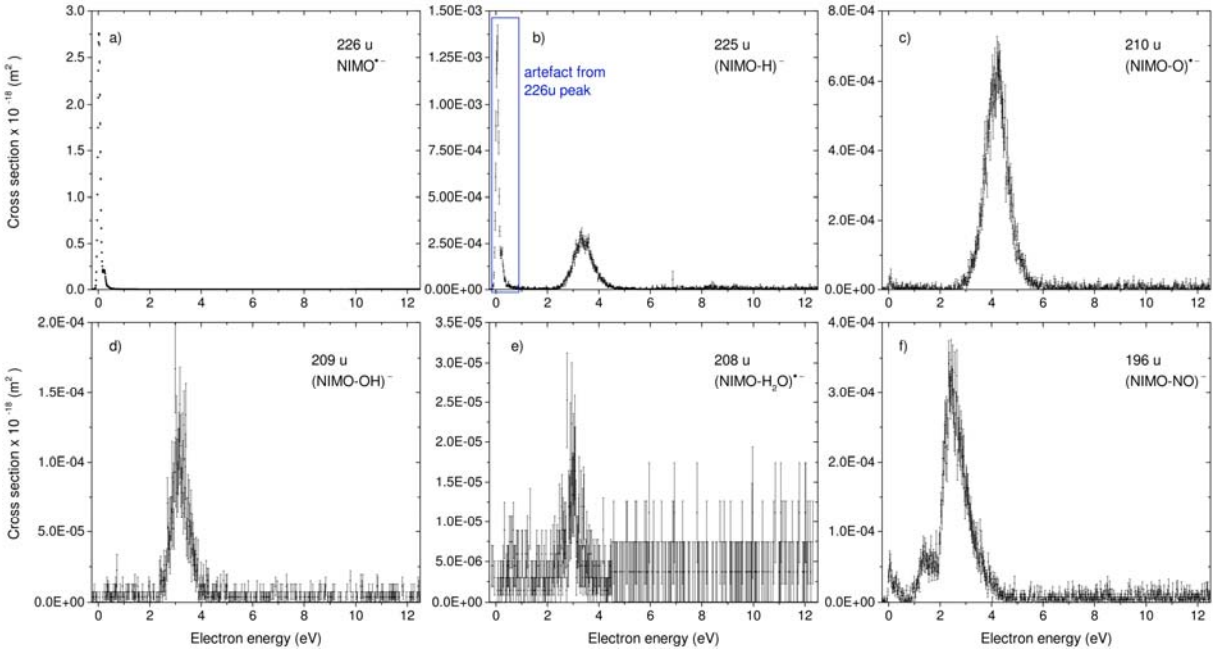

Supplementary Figure 1. Cross-section as function of the initial electron energy. Cross-section for the formation of the nimorazole radical anion (mass 226 u) and fragment anions with masses between 225 u, $(NIMO - H)^-$, and 196 u, $(NIMO - NO)^-$, in the electron energy range between ~0 eV and 12 eV. The black dots represent the experimentally determined cross-section values as a function of the electron kinetic energy. Statistical error margins are included for each data point and refer to the standard error of the mean, see data analysis section for details in the main paper. The low energy feature in the $(NIMO - H)^-$ ion yield can be ascribed to an artefact from the finite mass resolution of the used quadrupole mass spectrometer and the far higher cross-section for formation of $NIMO^{\bullet-}$, which contaminates here $(NIMO - H)^-$. Source data are provided as a Source Data file.

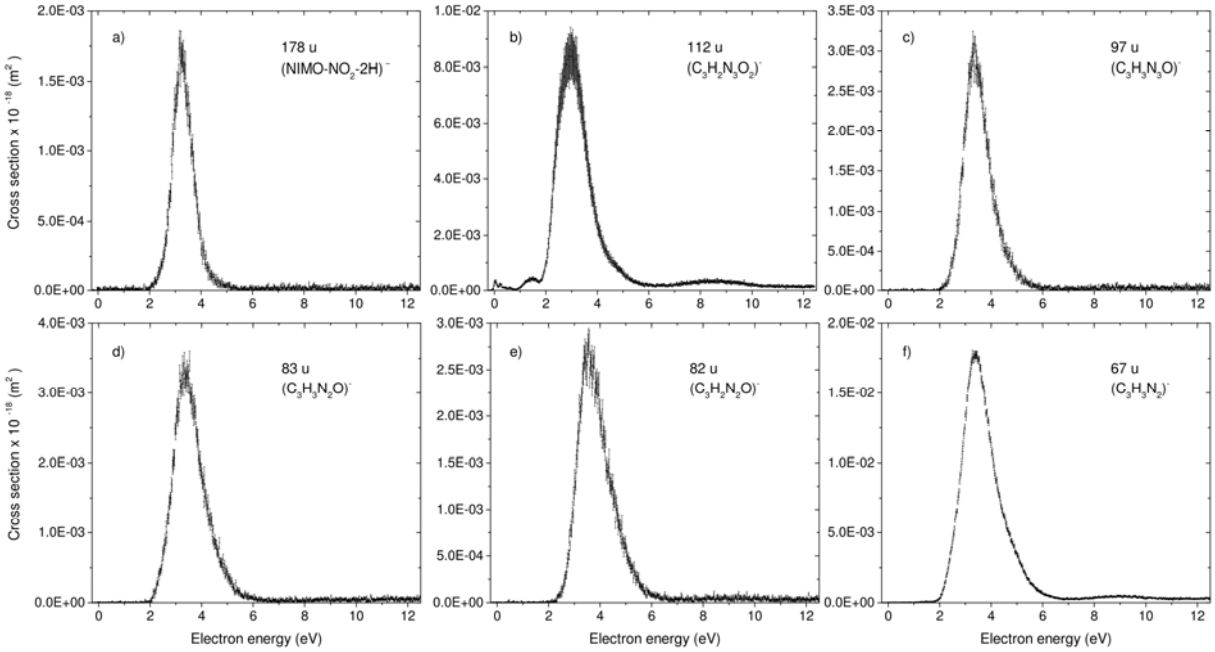

Supplementary Figure 2. Cross-section as function of the initial electron energy. DEA Cross-section for the formation of fragment anions with masses between 178 u, $(NIMO – NO_2 – 2H)^–$, and 67 u, $(C_3H_3N_2)^–$, in the electron energy range between ~0 eV and 12 eV. The black dots represent the experimentally determined cross-section values as a function of the electron kinetic energy. Statistical error margins are included for each data point and refer to the standard error of the mean, see data analysis section for details in the main paper. Source data are provided as a Source Data file.

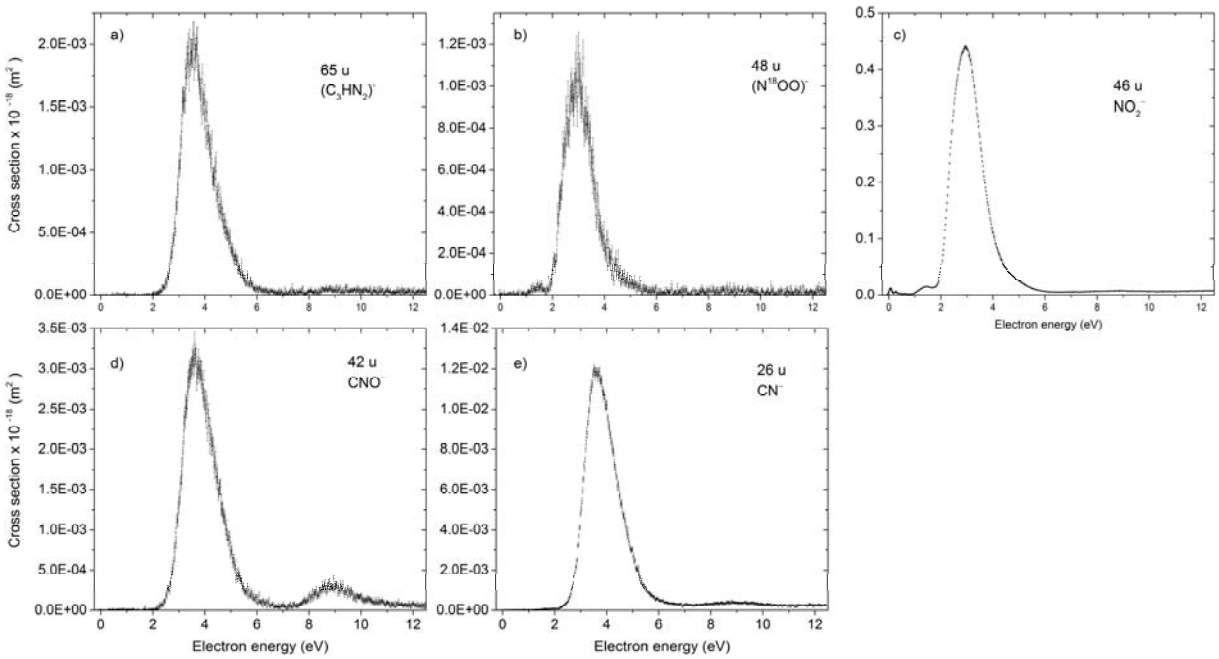

Supplementary Figure 3. Cross-section as function of the initial electron energy. DEA Cross-section for the formation of fragment anions with masses between 65 u, $(C_3HN_2)^-$, and 26 u, $(CN)^-$, in the electron energy range between ~0 eV and 12 eV. The black dots represent the experimentally determined cross-section values as a function of the electron kinetic energy. Statistical error margins are included for each data point and refer to the standard error of the mean, see data analysis section for details in the main paper. Source data are provided as a Source Data file.

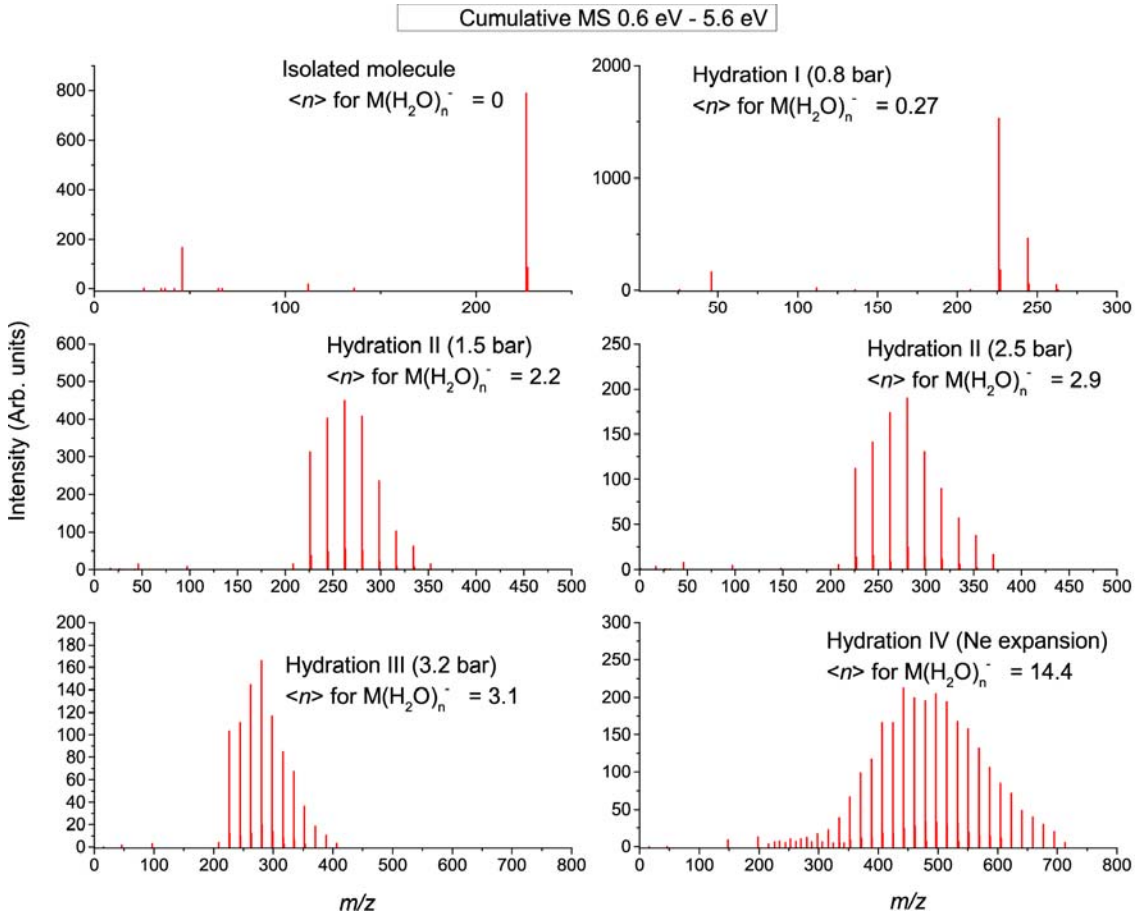

Supplementary Figure 4. Cumulative mass spectra for different hydration conditions. The cumulative mass spectra are used for calculation of intensity ratio of NO_2^- to $NIMO(H_2O)_n^-$ ion signal and mean number of water molecules <*n*> in the mixed cluster $NIMO(H_2O)_n^-$, which are plotted in the Figure 3. Source data are provided as a Source Data file.

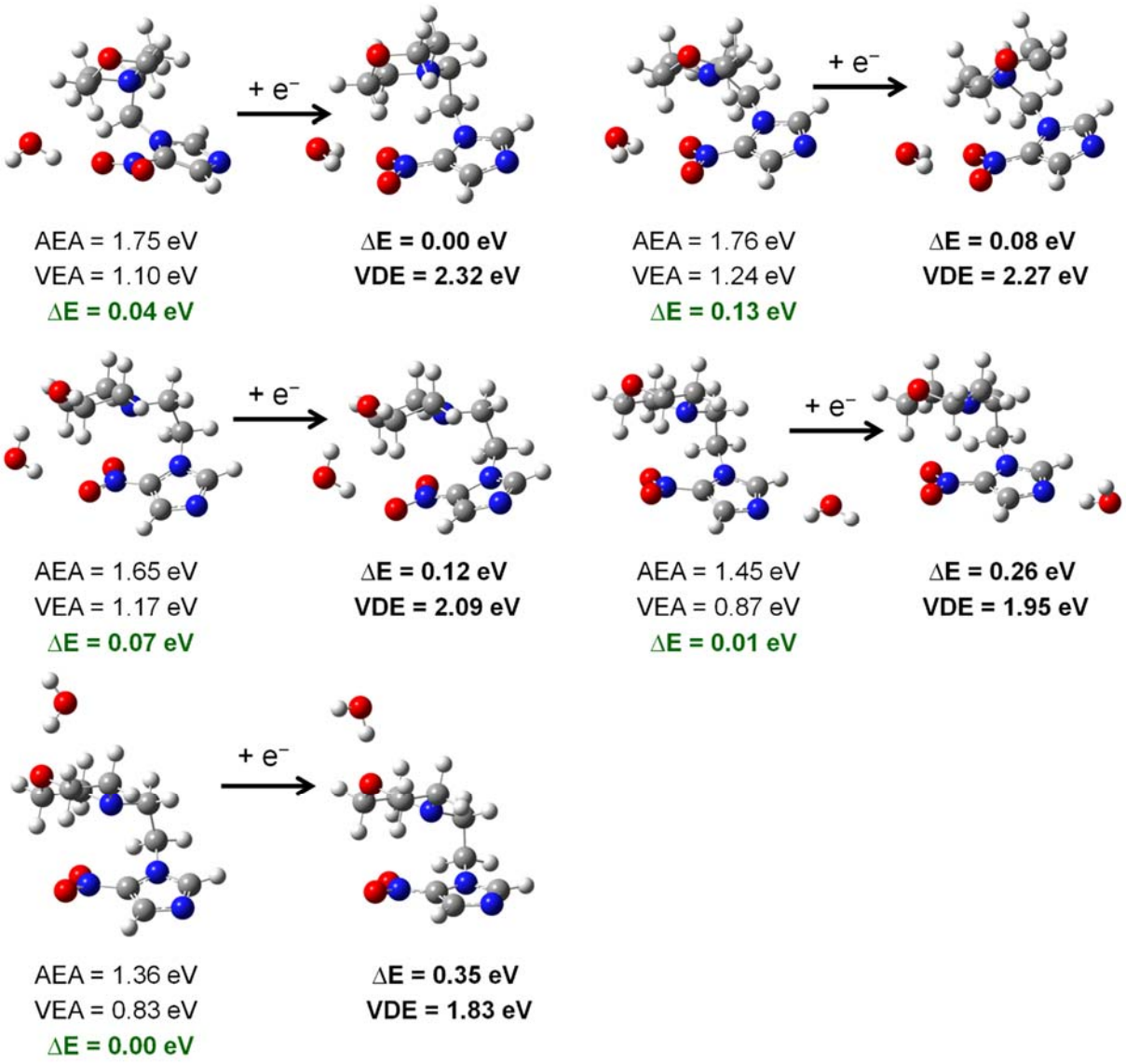

Supplementary Figure 5. Nimorazole hydrated by one water molecule. M062x/6-31+G(d,p) optimized structures of neutral and anionic NIMO hydrated by one water molecule. Adiabatic electron affinities (AEA), vertical electron affinities (VEA) are shown below the neutral structures together with relative energies in green. The relative energies of anionic structures and corresponding vertical detachment energies (VDE) are shown below the structures of the anions. Colour coding: Carbon (grey), hydrogen (white), nitrogen (blue), oxygen (red).

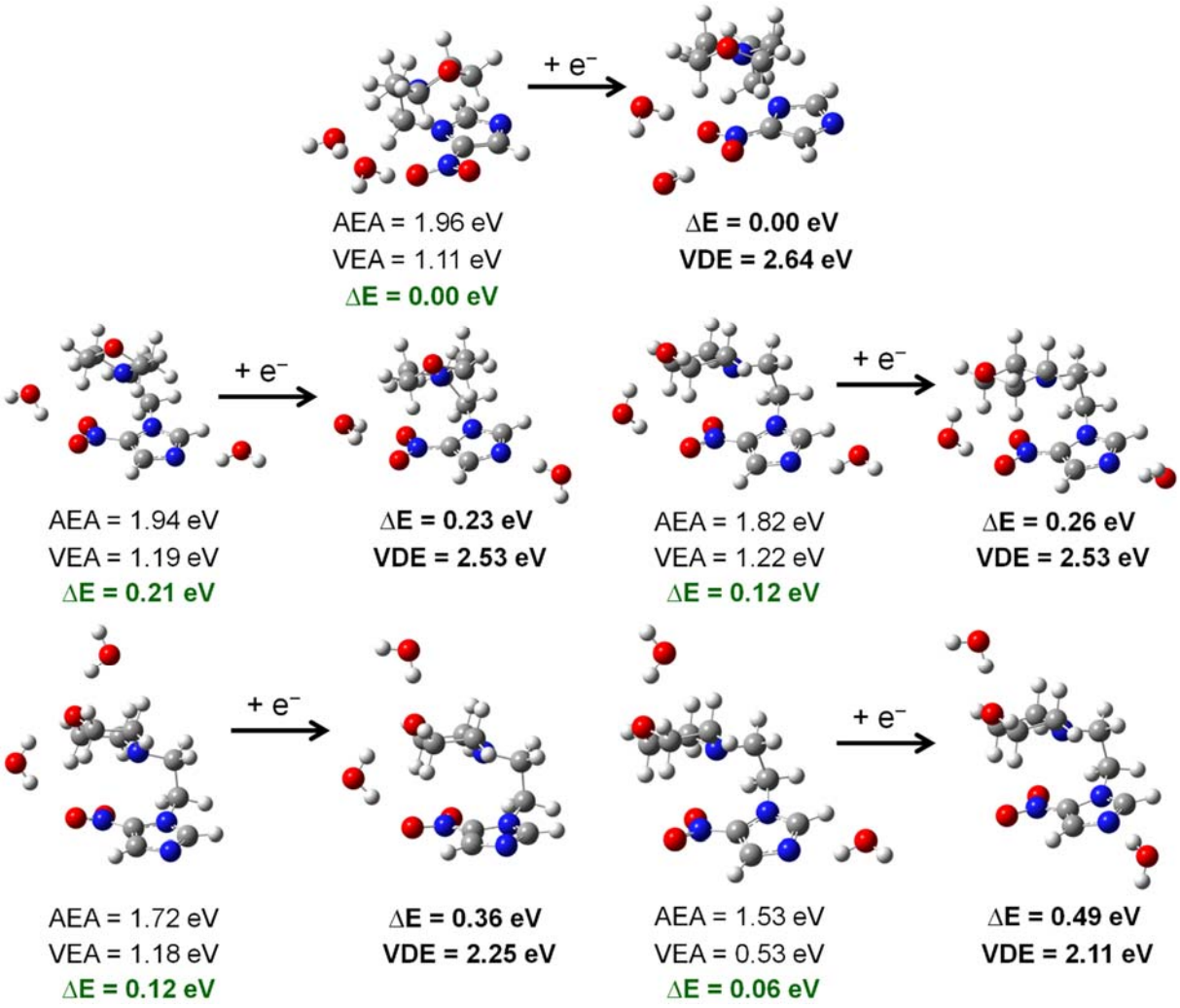

Supplementary Figure 6. Nimorazole hydrated by two water molecules. M062x/6-31+G(d,p) optimized structures of neutral and anionic NIMO hydrated by two water molecules. Adiabatic electron affinities (AEA), vertical electron affinities (VEA) are shown below the neutral structures together with relative energies in green. The relative energies of anionic structures and corresponding vertical detachment energies (VDE) are shown below the structures of the anions. Colour coding: Carbon (grey), hydrogen (white), nitrogen (blue), oxygen (red).

5.2 Doped Neon Cluster

Rare gas clusters are an interesting field of research since they are only bound by the weak van der Waals force if no excess charge is present. Due to their low binding energies, they only form at low temperatures and thus provide very cold environments (see sections 2.4 and 2.4.3).

Here, the focus lies on the study of doped neon clusters. In order to understand the motivation for doping rare gas clusters and the attributed gain of knowledge, a short overview of the current knowledge of bare rare gas clusters, with focus on neon, is provided here. This covers the structure of the clusters and especially stable configurations, the temperature of clusters, and finally the state of matter they appear in.

The structure of clusters with focus on stable configurations is investigated by combining experimental data of mass spectra and calculations concerning which arrangements of atoms are energetically favourable. The mass spectra provide information about the ion yields of the cations of all clusters sizes. By comparing their relative intensities, particularly stable sizes can be identified. Those cations which exhibit a higher ion signal than the previous peak of the series are referred to as magic numbers. Early studies of electron ionisation of rare gas clusters have found a common set of magic numbers, see reference [54] and references within. Calculations of their structures define certain series in dependence on their packing styles. For example, the stable cluster sizes of 13 and 55 rare gas atoms belong to the close packing style structure formed by icosahedral shells [51, 243]. The series containing, among others, 19 and 25 arise from the addition of an incomplete shell to an icosahedral shell, thus closing a sub-shell [51]. But not all studies could reliably reproduce the magic numbers, see reference [244] and references within. A recent study by Gatchell *et al.* was able to attribute the common set of magic numbers to contributions from protonated rare gas clusters [244]. The protonation can arise from impurities like water molecules in the vacuum chamber. According to their study, only the protonated cluster series form magic numbers, while the charged systems show only few annomalies [244]. Besides the magic numbers which are common for protonated and neutral systems, each rare gas also features characteristic stable configurations. For neon, Märk *et al.* reported neon clusters with a size of 21 and 75 atoms to be particularly stable. They discuss that these features must be an individual property and assign the structure of Ne_{21} to a dodecahedron [245].

The temperature of rare gas clusters was already discussed in chapter 2.4 and is just briefly summarised here for reasons of completeness. In contrast to the structure of rare gas clusters, which shows size dependent effects, the temperature of a cluster is size independent but characteristic for each gas. The temperature for clusters in vacuum is lowest for the lightest rare gas, helium, (0.37 K) and increases via neon (10 ± 4 K) to the higher mass rare gases [54, 56]. These values are determined from a electron diffraction study of cluster sizes above 800 components combined with a theoretical model covering smaller clusters sizes not accessible with this method [56].

Another property of clusters is the state of matter they appear in. Helium clusters are fluid and, depending on their size and ultimately temperature, with a superfluid core [54], while argon clusters have both solid and liquid forms, with the state of matter being dependent on their size [246]. For neon clusters, several studies were conducted to determine their state of matter. They all predict a phase transition from liquid like clusters to solid clusters at a certain size. A photodissociation study of neon clusters doped with hydrogen halides by Slavíček *et al.* combined with calculations reported a semi-liquid core for Ne_{130} and a fully solid core for Ne_{300}, both with a liquid outer shell

[247]. In an electron diffraction experiment by Torchet *et al.*, the transition from liquid to solid clusters was predicted at around Ne_{150} [247]. Slavíček *et al.* explain the slight deviation to their values by the method used by Torchet *et al.*, which is mainly sensitive to the volume of the cluster. The phase behaviour was also studied by von Pietrowski *et al.* with fluorescence excitation spectra of neon clusters doped with xenon [248]. For pick-up experiments performed at mean cluster sizes of 100 neon atoms, they report the observations of interior xenon states, indicating fluid neon clusters. Increasing the mean neon cluster size in co-expansion experiments, they extended the cluster range to a mean size of 200 neon atoms, for which interior like bulk states, in contrast to surface states, were observed. For Ne_{300} and higher, they started measuring a mixture of bulk and surface states, the latter indicating solid neon clusters as the xenon can no longer penetrate them [248]. In summary, all studies agree that small neon clusters are liquid and experience a phase transition to solid clusters towards higher cluster sizes, though the exact transition point is still a matter of discussion. All studies investigating the state of matter of a cluster involve doped neon clusters. The conclusions are drawn either by comparing the expected behaviour of the dopant inside and on the surface of the neon cluster with calculations, or on the signal, which is characteristic for a dopant in the bulk or on the surface of the cluster. Additionally, dopants inside a liquid cluster can move, accumulate and form a cluster by themselves, a process not possible for a solid cluster.

Thus, it is obvious that the study of doped rare gas clusters is a useful tool to extend the knowledge about the characteristics and properties of the clusters themselves. This is also the motivation to study these in the course of this thesis.

One example among the characteristics that are accessible by the investigation of doped neon clusters are energy bands. These usually form in condensed matter, an effect caused by the coalescence of the energy levels of the individual atoms. It is yet unclear whether a cluster forms those energy bands and if so, from which cluster size onward this occurs. This effect can be studied by doping the cluster. If energy bands are present, the cluster's environment provides an energetic barrier that an incoming electron needs to overcome in order to interact with the dopant inside of the cluster. By comparing results of electron attachment studies from isolated compounds with data from compounds embedded in clusters, this barrier can be measured and quantified.

Besides acquiring knowledge about neon clusters themselves, the effects of the cluster on the dopant can be studied. For this thesis, this especially includes the stabilisation of both cations and anions by the cluster environment. The cluster provides a medium for energy dissipation so that fragmentation caused by excess energy can be quenched.

In the next sections, the results of measurements taken of neon clusters doped with carbon dioxide, water, heavy water, and molecular oxygen are presented. The experimental setup used for data acquisition is the Wippi apparatus as described in chapter 3.1. Studies performed on bare neon clusters in the course of this thesis were a joint project with other PhD and master students and were already described in their theses [70, 249].

Section 5.2.1 addresses cationic mass spectra from electron ionisation of doped neon clusters. The dopants form clusters during the pick-up process, using the neon as condensation nuclei. Thus, the mass spectra both provide insights into characteristics of the neon cluster, especially their state of matter, and can be used to identify magic numbers of the dopants. Those are compared to measurements of bare cluster beams of those compounds, if data is available.

Section 5.2.2 focuses on dopant anions produced by dissociative electron attachment.

The data is compared to results obtained by previous studies of the bare compounds. Hence, the influence of the neon cluster on the dopant can be studied, including stabilisation processes. Additionally, the data provides insights about the nature of neon clusters and whether at the produced mean clusters sizes a band structure forms, which would show up as energy shift in the resonance positions of the dopant anions.

5.2.1 Cationic Mass Spectra upon Electron Ionisation

In general, the cationic ion yields from a given compound produced by electron ionisation are higher than the anionic signals formed by (dissociative) electron attachment. Thus, most mass-spectrometric experimental investigations include cationic mass spectra, which also provide information for further analysis. This includes, for example, the fragmentation pattern for gas phase studies or the distribution of cluster sizes for cluster experiments, and which cluster series can be observed. For doped clusters, several series are possible, including the bare parent cluster series, the dopant cluster series, a combination of both, or even series including fragments of the dopant. Here, mass spectra of neon clusters doped with four different molecular species are presented, namely carbon dioxide (CO_2), molecular oxygen (O_2), water (H_2O), and heavy water (D_2O).

For liquid neon clusters, the dopant molecules can move within the cluster and form clusters of their own. The formation of dopant clusters is driven by polarisation effects. As has been discussed in chapter 2.4, rare gas clusters provide cold environments, especially when compared to molecular clusters. In order to produce molecular clusters at such cold energies, they can either be formed by co-expansion with a rare gas, or alternatively by pick-up processes. Previously, groups like the group of Möller at DESY have demonstrated the efficiency of those processes [250, 251].

For the studies presented in this chapter, the molecular clusters were formed in a pick-up process by the neon clusters. The neon clusters were produced by supersonic expansion. The neon gas of purity 99.999 % was purchased from Messer. For the expansion, a stagnation pressure of (19–20) bar was adjusted and the gas was cooled down to temperatures between (60–105) K, depending on the measurement. The diameter of the nozzle used is 10 µm. This resulted in typical background pressures in the cluster source chamber of up to $1 \cdot 10^{-4}$ mbar. Higher stagnation pressures and warmer temperatures resulted in increased background pressures, which caused the destruction of the neon clusters and thus unfavourable measurement conditions. Lower temperatures caused nozzle clogging caused by impurities and were hence experimentally not accessible for data gathering. Lower stagnation pressures reduce the neon mean cluster size according to equations 2.56, 2.57, and 2.58. During the pick-up process of each molecule, energy is brought into the cluster. As soon as it exceeds the binding energy of neon, neon atoms are evaporated in the process of evaporative cooling, described in section 2.4.3. As a consequence, as large neon clusters as possible are preferred to start with in order to produce molecular clusters of reasonable size and stability. Thus, the stagnation pressure of neon was kept at the highest possible value while still resulting in reasonable background pressures in the chamber. Additionally, this implicates that different initial conditions affect both the neon cluster size and the molecular cluster size distribution. The nozzle to skimmer distance is adjusted to about 15 mm. The pick-up pressure was optimised for each component and is on the order of 10^{-4} mbar. Specific values are given in the discussion of each molecule. In order to avoid confusion, N is used when referring to the neon cluster size, and n when referring to the dopant cluster size.

Carbon Dioxide

Carbon dioxide (CO_2) is omnipresent in nature, for example as major component in the carbon cycle. It is formed by both natural sources, such as in the respiration process of aerobic organisms, as well as by synthetic sources, including mainly the burning of fossil fuels. CO_2 clusters might thus have atmospherical and industrial importance.

For the mass spectrometry experiments conducted in the course of this thesis, the CO_2 analyte gas (purchased from Messer with a purity of 99.9995 %) was introduced into the pick-up chamber, adjusting the pressure of approximately $9 \cdot 10^{-4}$ mbar for maximal ion yields. The neon gas was cooled down to 74 K, giving together with the nozzle diameter of 10 µm and the stagnation pressure of 19 bar a mean neon cluster size of $\bar{N} = 61$, as calculated with equations 2.56, 2.57, and 2.58. The mass spectrum recorded at 70 eV incident electron energy and 20 nA electron current as measured at the Faraday cup is shown in figure 5.8. The electron energy scale was calibrated as described in chapter 3.3.2.

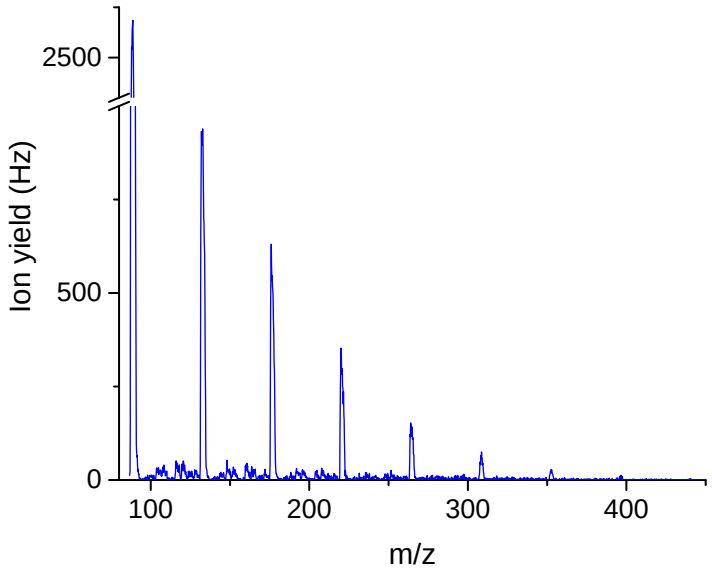

Figure 5.8: Cationic mass spectrum upon electron ionisation of neon clusters doped with carbon dioxide in a pick-up process, starting from the carbon dioxide dimer. The calculated neon mean cluster size after supersonic expansion is $\bar{N} = 61$, the electron energy is 70 eV, and the electron current is 20 nA. The main peaks belong to the $(CO_2)_n^+$ series.

The cluster series of $(CO_2)_n^+$ is dominating the spectrum and shown from the dimer onward to $n = 9$, see figure 5.8. In order to facilitate the analysis, the mass spectrum was analysed with the program IsotopeFit and the cluster series were extracted, see chapter 3.3.1 and reference [115] for details. Figure 5.9 shows the extracted cluster series for $(CO_2)_n^+$ (a)), and for $(CO_2)_nCO^+$ and $(CO_2)_nNe^+$ (b)). The cluster series for the bare dopant is the strongest observed. As shown in figure 5.9 b), there is a contribution of the dopant cluster series with one attached Neon atom, but at far weaker ion yields.

The reason for this effect is likely found in the formation process of the carbon dioxide clusters. When a CO_2 molecule attaches to another one, or to a cluster of carbon dioxide, the binding energy is released. The exact value depends on the cluster size, for the dimer it amounts to $E_B((CO_2)_2) \approx 60$ meV [252] and for an individual bond between two carbon dioxide molecules in the trimer $E_B((CO_2)_3) \approx 100$ meV [253]. The general

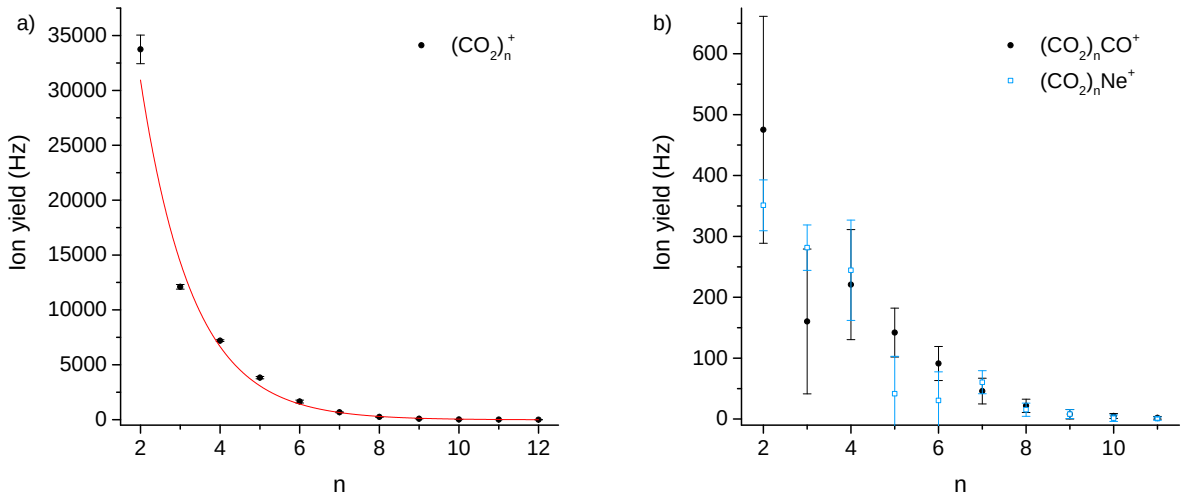

Figure 5.9: Extracted cluster series a) for $(CO_2)_n^+$, including an exponential decay fit (red line) and b) for $(CO_2)_nCO^+$ and $(CO_2)_nNe^+$.

trend is an increasing binding energy with increasing cluster size, with a few exceptions [253]. The binding energy between two neon atoms amounts to $E_B(\mathrm{Ne}) \approx 3.5\,\mathrm{meV}$ [254]. As an approximation, an average binding energy for a CO_2 molecule of 75 meV can be assumed as a typical energy for all cluster sizes. If all this energy is carried away by neon evaporation, about 20 neon atoms would be ejected of the cluster for each CO_2 binding to the carbon dioxide cluster. With the calculated mean neon cluster size of 61 atoms, only 3 bonds between carbon dioxide clusters could be formed, leading to a trimer. Thus, either the original mean neon cluster size is underestimated, only the large clusters from the distributions contribute, or the stabilisation process of CO_2 clusters is driven, at least partly, by additional processes. These could include collisional cooling or the redistribution of energy within the cluster leading to stabilisation.

In general, the cluster series are expected to follow an exponential decay distribution. Notable deviations from this behaviour indicate either a very stable cluster configuration (magic numbers), or an unstable structure (anti-magic). An exponential function was fitted to the cluster series of $(CO_2)_n^+$ as shown by the red line in figure 5.9 a). While the pentamer exhibits an ion yield slightly higher than expected from the exponential fit, the trimer exhibits an ion yield below the expected one by the fitted distribution. The latter phenomenon is also seen for $(CO_2)_3CO^+$. This observation is supported by the data taken of bare carbon dioxide clusters by Knapp *et al.*, who report electron ionisation mass spectra at 30 eV incident energy [255]. These also show a weak trimer ion yield. Unfortunately, no complete study on binding energies of neither neutral nor ionic carbon dioxide clusters exists for the full range of the observed cluster sizes. The most extensive study by Norooz Oliaee *et al.* reports the binding energy of neutral CO_2 clusters starting only from $n = 3$ onward, not allowing for an explanation why the trimer is particularly unstable [253].

Another factor which should be mentioned is that besides the initial expansion conditions, the electron energy influences the ion yield distribution, too. In general, higher impact energies are more likely to cause fragmentation of the cluster, resulting in a distribution favouring small cluster sizes. The effects of the stagnation pressure and the electron incident energy on bare CO_2 clusters were reported by Romanowski *et al.* [256].

Besides the bare cluster series of the dopant and the series with one neon atom

attached, it is worth noting the cluster series which involves fragmentation of the carbon dioxide molecule, the $(CO_2)_nCO^+$. Its ion yield is comparable with the $(CO_2)_nNe^+$ series. The decrease of intensity with increasing n seems to follow an exponential decay, but the high fluctuations do not allow for a definite assignment. Additionally, the large uncertainties do not allow for the identification of magic numbers, although $n = 3$ looks less abundant, thus anti-magic. Whether the dopant clusters form the dominant series or rather the dopant clusters with an additional fragment depends on the molecule under investigation, as can be seen in the subsequent sections.

(Deuterated) Water

Water is probably one of the most extensively studied chemical compounds, as it is the most abundant substance on the surface of the Earth where it can be found in gas, liquid, and solid phase [257]. Fully deuterated, or heavy water has instead of the two hydrogen atoms two deuterium atoms, and thus has the chemical formula D_2O.

Both for H_2O and D_2O doped neon clusters, cationic mass spectra were recorded. They were taken at neon stagnation pressures of 20 bar and a nozzle temperature of 70 K. Hence, the mean neon cluster size amounts to $\bar{N} = 79$, as calculated with equations 2.56, 2.57, and 2.58. The water used in this experiment was de-ionised and the deuterated water was purchased from Sigma Aldrich with a stated purity of 99.9 %. The pick-up pressure was optimised for maximal ion yields and amounts to $3.5 \cdot 10^{-4}$ mbar for H_2O, and $5 \cdot 10^{-4}$ mbar for D_2O. The mass spectra were recorded at 70 eV incident electron energy with a current of approximately 30 nA as measured at the Faraday cup, and shown in figures 5.10 and 5.11. The electron energy scale was calibrated as described in chapter 3.3.2.

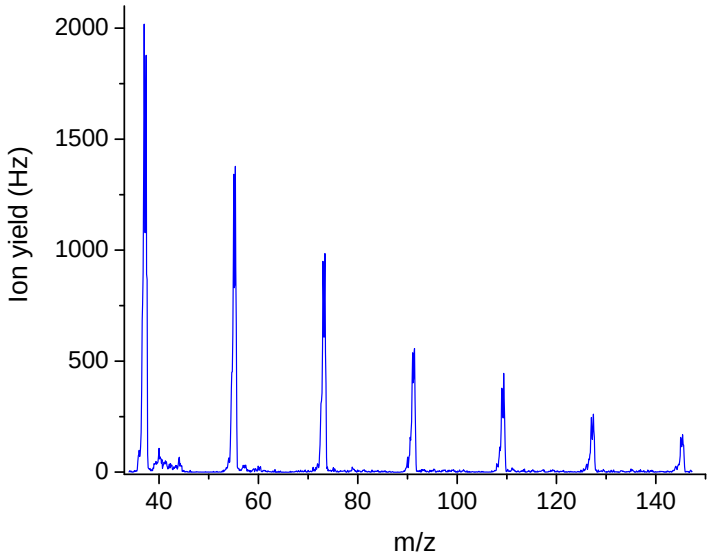

Figure 5.10: Cationic mass spectrum upon electron ionisation of neon clusters doped with water in a pick-up process. The calculated neon cluster size after supersonic expansion is $\bar{N} = 79$, the electron energy is 70 eV, and the electron current is 30 nA. The main peaks belong to the $(H_2O)_nH^+$ series, with n=2-8.

Both molecules feature the $(H_2O)_nH^+$, or $(D_2O)_nD^+$ series as most dominant one, equivalent to $H_3O(H_2O)^+_{n-1}$, or $D_3O(D_2O)^+_{n-1}$, respectively, which are indistinguishable for the mass spectrometer. For both mass spectra, there are additional minor peaks observable around the main cluster series, as shown for one example peak region for heavy

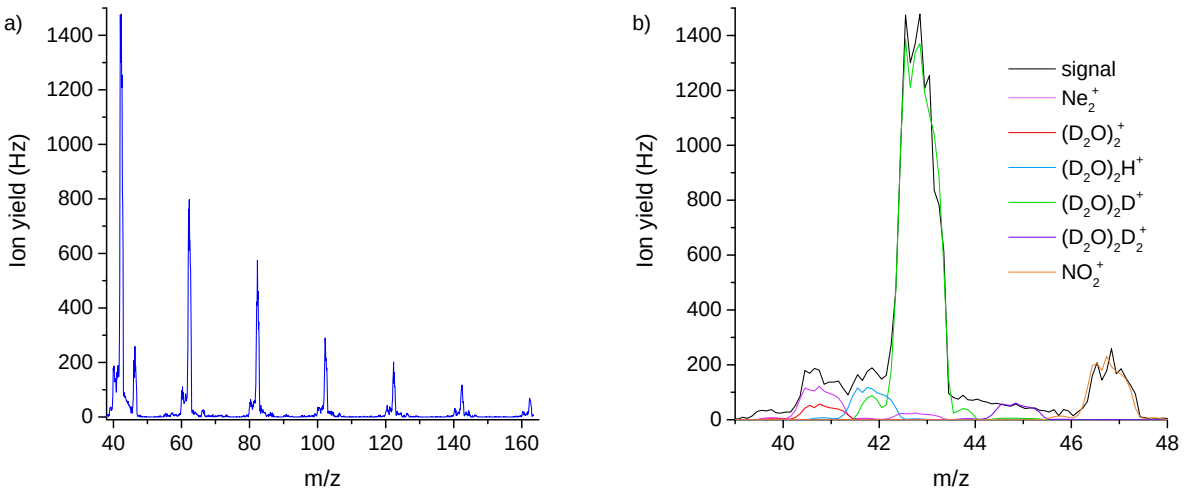

Figure 5.11: Cationic mass spectrum upon electron ionisation of neon clusters doped with heavy water in a pick-up process. The calculated neon cluster size after supersonic expansion is $\bar{N} = 79$, the electron energy is 70 eV, and the electron current is 30 nA. a) The main peaks belong to the $(D_2O)_nD^+$ series. b) The detailed view of the region between m/z=40 and 48 reveal further minor peaks around the $(D_2O)_2D^+$ peak where unambiguous assignment of contributors is difficult.

water in figure 5.11 b). The detailed view reveals that the unambiguous assignment of constituents is not always possible. For example, at m/z=40, contributions from Ne_2^+ and $(D_2O)_2^+$ are possible. The use of a quadrupole mass analyser does not allow for a more distinct evaluation as its mass resolution is rather poor as when compared to a time-of-flight analyser. Nevertheless, cluster series were extracted with IsotopeFit for both molecules and are shown in figures 5.12 and 5.13, see chapter 3.3.1 for details.

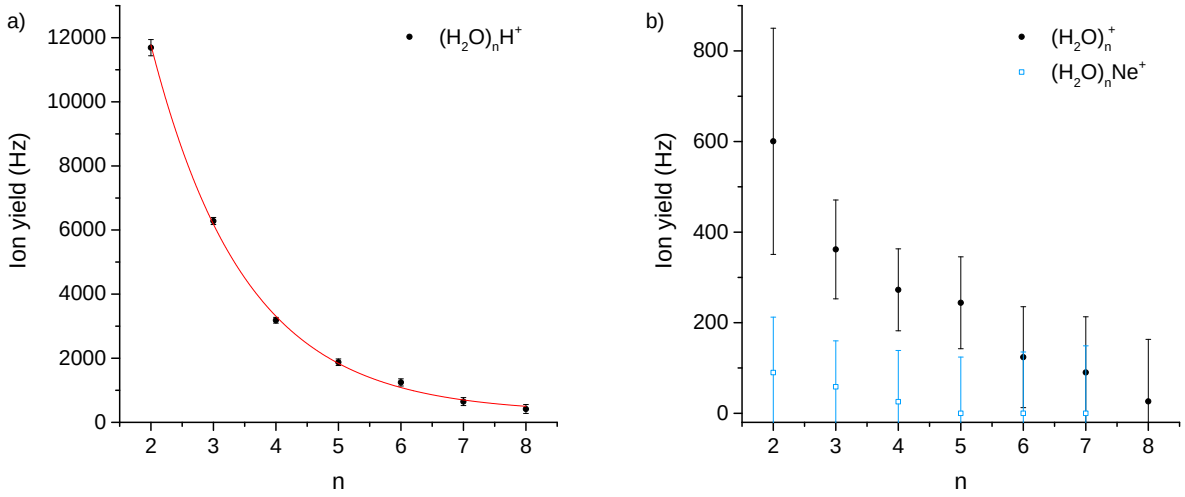

Figure 5.12: Extracted cluster series for a) $(H_2O)_nH^+$, including an exponential decay fit (red line) and for b) $(H_2O)_n^+$ and $(H_2O)_nNe^+$.

For water, the cluster series of $(H_2O)_nH^+$ does not reveal any magic numbers, but the data coincides with the fitted exponential function within the uncertainties. For heavy water, the $(D_2O)_4D^+$ is slightly above the fitted curve, indicating that this is a stable configuration. Electron ionisation studies of pure water clusters were already published by Huang *et al.* and Lengyel *et al.* [258, 259]. Mass spectra were recorded for different mean cluster sizes. They all featured a magic number for $(H_2O)_4H^+$ and additional ones

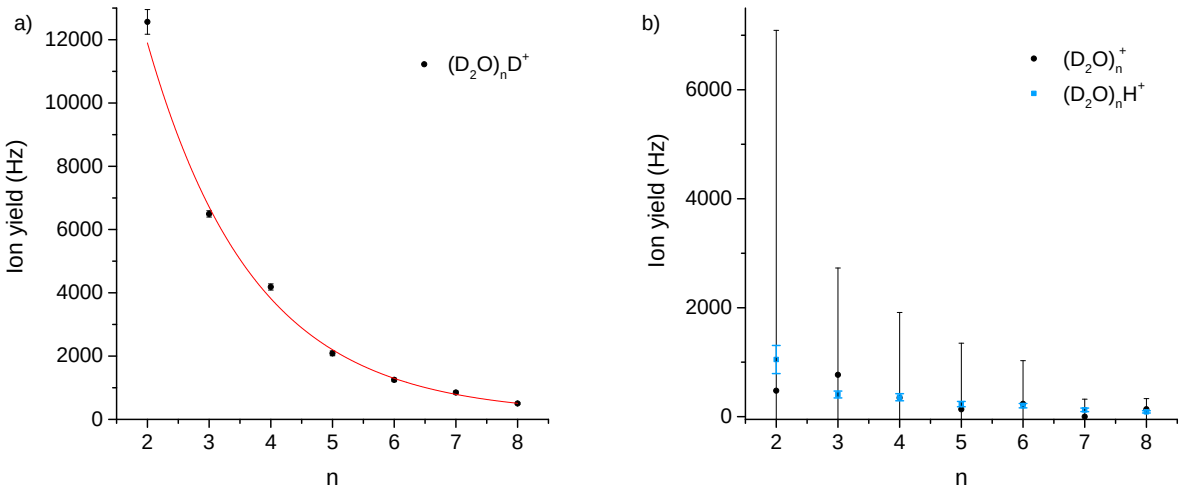

Figure 5.13: Extracted cluster series for a) $(D_2O)_nD^+$, including an exponential decay fit (red line) and for b) $(D_2O)_n^+$ and $(D_2O)_nH^+$.

showed up for spectra taken for distributions with a higher mean cluster size. Compared to the data reported here, all spectra in reference [259] were taken for higher mean cluster sizes, i.e. the maximal cluster size observed was much higher. Thus, a possible explanation for the absence of magic numbers for the data shown in figure 5.12 could be that the initial conditions did not allow for the formation of a cluster distribution with a high enough mean cluster size where magic numbers in the $(H_2O)_nH^+$ series form. At this point, it should also be mentioned that the detected cluster sizes do not have to coincide with the cluster sizes of the produced neutral clusters, as electron ionisation is a hard ionisation method which can lead to the fragmentation of the cluster. Additionally, the ionisation process is usually the driving force behind forming magic sizes in cluster experiments. The pickup statistics have little preference for magic sizes, but after ionisation, the excess energy will deplete weaker systems and exaggerate more stable ones [260, 261].

In contrast to the carbon dioxide clusters, the non-fragmented cluster series are strongly suppressed for both water and heavy water, see figures 5.12 b) and 5.13 b). Due to the large uncertainties caused by overlapping contributions, particularly stable configurations could not be identified. Interestingly, in the case of heavy water also a $(D_2O)_nH^+$ series is observed. The hydrogen can either result from H_2 or H_2O from the background, or impurities in the sample, since the D-H exchange is very efficient. Again, mixed series of water and neon are not observed.

Several theoretical studies investigated the binding energy of pure water clusters, e.g. references [262–264] and references within. The results strongly depend on the level of theory used, and also on the structure assumed. A common result is that the binding energy consistently increases with cluster size, as does the binding energy per water molecule. Just to state some example values, the binding energy for the dimer is reported to be approximately 0.2 ± 0.1 eV, for the trimer around 0.6 ± 0.2 eV, and for the tetramer it is 1.7 ± 0.4eV [262–264]. Since the binding energy increases continuously without characteristic features indicating particularly stable or unstable configurations, this cannot explain the formation of magic numbers. Qian *et al.* additionally showed the configurations of the studied cluster sizes and reported a change from planar ($n = 2-5$) to 3D ($n > 5$) conformers, but the geometry change does not result in higher binding energies [262] or magic numbers.

Molecular Oxygen

Molecular oxygen is, like carbon dioxide and water, omnipresent in the environment [265]. Molecular oxygen is covalently bound and chemically active. O_2 is essential for human life and has wide applications in industry, e.g. in the textile industry [266].

Molecular oxygen, purchased from Messer with stated purity of 99.998 %, is introduced into the pick-up chamber and a pressure of around $1 \cdot 10^{-3}$ mbar was set. The stagnation pressure of neon was 19 bar and the nozzle temperature 85 K, resulting in a calculated neon cluster size of $\bar{N} = 38$ atoms. The recorded mass spectrum is shown in figure 5.14 at 70 eV impinging electron energy and 20 nA electron current. The electron energy scale was calibrated as described in chapter 3.3.2.

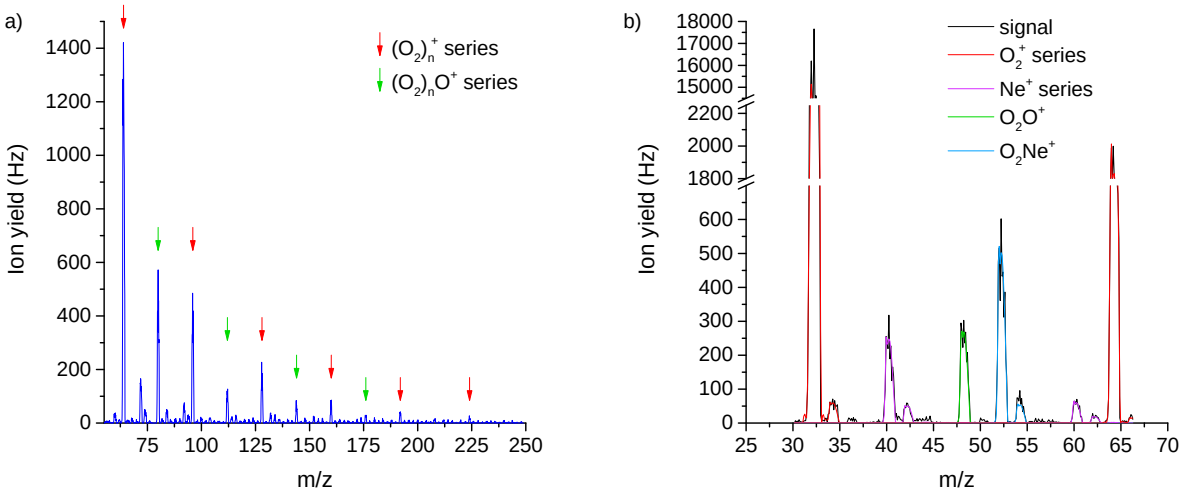

Figure 5.14: Cationic mass spectrum upon electron ionisation of neon clusters doped with molecular oxygen in a pick-up process. The calculated neon cluster size after supersonic expansion is $\bar{N} = 38$, the electron energy is 70 eV, and the electron current is 20 nA. a) The main peak series belong to the $(O_2)_n^+$ (red arrows), but the $(O_2)_nO^+$ series (green arrows) is also clearly visible. b) The detailed view into the region between m/z=30 and 65 reveals further series, including Ne_n^+ (purple) and O_nNe^+ (blue). The accumulated ion yield of all series is shown as black line and labelled as signal.

In contrast to the previously discussed mass spectra, the data of neon clusters doped with molecular oxygen features at least two cluster series with similarly high ion yields. The most prominent is given by the $(O_2)_n^+$ series, indicated by red arrows in figure 5.15 a). The green arrows in the same figure display the position of the $(O_2)_nO^+$ series. As the detailed view into the region between O_2^+ and $(O_2)_2^+$ in figure 5.15 b) shows, O_2Ne^+ exhibits an even higher signal than O_2O^+ (or O_3^+), but otherwise the peaks of the $(O_2)_nO^+$ series are higher than the peaks of the $(O_2)_nNe^+$ series. The highest ion yield of the neon dimer cation in any of the presented cationic mass spectra is found for the doping with molecular oxygen with a contribution similar to the O_2O^+ signal. This is surprising since the pressure in the pick-up region was highest for the molecular oxygen investigations. A possible explanation is that the high pickup pressure causes a fragmentation of the neutral neon clusters. The smaller neon clusters cannot efficiently pick up oxygen molecules and as a consequence, the bare neon cluster is ionised and the positively charged neon dimer is detected. In figure 5.15, the cluster series as extracted with IsotopeFit are shown for the $(O_2)_n^+$ series (a)), and the $(O_2)_nO^+$ and $(O_2)_nNe^+$ series (b)).

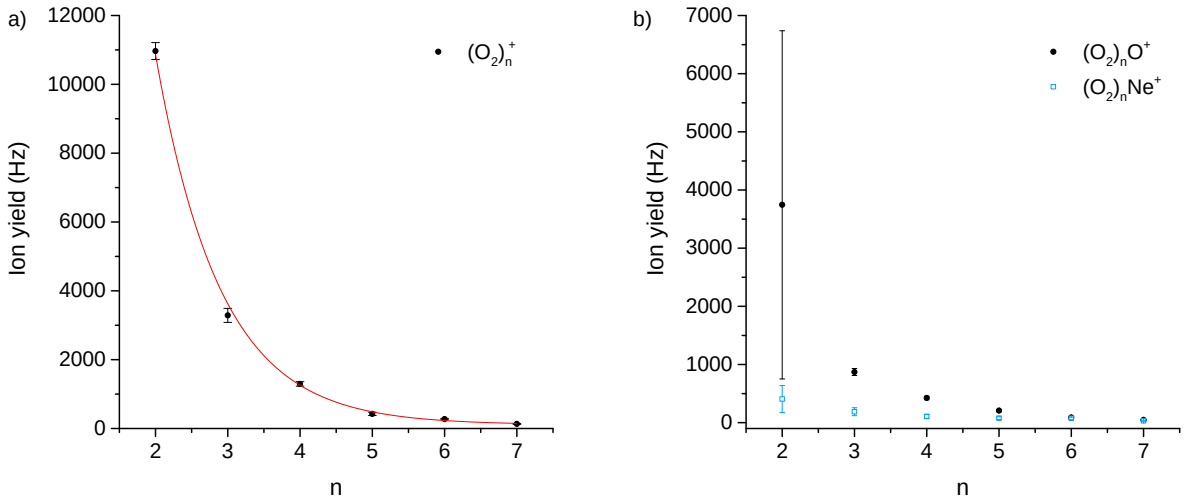

Figure 5.15: Extracted cluster series a) for $(O_2)_n^+$, including an exponential decay fit (red line) and b) for $(O_2)_nO^+$ and $(O_2)_nNe^+$.

The $(O_2)_n^+$ series matches the fitted exponential function within the uncertainties, but it is noticeable that clusters of even number of O_2 systematically lie above the fitted curve and clusters of odd numbers of O_2 lie systematically below the line. The cluster series for $(O_2)_nO^+$ exhibits a large uncertainty for $n = 2$, mainly caused by the possible assignment of the peak to the neon tetramer cation since both have the same mass and the quadrupole mass analyser is not sensitive enough to distinguish both. As the neon cluster series can be inferred from the other sizes and a large increase in the ion yield for the tetramer is rather unlikely, and additionally the $(O_2)_2O^+$ fits into an exponential decay distribution, this uncertainty is likely being overestimated by IsotopeFit.

Binet *et al.* reported mass spectra of bare molecular oxygen clusters after electron impact ionisation for different stagnation pressures and they observed both above mentioned cluster series [267]. They also reported that the $(O_2)_n^+$ series is stronger than the $(O_2)_nO^+$ series and described its alteration in intensities [267]. They explained this effect by the threshold of formation which is higher for an odd amount of oxygen in the final cluster, since at least one covalent double-bond needs to be broken [267]. While in the spectrum of Binet *et al.* the O_2O^+ peak was completely absent, it appears in the mass spectrum taken here and shown in figure 5.14 b). Thus, this might be a stabilisation effect caused by the presence of a neon cluster.

The behaviour of the $(O_2)_nNe^+$ series is comparable to $(CO_2)_nNe^+$, having a measurable contribution to the mass spectrum but with fluctuations within an exponential distribution.

In summary, the cationic mass spectra taken after electron ionisation all show cluster series of the dopant compound. While for carbon dioxide and molecular oxygen the dopant cluster series were most intense, for water and heavy water the protonated and deuterated cluster series are the dominant ones as was already observed in previous studies, as for example in reference [259]. The comparison of the data to previous studies of bare clusters of the dopant show many similarities. But there are also some indications that the neon cluster provides a stabilising environment, one of them is the observation of O_2O^+ which is not observed for bare oxygen clusters. Additionally, some series miss magic numbers observed in the case of bare cluster studies. A possible reason is that the clusters produced here are too small. Generally, the results support the studies addressing the size dependency of the state of matter of neon clusters. The

maximal mean cluster size as calculated with the Hagena parameter was $\bar{N} = 79$. For this size and lower ones, all studies agree on a liquid behaviour of the neon cluster [247, 248]. Only then, the dopant can travel within the cluster and aggregate into a cluster of its own. Since all results presented above contain dopant clusters, this study confirms the liquid nature of small neon clusters.

5.2.2 Electron Attachment to Neon Clusters Doped with Carbon Dioxide

In the following section, the results of (dissociative) electron attachment processes to neon clusters doped with carbon dioxide are described. The experimental setup remains unchanged to the one described in the previous section. Mass spectra and electron efficiency curves were recorded for electron energies between (0–10) eV. As has been shown in the previous section, the produced neon clusters are of liquid nature and the dopants form clusters of their own. After a short summary about the current knowledge on CO_2 clusters concerning electron attachment, the results from the doped neon cluster measurements are compared to previous measurements performed with bare carbon dioxide clusters, and, if available, with studies of doped helium clusters with the same compound as dopant.

Electron Attachment to Carbon Dioxide (Clusters)

In its ground state, neutral carbon dioxide is a linear molecule with double bonds between the carbon and oxygen atoms. In the anionic state, the carbon-oxygen bond is a single bond only and the length is increased. Additionally, the geometry changes from a 180° to 134° angle [268, 269]. The isolated CO_2^- anion is metastable with lifetimes of tens of µs to ms. The reason for the metastability is that the vibrationally excited levels of the neutral compound and the ground level of the anion are energetically close, separated by less than 0.3 eV [268, 269]. As a consequence, the CO_2^- anion is not observed in electron attachment experiments of the isolated molecule, instead either the electron detaches or the molecule dissociates into neutral carbon monoxide molecule (CO) and an atomic oxygen anion (O^-) [270, 271]. Solvation or cluster environments can stabilise the CO_2^- anion [272]. Hence, most experiments on that anion are performed either in rare gas clusters or in alkali halide matrices [272]. Additionally, studies on bare carbon dioxide clusters (supersonic expansion of pure CO_2) were performed, where the process of monomer anion formation can be described by

$$(CO_2)_N + e^- \longrightarrow (CO_2)_N^{-\,*} \longrightarrow (CO_2)_n^- + (N-n)\ CO_2 \tag{5.2}$$

with $n \geq 1$. Those studies report several resonances. The energetically lowest observed resonance is at 0 eV [271, 273, 274]. It was assigned to a vibrational Feshbach resonance [275]. A further broad resonance features a maximum at around 3.8 eV and can be described as the cluster analogue of the $^2\Pi_u$ shape resonance in the isolated CO_2 molecule [271, 273, 276]. Yet another structure is reported at around 12 eV which is assigned to a core-excited resonance [273, 276].

Comparing electron interaction processes with isolated carbon dioxide to the processes with clustered carbon dioxide, the reactions involving the latter one are more complex. First, it should be noted that electron attachment to clusters involves an additional number of possible reaction pathways compared to the isolated molecules. Redistribution of energy within the cluster exhibits many more degrees of freedom.

This includes mechanisms where energy can be transferred into vibrational degrees of freedom of the cluster, which subsequently can lead to the evaporation of neutral monomers [272]. The neutral CO_2 clusters are all energetically lower than their according anionic states which means they posses negative electron affinities, as investigated for clusters up to 5 constituents [277]. The adiabatic electron affinity of the isolated molecule is, with (-0.6 ± 0.2) eV, the highest absolute value and approaches zero with increasing cluster size [268, 269, 277]. Regarding the accommodation of the additional charge, two possibilities, called motifs, exist, as calculated at the Hartree-Fock and post-Hartree-Fock levels [278–280]. The first is referred to as monomer anion motif. The charge is localised at one of the CO_2 molecules while the others act as a solvent. In the second model, the dimer anion motif, the additional charge is distributed symmetrically among both carbon dioxide molecules, forming a C-C bond between them. Studies of the vertical detachment energies of carbon dioxide clusters provide insights into which of the two motifs prevails. Discontinuities were reported at $n = 2$, 6 and 14, which was interpreted as change of the charge carrying species at those sizes [281, 282]. Further studies report on anionic mass spectra taken at varying electron energies in order to identify magic numbers. In the study by Knapp *et al.* mass spectra recorded at 0.5 eV, 3 eV, and 7 eV electron energy were reported. They observed particularly stable configurations for $n = 7,\ 10,\ 14$, and 16. For mass spectra taken at 0.5 eV and 3 eV, additionally the tetramer proved to be stable, while for 3 eV and 7 eV in addition to the $(CO_2)_n^-$ cluster series, the $(CO_2)_nO^-$ was observed [255]. A subsequent photodissociation study by Alexander *et al.* confirmed those numbers [283].

Further studies investigated the formation and properties of CO_2 anions by electron attachment [271, 273, 274, 276]. For the results presented in this thesis, the focus lies on the formation of the $(CO_2)_4^-$ anion by electron attachment. It belongs to the group of stable configurations (magic numbers) and was studied in detail both in bare carbon dioxide cluster experiments and by electron attachment to CO_2 embedded in superfluid helium droplets [273, 274, 284], making it favourable for comparisons among the three systems. Additionally, results of $(CO_2)_2^-$, $(CO_2)_3^-$, and $(CO_2)_5^-$ are reported to complete the study.

The results of electron attachment to carbon dioxide embedded in neon clusters resulting in the $(CO_2)_4^-$ anion are displayed in figure 5.16. The neon clusters were produced by supersonic expansion at 19 bar stagnation pressure and at nozzle temperatures between (60 - 105) K. The nozzle diameter amounts to 10 µm. Depending on the temperature set, the mean neon cluster size ranges between $\bar{N} = 16 - 133$, for 105 K to 60 K, respectively. The size was calculated with equations 2.56, 2.57, and 2.58. The background pressure in the cluster source chamber amounted to $(0.8 - 1.2) \cdot 10^{-4}$ mbar. The carbon dioxide pick-up pressure was set to approximately $1 \cdot 10^{-3}$ mbar to achieve maximal ion yields for the $(CO_2)_n^-$ anions. Data was recorded in an electron energy range between 0 eV and 5 eV. Between 300 and 500 scans were taken for each mean cluster size.

Resonance Thresholds and Maxima

For the determination of the thresholds (or onset), maxima, and areas of the resonances, Gaussian distributions were fitted to the ion yield curves as described in chapter 3.3.1. The individual distributions and the cummulative fits (solid red lines) for all mean neon cluster sizes studied are shown in figure 5.16. The resonance onsets for each initial condition, given by the nozzle temperatures, are summarised in table 5.1 together with the mean neon cluster size.

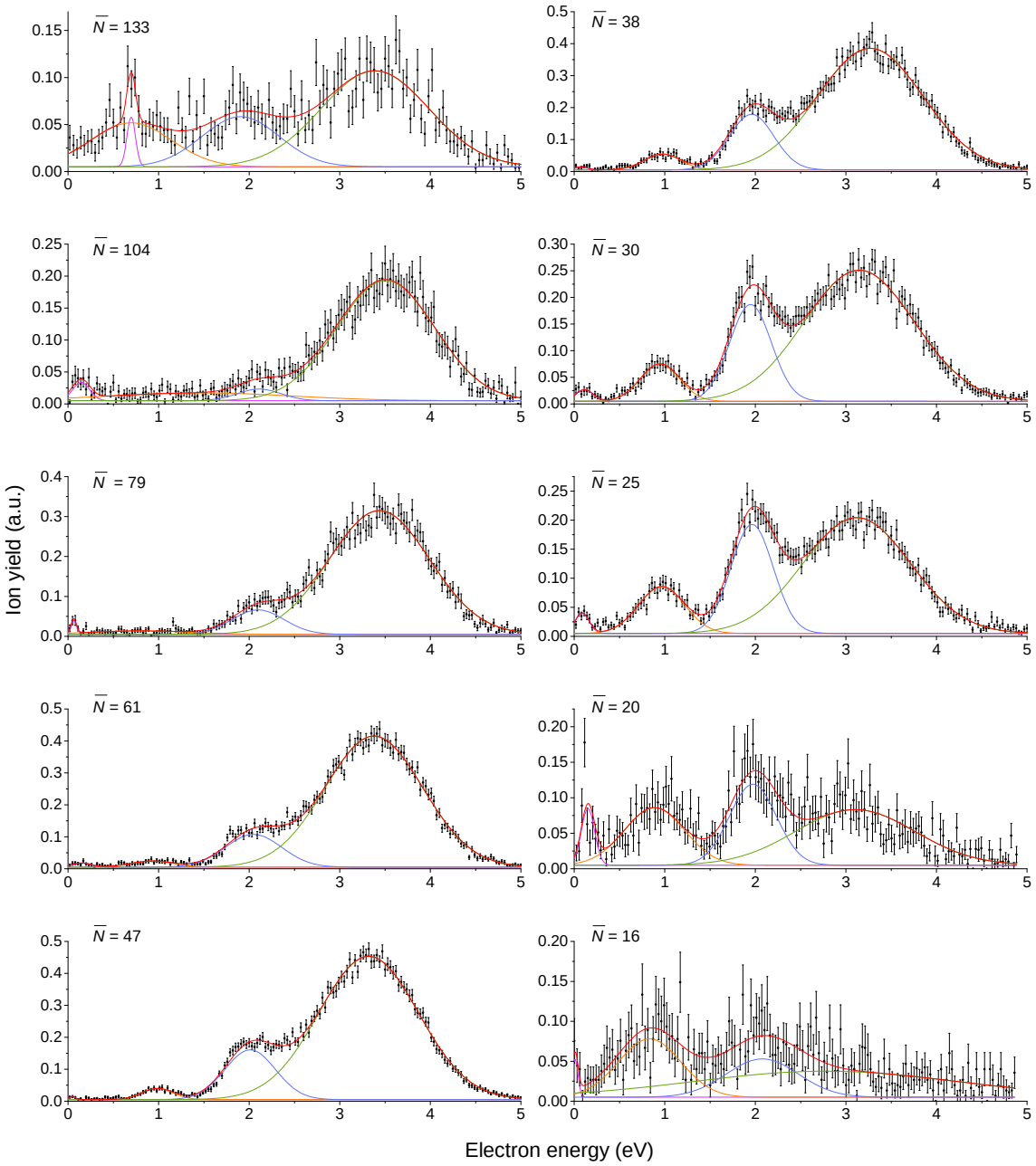

Figure 5.16: Ion yield of the $(CO_2)_4^-$ anion after electron attachment to neon clusters doped with carbon dioxide as a function of electron energy. Different initial expansion conditions result in varying mean neon cluster sizes $\bar{N}$. The relative ion yields between the panels are comparable. Data points are shown in black. Gaussian distributions are fitted to each resonance (coloured solid lines), the cummulative fit is always shown in red.

In order to facilitate the analysis, the peak thresholds, and the position of the peak maxima were fitted for each mean cluster size, see figure 5.17 a), and b), respectively. Three different colours were used in order to make a comparison among the different cluster sizes easier. The green points symbolise the lowest energy peaks not assigned to background signals, the data in red represent the second peak with maxima around 2 eV and the black data points belong to the peak around 3 eV. Since the first peak is very weak for large cluster sizes, the parameters of the fit are associated with large

$\bar{N}$	T_{Ne}/K	resonance onset position (eV)		
		1	2	3
133	60	-0.3 ± 0.3	0.9 ± 0.3	2.0 ± 0.1
104	64	0.9 ± 2.3	1.5 ± 0.3	2.23 ± 0.06
79	69	0.5 ± 0.8	1.42 ± 0.09	2.13 ± 0.02
61	74	0.4 ± 0.1	1.32 ± 0.04	2.11 ± 0.01
47	79	0.58 ± 0.06	1.35 ± 0.02	2.03 ± 0.01
38	84	0.50 ± 0.06	1.38 ± 0.02	1.90 ± 0.01
30	89	0.44 ± 0.04	1.40 ± 0.02	1.72 ± 0.03
25	94	0.36 ± 0.03	1.41 ± 0.02	1.72 ± 0.03
20	100	0.10 ± 0.07	1.36 ± 0.05	1.6 ± 0.1
16	105	0.02 ± 0.13	1.1 ± 0.2	-0.6 ± 0.9

Table 5.1: Mean neon cluster size $\bar{N}$, temperature of the neon gas before expansion, and peak threshold (onset) positions of the three resonance structures observed for the $(CO_2)_4^-$ anion.

uncertainties. Thus, those data points are excluded from figure 5.17. In general, the thresholds and maxima of peak series 1 (green) and 3 (black) show a tendency to increase to higher energies with increasing mean cluster size. The last point of each series lies energetically lower, indicating a reverse trend, but no definite statement can be made based on the single point. The thresholds and maxima of peak series 2 (red) show a dependency on the mean cluster size which is harder to quantify. While the threshold position increases with increasing cluster size before decreasing after $\bar{N} \approx 30$, the peak maximum starts off with a decrease before increasing to higher energies at a cluster size of $\bar{N} \approx 38$. The last data points for both thresholds and maxima indicate a decrease to energetically lower positions, as for the other two peak series.

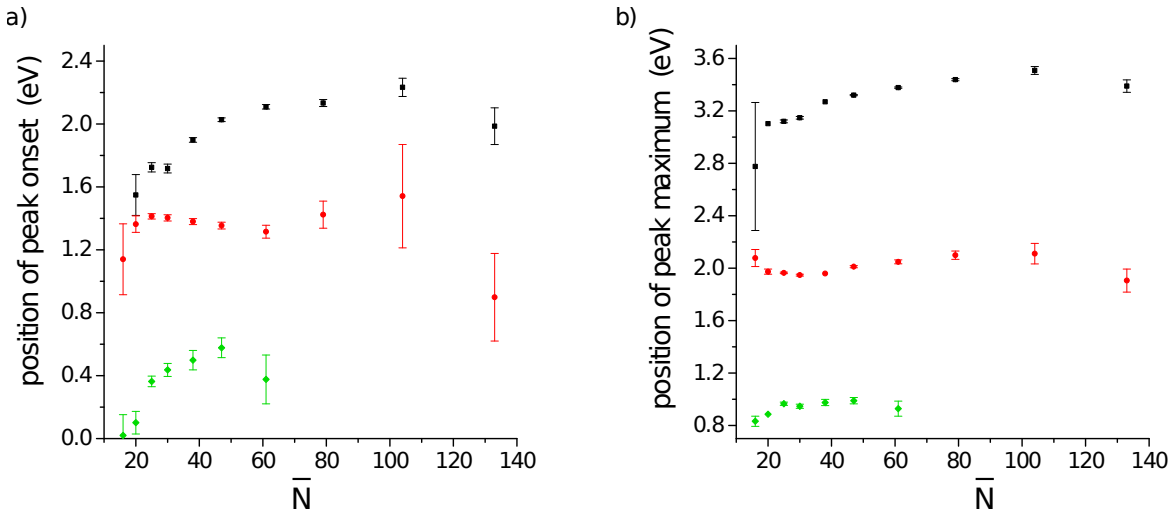

Figure 5.17: Position of the peak onset (a)) and maximum (b)) in eV of the $(CO_2)_4^-$ resonance in dependency of the mean neon cluster size $\bar{N}$. The different colours symbolise peak series 1 (peak maxima at around 0.8-1 eV; green), 2 (peak maxima at around 2 eV; red), and 3 (peak maxima at around 3.1-3.3 eV; black) as referred to in the text.

Comparison to Previous Studies

Previous studies investigated electron attachment processes to pristine carbon dioxide clusters [271, 273, 274, 285, 286]. They report cluster series of the non-decomposed $(CO_2)_n^-$ and the fragment ions $(CO_2)_nO^-$. Two of those studies devoted a main part of their work to the $(CO_2)_4^-$ anion [273, 274]. In both of them ion yield curves were recorded in an electron energy range between (0 - 10) eV. Since they only state the initial conditions of supersonic expansion but not the mean cluster size, these will be re-evaluated here. Harnes *et al.* reported a formula similar to the Hagena parameter and the calculation of the mean cluster size for rare gas clusters, but for carbon dioxide clusters [287]. According to them, the Hagena parameter for bare CO_2 clusters can be calculated with equation 2.56 and setting $k = 5.58 \cdot 10^5$, $b = 0.6$, and $c = 3.05$, leading to

$$\Gamma^* = 5.58 \cdot 10^5 \cdot \left(\frac{p_0}{\text{mbar}}\right) \cdot \left(\frac{d_{eq}}{\mu\text{m}}\right)^{0.6} \cdot \left(\frac{\text{K}}{T_0}\right)^{3.05} \tag{5.3}$$

The mean cluster size is also derived analogously to the rare gas clusters in equation 2.58, with $a = 99 \pm 10$, and $u = 2.23 \pm 0.15$, leading to

$$\bar{N} = 99 \cdot \left(\frac{\Gamma^*}{1000}\right)^{2.23} \tag{5.4}$$

According to these equations, the mean cluster size of the studies reported by Stamatovic *et al.* [274] and Denifl *et al.* [273] can be calculated. Stamatovic *et al.* report initial expansion conditions of a nozzle diameter of 10 µm, a nozzle temperature of 303 K, and a stagnation pressure of 5 bar, giving a mean cluster size of $\bar{N} = 7$. Denifl *et al.* reported anion yields for $(CO_2)_4^-$ at different initial conditions, the ones resulting in the highest mean cluster size being $d_{eq} = 10\,\mu\text{m}$, $T_0 = 211\,\text{K}$, and $p_0 = 3\,\text{bar}$, yielding $\bar{N} = 28$, and the conditions resulting in the lowest mean cluster size are the same except for the nozzle temperature which was increased to 300 K, changing the mean cluster size to 5. Denifl *et al.* identified three resonances with peak maxima at 0 eV, 2.2 eV, and 3.1 eV. The 0 eV resonance was assigned to a vibrational Feshbach resonance (VFR), as first described by Leber *et al.* [275], and is observed for all experimental conditions. This peak is also observed by Stamatovic *et al.* The peaks at 2.2 eV and 3.1 eV merge into one broad structure, which can be analysed by fitting Gaussian profiles into the region. No uncertainties are provided by Denifl *et al.* [273], neither on the fitting method nor on the peak position. The peak at 2.2 eV is assigned to a resonant scattering feature assigned to a selective excitation of the energetically higher states of the Fermi dyad, first reported for isolated CO_2 by Allan [288]. It arises from the coupling of a bending and streching mode that are energetically close. The peak at 3.1 eV was attributed to a $^2\Pi_u$ resonance with subsequent intracluster relaxation processes. For isolated carbon dioxide molecules, the corresponding resonance structure was reported at 3.7 eV [289, 290], and according to Denifl *et al.*, a red shift in the energy is expected for cluster environments [273]. Stamatovic *et al.* also report this broad resonance from 2 - 4.5 eV but without further specifications [274]. Additionally, they observe a resonance with a lower intensity between the VFR at 0 eV and the broad resonance structure between 2 and 4 eV, which is not present in the data by Denifl *et al.* [273].

This structure was taken up again by a re-evaluation of the data of Denifl *et al.* [273] by Postler *et al.* in a study of carbon dioxide embedded in helium droplets [284]. They

reported slightly altered values of the position of the peak maxima with 0.2 eV, 1.4 eV, 2.2 eV, and 3.1 eV, respectively. In their study, Postler *et al.* measured the anion yield of $(CO_2)_4^-$ produced by electron attachment to carbon dioxide embedded in helium clusters [284]. They reported the peak maxima position at 1.8 eV, 3.1 eV and 3.8 eV. Based on previous studies of dopants embedded in helium droplet, they expected an energy shift of 1.6 eV towards higher energies. This effect of the helium matrix affects the electron energy still available to be deposited into the dopant clusters. The electron needs to overcome an energy barrier in order to be injected into the helium droplet that corresponds to entering the conduction band. While this quantity is a matter of the current investigations for this thesis for neon clusters, it is already well defined for helium clusters to be $V_0 = -1.15\,\text{eV}$ [291]. Additionally, some energy is required for the formation of an electron bubble within the helium cluster [291]. Overall, this results in an energy shift of 1.6 eV. Comparing the values by Postler *et al.* to the newly analysed values of Denifl *et al.*, they were able to confirm the 1.6 eV shift for all but one resonance. The reason for the one exception remains an issue of further investigations [273, 284]. Additionally, they noted that the relative intensities differ for their data when compared to the bare carbon dioxide clusters [284].

Energy Barrier of the Neon Cluster

In order to draw conclusions on the energy barrier of a neon cluster caused by the formation of a conduction band, if any exists from a certain size of neon clusters onward, a similar analysis of the present data and comparison to the data by Denifl *et al.* [273] and Stamatovic *et al.* [274] is performed as was done by Postler *et al.* [284]. In figure 5.18, the $(CO_2)_4^-$ anion ion yield curves arising from electron attachment to pristine carbon dioxide clusters, CO_2 clusters in helium, and CO_2 clusters in neon are compared. The peak positions for the present study are approximately 1 eV, 1.9 eV, and 3.4 eV, respectively. When comparing these values to the peak positions found for bare clusters, the enery shifts amount to 0.8 eV, 0.5 eV, and 1.2 eV, respectively. Thus, no constant energy shift can be found as in case of the helium droplets.

As can be seen in figure 5.17 b), the position of the peak maxima slightly depends on the cluster size. Ignoring the points with large uncertainties for large mean cluster sizes for a moment, it seems as if, at least for peak series 1 and 3, both the thresholds and the peak maxima approach asymptotically a stable value for increasing mean cluster sizes. The threshold of peak series 1 approaches approximately 0.8 eV, while the threshold of peak series 3 approaches 2.2 eV. For small neon cluster sizes, the peak threshold in series 1 in figure 5.17 a) is consistent with 0 eV. This is the same value as for the bare carbon dioxide clusters, thus indicating no formation of a conduction band. It is also possible that all neon atoms were evaporated during the pick-up process, before the electron interaction. Hence, this would represent a bare carbon dioxide scenario. While no explicit onset data is avaiable from Denifl *et al.* [273], the threshold values for peak series 2, $(0.9 \pm 0.3)\,\text{eV}$, and peak series 3, $(2.0 \pm 0.1)\,\text{eV}$ as listed in table 5.1 also seem to be in good agreement with the fit parameters by Denifl *et al.* when comparing the results visually [273], supporting this assumption. Towards higher initial neon cluster sizes, not all neon atoms are evaporated during the pick-up process and at some point the remaining cluster is large enough to form a conduction band, which the incoming electrons experience as energy barrier. This value can be taken from figure 5.17 a) as the asymptotic value of peak series 1 and amounts to about 0.8 eV.

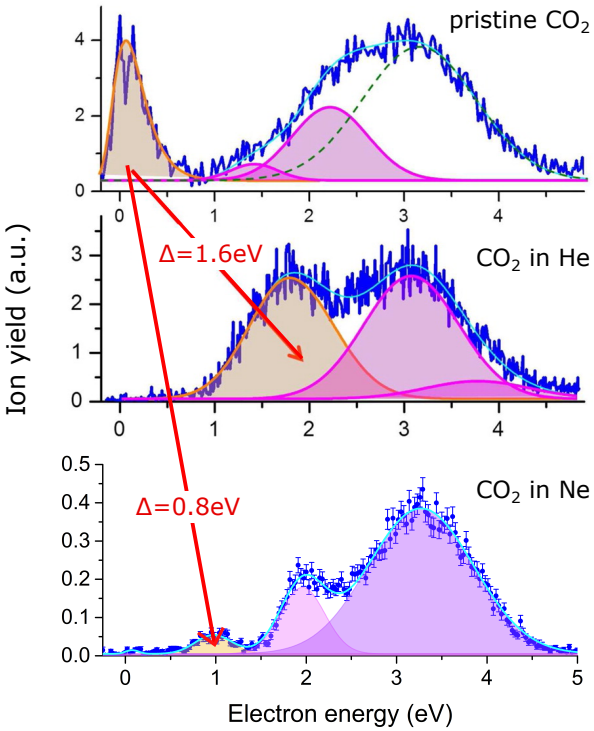

Figure 5.18: Comparison of the $(CO_2)_4^-$ anion yield as a function of the electron energy for pristine carbon dioxide clusters, CO_2 embedded in helium droplets and CO_2 doped in neon clusters. The resonance positions are shifted in a rare gas environment, representing the energy barrier that arises from the formation of a conduction band within the rare gas clusters. The upper two panels are taken from [284].

Influence of the Initial Cluster Size

Another observation by both Denifl *et al.* and Postler *et al.* is that the relative intensities of the resonance peaks strongly depend on the initial conditions [273, 284]. As can be seen in figure 5.16, this is also true for the present data. In order to quantify this effect, the area of each resonance peak is calculated as described in chapter 3.3.1. The results are summarised in table 5.2. In the case of the bare carbon dioxide cluster experiments, the relative intensity change was explained by evaporative cooling. The electron attachment and subsequent stabilisation by evaporation can be written as

$$e^- + (CO_2)_n \longrightarrow (CO_2)_n^{-*} \longrightarrow (CO_2)_4^- + (n-4)CO_2 \tag{5.5}$$

for the example of $(CO_2)_4^-$ formation. To form a stable cluster anion, the relaxation, or excess energy needs to be evaporated. This is composed of the energy carried by the initial electron plus the adiabatic electron affinity of $(CO_2)_n$. The latter was reported to be very small [277]. For small initial mean cluster sizes, the relaxation energy cannot be evaporated due to the limited amount of cluster constituents. Thus, only the 0 eV resonance results in the formation of the $(CO_2)_4^-$ cluster anion. Increasing the mean cluster size, first the 2.2 eV resonance and later the 3.3 eV lead to a stable cluster anion within the timespan of the experiment [273]. For the study of carbon dioxide molecules embedded in helium clusters, the explanation is similar: energetically higher resonances increase in relative ion yield intensities with increasing initial helium droplet size [284]. Again, it is argued that the larger clusters provides more degrees of freedom to distribute and dissipate the excess energy. The results of the present study are

graphically summarised in figure 5.19. The ratios between peak series 2 and 3 (red), and 1 and 3 (green) show that for increasing cluster size, the ratios decrease, implying that the relative abundance of the highest energetic resonance (peak 3) increases. Thus, the results are in agreement with the previous finding by Postler *et al.* [284] and can be tranferred from the helium matrix to the neon cluster.

N	**resonance area (eV·counts)**			**area ratio**	
	1	2	3	1/3	2/3
133	0.05 ± 0.01	0.05 ± 0.02	0.10 ± 0.01	0.50 ± 0.05	0.50 ± 0.15
104	0.01 ± 0.01	0.02 ± 0.01	0.19 ± 0.01	0.05 ± 0.05	0.10 ± 0.09
79	0.01 ± 0.01	0.06 ± 0.01	0.31 ± 0.01	0.03 ± 0.02	0.20 ± 0.03
61	0.02 ± 0.01	0.10 ± 0.01	0.41 ± 0.01	0.05 ± 0.02	0.25 ± 0.02
47	0.03 ± 0.01	0.16 ± 0.01	0.45 ± 0.01	0.08 ± 0.05	0.35 ± 0.02
38	0.05 ± 0.01	0.17 ± 0.01	0.38 ± 0.01	0.13 ± 0.03	0.46 ± 0.03
30	0.07 ± 0.01	0.18 ± 0.01	0.25 ± 0.01	0.29 ± 0.03	0.74 ± 0.05
25	0.08 ± 0.01	0.19 ± 0.01	0.20 ± 0.01	0.40 ± 0.04	0.94 ± 0.06
20	0.08 ± 0.01	0.11 ± 0.01	0.08 ± 0.01	1.03 ± 0.20	1.46 ± 0.30
16	0.07 ± 0.02	0.05 ± 0.02	0.03 ± 0.01	2.33 ± 0.11	1.67 ± 0.11

Table 5.2: Mean neon cluster size $\bar{N}$, area of the resonance peak structure of the three resonance structures observed for the $(CO_2)_4^-$ anion, and the ratio of areas 1 to 3, and 2 to 3.

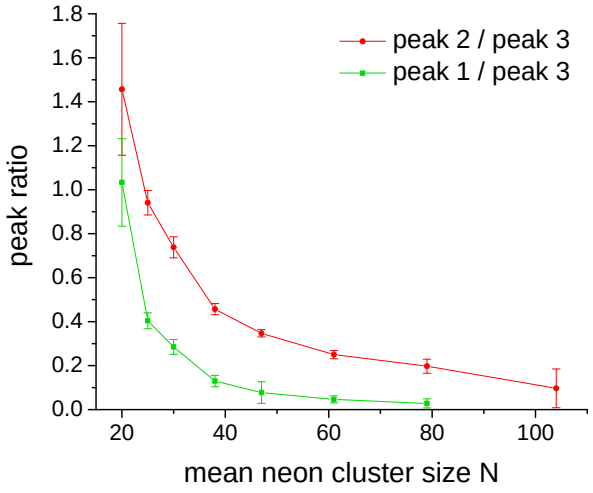

Figure 5.19: Peak ratio of the area of the resonance structure around 2 eV (peak 2) and the resonance peaking at 3 - 4 eV (peak 3), and of the peak area of the resonance centered at around 1 eV over peak 3 in dependence of the mean neon cluster size.

Further $(CO_2)_n^-$ Anions

In order to complete the study, the anions $(CO_2)_2^-$, $(CO_2)_3^-$, and $(CO_2)_5^-$ were also measured. For $n = 5$ and $n = 3$ ($m/z = 220$ and 132, respectively), the anion yield curves were taken at three different initial neon expansion conditions, see figure 5.20. The resonances of these anions show the same behaviour as the $(CO_2)_4^-$ anion, meaning the resonance positions shift to higher energies for increasing neon cluster sizes and

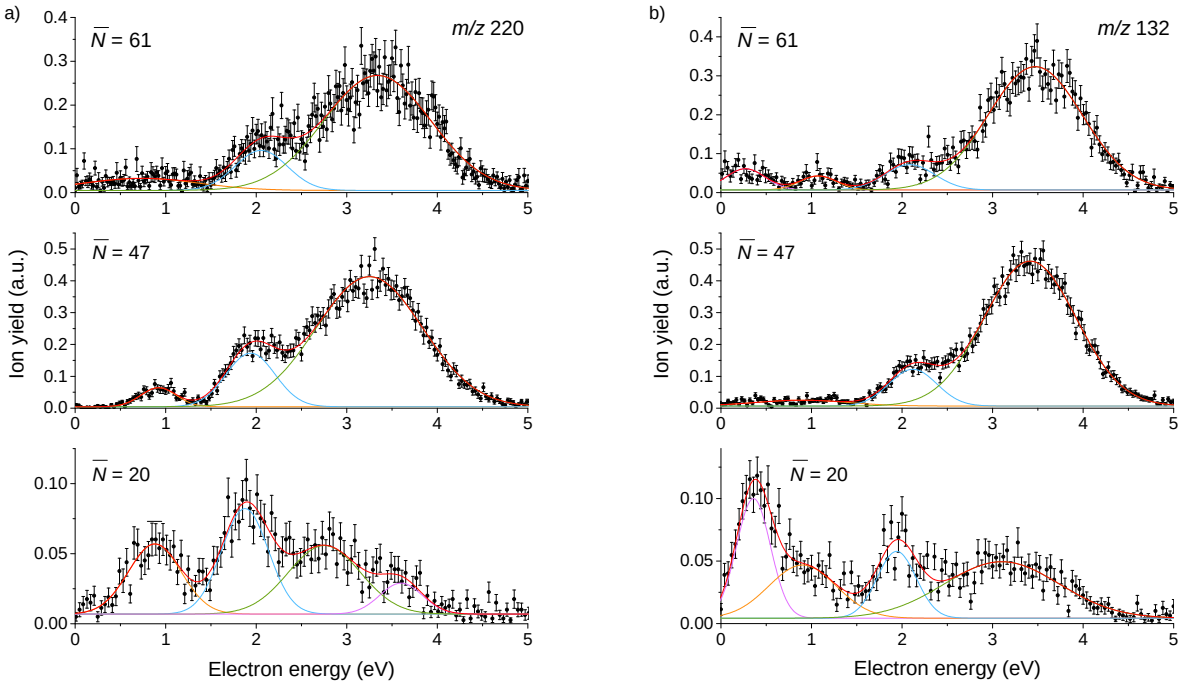

Figure 5.20: Ion yields of the $(CO_2)_5^-$ (a)) and $(CO_2)_3^-$ (b)) anions after electron attachment to neon clusters doped with carbon dioxide molecules as a function of electron energy. Different initial expansion conditions result in varying mean neon cluster sizes $\bar{N}$. The relative ion yields between the panels are comparable. Data points are shown in black. Gaussian distributions are fitted to each resonance (coloured solid lines), the cummulative fit is always shown in red.

the change in the relative intensities of the individual peaks. No detailed analysis is provided here but instead only a qualitative one.

The peak positions for the $(CO_2)_n^-$ anions with $n = 2 - 5$ at the same initial mean cluster size are summarised in figure 5.21. Although the ion yield curves vary, comparable resonances can be assigned. The absolute peak position coincides for the resonance at 3 - 4 eV and the positions of the resonances at around 1 and 2 eV show small variations. The relative intensities are different for each $(CO_2)_n^-$ anions. In general, the larger the carbon dioxide cluster anion, the more important the resonances at around 1 eV and 2 eV become relative to the resonance at 3 - 4 eV. Two possible explanations can be found for this phenomenon. In the first option, it is assumed that all $(CO_2)_n^-$ anions arise from the same neutral $(CO_2)_m Ne_N$ cluster with $m > n$ before the electron interaction. This assumption is explained by the initial expansion conditions, which are the same for all recorded $(CO_2)_n^-$ anions in figure 5.21. Then, $m - n$ is higher for smaller $(CO_2)_n^-$ anions, meaning more CO_2 molecules need to be evaporated. Thus, more energy is required, which means the resonance at 3 - 4 eV is favoured for small carbon dioxide cluster anions while if less energy is available, larger cluster anions are formed. In the second option it is assumed that the intial $(CO_2)_m Ne_N$ vary in size, motivated by the neon cluster distribution at constant expansion conditions. In that scenario, smaller neutral carbon dioxide clusters are more commonly formed than large CO_2 clusters, also due to the limited size of the neon clusters. Additionally, it is assumed that the resonance at around 2 eV results from smaller initial $(CO_2)_m Ne_N$ (especially smaller m) than the 3 eV resonance. This is motivated by saying that the additional 1 eV transferred into the carbon dioxide cluster requires the evaporation of more carbon

dioxide molecules in order to stabilise the (CO_2) cluster, thus a larger initial cluster is required to form the same size final cluster anion. This is to say, the small $(CO_2)_m Ne_N$ precursor clusters give rise to the 2 eV resonance in small $(CO_2)_n^-$ anions. Increasing the size of the $(CO_2)_m Ne_N$ precursor clusters gives access to both the 3 eV resonance of small $(CO_2)_n^-$ anions and the 2 eV resonance of larger $(CO_2)_n^-$ anions. The precursor cluster needs to be even larger to additionally form the 3 eV resonance of large $(CO_2)_n^-$ anions. Since the $(CO_2)_m Ne_N$ precursor clusters follow a cluster distribution with limited maximum size, the resonance at 3 eV has a higher relative intensity for small carbon dioxide anions. Thus, the relative abundance of the 1 eV and 2 eV resonances for larger detected anions would be a direct result of the initial cluster size distribution. Detailed studies on the influence of the initial expansion conditions on the $(CO_2)_n^-$ anions yields for all n would be required to determine the correct explanation.

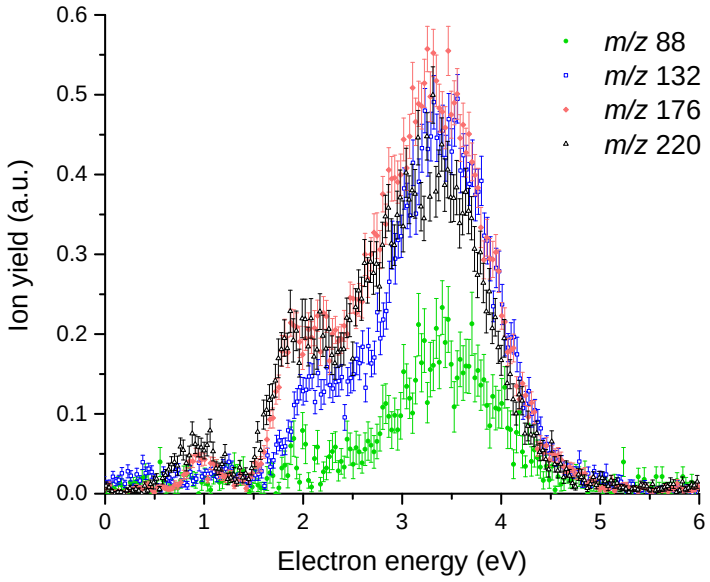

Figure 5.21: Comparison of the ion yield of $(CO_2)_n^-$ clusters with $n = 2 - 5$ as a function of the electron energy.

At the end of this chapter it should be mentioned that peaks at around 0 eV were not taken into account for the current analysis. The reason for this is that those peaks were attributed to background or noise peak structures. An example is shown in figure 5.22 for $(CO_3)_n^-$. The entire ion current is described by the background signal in this region, meaning no $(CO_2)_n^-$ signal was detected at around 0 eV.

5.2.3 Electron Attachment to Neon Clusters Doped with Molecular Oxygen

In addition to studying neon clusters doped with carbon dioxide, similar studies were performed with molecular oxygen as dopant. The experimental setup is identical to the one described above. Data on electron attachment processes was taken in an electron energy range between 0 and 19 eV. The initial expansion conditions comprise a nozzle temperature of 75 K or 85 K, a neon pressure of 19 bar and a nozzle diameter of 10 µm. The pressure in the pick-up region was adjusted to values between $(1.1 - 1.5) \cdot 10^{-4}$ mbar.

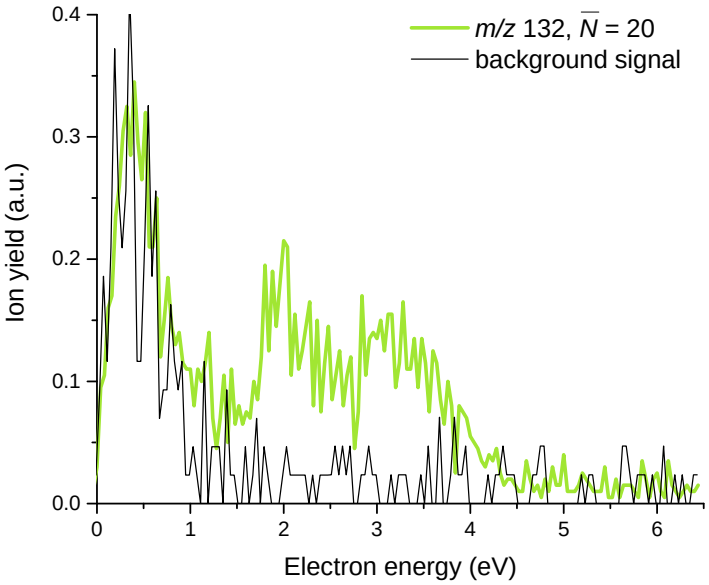

Figure 5.22: Signal (green) and background signal (black) for $m/z = 132$ recorded at the same conditions and the same settings. In the energy region below 1 eV, the complete ion current is caused by the background signal, thus no contributions from $(CO_2)_3^-$ account for the signal in this range.

Isolated Molecular Oxygen

Since molecular oxygen plays an important role in many natural and technological processes [265, 266], it is not surprising that electron attachment studies with this compound were already performed both in the gas-phase and as pristine oxygen clusters. A theoretical study on the O_2 molecule in the gas-phase reports a dissociative channel and an associative channel [292]. The latter is not observed experimentally due to its lifetime, which is short in comparison to the timescale of the experiment [293–296]. The dissociative channel leads to the formation of the O^- and occurs in an energy range between 4 and 10 eV, peaking at around 7 eV [294, 295, 297]. Theoretical studies, including the ones from Itikawa [298] and LaPorta *et al.* [292], assigned it to the process

$$O_2\,(X^3\,\Sigma_g^-\,;\,\nu) + e^- \longrightarrow O_2^{-*} \longrightarrow O^-(^2P) + O(^3P) \tag{5.6}$$

According to their simulations, a theoretical threshold of the reaction at 3.64 eV and a position of the peak maximum at 6.43 eV are expected, which is not to far off from the experimental values [292]. While several states are accessible to form the excited O_2^{-*} state, LaPorta *et al.* found that the main contribution is due to the $^2\Pi_u$ state of O_2^- with some contribution of the $^4\Sigma_4^-$ state for the high energy tail [292]. These findings were also experimentally deduced by measuring the angular distribution of O^- [299].

In addition to the dissociative process, an associative electron attachment reaction can be identified and described with consideration of the involved states according to

$$O_2\,(X^3\,\Sigma_g^-\,;\,\nu = 0) + e^- \longrightarrow O_2^{-*} \longrightarrow O_2^-\,(X^2\,\Pi_g\,;\,\nu' \geq 4) \tag{5.7}$$

[300]. This reaction leads to an unstable O_2^- anion. The adiabatic electron affinity of molecular oxygen is positive and amounts to (0.440 ± 0.008) eV [301]. Additionally, the bond length of molecular oxygen increases when attaching an extra electron [290].

Thus, a vertical Franck-Condon transition results in vibrational excitation of the anion with $\nu \geq 4$ [297]. These characteristics explain the short lifetime of the O_2^- anion of about 10^{-10} s [28], which basically does not allow for the detection of the anion by means of mass spectrometry.

Molecular Oxygen Clusters

In studies of pure molecular oxygen clusters, usually two cluster series were observed, $(O_2)_n^-$ and $(O_2)_nO^-$ [297, 302–304]. For the $(O_2)_n^-$ series, two peak structures were reported upon electron attachment. The first is described by a 0 eV resonance. The exact position of the maximum varies in experimental studies between 0 and 0.7 eV [303, 304], which could possibly be due to a cluster size effect, i.e. possibly an energy shift is induced for increasing oxygen cluster sizes [297]. An electron attachment study of Matejčík *et al.* with a high electron energy resolution showed that the 0 eV resonance actually consists of several peaks that were assigned to vibrationally excited levels [293]. Based on the shape of the 0 eV resonance, it was assigned to an s-wave electron capture [293, 297, 305]. The second peak structure corresponds to the 7 eV resonance of the O^- anion from isolated O_2, but it is broader and shifted to higher energies. The exact shift or energy is not provided in the study.

The $(O_2)_nO^-$ anions also exhibits two peaks upon electron attachment. The general tendency is that the anions of that series show a similar behaviour as the O^- anion formed upon electron attachment to molecular oxygen. But, like for $(O_2)_n^-$, the 7 eV peak is broadened and shifted to higher energies [302]. Additionally, a weak peak centering at around 13 eV was reported [302, 303]. Two studies on dissociative attachment to condensed molecular oxygen presented resonances at the same electron energies as for the O^- anion yield from molecular oxygen. They assigned the 7 eV resonance to a $^2\Pi_u$ state of O_2^- and the 13 eV resonance to a combination of a $^2\Pi_u$ and $^2\Sigma_g^+$ state. Since for the latter a violation of the selection rule ($\Sigma^- \leftrightarrow \Sigma^+$) is required and it was not observed in the experiments of isolated molecular oxygen, they concluded that the O^- resonance must result from dimers or polymers present in the condensed phase [306, 307]. It is a well-known phenomenon that in the transitions forbidden in the gas phase may occur for example in liquid or solid states [308].

Since the resonances are at least partly similar to the ones observed for isolated molecular oxygen, Märk *et al.* suggested describing the reaction pathway for O_2O^- as follows

$$1) \quad (O_2)_n + e^- \longrightarrow (O_2)_{n-1} \cdot O_2^{-*} \longrightarrow (O_2)_{n-1}O^- + O \tag{5.8}$$

$$2) \quad (O_2)_{n-1}O^- \longrightarrow (O_2)_{n-2} \cdot O_3^{-*} \tag{5.9}$$

$$3) \quad (O_2)_{n-2} \cdot O_3^{-*} \longrightarrow O_3^- + (O_2)_{n-2} \tag{5.10}$$

where 2) describes the isomerisation and 3) the subsequent removal of a neutral oxygen cluster in order to evaporate the heat of isomerisation [302]. Analogously, the 7 eV peak of the $(O_2)_n^-$ series is formed by step 1) followed by

$$(O_2)_{n-1} \cdot O_2^{-*} \longrightarrow (O_2)_{n-1-p} \cdot O_2^- + p\,O_2 \tag{5.11}$$

Molecular Oxygen Clusters from Neon Matrices

In the present study, mainly electron attachment data of the $(O_2)_2^-$ anion was recorded. The results for a nozzle temperature of 75 K and 85 K, leading to a mean neon cluster

size of $\bar{N} = 58$ and 36, respectively, are shown in figure 5.23. The resonances were fitted with Gaussian functions and the cummulative fit is shown by the red solid line. The positions of the peak maxima were extracted from the fits and are summarised in table 5.3.

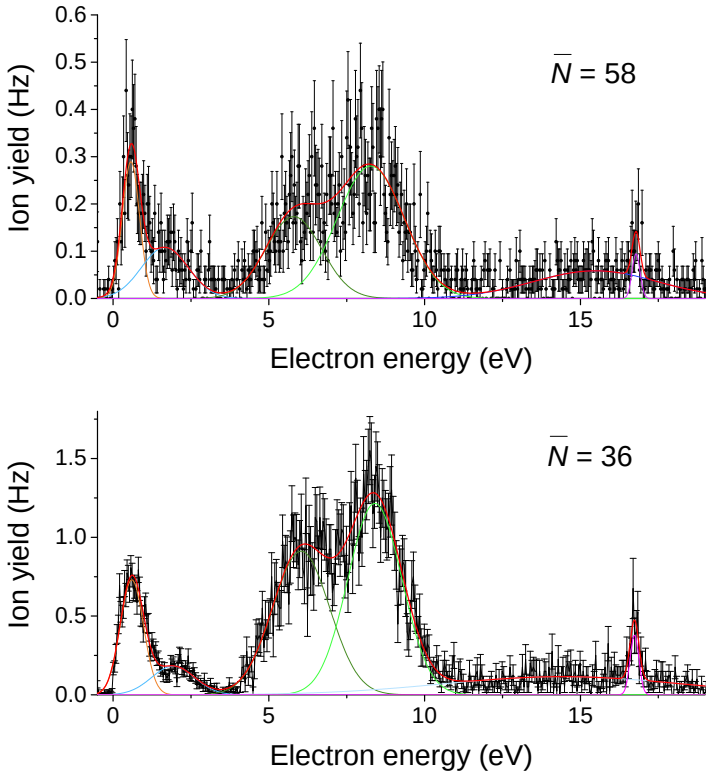

Figure 5.23: Ion yield of the $(O_2)_2^-$ anion after electron attachment to neon clusters doped with molecular oxygen as a function of electron energy. Different initial expansion conditions result in mean neon cluster sizes of $\bar{N} = 58$ and $\bar{N} = 36$, for the upper and lower panel, respectively. The relative ion yields between the panels are comparable. Data points are shown in black. Gaussian distributions are fitted to each resonance (coloured solid lines), the cummulative fit is always shown in red.

$\bar{\mathbf{N}}$	$\mathbf{T}_{Ne}$/K	resonance maximum position (eV)					
		1	2	3	4	5	6
58	75	0.57 ± 0.02	1.7 ± 0.1	5.8 ± 0.2	8.3 ± 0.1	15.5 ± 0.3	16.78 ± 0.04
36	85	0.60 ± 0.03	1.9 ± 0.2	6.0 ± 0.1	8.4 ± 0.1	14.4 ± 0.6	16.74 ± 0.02

Table 5.3: Mean neon cluster size $\bar{N}$, temperature of the neon gas before expansion, and peak maximum positions of the six resonance structures observed for the $(O_2)_2^-$ anion yield.

The values for the resonance maximum position reported in table 5.3 for both initial conditions are compatible with each other within the uncertainties. Hence, they are not showing an energy shift in the resonance positions for increasing initial neon cluster sizes as observed for neon clusters doped with carbon dioxide. In order to determine an energy shift or exlude one, more measurements at other initial conditions would be required. When comparing the results to the data reported for pure molecular oxygen clusters, the first observation is that more resonances are observed for oxygen doped in

neon clusters. The energetically lowest resonance is reported at values between 0 and 0.7 eV for pristine clusters [303, 304], which is compatible with the maximum of the first resonance presented in the present study. Since the energy range of the reported peak positions in the literature of the pristine clusters is rather large with 0.7 eV, it is difficult to identify a possible energy shift caused by the neon cluster environment. The second resonance observed here in the electron range of 1.7 - 1.9 eV does not have any corresponding peak in any of the data recorded earlier. In several background measurements, an artefact was ruled out. Thus, the resonance is attributed to an effect caused by the neon environment. Since at the moment no calculations or theoretical model with predictions are available for this phenomenon, the origin remains unclear.

The resonances at 5.8 - 6.0 eV and 8.3 - 8.4 eV are considered together for the comparison. In isolated molecular oxygen, a resonance is observed at 7 eV. In pristine oxygen clusters, the performed studies consistently report that the according resonance is shifted towards higher energies, without quantification of how large the shift is [297, 302–304]. As an example, the measured ion yields reported by Märk *et al.* are shown in figure 5.24 a) [302, 303]. The resonance of the $(O_2)_2^-$ anion is asymmetric, with a flat increase at low energies. This could be an indication of two resonances within the peak structure that could not be resolved. In order to get closer to the cause of two resonances within the energy region between 5.8 and 8.4 eV, the anion yield curves of O^- from O_2 and of O_2O^- from the neon doped with molecular oxygen were recorded. The results were normalised to match the resonance area for a comparison with the $(O_2)_2^-$ anion, see figure 5.24. The mean neon cluster size for those measurements was $\bar{N} = 36$. For O^-, the anion curve can be compared to the studies of the isolated molecule reported previously [294, 295, 297]. These report a resonance with maximum at 7 eV. In contrast, the maximum of the data presented here is at (6.3 ± 0.1) eV This is much closer to the theoretical study by Laporta *et al.* who predicted a value of 6.43 eV based on *ab initio* resonance curves calculated with the R matrix method [292]. This O^- resonance peak has a large overlap with the resonance of the $(O_2)_2^-$ cluster anion at 5.8 - 6.0 eV, indidating a common intermediate or transition state. For O_2O^-, the resonance structure centered around 8.3 eV coincides with the 8.3 - 8.4 eV peak of $(O_2)_2^-$ which is a hint for a common intermediate state. Thus, the comparable peak structures are speaking for common formation mechanisms.

The next very broad resonance structure is difficult to fit with a Gaussian profile due to the weak signal and comparably high uncertainties. This results in large uncertainties in the positions of the peak maxima, which are determined to be (15.5 ± 0.3) eV and (14.4 ± 0.6) eV, for an initial neon cluster size of 58 and 36 components, respectively. The energetically closest resonances reported previously in bare oxygen cluster sudies are at 13 eV [302, 303]. This is a large deviation that cannot be explained by the uncertainties. It should be mentioned that also the value given in the previous studies is rather an estimation than a fitted value. Besides, it is unlikely that only one resonance position in the ion yield curve of this study is shifted towards much higher values while all other resonance positions coincide with the values reported for bare oxygen cluster studies within the uncertainties, or the deviations can be explained otherwise. Thus, this structure remains to be investigated further with better statistics for both systems. This would allow for an improved determination of the peak positions and the deviation could be re-evaluated to either confirm or disprove this unusual shift.

The resonances structure observed at (16.78 ± 0.04) eV and (16.74 ± 0.02) eV for 75 K and 85 K, respectively, is a very interesting peak since it involves the excitation of neon and thus interactions with the rare gas cluster environment. The lowest excitation

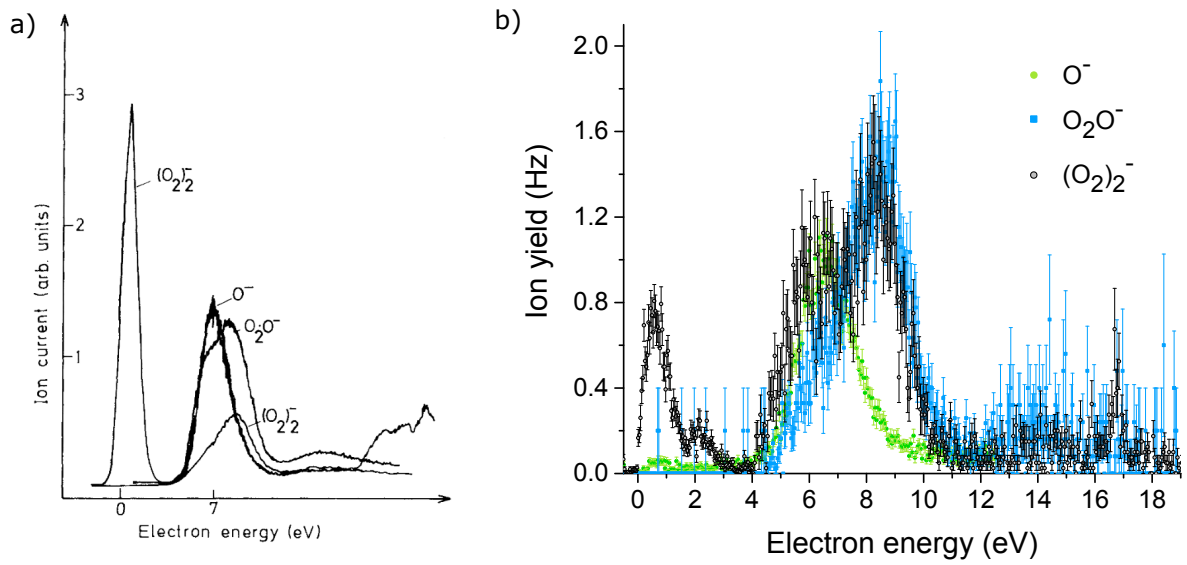

Figure 5.24: Comparison of the anion yields of O^-, O_2O^-, and $(O_2)_2^-$ as function of the electron energy. a) Results from Märk *et al.* for bare molecular oxygen clusters. Taken from [303]. b) Results from the present study. The mean neon cluster size was $\bar{N} = 36$. The yields of O^- and O_2O^- were normalised to match the $(O_2)_2^-$ resonances in order to facilitate the comparison of the shapes and position.

energy of neon was calculated to be 16.6 eV by Rapior *et al.* who developed a theoretical model predicting excitation energies based on the Franck-Hertz experiment [309]. In a first step within the formation of this resonance, the incoming electron excites a neon atom of the cluster. As a consequence, energy is transferred in the scattering event from the electron to neon resulting in the decrease of the kinetic energy of the electron. When interacting further with the molecular oxygen cluster inside of the neon cluster, it has an energy close to 0 eV. As has been discussed above, those energies give rise to the energetically lowest resonance. Hence, the resonances at energies around 0.6 eV maximum and 16.75 eV maximum basically coincide and are energetically only separated by the excitation energy of neon. The shape of both resonance peaks is rather sharp in comparison to the other resonances observed, further supporting the interpretation that both have the same origin.

Relative Intensities Effects

Another observation of the electron attachment studies with bare oxygen clusters performed by Märk *et al.* was that the peak ratio between the 0 eV and the 7 eV peaks change with the mean cluster size of the dopant cluster. The larger the cluster anion $(O_2)_n^-$, the higher the relative intensity of the 0 eV peak in the ion yield curve [302]. Märk *et al.* explained the effect to arise at least partly from the neutral cluster size distribution after supersonic expansion. They argue that the higher energetic resonances result from larger clusters than the resonance close to 0 eV. Higher energetic electrons carry more energy into the initial neutral oxygen cluster that needs to be dissipated, including by monomer emission. Thus, in order to stabilise a cluster anion at 3 eV, more initial constituents of the cluster were dissipated, meaning the initial neutral cluster must have been larger than when stabilising a 0 eV resonance [302].

In the present study, the abolute mean cluster size of the neutral oxygen cluster within the neon cluster is not accessible. Instead, the relative dependency of the mean neon

cluster size on the yield of the $(O_2)_2^-$ anion is studied. For larger inital neon cluster sizes, the relative ion yield of the resonance at 0.6 eV of the $(O_2)_2^-$ anion increases, see figure 5.23. This is, at first, a surprising result, since more neon atoms would be available to dissipate the additional 5 - 8 eV carried into the cluster by higher energetic electrons and it is in contrast to the finding in the carbon dioxide data. But the binding energy of neon is quite low compared to the intracluster bonding energy of O_2. In this case, the neon might not be all that important and the results are similar to Märk *et al.* because larger neon clusters would capture more O_2 and give larger neutral O_2 clusters. This result is deduced from only two different intial expansion conditions and requires further evidence in order to confirm it.

The relative intensities of the individual resonances is not only influenced by the initial neon cluster size, but also by the pick-up pressure of oxygen. In figure 5.25, the results of three different pressures in the pick-up chamber by otherwise stable conditions are shown. The higher the pick-up pressure, the more intense are the signals of the resonance peaks between 5 and 10 eV. Two possible explanations are conceivable. One option is that the effect just described for the neon cluster size dependency is applicable here as well. A higher pick-up pressure leads to more collisions in the pick-up chamber which can result in the evaporation of neon atoms. In that case, a higher pick-up pressure results in a lower neon cluster size before electron attachment and thus an enhancement of the 5 - 10 eV resonances as discussed above. Alternatively, a similar effect as for carbon dioxide doped neon clusters applies, as described in the previous chapter. A larger oxygen cluster is produced within the neon environment for higher pick-up pressures. Since large clusters are required for the stabilisation of higher energetic resonances, these are now provided, increasing the ratio with respect to the energetically lower resonances in comparison to lower pick-up pressures. Determining which explanation is correct requires more data, both of more diverse initial conditions leading to diverse initial neon cluster sizes and of different carbon dioxide cluster anions.

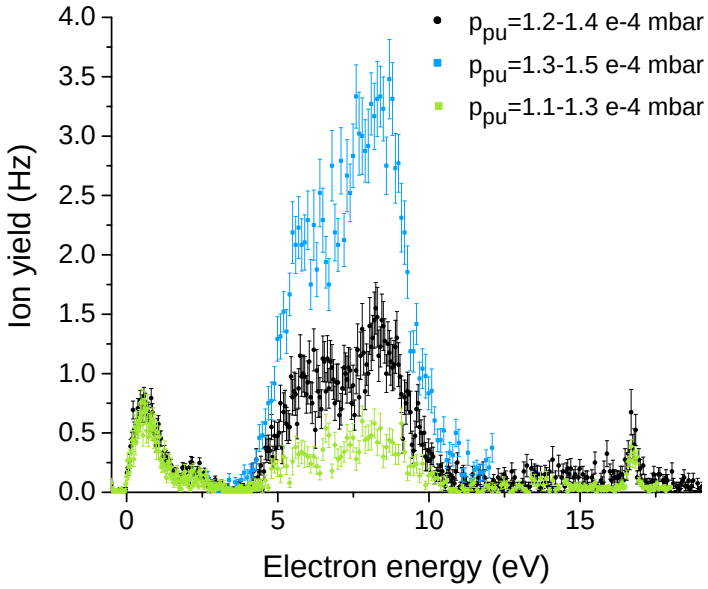

Figure 5.25: Ion yield of the $(O_2)_2^-$ anion as function of the electron energy for different pick-up pressures. All data was recorded for a mean neon cluster size of $\bar{N} = 36$.

Other Rare Gas Clusters Doped with Molecular Oxygen

To complete the discussion of neon clusters doped with molecular oxygen, two additional studies should be mentioned that investigated molecular oxygen doped in other rare gas cluster matrices. Foltin *et al.* studied electron attachment to mixed argon-oxygen clusters, which are produced by co-expansion of argon and oxygen [310]. Unfortunately, they do not report anion yields similar to the ones discussed above. Thus, a comparsion of the data is not possible. Another study by Renzler *et al.* investigated electron attachment to helium clusters doped with hydrogen/oxygen clusters and include, among others, the anion yield of $(O_2)_2^-$ [311]. They do not report a resonance structure around 0 eV, which can have two possible reasons. One possibility is that the 0 eV resonance is either suppressed or shifted in the helium cluster environment. Since the helium clusters are with a typical size of $\bar{N} \approx 5 \cdot 10^4$ much larger than the neon clusters, differences caused by the size of the surrounding cluster are also possible as second option. The resonance at 7 eV for pristine oxygen clusters is also present in the data from Renzler *et al.*, and features a shoulder at the low energy side [311]. This is in indication of an additional resonance, as is observed in the present data for doped neon clusters. The 13 eV resonance is also observed as a broad structure in the helium data. Additionally, a peak appears at electron energies slightly above 20 eV. In order to verify whether this structure may also arise from a previously occurring helium excitation event, as is the case for neon as described above, the exact peak position would have to be determined in a study with higher statistics and compared with the excitation values of helium [31].

Overall, the anion yields of $(O_2)O_2^-$ show a good agreement for oxygen doped neon and helium clusters. Some deviations were observed, which can possibly be attributed to the properties of the rare gases.

5.2.4 Conclusions

The results, analylsis and interpretation of the data for electron attachment to neon clusters doped with carbon dioxide or molecular oxygen are briefly summarised.

- The results of carbon dioxide doped neon clusters give an indication for the formation of a conduction band in neon from a certain size onward. It is estimated to approach around 0.8 eV for initial neon cluster sizes above $\bar{N} \approx 100$. In the ion yields, this is observable as a shift of the resonance maxima and onsets towards higher energies, since an energy barrier needs to be overcome in order for the electron to inject into the dopant cluster. In the data of oxygen doped neon clusters this tendency was not observed, which could be due to the limited amount of data.

- The relative peak heights of the resonances change, depending on the initial mean neon cluster size (CO_2 and O_2 data) and depending on the pick-up pressure (O_2 data). Here, carbon dioxide and oxygen data show different trends. While the energetically higher resonances are favoured for larger initial neon clusters in the carbon dioxide data, the situation is reversed for molecular oxygen as a dopant. Further data on molecular oxygen is required to confirm the trend and the study of further dopants could also help solve this puzzle.

- The data of neon clusters doped with molecular oxygen shows additional resonances as when compared to pristine oxygen cluster. A comparison with the previous study of molecular oxygen in helium droplets confirms the effect. One of

the additional resonances can be assigned to the interaction of an electron with the neon cluster via an excitation event prior to the interaction with oxygen.

Chapter 6

Conclusion and Outlook

This thesis covered electron interaction processes with samples with a prospect of direct applications, specifically the radiosensitisers, and with compounds which address fundamental research questions, in form of cluster measurements.

The first part of the thesis comprises the study of biomolecules and radiosensitisers where results from low-energy electron interactions with histidine, 5-selenocyanato-2'-deoxyuridine (SeCNdU), misonidazole, and nimorazole were presented. Histidine is an example of a biomolecule and completes the study of electron attachment to the standard aromatic amino acids. In agreement with the previous studies, no parent anion was observed, like in case of tryptophan to mention one example namely [312]. The most intense dissociative electron attachment (DEA) channel was observed at $m/z = 16$, and assigned to the isobaric contributions of O^- and NH_2^-. Additionally, the ionisation energy of histidine was determined to be (8.48 ± 0.03) eV. Generally, it is favourable for biomolecules to stay intact during irradiation in order to avoid cell damage. To improve the planification and treatment of the radiation therapy in terms of minimising the administered radiation dose, it is important to understand the underlying physico-chemical processes not only of malignant tissue but also of the healthy components. This study enhances the knowledge of the underlying microscopic processes which is the first step towards understanding the working mechanisms of radiosensitisers.

Among the radiosensitising agents, compounds of the group addressing highly proliferating cells and those specified on hypoxic cells were studied. The deoxyuridine derivative 5-selenocyanato-2'-deoxyuridine (SeCNdU) belongs to the first group. The potential radiosensitiser is based on a nucleoside which enables its efficient incorporation into the DNA molecule. It particularly addresses highly proliferating cells. The SeCN group serves as an efficient electron capturer. The agent was suggested based on a theoretical model and the predictions were tested in the course of this thesis. The study indeed confirmed the high reactivity of the compound since it forms both radicals and charged species efficiently upon dissociative electron attachment. The dominant dissociation channel was observed for the formation of the radical $(SeU\text{-}yl)^{\bullet-}$. It is closely followed by the CN^- anion in terms of intensity of the ion yield. Both pathways involve a cleavage of the Se-CN bond. Overall, the study demonstrated the efficiency of the compound and determined the reactive fragment species. Thus, the combination of applying the theoretical model to propose potential new radiosensitisers and testing them on a physico-chemical stage first could serve as a comparably cheap and fast first step analysis of new agents.

Established examples for radiosensitisers specifically addressing hypoxic tumours are nitroimidazoles [166, 231]. In this thesis, misonidazole and nimorazole were investigated. While nimorazole is currently applied for head and neck cancer treatment in Danish hospital units, misonidazole was excluded due to a high cytotoxicity [234]. The radiosensitising impact was proven for both compounds. While it is known that the reactions on a physico-chemical stage are initiated by electron interactions, the exact

working mechanism was still unclear. In this thesis, both compounds were studied in gas-phase experiments and showed very similar results. The associated electron attachment made up the by far most intense reaction product. The most intense fragment anion, NO_2^- is an order of magnitude lower in intensity, the remaining fragments at least two. Nimorazole was additionally studied in a water clusters, mimicking the tissue environment to some extent, which quenched the DEA channels even further in favour of the non-decomposed parent anion. This led to the conclusion that the principle of action arises from the associative attachment channel. The efficient reduction of the compound is necessary for the accumulation in the cell. For nimorazole, the cross section for the formation of the parent anion was determined in gas-phase studies and amounts to approximately $3 \cdot 10^{-18}\,\mathrm{m}^2$ at virtually 0 eV electron energy. This is close to the highest known cross sections upon electron attachment, among them associative electron attachment to SF_6 [117], and thus exceeds the cross sections of most already studied molecules. For misonidazole, the cross section is estimated to be of the same order of magnitude.

The second part of the thesis is dedicated to electron interactions with doped neon clusters to answer fundamental research questions. Cationic mass spectra upon electron ionisation were recorded with the dopant molecules CO_2, O_2, H_2O, and D_2O. The cluster series were extracted from the mass spectra and the comparison with pristine cluster data revealed a, in general, similar behaviour but also some additional peak structures, indicating stabilisation effects due to the neon environment. Since the clusters were rather small, hardly any magic numbers were observed. While the strongest cluster series for carbon dioxide is given by the stable molecule $(CO_2)_n^+$, water and heavy water are observed in a hydrated or deuterated form $((H_2O)_nH)^+$, and $((D_2O)_nD)^+$, respectively. Molecular oxygen is the only dopant studied for which two strong cluster series are observed with $(O_2)_n^+$ and $(O_2)_nO^+$. Mixed series with neon were either not detected or very weak in case of all dopants.

Additionally, for neon clusters doped with carbon dioxide and molecular oxygen, data on electron attachment was collected. Two effects were observed that correlate with the mean neon cluster size. The first effect is that the resonance thresholds and maxima depend on the mean neon cluster size. The CO_2 data shows indications for the formation of a conduction band in the neon clusters, but a minimal neon cluster size seems to be required. This results in an energy barrier for incoming electrons of approximately 0.8 eV. Since the number of measurements for neon clusters doped with oxygen is limited, the conduction band could neither be confirmed nor disproved. The second effect concerns the relative peak height of the resonances, which change depending on the neon cluster size. This effect was already observed for doped helium clusters [284]. Strikingly, the trend is reversed when comparing CO_2 and O_2 data. While for $(O_2)_n^-$ ion yields the high energy resonances are suppressed for larger neon clusters, it is the other way around for $(CO_2)_n^-$ ion yields. Yet another effect observed for neon clusters doped with molecular oxygen is the increased amount of resonances observed compared to pure O_2 clusters. One of those resonances is particularly interesting as it could be assigned to a previous excitation of a neon atom in which the electron transfers energy to the neon cluster before it attaches to the oxygen cluster.

Although this thesis provides new knowledge in the field of the working principle of radiosensitisers and reinforced an approach of proposing new potential agents based on a physico-chemical stage, these statements should be investigated further. This means additional nitroimidazolic compounds should be studied and compared to the behaviour of nimorazole and misonidazole, and additional studies in both water clusters and solu-

tions mimicking the environment of the human cell are necessary in order to prove that associative attachment is the key process that the action of nitroimidazole is based on. For SeCNdU and similar compounds, like 5-trifluoromethanesulfonyl-uracil (OTfU), the studies should also be taken one step further towards tests *in vitro*, remembering that associative attachment (AA) and DEA reactions do not provide sufficient information about the tolerability of the compound as a radiotherapeutic agent.

The study of doped neon clusters has also raised many new questions to be investigated in addition to answering some existing ones. Improving the cluster source in order to produce larger neon clusters would enable a better comparison to previous studies of doped helium clusters/droplets. Additionally, it can be expected that both magic numbers and mixed cluster series only appear for larger neon clusters. The data obtained by electron attachment to neon clusters doped with carbon dioxide molecules reveals a first indication for the formation of an energy band, but this requires confirmation. The study of different dopant molecules with an otherwise unchanged setup could provide clarity about whether this effect can definitely be assigned to an energy barrier. A puzzling observation was the relative peak height dependency on the mean neon cluster size. Since the trends are opposed for O_2 and CO_2, further dopant molecules must be studied to determine the origin of this effect. Last but not least, the study of electron attachment to neon clusters doped with molecular oxygen revealed that the electron can first interact with the neon atoms leading to electronic excitation of a neon atom before it attaches to the oxygen. For neon clusters doped with oxygen, an additional resonance was found which was not reported in previous studies of pristine oxygen clusters. A new study of pure oxygen clusters is required with higher statistics and resolution to improve the comparison of resonances and find the origin of this additional feature. Since its ion yield is comparably small and energetically close to the other resonances, it might have been overlooked in the previous studies. Additionally, more dopant molecules should be investigated regarding resonances revealing a previous interaction with the neon cluster.

Although many questions were answered, even more new ones came up during the course of this thesis. This is a clear indication for the richness of the field, and that it will keep arising interest, at least for some more years to come.

Bibliography

[1] E. A. Davis and I. J. Falconer. *J.J. Thompson and the Discovery of the Electron*. Taylor & Francis, (1997).

[2] J. Chang et al. *An Excess of Cosmic Ray Electrons at Energies of 300-800 GeV*. In: Nature 456.7220 (2008), pp. 362–365. DOI: 10.1038/nature07477.

[3] E. Illenberger and J. Momigny. *Gaseous Molecular Ions - An Introduction to Elementary Processes Induced by Ionization*. Steinkopff, (1992).

[4] E. Adli et al. *Acceleration of Electrons in the Plasma Wakefield of a Proton Bunch*. In: Nature 561.7723 (2018), pp. 363–367. DOI: 10.1038/s41586-018-0485-4.

[5] K. Kokurewicz et al. *Focused Very High-Energy Electron Beams as a Novel Radiotherapy Modality for Producing High-Dose Volumetric Elements*. In: Scientific Reports 9.1 (2019), p. 10837. DOI: 10.1038/s41598-019-46630-w.

[6] O. Ingólfsson. *Low-Energy Electrons: Fundamentals and Applications*. PAN Stanford Publishing, (2019).

[7] E. M. Zeman, E. C. Schreiber, and J. E. Tepper. *Basics of Radiation Therapy*. In: Abeloff's Clinical Oncology. Ed. by J. Niederhuber et al. Elsevier, (2019).

[8] P. Wardman. *Chemical Radiosensitizers for Use in Radiotherapy*. In: Clinical Oncology 19.6 (2007), pp. 397–417. DOI: 10.1016/j.clon.2007.03.010.

[9] H. Wang, X. Mu, and X.-D. Zhang. *Cancer Radiosensitizers*. In: Trends in Pharmacological Sciences 39.1 (2017), pp. 24–48. DOI: 10.1016/j.tips.2017.11.003.

[10] L. Sanche. *Beyond Radical Thinking*. In: Nature 461.7262 (2009), pp. 358–359. DOI: 10.1038/461358a.

[11] F. Martin et al. *DNA Strand Breaks Induced by 0-4 eV Electrons: The Role of Shape Resonances*. In: Physical Review Letters 93.6 (2004). DOI: 10.1103/physrevlett.93.068101.

[12] J. Overgaard. *Hypoxic Radiosensitization: Adored and Ignored*. In: Journal of Clinical Oncology 25.26 (2007), pp. 4066–4074. DOI: 10.1200/JCO.2007.12.7878.

[13] L. Sanche. *Nanoscale Dynamics of Radiosensitivity: Role of Low Energy Electrons*. In: Radiation Damage in Biomolecular Systems. Dordrecht: Springer, (2012), pp. 3–43. DOI: 10.1007/978-94-007-2564-5_1.

[14] H. Haberland. *Clusters of Atoms and Molecules: Theory, Experiment and Clusters of Atoms*. Springer, (1996).

[15] M. E. Jacox. *The Spectroscopy of Molecular Reaction Intermediates Trapped in the Solid Rare Gases*. In: Chemical Society Reviews 31.2 (2002), pp. 108–115. DOI: 10.1039/b102907j.

[16] A. Barnes et al. *Matrix Isolation Spectroscopy*. Vol. 76. Springer Science & Business Media, (2012).

[17] R. Lambo et al. *Electronic Spectroscopy of Ytterbium in a Neon Matrix*. In: The Journal of chemical physics 137.20 (2012), p. 204315. DOI: 10.1063/1.4768419.

[18] L. Wan et al. *Neon Matrix Isolation Spectroscopy of CO_2 Isotopologues*. In: Journal of Molecular Spectroscopy 257.2 (2009), pp. 217–219. DOI: 10.1016/j.jms.2009.07.006.

[19] W. Demtröder. *Experimentalphysik 1: Mechanik und Wärme*. Springer, (2008).

[20] W. Demtröder. *Atoms, Molecules and Photons*. Springer, (2010).

[21] W. Demtröder. *Molecular Physics*. Wiley VCH, (2007).

[22] P. A. Tipler and R. A. Llewellyn. *Modern physics*. W.H. Freeman, (2012).

[23] F. Schwabl. *Quantum Mechanics*. Springer-Verlag Berlin Heidelberg, (2010).

[24] I. N. Levine. *Quantum Chemistry*. Pearson Education, (2009).

[25] H. J. Eichler, J. Eichler, and O. Lux. *Lasers Basics, Advances and Applications*. Springer International Publishing, (2018).

[26] F. H. Field and J. L. Franklin. *Electron Impact Phenomena and the Properties of Gaseous Ions*. (1970).

[27] K. N. Joshipura and N. J. Mason. *Atomic-Molecular Ionization by Electron Scattering: Theory and Applications*. Cambridge University Press, (2019).

[28] L. G. Christophorou. *Electron-Molecule Interactions and Their Applications*. Acad. Press, (1984).

[29] J. H. Gross. *Mass Spectrometry*. 3rd ed. Springer International Publishing, (2017).

[30] R. M. Thorman et al. *The Role of Low-Energy Electrons in Focused Electron Beam Induced Deposition: Four Case Studies of Representative Precursors*. In: Beilstein Journal of Nanotechnology 6 (2015), pp. 1904–1926. DOI: 10.3762/bjnano.6.194.

[31] S. G. Lias and J. E. Bartmess. *Gas-Phase Ion Thermochemistry*. In: NIST Chemistry WebBook, NIST Standard Reference Database Number 69. Ed. by P. J. Linstrom and W. G. Mallard. Gaithersburg MD, 20899: National Institute of Standards and Technology, (2019). URL: https://webbook.nist.gov/chemistry/ion/.

[32] J. N. Bull, J. W. L. Lee, and C. Vallance. *Absolute Electron Total Ionization Cross-Sections: Molecular Analogues of DNA and RNA Nucleobase and Sugar Constituents*. In: Physical Chemistry Chemical Physics 16.22 (2014), pp. 10743–10752. DOI: 10.1039/c4cp00490f.

[33] T. Taylor. *Understanding Electron Ionization Processes for GC–MS*. In: LCGC North America 33.4 (2015), p. 290.

[34] T. D. Märk and G. H. Dunn. *Electron Impact Ionization*. Springer-Verlag, (1985).

[35] E. P. Wigner. *On the Behaviour of Cross Sections Near Threshold*. In: Physical Review 73.9 (1948), p. 1002. DOI: 10.1103/PhysRev.73.1002.

[36] G. H. Wannier. *The Threshold Law for Single Ionization of Atoms or Ions by Electrons*. In: Physical Review 90.5 (1953), pp. 817–825. DOI: 10.1103/physrev.90.817.

[37] S. Geltman. *Theory of Ionization Probability Near Threshold*. In: Physical Review 102.1 (1956), pp. 171–179. DOI: 10.1103/physrev.102.171.

[38] H. Klar and W. Schlecht. *Threshold Multiple Ionization of Atoms. Energy Dependence for Double and Triple Escape*. In: Journal of Physics B: Atomic and Molecular Physics 9.10 (1976), pp. 1699–1711. DOI: 10.1088/0022-3700/9/10/015.

[39] G. H. Wannier. *Threshold Law for Multiple Ionization*. In: Physical Review 100.4 (1955), pp. 1180–1180. DOI: 10.1103/physrev.100.1180.

[40] O. Ingólfsson, F. Weik, and E. Illenberger. *The Reactivity of Slow Electrons with Molecules at Different Degrees of Aggregation: Gas Phase, Clusters and Condensed Phase*. In: International Journal of Mass Spectrometry and Ion Processes 155.1-2 (1996), pp. 1–68. DOI: 10.1016/s0168-1176(96)04392-3.

[41] D. T. Birtwistle and A. Herzenberg. *Vibrational Excitation of N_2 by Resonance Scattering of Electrons*. In: Journal of Physics B: Atomic and Molecular Physics 4.1 (1971), pp. 53–70. DOI: 10.1088/0022-3700/4/1/009.

[42] M. Fenzlaff, R. Gerhard, and E. Illenberger. *Associative and Dissociative Electron Attachment by SF_6 and SF_5Cl*. In: The Journal of Chemical Physics 88.1 (1988), pp. 149–155. DOI: 10.1063/1.454646.

[43] T. Jaffke et al. *Formation of C_{60}^- and C_{70}^- by Free Electron Capture. Activation Energy and Effect of the Internal Energy on Lifetime*. In: Chemical physics letters 226.1-2 (1994), pp. 213–218. DOI: 10.1016/0009-2614(94)00704-7.

[44] I. Bald et al. *From Isolated Molecules Through Clusters and Condensates to the Building Blocks of Life*. In: International Journal of Mass Spectrometry 277.1-3 (2008), pp. 4–25. DOI: 10.1016/j.ijms.2008.06.013.

[45] H. S. Taylor, G. V. Nazaroff, and A. Golebiewski. *Qualitative Aspects of Resonances in Electron-Atom and Electron-Molecule Scattering, Excitation, and Reactions*. In: The Journal of Chemical Physics 45.8 (1966), pp. 2872–2888. DOI: 10.1063/1.1728041.

[46] K. Hansen et al. *Spontaneous Decay of Small Copper-Cluster Anions Cu_n^- (n=3–6), on Long Time Scales*. In: Physical Review A 95.2 (2017), p. 022511. DOI: 10.1103/PhysRevA.95.022511.

[47] B. Ómarsson. *Promoting Reaction Channels in Dissociative Electron Attachment Through Bond Formation and Rearrangement*. PhD thesis. University of Iceland, (2014).

[48] L. Bergmann and C. Schaefer. *Lehrbuch der Experimentalphysik, Gase, Nanosysteme, Flüssigkeiten*. Walter de Gruyter, (2006).

[49] T. D. Märk. *Free Electron Attachment to van der Waals Clusters*. In: International Journal of Mass Spectrometry and Ion Processes 107.2 (1991), pp. 143–163. DOI: 10.1016/0168-1176(91)80055-r.

[50] H. Pauly. *Atom, Molecule, and Cluster Beams*. Springer, (2000).

[51] R. L. Johnston. *Atomic and Molecular Clusters*. Taylor & Francis, (2005).

[52] E. Illenberger. *Electron-Attachment Reactions in Molecular Clusters*. In: Chemical Reviews 92.7 (1992), pp. 1589–1609. DOI: 10.1021/cr00015a006.

[53] E. R. Bernstein. *Chemical Reactions in Clusters*. Oxford Univ. Press, (1996).

[54] A. Mauracher et al. *Cold Physics and Chemistry: Collisions, Ionization and Reactions Inside Helium Nanodroplets Close to Zero K*. In: Physics Reports 751 (2018), pp. 1–90. DOI: 10.1016/j.physrep.2018.05.001.

[55] C. E. Klots. *Evaporative Cooling*. In: The Journal of Chemical Physics 83.11 (1985), pp. 5854–5860. DOI: 10.1063/1.449615.

[56] J. Farges et al. *Structure and Temperature of Rare Gas Clusters in a Supersonic Expansion*. In: Surface Science Letters 106.1-3 (1981), pp. 95–100. DOI: 10.1016/0167-2584(81)90311-x.

[57] O. F. Hagena. *Condensation in Free Jets: Comparison of Rare Gases and Metals*. In: Zeitschrift für Physik D - Atoms, Molecules and Clusters 4.3 (1987), pp. 291–299. DOI: 10.1007/bf01436638.

[58] O. F. Hagena and W. Obert. *Cluster Formation in Expanding Supersonic Jets: Effect of Pressure, Temperature, Nozzle Size, and Test Gas*. In: The Journal of Chemical Physics 56.5 (1972), pp. 1793–1802. DOI: 10.1063/1.1677455.

[59] U. Buck and R. Krohne. *Cluster Size Determination from Diffractive He Atom Scattering*. In: The Journal of Chemical Physics 105.13 (1996), pp. 5408–5415. DOI: 10.1063/1.472406.

[60] H. Lu et al. *An Experimental Investigation on the Performance of Conical Nozzles for Argon Cluster Formation in Supersonic Jets*. In: The Journal of Chemical Physics 132.12 (2010), p. 124303. DOI: 10.1063/1.3356024.

[61] O. F. Hagena. *Nucleation and Growth of Clusters in Expanding Nozzle Flows*. In: Surface Science Letters 106.1-3 (1981). DOI: 10.1016/0167-2584(81)90312-1.

[62] M. D. Morse. *Supersonic Beam Sources*. In: Experimental Methods in the Physical Sciences; Atomic, Molecular, and Optical Physics: Atoms and Molecules 29 (1996), pp. 21–47. DOI: 10.1016/s0076-695x(08)60784-x.

[63] T. Rogers et al. *Structural Characteristics of Hydrogen and Compressed Natural Gas Fuel Jets*. In: International Journal of Hydrogen Energy 40.3 (2015), pp. 1584–1597. DOI: 10.1016/j.ijhydene.2014.10.140.

[64] K. Jousten. *Wutz Handbuch Vakuumtechnik*. Vieweg und Teubner Verlag, (2004).

[65] M. Neustetter. *Low-Energy Electron Interactions with Small Molecular Clusters*. PhD thesis. University of Innsbruck, (2016).

[66] B. Haslwanter. *Construction of a Pulsed Cluster Source for the Production of Hydrated Biomolecules*. MA thesis. University of Innsbruck, (2016).

[67] CTI Cryogenics. *CTI-Cryogenics 8200 Compressor*. http://uhv.cheme.cmu.edu/manuals/cryopumpcompressor8200.pdf, (2009).

[68] Lake Shore Cryotronics, Inc. *User's Manual Model 325 Temperature Controller*. https://lakeshore.com, (2017).

[69] P. Walker and W. H. Tarn. *Handbook of Metal Etchants*. CRC Press, (1991).

[70] G. A. Holzer. *Investigation of Appearance Energies of Neon Cluster Ions and Carbon Dioxide Cluster Ions Formed by Electron Ionisation of Pure and Doped Neon Clusters*. MA thesis. University of Innsbruck, (2017).

[71] S. Matejcik. *Experimental Studies of Electron Attachment to Molecules Using Swarm and Beam Techniques*. PhD thesis. University of Innsbruck, (1995).

[72] D. Muigg. *Inelastic Interaction of Monochromatized Electrons with Molecules and Clusters of Atmospheric Relevance*. PhD thesis. University of Innsbruck, (1998).

[73] G. Denifl. *Electron Attachment and Ionization of Molecules and Clusters of Atmospheric Relevance*. PhD thesis. University of Innsbruck, (1998).

[74] agar scientific. *Agar Filaments AGA054*. http://agarscientific.com/agar-filaments.html, (2019).

[75] Kimball Physics Inc. *Tungsten Filaments; Hairpin Thermionic Emitters*. https://kimballphysics.com/cathode-specs-w, (2019).

[76] I. V. Hertel and C.-P. Schulz. *Atoms, Molecules and Optical Physics 2*. Springer-Verlag Berlin Heidelberg, (2016).

[77] R. Herzog. *Ablenkung von Kathoden- und Kanalstrahlen am Rande eines Kondensators, dessen Streufeld durch eine Blende begrenzt ist*. In: Zeitschrift für Physik 97.9-10 (1935), pp. 596–602. DOI: 10.1007/bf01333901.

[78] O. Sise. *A Study of the Electron Optical Properites of Hemispherical Deflection Analyzers Aimed at Optimizing Their Fringing Field Correction Schemes*. In: UPB Scientific Bulletin, Series A 77.1 (2015), pp. 213–222.

[79] D. Roy and D. Tremblay. *Design of Electron Spectrometers*. In: Reports on Progress in Physics 53.12 (1990), pp. 1621–1674. DOI: 10.1088/0034-4885/53/12/003.

[80] G. Hanel et al. *Dissociative Electron Attachment to N_2O Clusters: Attachment Spectra for $(N_2O)_nO^-$ Anions (n=0-7) From About 0 up to 25 eV*. In: International Journal of Mass Spectrometry 205.1-3 (2001), pp. 65–75. DOI: 10.1016/s1387-3806(00)00274-8.

[81] Pfeiffer Vacuum GmbH. *The Vacuum Technology Book Volume 2; Know-how Book*. http://pfeiffer-vacuum.com/de/, (2013).

[82] P. E. Miller and M. B. Denton. *The Quadrupole Mass Filter: Basic Operating Concepts*. In: Journal of Chemical Education 63.7 (1986), p. 617. DOI: 10.1021/ed063p617.

[83] R. E. March and J. F. J. Todd. *Quadrupole Ion Trap Mass Spectrometry*. Wiley-Interscience, (2005).

[84] K. Blaum. *High-Accuracy Mass Spectrometry with Stored Ions*. In: Physics Reports 425.1 (2006), pp. 1–78. DOI: 10.1016/j.physrep.2005.10.011.

[85] AZO Materials. *Using Graphical Tools to Understand Quadrupole Theory*. http://azom.com/article.aspx?ArticleID=10996, (2014).

[86] Pfeiffer Vacuum GmbH. *HiQuad Quadrupole Mass Spectrometry Systems; QMG 700*. http://pfeiffer-vacuum.net, (2004).

[87] Pfeiffer Vacuum GmbH. *High Frequency Generators; QHM 400-1 QMH 400-5 QMH 410-1 QMH 410-2 QMH 410-3*. http://pfeiffer-vacuum.net, (2001).

[88] Pfeiffer Vacuum GmbH. *QMG 422 Analyzers; QMA 400 QMA 410 QMA 430*. www.pfeiffer-vacuum.net, (2001).

[89] J. T. Watson and O. D. Sparkman. *Introduction to Mass Spectrometry: Instrumentation, Applications and Strategies for Data Interpretation*. J. Wiley & Sons, (2011).

[90] E. D. Hoffmann and V. Stroobant. *Mass Spectrometry: Principles and Applications*. Wiley, (2013).

[91] Dr. Sjuts Optotechnik GmbH. *Final Test Sheet Model KBL510*. http://sjuts.com, (2018).

[92] J. H. Moore, M. A. Coplan, and C. C. Davis. *Building Scientific Apparatus: A Practical Guide to Design and Construction*. Cambridge Univ. Press, (2009).

[93] Winkelnkemper Engineering. *Pulse Preamplifier/Discriminator WMT PAD 06A*. http://winkelnkemper-engineering.de, (2018).

[94] vacuubrand. *Chemistry Diaphragm Pumps, Chemistry Vacuum Systems, Chemistry Pumping Units*. http://vacuubrand.com, (2018).

[95] Agilent Technologies. *Agilent Vacuum Product Catalog*. https://agilent.com/en/products/vacuum-technologies, (2015).

[96] K. Tanzer. *Studying the Molecular Mechanisms of Radiation Damage: Low-energy Electron Interactions with Biomolecules and Medically Relevant Molecules*. PhD thesis. University of Innsbruck, (2015).

[97] J. F. O'Hanlon. *A User's Guide to Vacuum Technology*. Wiley, (2003).

[98] Pfeiffer Vacuum GmbH. *The Vacuum Technology Book Volume 2; Vacuum Generation*. http://pfeiffer-vacuum.com/de/, (2013).

[99] N. H. Nahler. *Photodissoziation von Halogenwasserstoff- und orientierten Wasserstoff-Edelgas-Halogen-Molekülen in Clusterumgebungen*. PhD thesis. Georg-August-Universität Göttingen, (2002).

[100] M. Fárník. *Molecular Dynamics in Free Clusters and Nanoparticles Studied in Molecular Beams*. PhD thesis. J. Heyrovský Institute of Physical Chemistry, v.v.i. Academy of Sciences of the Czech Republic, (2011).

[101] J. Kočišek. *Implementation of Ion Imaging Technique in Experiments with Free Molecules, Clusters and Nanoparticles*. PhD thesis. Charles University, Prague, (2013).

[102] J. Lengyel. *Cluster in Molecular Beams: Nucleation and Reactivity*. PhD thesis. University of Chemistry and Technology Prague, (2015).

[103] M. Fárník and V. Poterya. *Atmospheric Processes on Ice Nanoparticles in Molecular Beams*. In: Frontiers in Chemistry 2.4 (2014). DOI: 10.3389/fchem.2014.00004.

[104] J. Kočišek et al. *Microhydration Prevents Fragmentation of Uracil and Thymine by Low-Energy Electrons*. In: The Journal of Physical Chemistry Letters 7.17 (2016), pp. 3401–3405. DOI: 10.1021/acs.jpclett.6b01601.

[105] Elemental Scientific. *pergo - Argon Nebulizer Gas Humidifier for High TDS Sample Analysis*. http://icpms.com/products/pergo.php, (2019).

[106] J. Poštulka et al. *Energy Transfer in Microhydrated Uracil, 5-Fluorouracil, and 5-Bromouracil*. In: The Journal of Physical Chemistry B 121.38 (2017), pp. 8965–8974. DOI: 10.1021/acs.jpcb.7b07390.

[107] Stefan Kaesdorf - Geräte für Forschung und Industrie. *Reflectron RFT50*. https://kaesdorf.de/RFT50.html, (2019).

[108] J. Kočišek, J. Lengyel, and M. Fárník. *Ionization of Large Homogeneous and Heterogeneous Clusters Generated in Acetylene–Ar Expansions: Cluster Ion Polymerization*. In: The Journal of Chemical Physics 138.12 (2013), p. 124306. DOI: 10.1063/1.4796262.

[109] H. H. Telle and Á. G. Ureña. *Laser Spectroscopy and Laser Imaging: An Introduction*. CRC Press / Taylor & Francis Group, (2018).

[110] Andreas06. *Mcp-de.svg*. https://commons.wikimedia.org/wiki/File:Mcp-de.svg, (2019).

[111] Edwards. *World Class Vacuum Solutions; Product Catalogue*. http://edwardsvacuum.com, (2015).

[112] Alcatel. *High Vacuum Technology; Instruction Manual*. http://idealvac.com, (2009).

[113] Leybold. *Full Line Catalog; Vacuum Components and Vacuum Technology*. http://leybold.com/epaper/en, (2018).

[114] Agilent Technologies. *VHS-4, VHS-6 and VHS-250 Diffusion Pumps; Instruction Manual*. http://agilent.com/cs/library/usermanuals/Public/, (2013).

[115] S. Ralser et al. *Extracting Cluster Distributions from Mass Spectra: IsotopeFit*. In: International Journal of Mass Spectrometry 379 (2015), pp. 194–199. DOI: 10.1016/j.ijms.2015.01.004.

[116] M. M. Dawley et al. *Electron Ionization of the Nucleobases Adenine and Hypoxanthine near the Threshold: A Combined Experimental and Theoretical Study*. In: Physical Chemistry Chemical Physics 16.45 (2014), pp. 25039–25053. DOI: 10.1039/C4CP03452J.

[117] L. G. Christophorou and J. K. Olthoff. *Electron Attachment Cross Sections and Negative Ion States of SF_6*. In: International Journal of Mass Spectrometry 205.1 (2001), pp. 27–41. DOI: 10.1016/S1387-3806(00)00280-3.

[118] J. P. Gauyacq and A. Herzenberg. *The Attachment of Very Slow Electrons to Polyatomic Molecules*. In: Journal of Physics B: Atomic and Molecular Physics 17.6 (1984), pp. 1155–1171. DOI: 10.1088/0022-3700/17/6/025.

[119] I. I. Fabrikant, H. Hotop, and M. Allan. *Elastic Scattering, Vibrational Excitation, and Attachment in Low-Energy Electron-SF_6 Scattering: Experiment and Effective Range Theory*. In: Physical Review A 36.39 (2005), p. 022712. DOI: 10.1103/PhysRevA.71.022712.

[120] I. I. Fabrikant et al. *Recent Progress in Dissociative Electron Attachment: From Diatomics to Biomolecules*. In: Advances In Atomic, Molecular, and Optical Physics. Ed. by E. Arimondo, C. C. Lin, and S. F. Yelin. Vol. 66. Academic Press, (2017), pp. 545–657. DOI: 10.1016/bs.aamop.2017.02.002.

[121] A. Kalamarides et al. *Use of Rydberg Atoms to Probe Negative Ion Lifetimes*. In: The Journal of Chemical Physics 93.6 (1990), pp. 4043–4046. DOI: 10.1063/1.458736.

[122] R. A. Popple et al. *Dissociative Electron Attachment to CCl_4: Lifetime of the CCl_4^- Intermediate*. In: The Journal of Chemical Physics 104.21 (1996), pp. 8485–8489. DOI: 10.1063/1.471597.

[123] S. Matejcik et al. *Dissociative Electron Attachment Cross Section to $CHCl_3$ Using a High Resolution Crossed Beams Technique*. In: The Journal of Chemical Physics 107.21 (1997), pp. 8955–8962. DOI: 10.1063/1.475187.

[124] D. Smith and P. Spanel. *Studies of Electron Attachment at Thermal Energies Using the Flowing Afterglow–Langmuir Probe Technique*. In: Advances In Atomic, Molecular, and Optical Physics. Ed. by B. Bederson and A. Dalgarno. Vol. 32. Academic Press, (1994), pp. 307–343. DOI: 10.1016/S1049-250X(08)60022-1.

[125] O. J. Orient et al. *Comparison of Experimental and Calculated Attachment Rate Constants for $CFCl_3$ and CCl_4 in the Temperature Range 294-500 K*. In: Physical Review A 39.9 (1989), pp. 4494–4501. DOI: 10.1103/PhysRevA.39.4494.

[126] D. Klar, M. W. Ruf, and H. Hotop. *Dissociative Electron Attachment to CCl_4 Molecules at Low Electron Energies with meV Resolution*. In: International Journal of Mass Spectrometry 205.1 (2001), pp. 93–110. DOI: 10.1016/S1387-3806(00)00271-2.

[127] S. C. Chu and P. D. Burrow. *Dissociative Attachment of Electrons in the Chloromethanes*. In: Chemical Physics Letters 172.1 (1990), pp. 17–22. DOI: 10.1016/0009-2614(90)87209-A.

[128] T. Oster, A. Kühn, and E. Illenberger. *Gas Phase Negative Ion Chemistry*. In: International Journal of Mass Spectrometry and Ion Processes 89.1 (1989), pp. 1–72. DOI: 10.1016/0168-1176(89)85031-1.

[129] K. Aflatooni and P. D. Burrow. *Total Cross Sections for Dissociative Electron Attachment in Dichloroalkanes and Selected Polychloroalkanes: The Correlation with Vertical Attachment Energies*. In: The Journal of Chemical Physics 113.4 (2000), pp. 1455–1464. DOI: 10.1063/1.481963.

[130] H. U. Scheunemann, E. Illenberger, and H. Baumgärtel. *Dissociative Electron Attachment to CCl_4, $CHCl_3$, CH_2Cl_2 and CH_3Cl*. In: Berichte der Bunsengesellschaft für physikalische Chemie 84.6 (1980), pp. 580–585. DOI: 10.1002/bbpc.19800840612.

[131] A. Kramida et al. *NIST Atomic Spectra Database (ver. 5.6.1), [Online]*. Available: https://physics.nist.gov/asd [2015, April 16]. National Institute of Standards and Technology, Gaithersburg, MD. (2018).

[132] D. R. Lide. *CRC Handbook of Chemistry and Physics*. CRC Press, (2008).

[133] E. J. Hall and A. J. Giaccia. *Radiobiology for the Radiologist*. Wolters Kluwer, (2019).

[134] S. R. Cherry, M. E. Phelps, and J. A. Sorenson. *Physics in Nuclear Medicine*. W. B. Saunders Company, (2012).

[135] T. D. Märk, Y. Hatano, and F. Linder. *Electron Collision Cross Sections*. In: Vienna: IAEA-TECDOC-799; International Atomic Energy Agency (IAEA), (1995), pp. 163–27.

[136] Y. Hatano and M. Inokuti. *Photoabsorption, Photoionization and Photodissociation Cross Sections*. In: Vienna: IAEA-TECDOC-799; International Atomic Energy Agency (IAEA), (1995), pp. 331–369.

[137] S. M. Pimblott and J. A. Laverne. *Production of Low-Energy Electrons by Ionizing Radiation*. In: Radiation Physics and Chemistry 76.8-9 (2007), pp. 1244–1247. DOI: 10.1016/j.radphyschem.2007.02.012.

[138] E. Alizadeh and L. Sanche. *Precursors of Solvated Electrons in Radiobiological Physics and Chemistry*. In: Chemical Reviews 112.11 (2012), pp. 5578–5602. DOI: 10.1021/cr300063r.

[139] E. Alizadeh, T. M. Orlando, and L. Sanche. *Biomolecular Damage Induced by Ionizing Radiation: The Direct and Indirect Effects of Low-Energy Electrons on DNA*. In: Annual Review of Physical Chemistry 66.1 (2015), pp. 379–398. DOI: 10.1146/annurev-physchem-040513-103605.

[140] S. M. Pimblott and A. Mozumder. *Structure of Electron Tracks in Water. 2. Distribution of Primary Ionizations and Excitations in Water Radiolysis*. In: The Journal of Physical Chemistry 95.19 (1991), pp. 7291–7300. DOI: 10.1021/j100172a036.

[141] C. G. Elles et al. *Excitation-Energy Dependence of the Mechanism for Two-Photon Ionization of Liquid H_2O and D_2O from 8.3 to 12.4 eV*. In: The Journal of Chemical Physics 125.4 (2006), p. 044515. DOI: 10.1063/1.2217738.

[142] C. von Sonntag. *Free Radical Induced DNA Damage and its Repair: A Chemical Perspective; with 100 Tables*. Springer, (2006).

[143] R. Farhataziz and M. A. J. Rodgers. *Radiation Chemistry: Principles and Applications*. Wiley VCH, (1987).

[144] Y. Frongillo et al. *Monte Carlo Simulation of Fast Electron and Proton Tracks in Liquid Water - II. Nonhomogeneous Chemistry*. In: Radiation Physics and Chemistry 51.3 (1998), pp. 245–254. DOI: 10.1016/S0969-806X(97)00096-0.

[145] T. Kai et al. *A Significant Role of Non-Thermal Equilibrated Electrons in the Formation of Deleterious Complex DNA Damage*. In: Physical Chemistry Chemical Physics 20.4 (2018), pp. 2838–2844. DOI: 10.1039/c7cp06903k.

[146] Q.-B. Lu. *Effects and Applications of Ultrashort-Lived Prehydrated Electrons in Radiation Biology and Radiotherapy of Cancer*. In: Mutation Research/Reviews in Mutation Research 704.1-3 (2010), pp. 190–199. DOI: 10.1016/j.mrrev.2010.01.012.

[147] K. R. Siefermann et al. *Binding Energies, Lifetimes and Implications of Bulk and Interface Solvated Electrons in Water*. In: Nature Chemistry 2.4 (2010), pp. 274–279. DOI: 10.1038/nchem.580.

[148] P. W. K. Rothemund. *Folding DNA to Create Nanoscale Shapes and Patterns*. In: Nature 440.7082 (2006), pp. 297–302. DOI: 10.1038/nature04586.

[149] J. Nguyen et al. *Direct Observation of Ultrafast-Electron-Transfer Reactions Unravels High Effectiveness of Reductive DNA Damage*. In: Proceedings of the National Academy of Sciences 108.29 (2011), pp. 11778–11783. DOI: 10.1073/pnas.1104367108.

[150] F. Hutchinson. *Molecular Basis for Action of Ionizing Radiations: A Simple Model Describes the Inactivation by Ionizing Radiations of Molecules in the Living Cell*. In: Science 134.3478 (1961), pp. 533–538. DOI: 10.1126/science.134.3478.533.

[151] S. L. Caër. *Water Radiolysis: Influence of Oxide Surfaces on H_2 Production under Ionizing Radiation*. In: Water 3.1 (2011), pp. 235–253. DOI: 10.3390/w3010235.

[152] C. Molnar and J. Gair. *Concepts of Biology*. BCcampus, (2015).

[153] S. Clancy and W. Brown. *Translation: DNA to mRNA to Protein*. In: Nature Education 1.1 (2008), p. 101.

[154] A. Mozumder and Y. Hatano. *Charged Particle and Photon Interactions with Matter - Chemical, Physicochemical, and Biological Consequences with Applications*. CRC Press, (2004).

[155] M. Löbrich, B. Rydberg, and P. K. Cooper. *Repair of X-Ray-Induced DNA Double-Strand Breaks in Specific Not I Restriction Fragments in Human Fibroblasts: Joining of Correct and Incorrect Ends*. In: Proceedings of the National Academy of Sciences 92.26 (1995), pp. 12050–12054. DOI: 10.1073/pnas.92.26.12050.

[156] L. L. Gunderson, J. E. Tepper, and J. A. Bogart. *Clinical Radiation Oncology*. Elsevier, (2016).

[157] S. W. Yusuf and J. Banchs. *Cancer and Cardiovascular Disease: A Concise Clinical Atlas*. Springer International Publishing, (2018).

[158] J. J. Lu, L. W. Brady, and A. A. Abitbol. *Radiation Oncology: An Evidence-Based Approach*. Springer, (2010).

[159] G. M. Cooper and R. E. Hausman. *The Cell: A Molecular Approach*. Sinauer Associates, (2019).

[160] G. I. Evan and K. H. Vousden. *Proliferation, Cell Cycle and Apoptosis in Cancer*. In: Nature 411.6835 (2001), pp. 342–348. DOI: 10.1038/35077213.

[161] K. Graham and E. Unger. *Overcoming Tumor Hypoxia as a Barrier to Radiotherapy, Chemotherapy and Immunotherapy in Cancer Treatment*. In: International Journal of Nanomedicine Volume 13 (2018), pp. 6049–6058. DOI: 10.2147/ijn.s140462.

[162] T. Herrmann. *Klinische Strahlenbiologie kurz und bündig*. Elsevier, Urban & Fischer, (2006).

[163] G. E. Adams and D. L. Dewey. *Hydrated Electrons and Radiobiological Sensitisation*. In: Biochemical and Biophysical Research Communications 12.6 (1963), pp. 473–477. DOI: 10.1016/0006-291x(63)90318-8.

[164] P. W. Grigsby et al. *Irradiation with or without Misonidazole for Patients with Stages IIIb and IVa Carcinoma of the Cervix: Final Results of RTOG 80-05*. In: International Journal of Radiation Oncology Biology Physics 44.3 (1999), pp. 513–517. DOI: 10.1016/s0360-3016(99)00054-1.

[165] J. Overgaard et al. *Misonidazole Combined with Split-Course Radiotherapy in the Treatment of Invasive Carcinoma of Larynx and Pharynx: Report from the DAHANCA 2 Study*. In: International Journal of Radiation Oncology Biology Physics 16.4 (1989), pp. 1065–1068. DOI: 10.1016/0360-3016(89)90917-6.

[166] J. Overgaard et al. *A Randomized Double-Blind Phase III Study of Nimorazole as a Hypoxic Radiosensitizer of Primary Radiotherapy in Supraglottic Larynx and Pharynx Carcinoma. Results of the Danish Head and Neck Cancer Study (DAHANCA) Protocol 5-85*. In: Radiotherapy and Oncology 46.2 (1998), pp. 135–146. DOI: 10.1016/s0167-8140(97)00220-x.

[167] C. E. Crespo-Hernandez et al. *Ultrafast Excited-State Dynamics in Nucleic Acids*. In: ChemInform 35.24 (2004), pp. 1977–2019. DOI: 10.1002/chin.200424297.

[168] B. Boudaïffa et al. *Resonant Formation of DNA Strand Breaks by Low-Energy (3 to 20 eV) Electrons*. In: Science 287.5458 (2000), pp. 1658–1660. DOI: 10.1126/science.287.5458.1658.

[169] M. A. Huels et al. *Single, Double, and Multiple Double Strand Breaks Induced in DNA by 3-100 eV Electrons*. In: Journal of the American Chemical Society 125.15 (2003), pp. 4467–4477. DOI: 10.1021/ja029527x.

[170] N. S. Hush and A. S. Cheung. *Ionization Potentials and Donor Properties of Nucleic Acid Bases and Related Compounds*. In: Chemical Physics Letters 34.1 (1975), pp. 11–13. DOI: 10.1016/0009-2614(75)80190-4.

[171] C. E. Crespo-Hernández et al. *Ultrafast Excited-State Dynamics in Nucleic Acids*. In: Chemical Reviews 104.4 (2004), pp. 1977–2020. DOI: 10.1021/cr0206770.

[172] C.-R. Wang, J. Nguyen, and Q.-B. Lu. *Bond Breaks of Nucleotides by Dissociative Electron Transfer of Nonequilibrium Prehydrated Electrons: A New Molecular Mechanism for Reductive DNA Damage*. In: Journal of the American Chemical Society 131.32 (2009), pp. 11320–11322. DOI: 10.1021/ja902675g.

[173] J. Ma et al. *Reactivity of Prehydrated Electrons Toward Nucleobases and Nucleotides in Aqueous Solution*. In: Science Advances 3.12 (2017), e1701669. DOI: 10.1126/sciadv.1701669.

[174] K. Westphal et al. *Irreversible Electron Attachment - A Key to DNA Damage by Solvated Electrons in Aqueous Solution*. In: Organic & Biomolecular Chemistry 13.41 (2015), pp. 10362–10369. DOI: 10.1039/c5ob01542a.

[175] A. Kumar et al. *Do Solvated Electrons (e^-_{aq}) Reduce DNA Bases? A Gaussian 4 and Density Functional Theory-Molecular Dynamics Study*. In: The Journal of Physical Chemistry B 120.9 (2016), pp. 2115–2123. DOI: 10.1021/acs.jpcb.5b11269.

[176] L. Sanche. *Low Energy Electron Damage to DNA*. In: Radiation Induced Molecular Phenomena in Nucleic Acids. Ed. by M. K. K. Shukla and J. Leszczynski. Springer Netherlands, (2008).

[177] C. König et al. *Dissociative Electron Attachment to Phosphoric Acid Esters: The Direct Mechanism for Single Strand Breaks in DNA*. In: Physical Review Letters 97.1 (2006), p. 018105. DOI: 10.1103/physrevlett.97.018105.

[178] P. Sulzer et al. *Dissociative Electron Attachment to Furan, Tetrahydrofuran, and Fructose*. In: The Journal of Chemical Physics 125.4 (2006), p. 044304. DOI: 10.1063/1.2222370.

[179] S. Ptasińska et al. *Inelastic Electron Interaction (Attachment/Ionization) with Deoxyribose*. In: The Journal of Chemical Physics 120.18 (2004), pp. 8505–8511. DOI: 10.1063/1.1690231.

[180] I. Bald, J. Kopyra, and E. Illenberger. *Selective Excision of C5 from D-Ribose in the Gas Phase by Low-Energy Electrons (0–1 eV): Implications for the Mechanism of DNA Damage*. In: Angewandte Chemie International Edition 45.29 (2006), pp. 4851–4855. DOI: 10.1002/anie.200600303.

[181] H. Abdoul-Carime, S. Gohlke, and E. Illenberger. *Site-Specific Dissociation of DNA Bases by Slow Electrons at Early Stages of Irradiation*. In: Physical Review Letters 92.16 (2004), p. 168103. DOI: 10.1103/physrevlett.92.168103.

[182] S. Ptasińska et al. *Bond- and Site-Selective Loss of H-from Pyrimidine Bases*. In: Physical Review Letters 95.9 (2005), p. 093201. DOI: 10.1103/physrevlett.95.093201.

[183] S. Denifl et al. *Electron Attachment to the DNA Bases Thymine and Cytosine*. In: Chemical Physics Letters 377.1-2 (2003), pp. 74–80. DOI: 10.1016/s0009-2614(03)01096-0.

[184] S. Denifl et al. *Electron Attachment to the Gas-Phase DNA Bases Cytosine and Thymine*. In: The Journal of Physical Chemistry A 108.31 (2004), pp. 6562–6569. DOI: 10.1021/jp049394x.

[185] S. Denifl et al. *Influence of Functional Groups on the Site-Selective Dissociation of Adenine upon Low-Energy Electron Attachment*. In: Angewandte Chemie International Edition 46.27 (2007), pp. 5238–5241. DOI: 10.1002/anie.200700032.

[186] S. Denifl et al. *Electron Attachment to Gas-Phase Uracil*. In: The Journal of Chemical Physics 120.14 (2004), pp. 6557–6565. DOI: 10.1063/1.1649724.

[187] G. Hanel et al. *Electron Attachment to Uracil: Effective Destruction at Subexcitation Energies*. In: Physical Review Letters 90.18 (2003), p. 188104. DOI: 10.1103/physrevlett.90.188104.

[188] S. Denifl et al. *Dissociative Electron Attachment to DNA Bases Near Absolute Zero Temperature: Freezing Dissociation Intermediates*. In: ChemPhysChem 9.10 (2008), pp. 1387–1389. DOI: 10.1002/cphc.200800245.

[189] J. Berdys et al. *Damage to Model DNA Fragments from Very Low-Energy (<1 eV) Electrons*. In: Journal of the American Chemical Society 126.20 (2004), pp. 6441–6447. DOI: 10.1021/ja049876m.

[190] J. Gu, J. Wang, and J. Leszczynski. *Electron Attachment-Induced DNA Single Strand Breaks: C3'-O3'σ-Bond Breaking of Pyrimidine Nucleotides Predominates*. In: Journal of the American Chemical Society 128.29 (2006), pp. 9322–9323. DOI: 10.1021/ja063309c.

[191] J. Gu, Y. Xie, and H. F. Schaefer. *Near 0 eV Electrons Attach to Nucleotides*. In: Journal of the American Chemical Society 128.4 (2006), pp. 1250–1252. DOI: 10.1021/ja055615g.

[192] J. Gu, J. Wang, and J. Leszczynski. *Low Energy Electron Attachment to the Adenosine Site of DNA*. In: The Journal of Physical Chemistry B 115.49 (2011), pp. 14831–14837. DOI: 10.1021/jp207801e.

[193] J. Kohanoff et al. *Interactions Between Low Energy Electrons and DNA: A Perspective from First-Principles Simulations*. In: Journal of Physics: Condensed Matter 29.38 (2017), p. 383001. DOI: 10.1088/1361-648x/aa79e3.

[194] A. Kumar and M. D. Sevilla. *Low-Energy Electron Attachment to 5'-Thymidine Monophosphate: Modeling Single Strand Breaks Through Dissociative Electron Attachment*. In: The Journal of Physical Chemistry B 111.19 (2007), pp. 5464–5474. DOI: 10.1021/jp070800x.

[195] A. Kumar and M. D. Sevilla. *The Role of πσ* Excited States in Electron-Induced DNA Strand Break Formation: A Time-Dependent Density Functional Theory Study*. In: Journal of the American Chemical Society 130.7 (2008), pp. 2130–2131. DOI: 10.1021/ja077331x.

[196] J. Kopyra. *Low Energy Electron Attachment to the Nucleotide Deoxycytidine Monophosphate: Direct Evidence for the Molecular Mechanisms of Electron-Induced DNA Strand Breaks*. In: Physical Chemistry Chemical Physics 14.23 (2012), pp. 8287–8289. DOI: 10.1039/c2cp40847c.

[197] J. Gu, J. Leszczynski, and H. F. Schaefer. *Interactions of Electrons with Bare and Hydrated Biomolecules: From Nucleic Acid Bases to DNA Segments*. In: Chemical Reviews 112.11 (2012), pp. 5603–5640. DOI: 10.1021/cr3000219.

[198] M. Gaba and C. Mohan. *Development of Drugs Based on Imidazole and Benzimidazole Bioactive Heterocycles: Recent Advances and Future Directions*. In: Medicinal Chemistry Research 25.2 (2015), pp. 173–210. DOI: 10.1007/s00044-015-1495-5.

[199] H. Rosemeyer. *The Chemodiversity of Purine as a Constituent of Natural Products*. In: Chemistry & Biodiversity 1.3 (2004), pp. 361–401. DOI: 10.1002/cbdv.200490033.

[200] R. Sharma. *Nitroimidazole Radiopharmaceuticals in Hypoxia: Part II Cytotoxicity and Radiosensitization Applications*. In: Current Radiopharmaceuticalse 4.4 (2011), pp. 379–393. DOI: 10.2174/1874471011104040379.

[201] A. Ribar et al. *Stripping off Hydrogens in Imidazole Triggered by the Attachment of a Single Electron*. In: Physical Chemistry Chemical Physics 19.9 (2017), pp. 6406–6415. DOI: 10.1039/c6cp08773f.

[202] A. Ribar et al. *Isomer Selectivity in Low-Energy Electron Attachment to Nitroimidazoles*. In: Chemistry - A European Journal 23.52 (2017), pp. 12892–12899. DOI: 10.1002/chem.201702644.

[203] K. Tanzer et al. *Reactions in Nitroimidazole and Methylnitroimidazole Triggered by Low-Energy (0-8 eV) Electrons*. In: The Journal of Physical Chemistry A 119.25 (2015), pp. 6668–6675. DOI: 10.1021/acs.jpca.5b02721.

[204] M. Neustetter et al. *The Effect of Solvation on Electron Attachment to Pure and Hydrated Pyrimidine Clusters*. In: Angewandte Chemie International Edition 54.31 (2015), pp. 9124–9126. DOI: 10.1002/anie.201503733.

[205] M. Neustetter, M. Mahmoodi-Darian, and S. Denifl. *Study of Electron Ionization and Fragmentation of Non-Hydrated and Hydrated Tetrahydrofuran Clusters*. In: Journal of The American Society for Mass Spectrometry 28.5 (2017), pp. 866–872. DOI: 10.1007/s13361-017-1634-y.

[206] M. Smyth, J. Kohanoff, and I. I. Fabrikant. *Electron-Induced Hydrogen Loss in Uracil in a Water Cluster Environment*. In: The Journal of Chemical Physics 140.18 (2014), p. 184313. DOI: 10.1063/1.4874841.

[207] M. Kuhn et al. *Electron-Induced Chemistry in Imidazole Clusters Embedded in Helium Nanodroplets*. In: The European Physical Journal D 72.2 (2018), p. 38. DOI: 10.1140/epjd/e2017-80627-2.

[208] S. Makurat et al. *5-Selenocyanato and 5-Trifluoromethanesulfonyl Derivatives of 2'-Deoxyuridine: Synthesis, Radiation and Computational Chemistry as well as Cytotoxicity*. In: RSC Advances 8.38 (2018), pp. 21378–21388. DOI: 10.1039/C8RA03172J.

[209] R. Meißner et al. *Positive and Negative Ions of the Amino Acid Histidine Formed in Low-Energy Electron Collisions*. In: Journal of Mass Spectrometry (2019), pp. 1–2. DOI: 10.1002/jms.4427.

[210] F. A. Bettelheim et al. *General, Organic, and Biochemistry*. 8th ed. Thomson Brooks/Cole, (2007).

[211] Z. Huang, Z. Lin, and C. Song. *Protonation Processes and Electronic Spectra of Histidine and Related Ions*. In: The Journal of Physical Chemistry A 111.20 (2007), pp. 4340–4352. DOI: 10.1021/jp067280a.

[212] D. M. Close. *Calculated Vertical Ionization Energies of the Common α-Amino Acids in the Gas Phase and in Solution*. In: The Journal of Physical Chemistry A 115.13 (2011), pp. 2900–2912. DOI: 10.1021/jp200503z.

[213] K. R. Wilson et al. *Direct Determination of the Ionization Energy of Histidine with VUV Synchrotron Radiation*. In: International Journal of Mass Spectrometry 249 (2006), pp. 155–161. DOI: 10.1016/j.ijms.2005.12.044.

[214] R. Meißner et al. *Electron Ionization of Imidazole and Its Derivative 2-Nitroimidazole*. In: Journal of The American Society for Mass Spectrometry (2019), pp. 1–14. DOI: 10.1007/s13361-019-02337-w.

[215] M. Schwell et al. *VUV Photophysics and Dissociative Photoionization of Pyrimidine, Purine, Imidazole and Benzimidazole in the 7-18 eV Photon Energy Range*. In: Chemical Physics 353.1-3 (2008), pp. 145–162. DOI: 10.1016/j.chemphys.2008.08.009.

[216] K. J. Klebe, J. J. Van Houte, and J. Van Thuijl. *Loss of HCN and H· From the Molecular Ion of Imidazole*. In: Organic Mass Spectrometry 6.12 (1972), pp. 1363–1368. DOI: 10.1002/oms.1210061211.

[217] T. S. Lawrence et al. *The Effect of Single versus Double-Strand Substitution on Halogenated Pyrimidine-Induced Radiosensitization and DNA Strand Breakage in Human Tumor Cells*. In: Radiation Research 123.2 (1990), pp. 192–198.

[218] R. Watanabe and H. Nikjoo. *Modelling the Effect of Incorporated Halogenated Pyrimidine on Radiation-Induced DNA Strand Breaks*. In: International Journal of Radiation Biology 78.11 (2002), pp. 953–966. DOI: https://doi.org/10.1080/0955300021000024270.

[219] C. Webb et al. *Mechanisms of Radiosensitization in Bromodeoxyuridine-Substituted Cells*. In: International Journal of Radiation Biology 64.6 (1993), pp. 695–705. DOI: 10.1080/09553009314551941.

[220] G. Iliakis et al. *Mechanism of Radiosensitization by Halogenated Pyrimidines: Effect of BrdU on Radiation Induction of DNA and Chromosome Damage and Its Correlation with Cell Killing*. In: Radiation Research 119.2 (1989), pp. 286–304. DOI: 10.2307/3577620.

[221] T. J. Kinsella et al. *Enhancement of X-Ray Induced DNA Damage by Pre-Treatment with Halogenated Pyrimidine Analogs*. In: International Journal of Radiation Oncology Biology Physics 13.5 (1987), pp. 733–739. DOI: 10.1016/0360-3016(87)90292-6.

[222] M.-E. Dextraze, J. R. Wagner, and D. J. Hunting. *5-Bromodeoxyuridine Radiosensitization: Conformation-Dependent DNA Damage*. In: Biochemistry 46.31 (2007), pp. 9089–9097. DOI: 10.1021/bi062114e.

[223] M.-E. Dextraze et al. *Reaching for the Other Side: Generating Sequence-Dependent Interstrand Cross-Links with 5-Bromodeoxyuridine and γ-Rays*. In: Biochemistry 48.9 (2009), pp. 2005–2011. DOI: 10.1021/bi801684t.

[224] Y. Park et al. *Fundamental Mechanisms of DNA Radiosensitization: Damage Induced by Low-Energy Electrons in Brominated Oligonucleotide Trimers*. In: The Journal of Physical Chemistry B 116.32 (2012), pp. 9676–9682. DOI: 10.1021/jp304964r.

[225] L. Chomicz et al. *How to Find Out Whether a 5-Substituted Uracil Could Be a Potential DNA Radiosensitizer*. In: The Journal of Physical Chemistry Letters 4.17 (2013), pp. 2853–2857. DOI: 10.1021/jz401358w.

[226] S. Makurat, L. Chomicz-Mańka, and J. Rak. *Electrophilic 5-Substituted Uracils as Potential Radiosensitizers: A Density Functional Theory Study*. In: ChemPhysChem 17.16 (2016), pp. 2572–2578. DOI: 10.1002/cphc.201600240.

[227] J. Ameixa et al. *Low-Energy Electron-Induced Decomposition of 5-Trifluoromethanesulfonyl-Uracil: A Potential Radiosensitizer*. In: The Journal of Chemical Physics 149.16 (2018), p. 164307. DOI: 10.1063/1.5050594.

[228] M. Sosnowska et al. *5-Selenocyanatouracil: A Potential Hypoxic Radiosensitizer. Electron Attachment Induced Formation of Selenium Centered Radical*. In: The Journal of Physical Chemistry B 121.25 (2017), pp. 6139–6147. DOI: 10.1021/acs.jpcb.7b03633.

[229] R. Meißner et al. *Electron-Induced Dissociation of the Potential Radiosensitizer 5-Selenocyanato-2'-deoxyuridine*. In: The Journal of Physical Chemistry B 123.6 (2019), pp. 1274–1282. DOI: 10.1021/acs.jpcb.8b11523.

[230] J. J. Manura and D. J. Manura. *Isotope Distribution Calculator and Mass Spec Plotter [Online]*. Available: https://sisweb.com/mstools/isotope.htm Scientific Instrument Services. (2019).

[231] J. Overgaard. *Hypoxic Modification of Radiotherapy in Squamous Cell Carcinoma of the Head and Neck - A Systematic Review and Meta-Analysis*. In: Radiotherapy and Oncology 100.1 (2011), pp. 22–32. DOI: 10.1016/j.radonc.2011.03.004.

[232] R. Meißner et al. *Reactions in the Radiosensitizer Misonidazole Induced by Low-Energy (0-10 eV) Electrons*. In: International Journal of Molecular Sciences 20.14 (2019), p. 3496. DOI: 10.3390/ijms20143496.

[233] M. Ončák et al. *Ring Formation and Hydration Effects in Electron Attachment to Misonidazole*. In: International Journal of Molecular Sciences 20.18 (2019), p. 4383. DOI: 10.3390/ijms20184383.

[234] J. Henk, K. Bishop, and S. F. Shepherd. *Treatment of Head and Neck Cancer with CHART and Nimorazole: Phase II Study*. In: Radiotherapy and Oncology 66.1 (2003), pp. 65–70. DOI: 10.1016/S0167-8140(02)00284-0.

[235] M. Baumann et al. *Radiation Oncology in the Era of Precision Medicine*. In: Nature Reviews 16.4 (2016), pp. 234–249. DOI: 10.1038/nrc.2016.18.

[236] A. R. Timothy, J. Overgaard, and M. Overgaard. *A Phase I Clinical Study of Nimorazole as a Hypoxic Radiosensitizer*. In: International Journal of Radiation Oncology Biology Physics 10.9 (1984), pp. 1765–1768. DOI: 10.1016/0360-3016(84)90545-5.

[237] J. Overgaard et al. *A Comparative Investigation of Nimorazole and Misonidazole as Hypoxic Radiosensitizers in a C_3H Mammary Carcinoma in vivo*. In: British Journal of Cancer 46.6 (1982), pp. 904–911. DOI: 10.1038/bjc.1982.300.

[238] M. A. H. Metwally et al. *IAEA-HypoX. A Randomized Multicenter Study of the Hypoxic Radiosensitizer Nimorazole Concomitant with Accelerated Radiotherapy in Head and Neck Squamous Cell Carcinoma*. In: Radiotherapy and Oncology 116.1 (2015), pp. 15–20. DOI: 10.1016/j.radonc.2015.04.005.

[239] M. A. H. Metwally, K. D. Frederiksen, and J. Overgaard. *Compliance and Toxicity of the Hypoxic Radiosensitizer Nimorazole in the Treatment of Patients with Head and Neck Squamous Cell Carcinoma (HNSCC)*. In: Acta Oncologica 53.5 (2013), pp. 654–661. DOI: 10.3109/0284186x.2013.864050.

[240] L. Feketeová et al. *Photoelectron Spectra and Electronic Structures of the Radiosensitizer Nimorazole and Related Compounds*. In: The Journal of Physical Chemistry A 119.39 (2015), pp. 9986–9995. DOI: 10.1021/acs.jpca.5b05950.

[241] S. Pandeti et al. *Nitroimidazolic Radiosensitizers Investigated by Electrospray Ionization Time-of-Flight Mass Spectrometry and Density Functional Theory*. In: RSC Advances 7.71 (2017), pp. 45211–45221. DOI: 10.1039/c7ra08312b.

[242] R. Meißner et al. *Low-Energy Electrons Transform the Nimorazole Molecule into a Radiosensitiser*. In: Nature Communications 10.1 (2019), p. 2388. DOI: 10.1038/s41467-019-10340-8.

[243] J. J. Sáenz, J. M. Soler, and N. García. *Magic Numbers for Positively Charged Rare-Gas Clusters*. In: Chemical Physics Letters 114.1 (1985), pp. 15–18. DOI: 10.1016/0009-2614(85)85045-4.

[244] M. Gatchell et al. *Magic Sizes of Cationic and Protonated Argon Clusters*. In: Physical Review A 98.2 (2018), p. 022519. DOI: 10.1103/PhysRevA.98.022519.

[245] T. D. Märk and P. Scheier. *Production and Stability of Neon Cluster Ions up to Ne_{90}*. In: Chemical Physics Letters 137.3 (1987), pp. 245–249. DOI: 10.1016/0009-2614(87)80213-0.

[246] P. J. Reynolds. *On Clusters and Clustering: From Atoms to Fractals*. North-Holland, (1993).

[247] P. Slavícek et al. *Pickup and Photodissociation of Hydrogen Halides in Floppy Neon Clusters*. In: The Journal of Physical Chemistry A 107.39 (2003), pp. 7743–7754. DOI: 10.1021/jp0357525.

[248] R. von Pietrowski et al. *Fluorescence Excitation Spectroscopy of Xenon Doped Neon Clusters: Size and Site Effects, and Cluster Melting*. In: Zeitschrift für Physik D, Atoms, Molecules and Clusters 40.1 (1997), pp. 22–24. DOI: 10.1007/s004600050149.

[249] A. Ribar. *Inelastic Interactions of Electrons with Molecules and Clusters Studied Using Crossed-Beam Methods*. PhD thesis. University of Innsbruck, (2017).

[250] T. Laarmann et al. *Energy Relaxation and Quenching Processes of Doped Rare-Gas Clusters with a Shell-Like Geometric Structure*. In: The Journal of Chemical Physics 118.7 (2003), pp. 3043–3051. DOI: 10.1063/1.1536982.

[251] A. Kanaev et al. *Photoexcitation of Rare-Gas Neon and Argon Clusters Doped with H_2O*. In: The European Physical Journal D 20.2 (2002), pp. 261–268. DOI: 10.1140/epjd/e2002-00136-9.

[252] R. Bukowski et al. *Intermolecular Potential of Carbon Dioxide Dimer from Symmetry-Adapted Perturbation Theory*. In: The Journal of Chemical Physics 110.8 (1999), pp. 3785–3803. DOI: 10.1063/1.479108.

[253] J. Norooz Oliaee et al. *High Resolution Infrared Spectroscopy of Carbon Dioxide Clusters up to $(CO_2)_{13}$*. In: The Journal of Chemical Physics 135.4 (2011), p. 044315. DOI: 10.1063/1.3615543.

[254] T. V. Mourik, A. K. Wilson, and T. H. Dunning. *Benchmark Calculations with Correlated Molecular Wavefunctions. XIII. Potential Energy Curves for He_2, Ne_2 and Ar_2 Using Correlation Consistent Basis Sets Through Augmented Sextuple Zeta*. In: Molecular Physics 96.4 (1999), pp. 529–547. DOI: 10.1080/002689799165396.

[255] M. Knapp et al. *Size Distributions of Negatively and Positively Charged Clusters: CO_2 and N_2O*. In: Surface Science Letters 156 (1985), pp. 313–320. DOI: 10.1016/0167-2584(85)90413-x.

[256] G. Romanowski and K. Wanczek. *The Influence of Stagnation Pressure and Electron Energy on the Unimolecular Decomposition of CO_2 Microclusters*. In: International Journal of Mass Spectrometry and Ion Processes 70.3 (1986), pp. 247–257. DOI: 10.1016/0168-1176(86)87001-x.

[257] E. K. Berner and R. A. Berner. *Global Environment: Water, Air, and Geochemical Cycles*. Princeton University Press, (2012).

[258] C. Huang et al. *Water Cluster Fragmentation Probed by Pickup Experiments*. In: The Journal of Chemical Physics 145.10 (2016), p. 104304. DOI: 10.1063/1.4962220.

[259] J. Lengyel et al. *Extensive Water Cluster Fragmentation After Low Energy Electron Ionization*. In: Chemical Physics Letters 612 (2014), pp. 256–261. DOI: 10.1016/j.cplett.2014.08.038.

[260] H. Haberland. *A Model for the Processes Happening in a Rare-Gas Cluster After Ionization*. In: Surface Science 156 (1985), pp. 305–312. DOI: 10.1016/0039-6028(85)90588-6.

[261] A. W. Castleman and K. H. Bowen. *Clusters: Structure, Energetics, and Dynamics of Intermediate States of Matter*. In: The Journal of Physical Chemistry 100.31 (1996), pp. 12911–12944. DOI: 10.1021/jp961030k.

[262] P. Qian et al. *Ab initio Investigation of Water Clusters $(H_2O)_n$ (n=2-34)*. In: International Journal of Quantum Chemistry 110.10 (2009), pp. 1923–1937. DOI: 10.1002/qua.22341.

[263] J. T. Su, X. Xu, and W. A. I. Goddard. *Accurate Energies and Structures for Large Water Clusters Using the X3LYP Hybrid Density Functional*. In: ChemInform 36.9 (2005), pp. 10518–10526. DOI: 10.1002/chin.200509001.

[264] B. Temelso, K. A. Archer, and G. C. Shields. *Benchmark Structures and Binding Energies of Small Water Clusters with Anharmonicity Corrections*. In: The Journal of Physical Chemistry A 115.43 (2011), pp. 12034–12046. DOI: 10.1021/jp2069489.

[265] K. Saha. *The Earth's Atmosphere: Its Physics and Dynamics*. Springer Science & Business Media, (2008).

[266] V. K. Gupta, S. Sreenivasaprasad, and R. L. Mach. *Fungal Bio-Molecules: Sources, Applications and Recent Developments*. John Wiley & Sons, (2015).

[267] A. Binet et al. *Oxygen Cluster Ions Formed by Electron Impact of an O_2 Molecular Beam*. In: International Journal of Mass Spectrometry and Ion Processes 83.1-2 (1988), pp. 13–22. DOI: 10.1016/0168-1176(88)80085-5.

[268] T. Sommerfeld, H.-D. Meyer, and L. S. Cederbaum. *Potential Energy Surface of the CO_2^- Anion*. In: Physical Chemistry Chemical Physics 6.1 (2004), pp. 42–45. DOI: 10.1039/b312005h.

[269] G. L. Gutsev, R. J. Bartlett, and R. N. Compton. *Electron Affinities of CO_2, OCS, and CS_2*. In: The Journal of Chemical Physics 108.16 (1998), pp. 6756–6762. DOI: 10.1063/1.476091.

[270] R. Dressler and M. Allan. *Energy Partitioning in the O^-/CO_2 Dissociative Attachment*. In: Chemical Physics 92.2-3 (1985), pp. 449–455. DOI: 10.1016/0301-0104(85)85038-2.

[271] M. Knapp et al. *Formation of Long-Lived CO_2^-, N_2O^-, and Their Dimer Anions, by Electron Attachment to van der Waals Clusters*. In: Chemical Physics Letters 126.3-4 (1986), pp. 225–231. DOI: 10.1016/s0009-2614(86)80074-4.

[272] J. M. Weber. *The Interaction of Negative Charge with Carbon Dioxide - Insight into Solvation, Speciation and Reductive Activation from Cluster Studies*. In: International Reviews in Physical Chemistry 33.4 (2014), pp. 489–519. DOI: 10.1080/0144235x.2014.969554.

[273] S. Denifl et al. *High Resolution Electron Attachment to CO_2 Clusters*. In: Physical Chemistry Chemical Physics 12.20 (2010), pp. 5219–5224. DOI: 10.1039/b924526j.

[274] A. Stamatovic et al. *Electron Attachment to Carbon Dioxide Clusters at Very Low Electron Energies*. In: The Journal of Chemical Physics 83.6 (1985), pp. 2942–2946. DOI: 10.1063/1.449830.

[275] E. Leber et al. *Vibrational Feshbach Resonances in Electron Attachment to Carbon Dioxide Clusters*. In: The European Physical Journal D 12.1 (2000), pp. 125–131. DOI: 10.1007/s100530070049.

[276] M. Lezius et al. *Production and Properties of CO_2 Cluster Anions*. In: Zeitschrift für Physik D Atoms, Molecules and Clusters 24.3 (1992), pp. 289–296. DOI: 10.1007/bf01425751.

[277] T. Sommerfeld and T. Posset. *Electron Attachment to CO_2 Clusters*. In: The Journal of Chemical Physics 119.15 (2003), pp. 7714–7724. DOI: 10.1063/1.1609395.

[278] A. R. Rossi and K. D. Jordan. *Comment on the Structure and Stability of $(CO_2)_2^-$*. In: The Journal of Chemical Physics 70.9 (1979), pp. 4422–4424. DOI: 10.1063/1.438018.

[279] M. Saeki, T. Tsukuda, and T. Nagata. *Ab initio Study of $(CO_2)_n^-$: Structures and Stabilities of Isomers*. In: Chemical Physics Letters 340.3-4 (2001), pp. 376–384. DOI: 10.1016/s0009-2614(01)00396-7.

[280] M. Saeki, T. Tsukuda, and T. Nagata. *Ab initio Study of $CO_2^- CO_2 \leftrightarrow C_2O_4^-$*. In: Chemical Physics Letters 348.5-6 (2001), pp. 461–468. DOI: 10.1016/S0009-2614(01)01146-0.

[281] T. Tsukuda, M. A. Johnson, and T. Nagata. *Photoelectron Spectroscopy of $(CO_2)_n^-$ Revisited: Core Switching in the 2<n<16 Range*. In: Chemical Physics Letters 268.5-6 (1997), pp. 429–433. DOI: 10.1016/s0009-2614(97)00223-6.

[282] M. J. Deluca, B. Niu, and M. A. Johnson. *Photoelectron Spectroscopy of $(CO_2)_n^-$ Clusters with 2<n<13: Cluster Size Dependence of the Core Molecular Ion*. In: The Journal of Chemical Physics 88.9 (1988), pp. 5857–5863. DOI: 10.1063/1.454548.

[283] M. L. Alexander et al. *Photodissociation of Mass-Selected $(CO_2)_n^-$ Clusters: Evaporation Leading to Magic Numbers in Fragment-Ion Distributions*. In: Physical Review Letters 57.8 (1986), pp. 976–979. DOI: 10.1103/physrevlett.57.976.

[284] J. Postler et al. *Electron Attachment to CO_2 Embedded in Superfluid He Droplets*. In: The Journal of Physical Chemistry A 118.33 (2014), pp. 6553–6559. DOI: 10.1021/jp503179d.

[285] C. E. Klots and R. N. Compton. *Electron Attachment to Carbon Dioxide Clusters in a Supersonic Beam*. In: The Journal of Chemical Physics 67.4 (1977), pp. 1779–1780. DOI: 10.1063/1.435044.

[286] C. E. Klots and R. N. Compton. *Electron Attachment to van der Waals Polymers of Carbon Dioxide and Nitrous Oxide*. In: The Journal of Chemical Physics 69.4 (1978), pp. 1636–1643. DOI: 10.1063/1.436738.

[287] J. Harnes et al. *Size of Free Neutral CO_2 Clusters from Carbon 1s Ionization Energies*. In: The Journal of Physical Chemistry A 115.38 (2011), pp. 10408–10415. DOI: 10.1021/jp206329m.

[288] M. Allan. *Selectivity in the Excitation of Fermi-Coupled Vibrations in CO_2 by Impact of Slow Electrons*. In: Physical Review Letters 87.3 (2001), p. 033201. DOI: 10.1103/physrevlett.87.033201.

[289] P. D. Burrow and L. Sanche. *Elastic Scattering of Low-Energy Electrons at 180° in CO_2*. In: Physical Review Letters 28.6 (1972), pp. 333–336. DOI: 10.1103/physrevlett.28.333.

[290] M. J. W. Boness and G. J. Schulz. *Vibrational Excitation in CO_2 via the 3.8-eV Resonance*. In: Physical Review A 9.5 (1974), pp. 1969–1979. DOI: 10.1103/physreva.9.1969.

[291] U. Henne and J. P. Toennies. *Electron Capture by Large Helium Droplets*. In: The Journal of Chemical Physics 108.22 (1998), pp. 9327–9338. DOI: 10.1063/1.476385.

[292] V. Laporta, R. Celiberto, and J. Tennyson. *Dissociative Electron Attachment and Electron-Impact Resonant Dissociation of Vibrationally Excited O_2 Molecules*. In: Physical Review A 91.1 (2015), p. 012701. DOI: 10.1103/PhysRevA.91.012701.

[293] S. Matejcik et al. *Electron Attachment to Oxygen Clusters Studied with High Energy Resolution*. In: The Journal of Chemical Physics 111.8 (1999), pp. 3548–3558. DOI: 10.1063/1.479637.

[294] D. Rapp and D. D. Briglia. *Total Cross Sections for Ionization and Attachment in Gases by Electron Impact. II. Negative-Ion Formation*. In: The Journal of Chemical Physics 43.5 (1965), pp. 1480–1488. DOI: 10.1063/1.1696958.

[295] G. J. Schulz. *Cross Sections and Electron Affinity for O^- Ions From O_2, CO, and CO_2 by Electron Impact*. In: Physical Review 128.1 (1962), pp. 178–186. DOI: 10.1103/physrev.128.178.

[296] L. G. Christophorou et al. *Determination of Electron-Capture Cross Sections with Swarm-Beam Techniques*. In: Journal of Chemical Physics 43.12 (2014), pp. 4273–4281. DOI: 10.1063/1.1696685.

[297] S. Matejcik et al. *Electron Attachment to Molecules and Clusters of Atmospheric Relevance: Oxygen and Ozone*. In: Plasma Sources Science and Technology 6.2 (1997), pp. 140–146. DOI: 10.1088/0963-0252/6/2/007.

[298] Y. Itikawa. *Cross Sections for Electron Collisions with Oxygen Molecules*. In: Journal of Physical and Chemical Reference Data 38.1 (2009), pp. 1–20. DOI: 10.1063/1.3025886.

[299] V. S. Prabhudesai, D. Nandi, and E. Krishnakumar. *On the Presence of the $^4\Sigma_u^-$ Resonance in Dissociative Electron Attachment to O_2*. In: Journal of Physics B 39.14 (2006), pp. L277–L283. DOI: 10.1088/0953-4075/39/14/L01.

[300] D. Spence and G. J. Schulz. *Three-Body Attachment in O_2 Using Electron Beams*. In: Physical Review A 5.2 (1972), pp. 724–732. DOI: 10.1103/PhysRevA.5.724.

[301] R. J. Celotta et al. *Molecular Photodetachment Spectrometry. II. The Electron Affinity of O_2 and the Structure of O_2^-*. In: Physical Review A 6.2 (1972), pp. 631–642. DOI: 10.1103/PhysRevA.6.631.

[302] T. D. Märk et al. *Electron Attachment to Oxygen Clusters at Low Electron Energies. Formation and Stability of $(O_2)_n^-$ and $(O_2)_nO^-$*. In: International Journal of Mass Spectrometry and Ion Processes 74.2 (1986), pp. 265–279. DOI: 10.1016/0168-1176(86)85011-X.

[303] T. D. Märk et al. *Low-Energy-Electron Attachment to Oxygen Clusters Produced by Nozzle Expansion*. In: Physical Review Letters 55.23 (1985), pp. 2559–2562. DOI: 10.1103/PhysRevLett.55.2559.

[304] T. Jaffke et al. *Mechanisms of Anion Formation in O_2, O_2/Ar and O_2/Ne Clusters; the Role of Inelastic Electron Scattering*. In: Zeitschrift für Physik D Atoms, Molecules and Clusters 25.1 (1992), pp. 77–85. DOI: 10.1007/BF01437522.

[305] S. Matejcik et al. *Vibrationally Resolved Electron Attachment to Oxygen Clusters*. In: Physical Review Letters 77.18 (1996), pp. 3771–3774. DOI: 10.1103/PhysRevLett.77.3771.

[306] R. Azria, L. Parenteau, and L. Sanche. *Dissociative Attachment from Condensed O_2: Violation of the Selection Rule $\Sigma^- \leftrightarrow \Sigma^+$*. In: Physical Review Letters 59.6 (1987), pp. 638–640. DOI: 10.1103/PhysRevLett.59.638.

[307] L. Sanche. *Dissociative Attachment in Electron Scattering from Condensed O_2 and CO*. In: Physical Review Letters 53.17 (1984), pp. 1638–1641. DOI: 10.1103/PhysRevLett.53.1638.

[308] G. Herzberg. *Molecular Spectra and Molecular Structure. Volume I: Spectra of Diatomic Molecules*. D. Van Nostrand, (1950).

[309] G. Rapior, K. Sengstock, and V. Baev. *New Features of the Franck-Hertz Experiment*. In: American Journal of Physics 74.5 (2006), pp. 423–428. DOI: 10.1119/1.2174033.

[310] M. Foltin, V. Grill, and T. Märk. *The Observation of Unusual Resonance Channels in the Electron Attachment to Mixed Argon-Oxygen Clusters*. In: Chemical Physics Letters 188.5 (1992), pp. 427–432. DOI: 10.1016/0009-2614(92)80842-Y.

[311] M. Renzler et al. *Resonant Electron Attachment to Mixed Hydrogen/Oxygen and Deuterium/Oxygen Clusters*. In: The Journal of Chemical Physics 147.19 (2017), p. 194301. DOI: 10.1063/1.5003428.

[312] H. Abdoul-Carime, S. Gohlke, and E. Illenberger. *Fragmentation of Tryptophan by Low-Energy Electrons*. In: Chemical physics letters 402.4-6 (2005), pp. 497–502. DOI: 10.1016/j.cplett.2004.12.073.

Acknowledgements

During the course of this thesis I could benefit of the diverse support of many people whom I would like to thank in the following.

The research was generously funded by the Fundação para a Ciência e a Tecnologia, Ministério da Ciência, Tecnologia e Ensino Superior (FCT-MCTES), Portugal, through scholarship grant number PD/BD/114452/2016. This work was also supported by the Radiation Biology and Biophysics Doctoral Training Programme (RaBBiT, PD/00193/2012); UID/FIS/00068/2019 (CEFITEC), UID/Multi/04378/2013 (UCIBIO). I thank Assoz. Prof. Stephan Denifl, University of Innsbruck, and Prof. Paulo Limão-Vieira, Universidade NOVA de Lisboa, for giving me the opportunity to work in this field of research. Having them both as supervisors certainly provided an environment for both technical training and personal growth. Additionally, I specifically thank Prof. Paul Scheier, University of Innsbruck, who always had an open door and was crucial for the success of this thesis. I am extremely grateful to both Andreas Mauracher and Michael Gatchell, to whom I was a frequent visitor in their office. They always took the time to discuss all my questions and ideas, also getting me to dig deeper into adjoining problems. I am grateful that the two of you offered to proof-read my dissertation. I was lucky enough to have had the chance to work together with many collaborators. Namely, Jaroslav Kočišek, Juraj Fedor and Michal Fárník whom I visited at the J. Heyrovský Institute of Physical Chemistry in Prague, Czech Republic; Linda Feketeová from the Université Claude Bernard, France; the working group of Prof. Janusz Rak from the University of Gdańsk, Poland, and the working group of Prof. Paulo Limão-Vieira, whom I all would like to express my sincere acknowledgements. Special thanks to Ana Cruz for guiding me through my time in Portugal so marvellously. Additionally, I very much appreciate the support of all group members from the AG Inelastische Elektronenstreuung. Especially Michl, Joschi, Anita, Julia, Bea and Alex for warmly welcoming me not only in the new working environment, but also in Tyrol. Also, Christine and João for joining in and adding their cheerful characters to it. A big thank you goes to the members of the AG nanobio, namely Josi, Stefan Raggl, Lorenz B. and K., Michael, Linnea (and Ben), green and tall Felix, Faro, little Paul, Sigi, Lukas, Arne, Fabio, and Marcelo. It was amazing working with you guys. The support given along the sometimes difficult path of my thesis will certainly not be forgotten. I owe a sincere thank you especially to Josi and little Paul for keeping an eye on that. I would like to give credit to Martin and Werner from the electronics workshop, without whom I would probably still be stuck in the laboratory. Of course, nothing would work the way it does without Chitra, who is the good and crazy soul, secretly running it all, I guess. Thanks!

Thanks to all my friends in Tyrol and in the Rhineland, for being the great people you are and for all the awesome time spent together. This is worth much more than just the perfect balance to work. This dissertation would not have been possible without the constant support of my family. A very warm thank you for always being there for me no matter what!

Declaration

I hereby declare that this PhD thesis is my own and autonomous work. All sources and aids used have been indicated as such. All texts either quoted directly or paraphrased have been indicated by in-text citations. Full bibliographic details are given in the list of works cited. This work is a cooperation between the Universität Innsbruck and the Universidade Nova de Lisboa and has not been submitted to any other examination authority than the aforementioned.

Innsbruck, 29 November 2019 Rebecca Meißner